



**HAL**  
open science

# Bottom-up fabrication of a plasmonic nanodevice for guiding light

Petra Ivaskovic

► **To cite this version:**

Petra Ivaskovic. Bottom-up fabrication of a plasmonic nanodevice for guiding light. Condensed Matter [cond-mat]. Université de Bordeaux, 2017. English. NNT : 2017BORD0580 . tel-01668475

**HAL Id: tel-01668475**

**<https://theses.hal.science/tel-01668475>**

Submitted on 20 Dec 2017

**HAL** is a multi-disciplinary open access archive for the deposit and dissemination of scientific research documents, whether they are published or not. The documents may come from teaching and research institutions in France or abroad, or from public or private research centers.

L'archive ouverte pluridisciplinaire **HAL**, est destinée au dépôt et à la diffusion de documents scientifiques de niveau recherche, publiés ou non, émanant des établissements d'enseignement et de recherche français ou étrangers, des laboratoires publics ou privés.

THÈSE PRÉSENTÉE  
POUR OBTENIR LE GRADE DE  
**DOCTEUR DE**  
**L'UNIVERSITÉ DE BORDEAUX**

ÉCOLE DOCTORALE DES SCIENCES CHIMIQUES  
SPÉCIALITÉ : Physico-Chimie de la Matière Condensée

Par Petra IVASKOVIC

**BOTTOM-UP FABRICATION OF A PLASMONIC  
NANODEVICE FOR GUIDING LIGHT**

Sous la direction de : Serge RAVAINÉ  
(co-directeur : Mireille BLANCHARD-DESCE)

Soutenue le 28 Avril 2017.

Membres du jury :

Mme ZAKRI Cécile,  
Mme RESSIER Laurence,  
M. BIDAULT Sébastien,  
M. PLUCHERY Olivier,  
M. VERLHAC Jean-Baptiste,  
M. RAVAINÉ Serge  
Mme BLANCHARD-DESCE Mireille,

Professeur, Université de Bordeaux,  
Professeur, INSA, Toulouse,  
Chargé de Recherche (HDR), CNRS,  
Maître de Conférences, UPMC,  
Professeur, Université de Bordeaux,  
Professeur, Université de Bordeaux,  
Directeur de Recherche, CNRS,

Président  
Rapporteur  
Rapporteur  
Examineur  
Examineur  
Directeur de thèse  
Invité







THÈSE PRÉSENTÉE  
POUR OBTENIR LE GRADE DE  
**DOCTEUR DE**  
**L'UNIVERSITÉ DE BORDEAUX**

ÉCOLE DOCTORALE DES SCIENCES CHIMIQUES  
SPÉCIALITÉ : Physico-Chimie de la Matière Condensée

Par Petra IVASKOVIC

**BOTTOM-UP FABRICATION OF A PLASMONIC  
NANODEVICE FOR GUIDING LIGHT**

Sous la direction de : Serge RAVAINÉ  
(co-directeur : Mireille BLANCHARD-DESCE)

Soutenue le 28 Avril 2017.

Membres du jury :

Mme ZAKRI Cécile,  
Mme RESSIER Laurence,  
M. BIDAULT Sébastien,  
M. PLUCHERY Olivier,  
M. VERLHAC Jean-Baptiste,  
M. RAVAINÉ Serge  
Mme BLANCHARD-DESCE Mireille,

Professeur, Université de Bordeaux,  
Professeur, INSA, Toulouse,  
Chargé de Recherche (HDR), CNRS,  
Maître de Conférences, UPMC,  
Professeur, Université de Bordeaux,  
Professeur, Université de Bordeaux,  
Directeur de Recherche, CNRS,

Président  
Rapporteur  
Rapporteur  
Examineur  
Examineur  
Directeur de thèse  
Invité



*To my family...*





## ACKNOWLEDGEMENTS

This work could not have been possible without the financial support of LAPHIA Cluster of Excellence and the joined efforts of Professor Serge Ravaine, Dr Renaud Vallée and Dr Mireille Blanchard-Desce.

I want to thank Dr Mireille Blanchard-Desce for giving me the opportunity to participate in this project and to learn many new things in the process.

I would especially like to thank my supervisor, Serge Ravaine, for his guidance, ideas and advice, which improved this work greatly, and made it possible to finish my doctorate.

The work of this thesis was divided between the Centre de Recherche Paul Pascal (CRPP) and Institut des Sciences Moléculaires (ISM) laboratories, which gave me the opportunity to interact with, and receive the assistance of, people working in varying fields of research.

From CRPP, I want to thank Dr Renaud Vallée for being so patient while helping me to understand the physics involved in this work. I also wish to thank Dr Atsushi Yamada who performed the simulations that gave rise to the experimental work presented in this thesis. Furthermore, I am grateful to my friends, Miguel Comesaña-Hermo, Alexandra Madeira, Sergio Gomez-Graña and Noelia Vilar-Vidal, who taught me the basics of nanoparticle synthesis. I want to thank them for their help and very useful discussions, that resulted in more successful experiments. To Hanbin Zheng, I give my thanks for being the best office-mate that I could ask for. Finally, I would also like to thank the students from my group, especially Mayte and Pierre-Etienne, for helping with everyday lab activities.

From ISM, I am particularly thankful to Jean-Baptiste Verlhac for being always available to discuss my work and give the ideas to improve it. I also thank him for his help with organic synthesis described in this work. To Maxime Klausen and Eduardo Cueto-Diaz, I thank them for their patience and willingness to explain to me the necessary organic chemistry, including fundamental principles.

I also have to thank our collaborators for their help in different areas. From ISM, I wish to thank David Talaga and Dr Sébastien Bonhommeau for performing the optical characterization of the samples. From Institut de Chimie & Biologie des Membranes & des Nano-objets (CBMN), I want to thank Juan Elezgaray for his help and efforts with DNA origami synthesis. From the University of Technology of Troyes, I thank Professor Renaud

Bachelot for hosting me in his lab and helping me to get more familiar with the equipment of the optics experiment.

I am very grateful to the members of the jury: Laurence Ressler, Cécile Zakri, Sébastien Bidault, Olivier Pluchery and Jean-Baptiste Verlhac. I thank them for giving their time to evaluate my work and for their useful comments and suggestions.

Over the last three years, I have also met amazing friends who filled the days with fun and laughter, making my stay in Bordeaux unforgettable. I thank the people who stayed with me from the beginning, especially Katerina and David, for their friendship and support. To my group of friends in CRPP, I thank them for the great moments we shared in the lab and in our free time. I am also grateful to Carlotta, Theo and Fernando for their tips concerning this manuscript.

The biggest “thank you” goes to my family, to my mom, my brother, grandparents and Nikola, for their encouragements, love, moral and financial support. Without them, it would not have been possible to move from my hometown and have this great Bordeaux experience. Finally, I have to thank Anida and Mathieu for staying around and helping me during the last months of my thesis, which was the hardest part, and full of different emotions, which was not always easy to handle.

## LIST OF ABBREVIATIONS

AA	Ascorbic acid
AFM	Atomic-force microscopy
AuHTs	Gold hollow nanotriangles
AuNRs	Gold nanorods
AuNTs	Gold nanotripods
CTAB	Cetyltrimethylammonium bromide
DCM	Dichloromethane
DFSM	Dark-field scattering microscopy
DNA	Deoxyribonucleic acid
dsDNA	Double-stranded DNA
EDX	Energy-dispersive X-ray spectroscopy
FDTD	Finite-difference time-domain
HRTEM	High resolution transmission electron microscopy
HyA	Hydroxylamine hydrochloride
LSPR	Localized surface plasmon resonance
NIR	Near-infrared
NMR	Nuclear magnetic resonance spectroscopy
NPs	Nanoparticles
PEG	Polyethylene glycol
PS	Polystyrene
PSS	Poly (sodium 4-styrenesulfonate)
PVP	Polyvinylpyrrolidone
SEM	Scanning electron microscopy
SP	Surface plasmon
SPPs	Surface plasmon polaritons
SPR	Surface plasmon resonance
ssDNA	Single-stranded DNA
TEM	Transmission electron microscopy
THF	Tetrahydrofuran
UV-Vis	Ultraviolet–visible spectroscopy



**TABLE OF CONTENTS**

Introduction.....	1
Motivation.....	3
Outline of the thesis.....	4
References.....	5
Chapter 1 : Bibliography review.....	7
Introduction.....	9
1. Nanoplasmonics.....	11
1.1. Surface plasmon polaritons.....	11
1.2. Localized surface plasmons.....	13
1.3. Coupling of surface plasmons.....	15
2. Nanoplasmonics for light manipulation.....	16
2.1. Plasmonic waveguides.....	17
2.2. Routing the light at the nanoscale.....	21
2.3. Energy loss and power compensation.....	27
3. Aim of the project.....	28
3.1. Computational simulations.....	28
3.2. Scope of the thesis.....	31
4. Conclusion.....	34
References.....	35
Chapter 2 : Synthesis of building blocks for plasmonic nanodevices.....	41
1. Introduction.....	43
2. Noble metal nanoparticles.....	44
2.1. Colloidal synthesis of noble metal nanoparticles.....	44
2.2. Tuning the optical properties of metallic nanoparticles.....	47
2.3. Self-assembly of plasmonic nanoparticles.....	49
3. Gold nanorods.....	50
3.1. Synthesis of gold nanorods.....	51
3.2. Characterization of gold nanorods.....	54
4. Gold hollow nanotriangles.....	55
4.1. Synthesis of the sacrificial template – Ag nanoprisms.....	56
4.2. Synthesis of Au-framed Ag nanoprisms.....	60
4.3. Synthesis of gold hollow nanotriangles.....	63

*Table of contents*

5. PdCu@Au core-shell nanotripods.....	66
5.1. Synthesis of PdCu nanotripods.....	67
5.2. Synthesis of PdCu@Au core-shell nanotripods.....	70
6. Conclusion.....	74
References.....	75
Chapter 3 : Directed assembly of gold nanorods.....	79
1. Introduction.....	81
2. AuNRs covalently linked through a thiol-terminated organic assembler.....	89
2.1. Synthesis of the organic assembler I.....	89
2.2. Synthesis of the organic assembler II.....	93
2.3. Phase transfer of AuNRs from water to DCM.....	95
2.4. AuNRs self-assembly in DCM.....	96
2.5. AuNRs self-assembly in water.....	98
2.6. Optical characterization of AuNRs trimers.....	104
3. Self-assembly of AuNRs via hydrophobic interactions.....	107
3.1. Synthesis of the organic assembler III.....	107
3.2. Synthesis of the organic assembler IV.....	108
3.3. Grafting of PS chains onto the tips of the AuNRs.....	109
3.4. AuNRs self-assembly via organic assembler III.....	110
3.5. AuNRs self-assembly via organic assembler IV.....	111
4. Conclusion.....	113
References.....	115
Chapter 4 : Assembly of gold hollow nanotriangles on DNA origami templates....	119
1. Introduction.....	121
2. Formation of a rectangular DNA origami.....	127
3. Modified DNA origami for the assembly of AuHTs and fluorescent dyes...	128
3.1. Synthesis of a nanostructure.....	129
3.2. Optical characterization of a nanostructure.....	132
4. Conclusion.....	136
References.....	137
Conclusions and perspectives.....	139
1. Conclusions.....	141
2. Perspectives.....	142

*Table of contents*

2.1. Fabrication of a plasmonic switching device based on a DNA origami template.....	142
2.2. Fabrication of a plasmonic switching device by surface-plasmon-triggered two-photon polymerization.....	145
References.....	149
Annexes.....	151
Annex 1 : Synthesis of the organic assemblers I-IV.....	153
Annex 2 : DNA strands used for the assembly of DNA origami.....	169
Annex 3 : Characterization techniques.....	173
References.....	176





# **INTRODUCTION**



## **MOTIVATION**

Nanotechnology, the science of manipulating matter at the near-atomic scale, has an enormous potential for the future development. In the modern society, the ever-increasing demand for smaller, faster and more efficient electronic devices is undeniable. Next generation technologies will thus require miniaturization and integration of existing devices and circuits.

Plasmonics is currently the key technology that enables the revolution in the integrated optical circuits. The intrinsic functionality of plasmonic nanodevices relies on the ability of metallic nanostructures to concentrate and manipulate light in the nanoscale regions. Owing to their unique optical properties, plasmonic nanoparticles offer powerful tools for optical signal processing, sensing and imaging [1].

However, the practical integration of plasmonic architectures into modern nanodevices requires the development of the synthetic techniques that provide the control over their optical features.

The most powerful mean for tailoring the optical properties is the control over plasmonic nanoparticle shape [2]. Additionally, the self-assembly of nanoparticle into the complex hierarchical architectures with a controllable manner provides a promising way to obtain the collective optical properties that exceed those of the individual subunits. In order to fully exploit the self-assembly of nanoparticles in technological applications, a high level of direction and control is required. Thus, the assembly of hybrid nanodevices from different photonic building blocks offers a route to create novel multifunctional nanomaterials for a wide range of applications such as optoelectronics, information transfer and storage, but also in enhancing certain optical processes as surface enhanced Raman scattering or fluorescence [3]–[5].

## **OUTLINE OF THE THESIS**

**Chapter 1** provides an introduction into the field of plasmonics, starting with the elementary description of surface plasmon polaritons and localized plasmons. A particular focus is put to light guiding and optical addressing via metallic nanostructures. In addition, the scope and the aims of this thesis are presented.

**Chapter 2** describes the synthetic routes that have been developed to prepare various noble metal nanostructures that have been employed as building blocks for the plasmonic nanodevice fabrication. In particular, the bottom-up synthesis and characterization of gold nanorods, gold hollow triangles and gold coated tripods are presented.

**Chapter 3** is devoted to the fabrication of gold trimers, *i.e.* three gold nanorods linked by different organic assemblers. Multistep syntheses of new organic molecules and their use as linkers are presented. The optical characterization of the fabricated gold trimers is also discussed.

**Chapter 4** describes the fabrication of nanoarchitectures composed of gold hollow triangles and fluorescent dyes assembled via DNA origami. The synthesis and modification of a DNA origami that enables the accurate positioning of gold hollow nanotriangles and fluorophores are shown. Light propagation in the fabricated nanodevice is investigated.

**Conclusions and perspectives** summarize the main results obtained during this thesis and describe some perspective of this work.

**Annexes** provide details about the multistep synthesis of the organic linkers, the list of the sequences used to fold a DNA origami, and the description of the equipment used for the structural and optical characterization of the samples.

## REFERENCES

- [1] D. K. Gramotnev and S. I. Bozhevolnyi, “Plasmonics beyond the diffraction limit,” *Nat. Photonics*, vol. 4, no. 2, pp. 83–91, 2010.
- [2] X. Lu, M. Rycenga, S. E. Skrabalak, B. Wiley, and Y. Xia, “Chemical synthesis of novel plasmonic nanoparticles,” *Annu. Rev. Phys. Chem.*, vol. 60, no. 1, pp. 167–192, 2009.
- [3] N. E. Motl, A. F. Smith, C. J. DeSantis, and S. E. Skrabalak, “Engineering plasmonic metal colloids through composition and structural design,” *Chem. Soc. Rev.*, vol. 43, no. 11, pp. 3823–3834, 2014.
- [4] C. Hamon and L. M. Liz-Marzán, “Hierarchical Assembly of Plasmonic Nanoparticles,” *Chem. - A Eur. J.*, vol. 21, no. 28, pp. 9956–9963, 2015.
- [5] O. Benson, “Assembly of hybrid photonic architectures from nanophotonic constituents,” *Nature*, vol. 480, no. 7376, pp. 193–199, 2011.



## **CHAPTER 1**

### **BIBLIOGRAPHY REVIEW**





## INTRODUCTION

In the age of the information and communication technology, there is a great need for faster information transport and processing capabilities.

Although the progress towards smaller, faster and more efficient electronic devices over the last five decades is undeniable, the scaling of those devices at nanometer level has brought up issues with a delay time for signal propagation and communication between different components. Optical interconnects have been suggested as an alternative because of their huge data carrying capacity, but they are limited in size by the laws of diffraction to about half a wavelength of light. The size mismatch between the two conventional technologies is an obvious obstacle to further advances in many areas of modern science, but can be overcome by the emerging field of plasmonics (Figure 1.1) [1], [2].

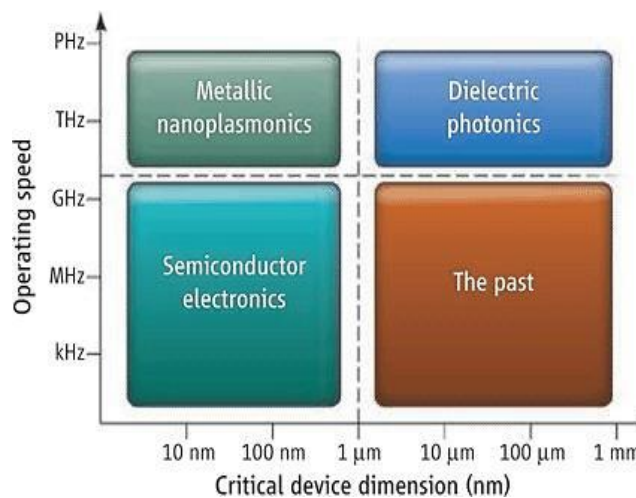


**Figure 1.1 : Plasmonics breaks the limits in the speed of nanoscale electronics and the size of terahertz dielectric photonics [3].**

The term plasmonics comes from the concept of plasmon, which refers to the resonant oscillations of free electrons in metal upon illumination. At the surface of a metal, the resonant interaction of charge oscillation and electromagnetic field of light creates surface plasmons (SPs), which are strongly influenced by boundary conditions. SPs are generated when a photon strikes the surface of a metal. They can be imagined as ripples created in a quiet pond upon tossing a rock. In this case, the ripples are composed of oscillating electrons with nanometer-scale wavelengths. Once in motion, these oscillations, or surface plasmons, can gather more light and carry it over substantial distance [4].

If such metallic structures are reduced to the nanometer scale, light can be concentrated and manipulated by objects much smaller than its wavelength [5].

SPs thus provide an opportunity to focus the light to tiny spots, direct and route it along complex circuits below the resolution limit of conventional technologies. As it offers the miniaturization of devices with a capacity of photonics, plasmonics can bridge the gap between existing devices and create high-speed, high-capacity and low-power next generation optical nanodevices.

Even though the first studies describing surface plasmons date back to the 1902, when Wood observed “anomalies” in spectra of optical reflection on metallic gratings [6], the history of plasmon based applications began 50 years after, when Ritchie predicted the existence of self-sustained collective excitations at metal surfaces [7]. In his pioneering work, he studied the impact of the film boundaries on these collective excitations and found the loss phenomena associated with excitation of surface collective oscillations. In the following years, the existence of those collective oscillations was experimentally confirmed by Powell and Swan [8]. Finally, in 1960, Stern and Ferrell extended Ritchie’s theory and linked it with surface plasmons [9]. From this date, scientists have been rediscovering the optical response of nanoparticles in a variety of different contexts, resulting in rapid advances in nanofabrication and subwavelength optical characterization, theoretical approaches and the expansion of plasmonics in broad areas of applications. The plasmonic nanostructures gained a great interest in data storage [10], microscopy [11], sensing [12], optoelectronics [1], optical computing [4], information transfer [13], but also disease diagnosis and therapy [14].

In the following sections, we will first introduce the topic of nanoplasmonics, and the different optical phenomena that make it so attractive for numerous applications. A particular focus will be put on surface plasmon generation, propagation and finally, manipulation and routing.

In the last section, we will describe the aim of our project dedicated to the fabrication of branched plasmonic nanostructures for the active guiding of light.

## **1. NANOPLASMONICS**

The most attractive research on SPs relies strongly on their ability to concentrate and channel light in subwavelength structures. The study of such optical phenomena in the nanoscale vicinity of metal surfaces is called nanoplasmonics [15].

When a bulk material is exposed to an external electromagnetic field, the charge inside it is set in motion. Electrons displace with respect to the lattice ions, creating the charges at the opposite surfaces. Due to the attraction forces between the charges, there is also a restoring force, which forms an electron oscillator. When the applied electromagnetic field is at the right frequency, its oscillations can couple to an oscillatory mechanical motion of charges in metal, creating a surface plasmon [16].

Also, SPs can be strongly confined at the surface of metallic nanoparticles. This effect, known as localized surface plasmon (LSP), occurs when the electrons in nanoparticle respond to illumination by absorption and radiation, enhancing the electromagnetic field around the nanoparticle. Both features of surface plasmons will be reviewed in the following sections.

### **1.1. Surface plasmon polaritons**

Propagating surface plasmons, also called surface plasmon polaritons (SPPs), are electromagnetic waves that propagate along the planar interface between a conductive metal and dielectric (a non-conductive medium like air or glass). Propagation arises from their hybrid nature - coupling between surface charges and electromagnetic field in the dielectric medium, which leads to different features of SPPs mode [17]. The basics of surface plasmons are shown in Figure 1.2.

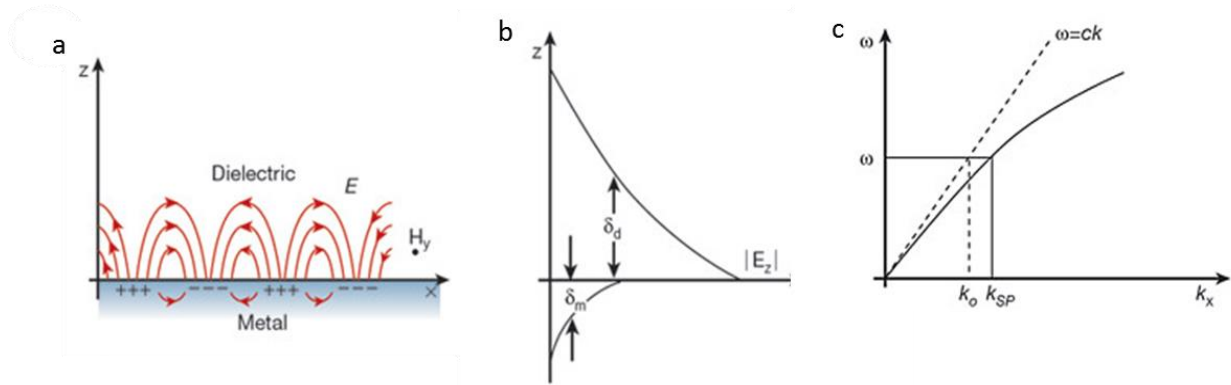


**Figure 1.2 : (a) Hybrid nature of SPPs – both electromagnetic wave and surface charge character at metal–dielectric interface. (b) The perpendicular field  $E_z$  decays exponentially with a decay length  $\delta_d$  in the dielectric and a decay length of  $\delta_m$  in the metal. (c) Momentum mismatch between the surface plasmon mode and a free space photon of the same frequency [17].**

SPPs can propagate at the interface as surface bound electromagnetic waves in single, flat interfaces or in dielectric/metal multilayers system. The intensity of those electromagnetic waves is maximal at the interface and decays exponentially into both the metal and the dielectric as the distance from the interface increases. In the dielectric medium, perpendicular to the surface of metal, the decay length into the dielectric ( $\delta_d$ ) is in range of the half wavelength of the light used, while the decay length into the metal ( $\delta_m$ ) is limited by the certain depth beyond which the electromagnetic field cannot penetrate in metal, so-called skin depth (Figure 1.2) [17].

Another significant feature of SPPs is that on a planar surface, the wave vector of the SP,  $k_{SP}$ , is always higher than the one of the electromagnetic wave of the same frequency propagating in the free space,  $k_0$ , where  $k_0 = \omega/c$  (Figure 1.2). The increased momentum of the SPP occurs due to the strong interaction between light and surface charges. Due to the larger propagation constant, SPPs on such interfaces cannot be excited directly by light propagating in the dielectric, and they cannot radiate into the dielectric. Thus, SPPs are also called “dark waves”. The momentum mismatch between the SPP mode and incident light can be overcome by modifying the wavevector of the incident light using different optical techniques, such as prism, grating or waveguide coupling to enhance the momentum of incident light or near-field excitation [18].

Owing to their unique optical properties, SPPs exhibit a great potential in a variety of applications. Their ability to control light at a scale much lower than its wavelength makes them an interesting tool in near-field optics.

Moreover, generation of SPPs enhances the electromagnetic field in the metal-dielectric interface, resulting in their extreme sensitivity to surface conditions. This sensitivity is a point of interest in the development of different surface plasmon polariton-based devices, because it is responsible for surface-enhanced optical phenomena such as Raman scattering and fluorescence. Such devices are commonly used for chemical and biological sensing, but as well in data storage and solar cells [19].

## 1.2. Localized surface plasmons

For centuries, humans have been using nanoparticles and their plasmonic effects in the creation of ornamental goblets and other stain glass without knowledge of their microscopic structure.

One of the oldest examples is the Lycurgus Cup, which dates from the fourth century A. D. When the cup is viewed in ambient lighting, the plasmonic scattering gives its green color, but when illuminated from the inside, it appears red (Figure 1.3). This effect occurs due to its transmission and absorption at longer and shorter wavelengths, respectively. Today, it is known that the dichroic nature arises from the gold and silver embedded in the glass and that the light scattering is attributed to localized surface plasmon resonance (LSPR) [20].



**Figure 1.3 : The Lycurgus cup in reflected (green) and transmitted (red) light [20].**

Unlike the SPPs, which propagate along a flat metal-dielectric interface, localized plasmon modes are stationary oscillations of the surface charge density at the boundaries of a metallic particle smaller than the wavelength of light (Figure 1.4).

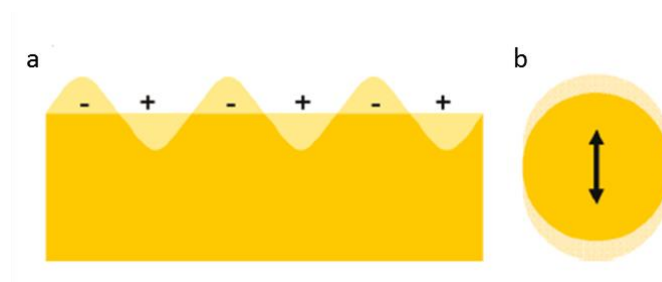


**Figure 1.4 : A scheme of (a) surface plasmon and (b) localized surface plasmon [21].**

When the incident light interacts with a metallic nanoparticle, its electric field periodically displaces the electrons inside the nanoparticle with respect to the lattice ions, creating charges at opposite surfaces which then feel repulsive forces. Due to the attraction between electrons and metallic nuclei, conduction electrons at the surface of the metal oscillate coherently in resonance with the incident light frequency. Those collective oscillations of electrons create a LSPR at the surface of the metallic nanoparticle (Figure 1.5) [22], [23].

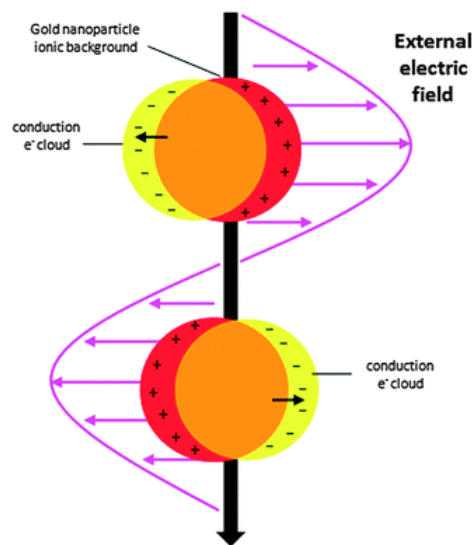


**Figure 1.5 : Collective oscillations of conduction electrons in a spherical metallic nanoparticle demonstrating the displacement of the conduction electron cloud relative to the nuclei [24].**

The optical extinction of noble metal nanoparticles has a maximum at the plasmon resonant frequency, which occurs in the visible or near-infrared part of the spectrum. Since the closed geometrical boundaries of nanoparticles sustain localized oscillations of the surface, LSPR response of metal nanostructures depends on their size and shape, but also on the chemical composition and refractive index of the nanoparticles and on the nature of the surrounding

environment. Variations of those parameters provide a powerful tool for controlling and manipulating the LSPR response, because even the slightest changes in aspect ratio or corner sharpness can have a large impact on the optical properties of nanoparticles [25].

The ability of LSPR to localize and enhance optical fields around the nanoparticle makes them very attractive in different applications such as surface-enhanced Raman scattering (SERS), fluorescence enhancement, refractive index (RI) measurement, biomolecular interaction detection and plasmon resonance energy transfer (PRET) [26].

### 1.3. Coupling of surface plasmons

Light-induced charge polarization on the nanoparticle surface leads to resonantly enhanced electromagnetic field inside the nanoparticle. Consequently, the concentration of EM energy strongly enhances the EM field in the immediate vicinity of the nanoparticle. When nanoparticles are in close proximity, their localized modes can thus couple via electromagnetic interactions, resulting in coupled plasmon oscillations.

For metallic particles much smaller than the wavelength of the exciting light, plasmon excitations produce an oscillating dipole field. Thus, each excited particle acts as an electric dipole, and an array of particles can be considered as an array of interacting dipoles. Due to electromagnetic interactions between the localized modes, nanoparticle assemblies induce a change in spectral position, width or amplitude, when compared to the single particle.

Two types of interparticle electromagnetic coupling can be distinguished by the magnitude of the distance between the nanostructures ( $d$ ): near-field and far-field coupling. If the particles are closely packed in a chain ( $d \ll \lambda$ ), they interact through their near-fields, while an increase of the inter-particle distance ( $d \approx \lambda$ ) induces a transition to far-field coupling. Once the inter-particle distance exceeds  $\sim 2.5$  times the particle size, the particles behave as isolated [27]–[29]. In small particle arrays, the coupling occurs mainly in the near-field.

The direction of coupling-induced shift of the plasmon resonance is determined by the Coulomb forces associated with the polarization of the incident light. For the longitudinal modes, the inner restoring force in each particle is weakened owing to the attractive forces between two charges of adjacent nanoparticles (Figure 1.6 b). Thus, the plasmon resonance maximum is red-shifted in comparison with the resonance of an individual particle. In



contrast, for the excitation of the transverse mode, the charge distributions of adjacent nanoparticles act cooperatively, increasing the restoring force, and causing the blue-shift of the LSP (Figure 1.6 c) [30], [31].

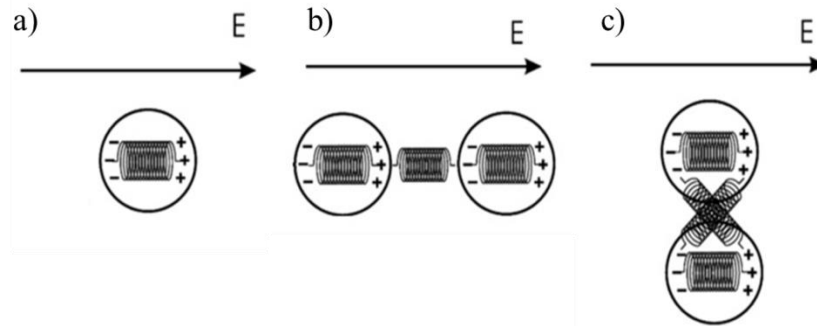


**Figure 1.6 : Electromagnetic interaction between closely spaced nanoparticles: (a) an isolated particle, (b) a pair of close particles with the polarization of the exciting field parallel to the long particle pair axis and (c) orthogonal to the long particle pair axis [32].**

In addition, the shifts in a resonance energy strongly depend on the geometry of the particle array, its length and the interparticle distance [18].

In a large array of nanoparticles, each particle is exposed to the near-field of a large number of particles and the coupling is stronger, leading to a larger red-shift. Moreover, the red shift can be induced by shortening the distance between the nanoparticles in the assembly, due to the rapid decay of a nanoparticle's near-field with distance [31].

The interparticle plasmon coupling thus offers an additional tool for tuning the NPs optical response. Great advances have been made in the fabrication of plasmonic assemblies by bottom-up and top-down techniques for different applications, such as surface enhanced Raman scattering (SERS), biosensing and medical applications [30].

## 2. NANOPLASMONICS FOR LIGHT MANIPULATION

For future development of chip-scale electronics and photonics, it is essential to provide communication channels that allow controlled information and energy transport at the nanometer level. Plasmon waveguides, fabricated from metallic NPs, offer a unique way to

concentrate and guide EM waves at the nanoscale, which makes them attractive as building blocks for modern nanodevices [33], [34].

However, the full integration of optical waveguides into all-optical circuits requires additional active control over the plasmonic response. The creation of active plasmonic devices like modulators and switchers, in which plasmonic signal can be specifically addressed as well as switched on and off, presents a next big step towards the complete development of the next-generation chips [35].

Another obstacle that holds back the implementation of plasmon waveguides in compact nanodevices is the propagation loss due to increased mode confinement.

In many cases, the attenuation of the electromagnetic wave due to absorption in the metal limits the energy propagation distance to several micrometers. Consequently, not all of the mentioned waveguides are able to guide the subwavelength plasmonic signal equally.

These energy losses can be compensated through the improvements of near-field coupling, or the use of low-loss substrates [36].

In the following sections, we will describe energy propagation in several plasmonic waveguides. Then, the propagation through sharp corners and the active switching of plasmonic signal will be reviewed. Finally, we will look at the possibilities to compensate the energy loss in such systems.

## **2.1. Plasmonic waveguides**

In the last 20 years, many researches have been focusing their attention to the light guiding and optical addressing via metallic nanostructures.

Various types of plasmon waveguides have been fabricated, mainly by top-down nanolithography techniques. Chains of nanoparticles, thin metal films, metal slits, grooves, nanowires and sharp metal wedges have been proposed to guide the electromagnetic energy for potential plasmonic nanodevices [37].

Although the use of such metal nanostructures as waveguides was described in different theoretical studies [38], [39] and numerical simulations [40], [41], experimental proofs remained rare.

Maier and co-workers [42] were the first ones to confirm the subwavelength-sized light guiding via near-field coupling between adjacent plasmonic nanoparticles over around a 0.5 $\mu\text{m}$  distance. By electron-beam lithography, they fabricated plasmonic waveguides consisting of silver nanorods with dimensions of 90 nm  $\times$  30 nm and a constant space of 50 nm between adjacent rods (Figure 1.7 a). The plasmon waveguides arranged in a grid are shown in Figure 1.7 c. The long axis of the individual nanorod was oriented perpendicular to the waveguide chains axis to allow an increased near-field coupling.

The scheme of the experiment is shown in Figure 1.7 b. The tip of a scanning near-field optical microscope (SNOM) was used as an illumination source for local excitation of the nanoparticle plasmon waveguide. Upon the excitation of one rod, the localized plasmon modes of rods in an array coupled via electromagnetic interactions, resulting in energy propagation.

Such electromagnetic energy transport through an array of particles was probed by randomly dispersing fluorescent nanospheres, which show strong absorption near the excitation wavelength, on the grid containing the waveguides. The excitation propagation along the array of nanostructures excited the fluorescent probes, whose fluorescence intensity was then collected in the far-field. The energy transport was visualized via the increase of the spatial width of the fluorescent probe close to a plasmon waveguide, compared to the width of an isolated probe (Figure 1.7 d) [43].

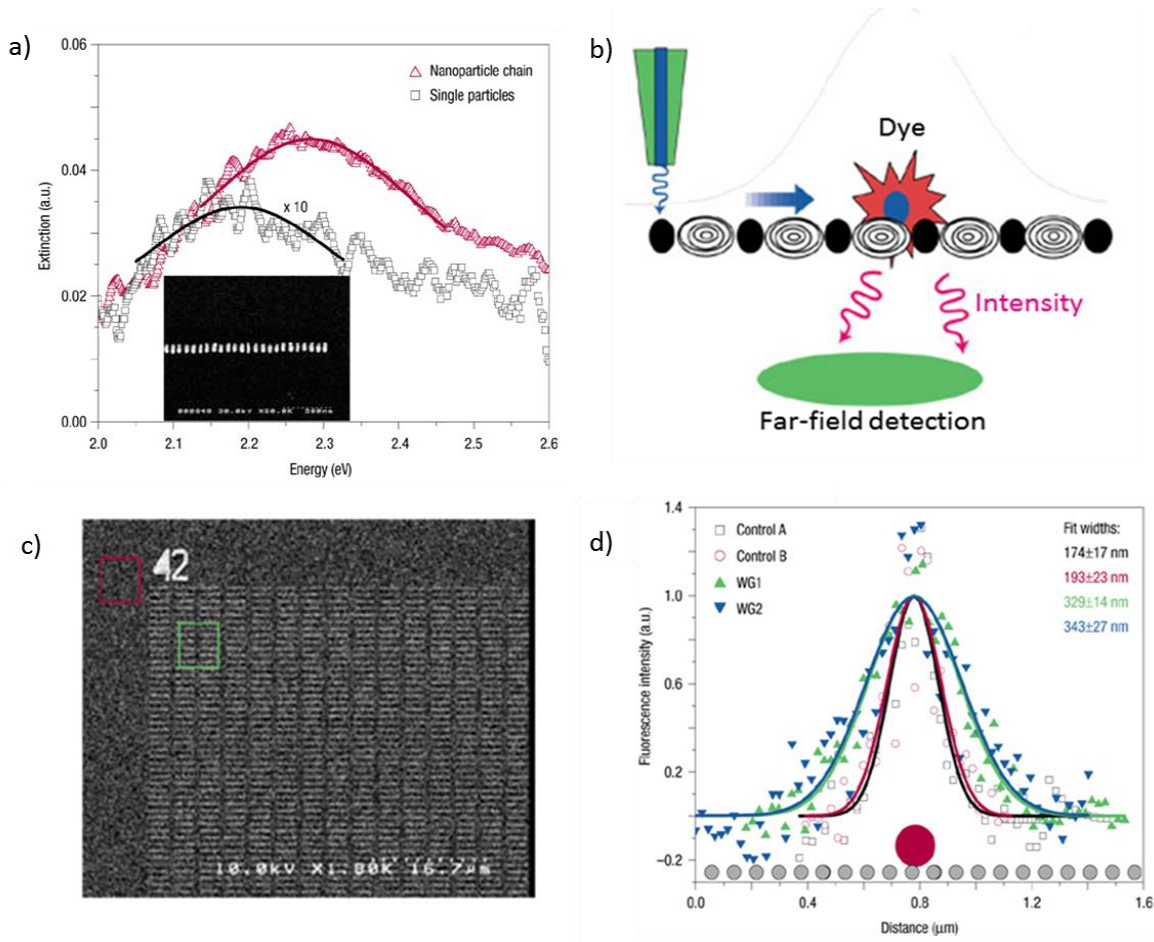


**Figure 1.7 : Light guiding via near-field coupling between adjacent plasmonic NPs: (a) Plasmon resonance of silver rods and a chain of closely spaced rods upon the transverse illumination with an inset showing a SEM image of a waveguide; (b) scheme of the experiment showing the local excitation and detection of the EM energy transport in a plasmonic NPs array; (c) SEM image of the waveguides arranged in a grid where red box shows the control area outside the grid, with free fluorescent probes only, and the green box shows an area where probes are in close proximity to the waveguides; (d) compared intensities of the fluorescent signals for the control probes and for the probes close to the plasmonic waveguides [42].**

Bozhevolnyi *et al.* [44] demonstrated the guiding of the SPPs along the grooves of a triangular shape milled into a gold surface. They experimentally confirmed the guiding of a plasmonic signal through 0.6 μm wide and 1 μm deep nanogrooves with the propagation length on the order of 100 μm. Examples of SPP propagation for functional structures such as waveguide splitters and interferometers is shown in Figure 1.8.

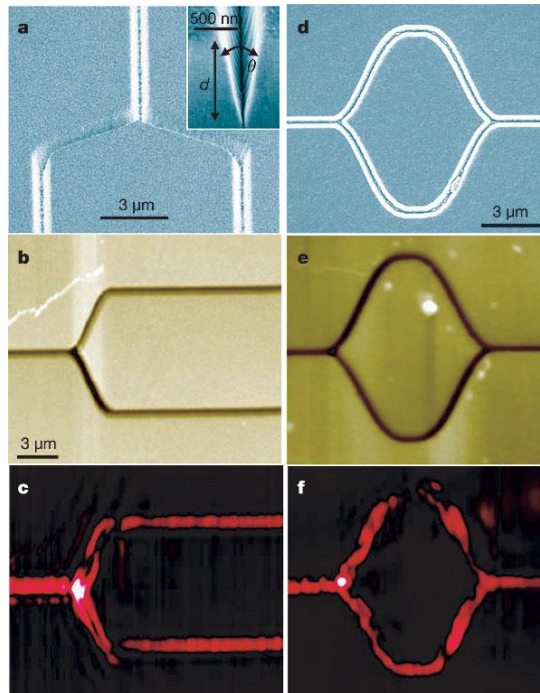


**Figure 1.8 :** (a, d) SEM images; (b,e) topographical and (c,f) near-field images of SPP groove waveguides milled into a metal film. Inset shows depth and angle of the groove [18].

Few examples of plasmonic waveguides synthesized by bottom-up synthetic approach (i.e. colloidal chemistry) include metal nanowires. For example, Ditzbner *et al.* [45] showed the SPPs propagation along silver nanowires. When they focused a laser beam onto one end face (polarization oriented along the nanowire axis) of a 18.6  $\mu\text{m}$  long nanowire, a part of the incident laser intensity was scattered into a surface plasmon mode, propagating towards the distal end of the wire. A part of the plasmon intensity was there scattered to light, which was then detected with a conventional optical microscope (Figure 1.9). The chemical synthesis of those nanostructures provided a better control over crystal and surface structure compared to the lithography fabrication, leading to minimized energy losses due to the metal absorption and thus a longer propagation length ( $\sim 10\mu\text{m}$ ).

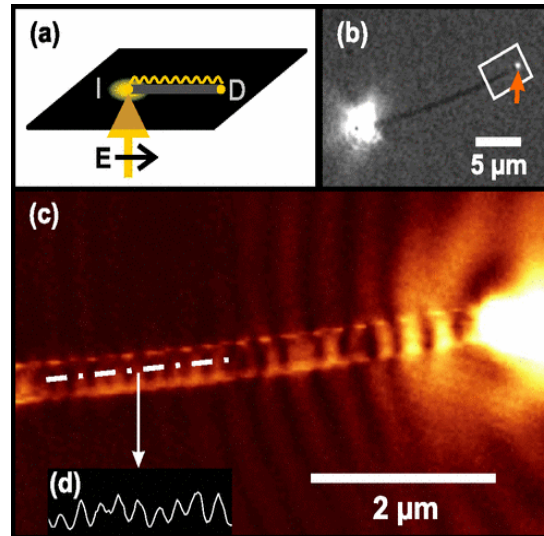


**Figure 1.9 : Silver nanowire as a plasmonic waveguide: (a) optical excitation scheme, where I is input and D is distal end of the wire; (b) microscopic image of the nanowire - the bright spot is focused exciting light, while the arrow points to light scattered from the distal wire end; (c) near-field image of an area in the white box in (b); (d) cross-cut along the chain shown in (c) [45].**

## 2.2. Routing the light at the nanoscale

Scaling down existing optical devices to ultimate limits for the fabrication of new, highly integrated photonic circuits strongly relies on nanoarchitectures able to manipulate the light at the nanoscale. However, more complex, functional elements such as controllable plasmon routers, multiplexers and switchers, are necessary for the development of modern information technologies. The key to the development of nanodevices is the fabrication of active components able to specifically address and route the plasmonic signal, as well switch it between on and off position.

Owing to their ability to simultaneously support different wavelengths of light and manipulate them independently, plasmon waveguides are good candidates for active switchers or routers in plasmonic circuits [46], [47]. However, a deep understanding of the ability of waveguides to bend the direction of a traveling wave at corners and intersections is necessary for the design of modern plasmonic switches.

Maier *et al.* [22] showed the design of an all-optical switch based on the EM energy guiding through corners and tee structures via the near-field coupling of adjacent NPs. By calculating

the power transmission coefficients ( $\eta$ ) for energy transport around such elements, they showed that coefficients close to 100 % are possible for propagation around  $90^\circ$  corners for certain polarizations, and that lossless signal splitting can occur in tee structures (Figure 1.10). Those coefficients depend on the geometry of the structure, the frequency, and the polarization directions of the plasmon waves which enter and exit a structure [22], [39].

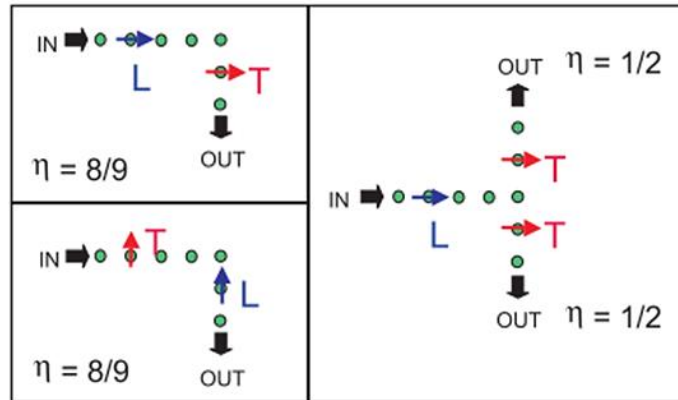


**Figure 1.10 : Calculated power transmission coefficient in nanoparticle chain for a  $90^\circ$  corner (left) and a tee structure (right) for the longitudinal (L) and transverse mode (T). The  $\eta$  value of 1 corresponds to 100 % transmission [22].**

Maier's study confirmed the ability of plasmon waveguides to transport EM energy around  $90^\circ$  corners and split via tee structures. However, the energy cannot propagate selectively in only one branch of the multi-branched structures. Due to the plasmon coupling effect, the energy propagates equally in the two branches of the nanoarchitectures, which then works only as a passive light guiding system.

Hence, the addressable routing of light and its switching between different elements needs to be developed to create controllable plasmonic structures with active functionality.

One possible way to selectively route the plasmonic signal into a branched metallic nanostructure is to control the polarization of the incoming light, as shown by Fang et al [46]. The branched nanowire system studied by the authors for directional guiding is shown in Figure 1.11.

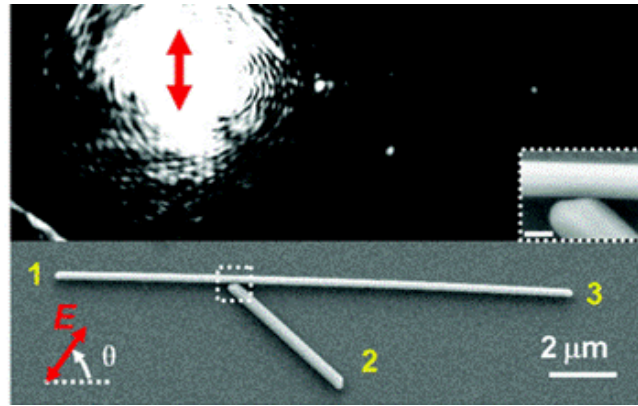


**Figure 1.11 : Optical image of branched silver nanowire structure excited by a laser. The inset shows a SEM image of the branch intersection, where the scale bar is 200 nm. The gap between the two wires is 10 nm [46].**

Upon illumination of end 1 of the wire, launched SPPs propagate and the light can be controlled to emit from end 2 or 3 through varying the illuminating polarization. For specific polarizations, emission of the main wire can be at the minimum, while the one of the side wire is at maximum, and vice versa.

Moreover, branched nanowires can selectively route SPPs launched with different free-space wavelengths towards different ends of the structure, as shown in Figure 1.12. When two lasers with different wavelengths, 633 and 785 nm, were focused at the end 1 of the structure, the rotation of the polarizer caused a 633 nm laser coming out mainly from the end 2 and a 785 nm laser coming out from the end 3. Such routers, which can work simultaneously for multiple wavelengths, fulfill the requirements given for the full development of future nanophotonic devices, circuits, and networks.



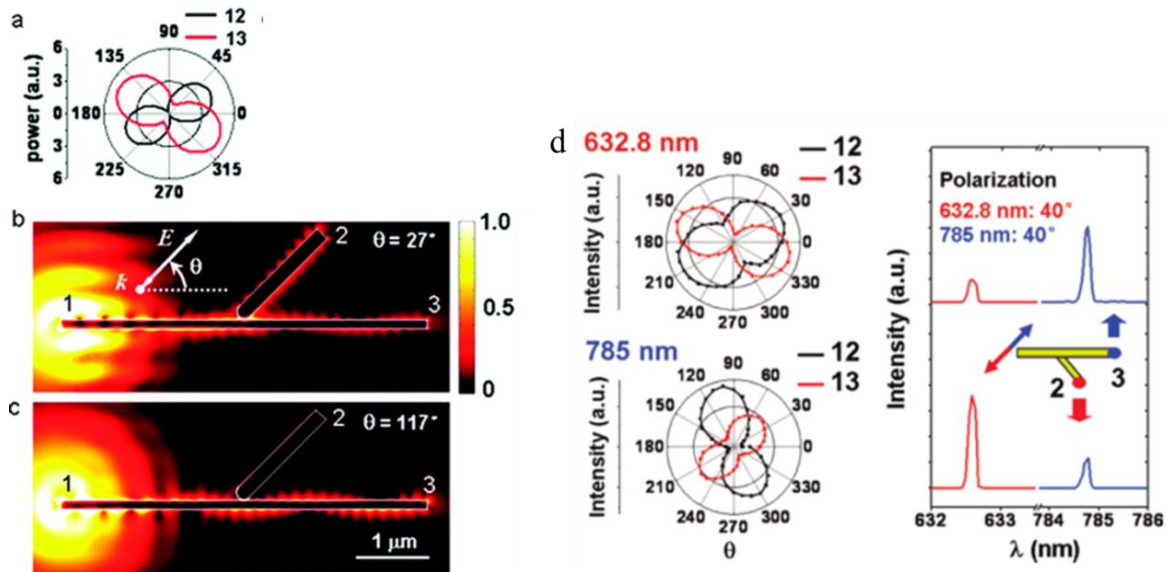


**Figure 1.12 :** (a) Emission power at the ends of the main and the branch wire as a function of the incident polarization angle  $\theta$ . Emission of the branched wire is maximal when  $\theta=27^\circ$  and minimal when  $\theta=117^\circ$ ; (b,c) local electric field distributions at the maximum (b) and minimum (c) emission of a branch wire; (d) routing for multiple wavelengths - emission intensity from ends 2 and 3 as a function of the polarization angle for 633 and 785 nm wavelength excitation and the corresponding spectra for the wires 2 (up) and 3 (down) [46].

Tuning the dielectric function of the surrounding medium is another approach to control the plasmonic response of nanostructures. Such active surrounding medium can be obtained by employing liquid crystals (LCs), stimuli-responsive polymers or photochromic molecules. For example, Hsiao *et al.* [48] described an all-optical switch composed of Au nanodisk arrays embedded in a photoresponsive LC (Figure 1.13). To induce the switching effect, they used azobenzene derivative as guest material in a LC matrix. Azobenzene molecules were used because they undergo a reversible photochemical reaction between two configurations, *trans*- and *cis*, inducing the realignment of LCs and thus changing the refractive index of the surrounding medium and the LSPR of the Au nanodisks.

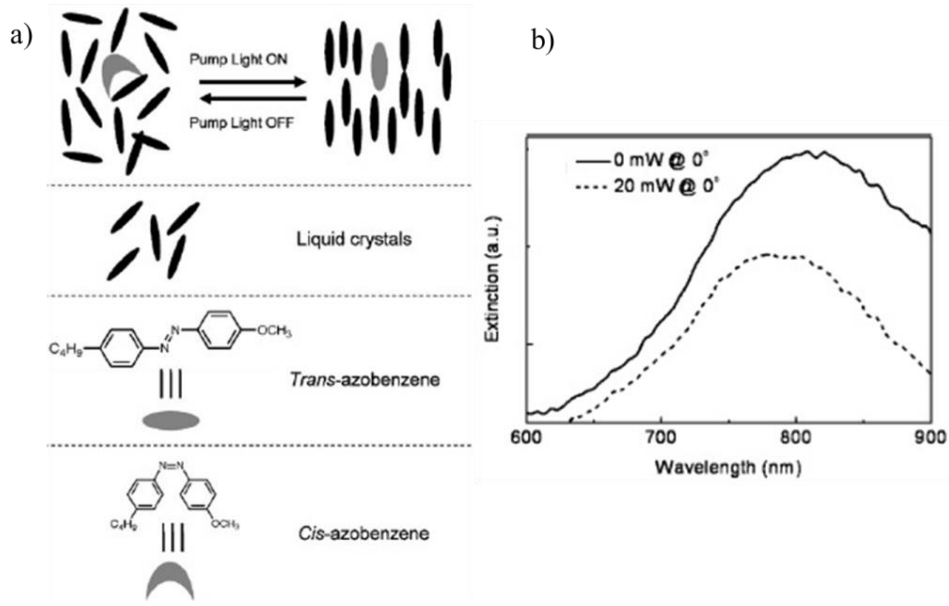


**Figure 1.13 : a) Phase transition process in photoresponsive LCs; b) extinction spectra of a photoresponsive LC/Au nanodisk array before (solid curve) and after illumination at normal incidence (dashed curve) [48].**

D. Neuhauser and co-workers [49]–[52] have investigated the guiding of plasmonic current via single molecules. Their studies led to the emergence of a new field, named nanopolaritonics. It refers to the ability of dipolar matter such as dye molecules to control the propagation of surface plasmon-polariton waves along metal nanostructures. In such energy transfer, the plasmon firstly affects the molecule by inducing electronic oscillations, and the molecule in turn affects the plasmon propagation through near-field interactions.

In their pioneering work, Neuhauser and Lopata [49] showed that a molecule that has an excitation energy similar to the plasmon resonance frequency of the metal can direct the motion of an electromagnetic radiation. Their system was composed of metal dots in a forklike arrangement, coupled to a two level system with a large transition-dipole moment. By varying the strength and orientation of the molecule, as well as its position with respect to the dots array, they controlled the path of the polariton flow in the forklike junction (Figure 1.14).

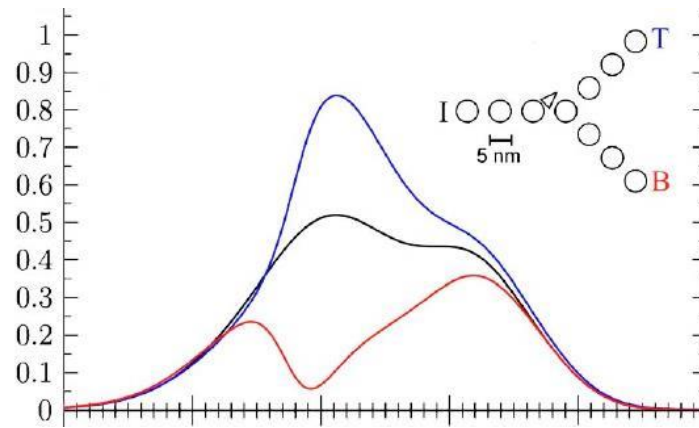


**Figure 1.14 :** A switching forklike junction, which is based on the coupling with a dipolar molecule (represented by the arrow) to guide a polarized polariton into one of two possible output paths (here the top one). Transmission spectra through the top and bottom branches are shown in blue and red, respectively. The transmission spectrum for the device without the molecule is shown in black. In this case, the output signals in both branches are identical [49].

More recently, Neuhauser [53] simulated the selectivity of plasmonic motion along a continuous Y-shape gold structure in the presence of a large number of molecules. He considered two cases – first where the space outside the Y-shape structure was filled with aligned molecules, and second where the gold structure was coated with a thin layer of molecules. For both cases, he observed that even at low molecular densities, the energy transport is significantly affected. At low molecular densities, an overall reduction in plasmonic transfer was observed, while the higher densities induced the selectivity due to the hybridization of the molecular and plasmonic field (Figure 1.15).

The field of nanopolaritonics, which enables the control over light transport by changing the direction of the guiding molecular dipoles through an external stimulus, represents a step forward toward light manipulation at the nanoscale. However, the controllable and addressable routing and multiplexing of light remains a big challenge and thus offers an attractive subject for further investigations.

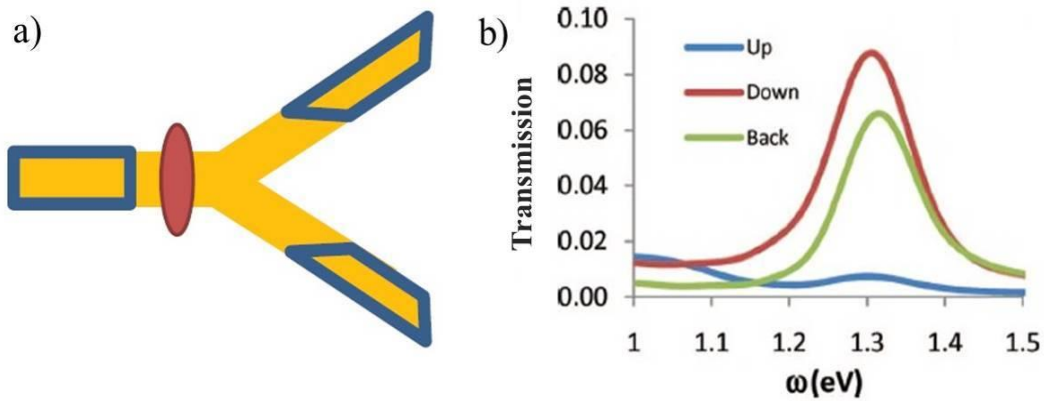


**Figure 1.15 :** a) Schematic illustration of the Y-shape gold structure. The red circle indicates the spot where an external electric field pulse is applied. The boxed regions show where the currents are measured. b) Energies in the two arms (up and down) and in the back arm as a function of frequency for a Y-shape gold structure in a space filled with aligned dipole molecules. For a high molecular density, a strong selectivity arises from the plasmon-dipole interaction [53].

### 2.3. Energy loss and power compensation

The attenuation of the SPPs propagating through a plasmonic waveguide due to the absorption in the metal limits their integration to compact optical circuits.

There is a trade-off between the confinement and loss - the more strongly the optical mode is confined to the metallic interface, the greater is the overlap with the metal, resulting in energy dissipation [54]. For example, nanoparticle arrays and nanowire waveguides can significantly enhance the confinement, but with large attenuation losses, which limits the light propagation length to few micrometers or less. On the other side, low loss over a propagation length of a few millimeters is possible in waveguides such as thin metal films embedded in homogeneous dielectric background, but the associated fields are weakly confined in the perpendicular direction [18].

Although some loss compensation can be realized through the optimization of the nanostructure synthesis with improvements of the geometry, material and structural imperfections, optical loss is also determined by the physical properties of the metal. Thus, further studies dedicated to the development of novel loss compensation methods are required.

Recently, hybrid plasmonic waveguides that consist of a metallic region separated from a dielectric zone with a high refractive index by a low index nano-slot, have been proposed to compensate the propagation losses. The low-index gap between the metal and the dielectric facilitates the hybridization of dielectric and plasmonic modes, allowing the efficient nanoscale light transport with reasonable propagation distances [36], [55], [56].

Another approach to simultaneously increase the localization of the field and the propagation length is the introduction of an optical gain medium in the structure. It was confirmed both theoretically and experimentally that metal nanostructures embedded into a medium with optical gain, such as dye molecules, quantum dots or fluorescent polymers can overcome confinement-loss trade-off [57].

### **3. AIM OF THE PROJECT**

The work-package ‘Nanopolaritonics’ of the InPhotArch (Integrated Photonics Architectures) LAPHIA project constitutes the frame of this thesis.

The overall objective of the project is to investigate the complex EM energy transfer in branched gold nanostructures by promoting the path selectivity via plasmon-dipole interaction.

Even though light routing in Y-shape gold nanostructure (engineered by top-down approaches) in the presence of molecules have been extensively studied theoretically by D. Neuhauser, nanoarchitectures comprising molecules and metallic nanoparticles produced by colloidal synthesis have not been investigated either theoretically or experimentally. Thus, predictions about path selectivity of light in Y-shaped nanostructures have been performed to guide the synthesis of the building blocks required for the nanodevice fabrication.

#### **3.1. Computational simulations**

In order to predict the path selectivity of light in the Y-shape gold nanodevice, computational simulations of the propagation of an electromagnetic pulse through a Y-shape gold structure overfilled with anisotropic material were performed. The predictions have been realized by Atsushi Yamada, a postdoc engaged for this purpose in the LAPHIA project.

Finite-Difference Time-Domain (FDTD) method was used for calculating the propagation of the electromagnetic field through the material. The time evolution of the electromagnetic field was described by solving Maxwell equations on a grid. Materials were treated classically and represented by a dielectric tensor (for the anisotropic molecular medium) and a Drude-Lorentz model (for gold). This method was applied to the system shown in Figure 1.16 a.

The system was composed of three gold nanorods combined in a Y-shape structure, surrounded by an anisotropic molecular medium with molecular polarization direction oriented toward the right-top gold rod, employed to create a change in the direction of a propagating light pulse. The length and the diameter of the gold rod were 20 nm and 10 nm, respectively. Each rod was separated by 5 nm from the center of the Y-shape and oriented with an angle of  $120^\circ$  one from the other (Figure 1.16 b).

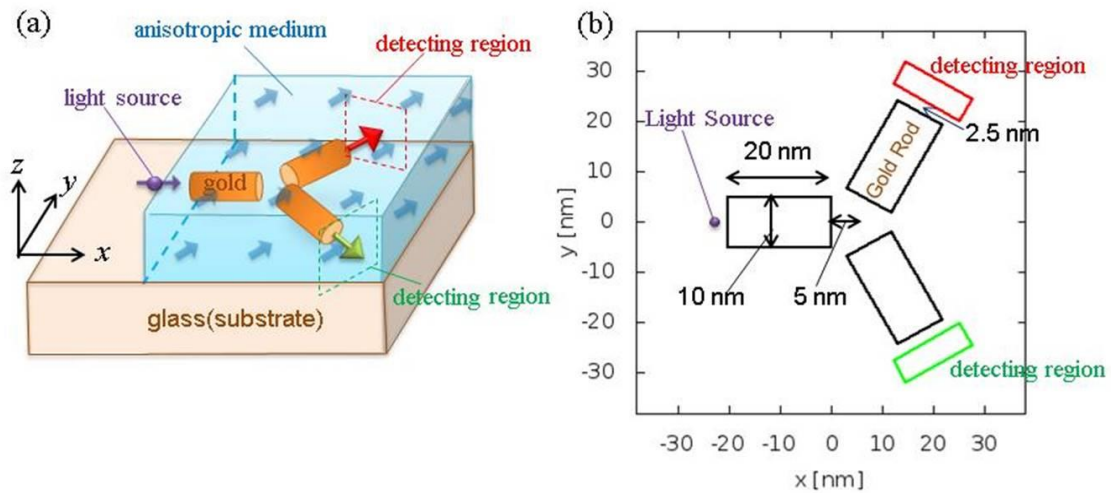


**Figure 1.16 : a) Schematic illustration of the Y-shape structure system. The positions of the incident light source (purple), the anisotropic layer (blue region and arrows) and the two detectors (red and green dotted line box regions) are illustrated. b) The size of the Y-shape structure system in the xy-plane.**

The molecular medium was a material aligned (molecular polarization) with an angle of  $35^\circ$  degree (result of an optimization process) with respect to the  $x$ -direction in the  $xy$  plane. This molecular part was described by dielectric tensor  $\epsilon$  so that:

$$\boldsymbol{\varepsilon} = \varepsilon_0 \begin{bmatrix} 1 & & \\ & 1 & \\ & & 1 \end{bmatrix} + \varepsilon_0 \mathbf{U}(\theta) \begin{bmatrix} \varepsilon_{\parallel} - 1 & & \\ & \varepsilon_{\perp} - 1 & \\ & & \varepsilon_{\perp} - 1 \end{bmatrix} \mathbf{U}(\theta)^{-1} \quad \text{Equation 1.1}$$

$\varepsilon_0$ ,  $\varepsilon_{\parallel}$ , and  $\varepsilon_{\perp}$  are the dielectric constant in vacuum and along parallel and perpendicular directions of molecules, respectively.  $\mathbf{U}(\theta)$  represents a rotation matrix allowing for the tuning of the angle  $\theta$  (tuning of molecular orientation). The second term of the right-hand side of Eq. 1 thus fixes the polarizations along the parallel and perpendicular directions of the molecules in the xy plane. In this study, no polarization in the perpendicular direction was assumed for simplicity, i.e.  $\varepsilon_{\perp}=1$ .

In the FDTD simulation, the model in Figure 16 was structured with a grid size of 1.25 nm, where absorbing boundary conditions (ABCs) were set in all directions. The time step was determined by a courant factor of 0.5. The incident light source is represented by a Gaussian point source in space, placed at around 2.5 nm from the edge of the left gold rod. The d-pulse (in time) is thus broadband (white) and polarized along the x-direction (that is, x-component of the electric field). The electric field spectra were measured at the two regions on the right sides of the top and bottom rods as shown by the red and green areas in Figure 1.16.

The electric field spectra measured at the two detected regions at the right-top and right-bottom with various values of the parameter  $\varepsilon_{\parallel}$  of the molecular medium are shown in the Figure 1.17. The figures clearly show that the right-top region detects stronger electric field than the right-bottom region, indicating path selectivity induced by the aligned molecular medium. The ratio of the two detected spectra (at the peak wavelength) increases from 2 to 5 while increasing the parameter  $\varepsilon_{\parallel}$  within the presented range. Furthermore, the path-selectivity is accompanied by a small shift in frequency, with the signal in the top-right detector always red-shifted with respect to the one in the green channel. Note that the adjustment of the spectra and spectral peaks in this part of the visible region was achieved by an optimization of the size of the gold rods, their inter-distance and their relative configuration. In addition, the path selectivity was optimized by tuning the angle  $\theta$ , reaching an optimal value of 35°.

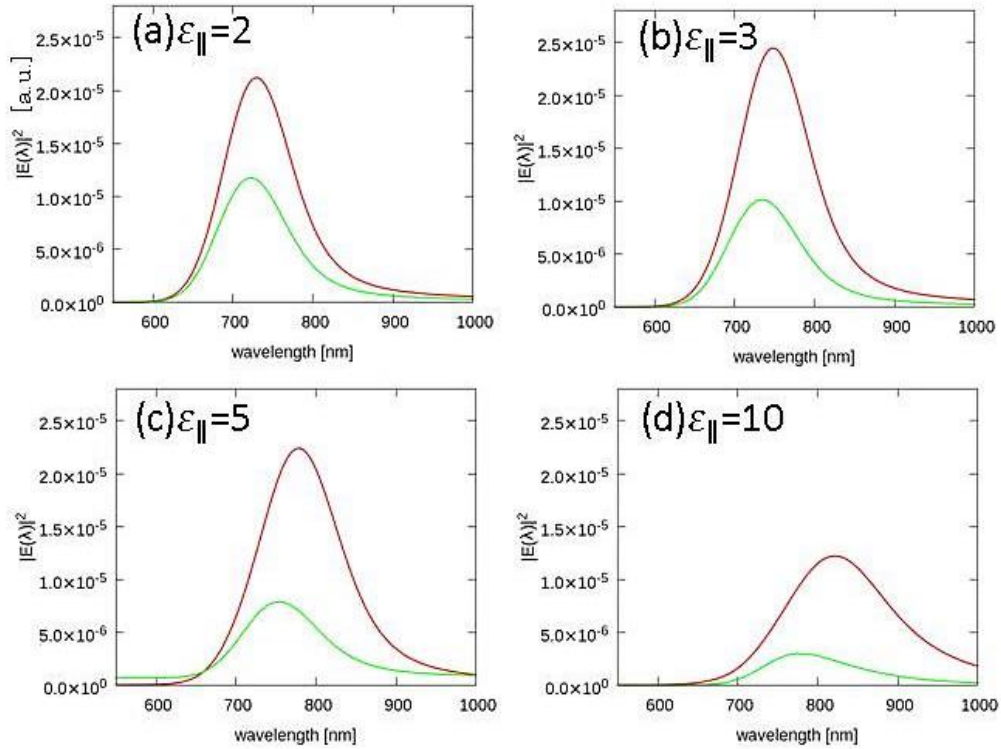


**Figure 1.17 :** Electric field spectra detected at the right-top (red) and right-bottom (green) regions of the Y-shape structure with the parallel component of various dielectric constants of the anisotropic medium: (a)  $\epsilon_{||}=2$ , (b)  $\epsilon_{||}=3$ , (c)  $\epsilon_{||}=5$ , (d)  $\epsilon_{||}=10$ .

The path-selectivity and the signals in the two branches of a Y-shaped nanostructure can be increased by orders of magnitude by introducing a gain medium in the system, compensating the Ohmic losses in the metal particles. Such results, based on a Y-shape structure of gold cubes, were shown by Yamada *et al.* [58], where a very realistic model has been used to represent both the gain and anisotropic media. Path selectivity, with a ratio of around 100, has been found in this study, with the concomitant apparition of path-selective lasing. Moreover, very similar results can be obtained while using gold open triangles or even fully joined tripod structures (all structures with three branches).

### 3.2. Scope of the thesis

In the framework of the InPhotArch project, this thesis was dedicated to the fabrication of multibranch gold nanostructures and to investigate the EM energy transfer in them. Three types of structures have been designed. The first one is similar to the one described in Figure



1.16 and is composed of three gold nanorods linked together via a tripodal organic molecule or precisely positioned from each other via a DNA origami template. The two others are hollow gold nanotriangles and gold-coated nanotripods.

Upon the local excitation of one branch of such multi-branched structures, plasmons propagate equally into the two other branches. The plasmon propagation can be visualized by placing close to the tips of these branches two different emitters that both efficiently adsorb at the wavelength of the propagating waves. Due to the local EM field enhancement induced by the propagating SPS, the emitters should emit light of similar intensity (Figure 1.18).

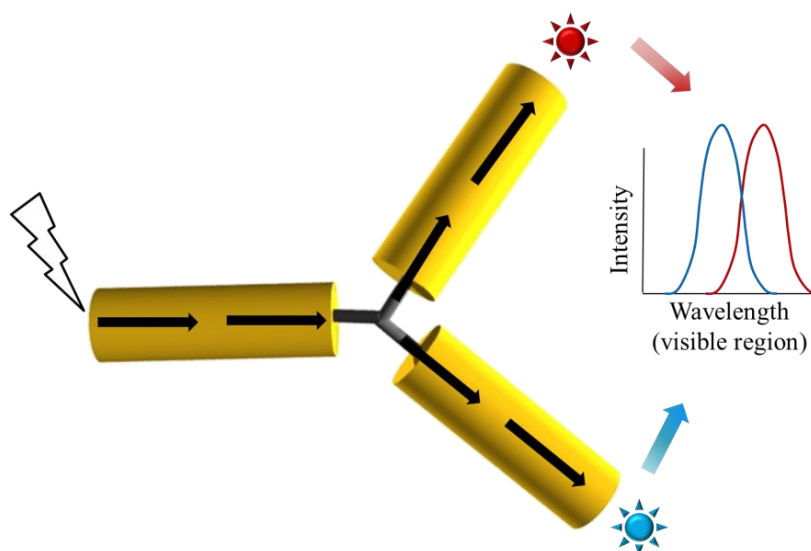


**Figure 1.18 : a) An illustration of a branched Y-shaped nanostructure composed of three gold nanorods assembled via a rigid organic linker; b) General scheme of light propagation inside the branched metallic nanostructure: Upon the excitation of one nanorod, the plasmonic signal propagates equally in the two other nanorods due to the plasmon coupling effect. The emitters localized near the tips of the nanorods emit light of similar intensity.**

As stated previously, immersing such Y-shape nanostructure in an anisotropic medium can favor the selective EM energy propagation towards one of the two possible pathways. Figure 1.19 (a) illustrates the plasmon transfer in Y-shaped structure in a medium where dipolar molecules are oriented parallel to its upper branch. The plasmonic signal, generated by the local excitation of one nanorod in a trimer structure, propagates mainly towards the upper branch of the structure. The enhanced EM field at the end of the upper rod consequently enhances the light emission of the emitter positioned at its proximity, demonstrating the selective routing of light. The reverse case is illustrated in Figure 1.19 (b), where the

plasmon-dipole interactions guide the light towards the lower branch of the structure, increasing the emission of the emitter localized close to its tip.

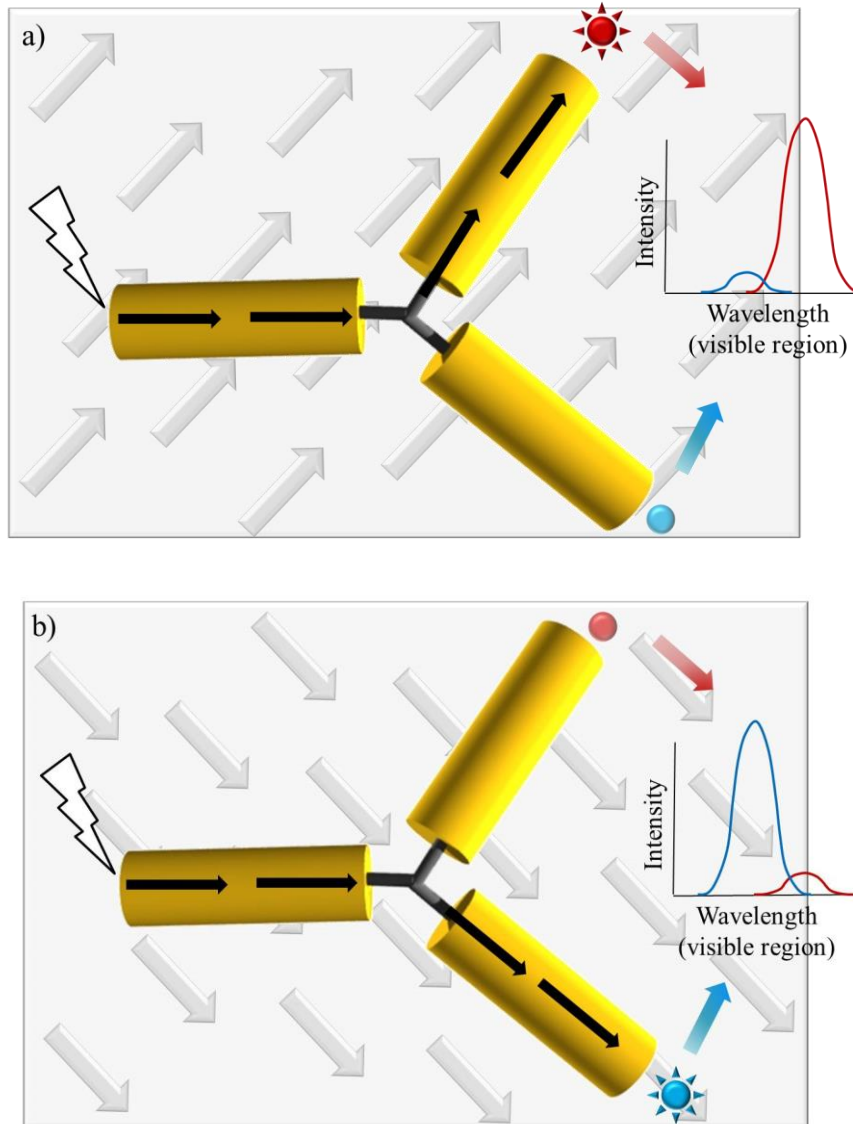


**Figure 1.19 : Schematic illustration of a plasmonic switching device where the plasmonic light transport is controlled by inducing a change in the direction of the guiding molecular dipoles through the application of an external stimulus. The grey arrows represent the dipoles with different orientations.**

## **4. CONCLUSION**

Owing to its capability to confine light to the surface of metallic nanostructures, plasmonics has unique prospects for the design of highly integrated photonic signal-processing systems, nanoresolution optical imaging techniques and sensors. For future developments in nanotechnology, it is essential to provide communication channels that allow controlled information and energy transport at the nanometer level.

By performing FDTD simulations, we showed that the combined design of a Y-shape plasmonic nanostructure and an anisotropic molecular medium could work as a path-selective device, very useful for the future of nanophotonic integrated circuits.

In the following chapters, we will describe the fabrication of plasmonic switching devices based on various Y-shaped plasmonic nanostructures and investigate their ability to route the light at the nanoscale.

## REFERENCES

- [1] R. Zia, J. A. Schuller, A. Chandran, and M. L. Brongersma, “Plasmonics: the next chip-scale technology,” *Mater. Today*, vol. 9, no. 7, pp. 20–27, 2006.
- [2] E. L. Hu, M. Brongersma, and A. Baca, “Applications: Nanophotonics and plasmonics,” pp. 318–340, 2008.
- [3] M. L. Brongersma and V. M. Shalaev, “The case for plasmonics,” *Science (80-. )*, vol. 328, no. 5977, pp. 440–441, 2010.
- [4] J. Heber, “Plasmonics: Surfing the wave,” *Nature*, vol. 461, no. 7265, pp. 720–722, 2009.
- [5] L. M. Liz-Marzán, C. J. Murphy, and J. Wang, “Nanoplasmonics,” *Chem. Soc. Rev.*, vol. 43, no. 11, pp. 3820–3822, 2014.
- [6] R. W. Wood, “On a remarkable case of uneven distribution of light in a diffraction grating spectrum,” *Proc. Phys. Soc. London*, vol. 18, no. 1, pp. 269–275, 1902.
- [7] R. H. Ritchie, “Plasma losses by fast electrons in thin films,” *Phys. Rev.*, vol. 106, no. 5, pp. 874–881, 1957.
- [8] C. J. Powell and J. B. Swan, “Origin of the characteristic electron energy losses in aluminum,” *Phys. Rev.*, vol. 115, no. 4, pp. 869–875, 1959.
- [9] E. A. Stern and R. A. Ferrell, “Surface plasma oscillations of a degenerate electron gas,” *Phys. Rev.*, vol. 120, no. 1, pp. 130–136, 1960.
- [10] H. Ditlbacher, J. R. Krenn, B. Lamprecht, A. Leitner, and F. R. Aussenegg, “Spectrally coded optical data storage by metal nanoparticles,” *Opt. Lett.*, vol. 25, no. 8, pp. 563–565, 2000.
- [11] M. Specht, J. D. Pedarnig, W. M. Heckl, and T. W. Hänsch, “Scanning plasmon near-field microscope,” *Phys. Rev. Lett.*, vol. 68, no. 4, pp. 476–479, 1992.
- [12] A. Brolo, “Plasmonics for future biosensors,” *Nat. Photonics*, vol. 6, pp. 709–713, 2012.
- [13] O. L. Berman, R. Y. Kezerashvili, and G. V. Kolmakov, “Harnessing the polariton drag

- effect to design an electrically controlled optical switch,” *ACS Nano*, vol. 8, no. 10, pp. 10437–10447, 2014.
- [14] C. M. Cobley, J. Chen, E. C. Cho, L. V Wang, and Y. Xia, “Gold nanostructures: a class of multifunctional materials for biomedical applications,” *Chem. Soc. Rev. Chem. Soc. Rev.*, vol. 40, no. 40, pp. 44–56, 2011.
- [15] M. I. Stockman, “Nanoplasmonics : The physics behind the applications,” *Phys. Today*, vol. 64, pp. 39–44, 2011.
- [16] E. A. Coronado, E. R. Encina, and F. D. Stefani, “Optical properties of metallic nanoparticles: manipulating light, heat and forces at the nanoscale,” *Nanoscale*, vol. 3, no. 10, pp. 4042–4059, 2011.
- [17] W. L. Barnes, A. Dereux, and T. W. Ebbesen, “Surface plasmons subwavelength optics,” *Nature*, vol. 424, pp. 824–830, 2003.
- [18] S. Maier, *Plasmonics: Fundamentals and applications*. Springer, 2007.
- [19] A. V. Zayats, I. I. Smolyaninov, and A. A. Maradudin, “Nano-optics of surface plasmon polaritons,” *Phys. Rep.*, vol. 408, no. 3–4, pp. 131–314, 2005.
- [20] I. Freestone, N. Meeks, M. Sax, and C. Higgitt, “The Lycurgus Cup - A Roman nanotechnology,” *Gold Bull.*, vol. 40, no. 4, pp. 270–277, 2007.
- [21] K. M. Mayer and J. H. Hafner, “Localized surface plasmon resonance sensors,” *Chem. Rev.*, vol. 111, no. 6, pp. 3828–3857, 2011.
- [22] S. Maier, M. Brongersma, and P. Kik, “Plasmonics - A route to nanoscale optical devices,” *Adv. Mater.*, no. 19, pp. 1501–1505, 2001.
- [23] S. Enoch and N. Bonod, *Plasmonics - From basics to advanced topics*. Springer, 2012.
- [24] K. E. Fong and L.-Y. L. Yung, “Localized surface plasmon resonance: a unique property of plasmonic nanoparticles for nucleic acid detection.” *Nanoscale*, vol. 5, no. 24, pp. 12043–12071, 2013.
- [25] K. L. Kelly, E. A. Coronado, L. L. Zhao, and G. C. Schatz, “The Optical Properties of Metal Nanoparticles: The Influence of Size, Shape, and Dielectric Environment,” *J. Phys. Chem. B*, vol. 107, no. 3, pp. 668–677, 2003.

- [26] Y. Chen and H. Ming, “Review of surface plasmon resonance and localized surface plasmon resonance sensor,” *Photonic Sensors*, vol. 2, no. 1, pp. 37–49, 2012.
- [27] A. O. Pinchuk and G. C. Schatz, “Nanoparticle optical properties: Far- and near-field electrodynamic coupling in a chain of silver spherical nanoparticles,” *Mater. Sci. Eng. B Solid-State Mater. Adv. Technol.*, vol. 149, no. 3, pp. 251–258, 2008.
- [28] S. Maier, M. Brongersma, P. Kik, and H. Atwater, “Observation of near-field coupling in metal nanoparticle chains using far-field polarization spectroscopy,” *Phys. Rev. B*, vol. 65, no. 19, pp. 1–4, 2002.
- [29] I. Tokarev and S. Minko, “Tunable plasmonic nanostructures from noble metal nanoparticles and stimuli-responsive polymers,” *Soft Matter*, vol. 8, no. 22, pp. 5980–5987, 2012.
- [30] X. Wang, P. Gogol, E. Cambril, and B. Palpant, “Near- and far-field effects on the plasmon coupling in gold nanoparticle arrays,” *J. Phys. Chem. C*, vol. 116, pp. 24741–24747, 2012.
- [31] P. K. Jain and M. A. El-Sayed, “Plasmonic coupling in noble metal nanostructures,” *Chem. Phys. Lett.*, vol. 487, no. 4–6, pp. 153–164, 2010.
- [32] W. Rechberger, A. Hohenau, A. Leitner, J. R. Krenn, B. Lamprecht, and F. R. Aussenegg, “Optical properties of two interacting gold nanoparticles,” *Opt. Commun.*, vol. 220, no. 1–3, pp. 137–141, 2003.
- [33] G. Lévêque and R. Quidant, “Channeling light along a chain of near-field coupled gold nanoparticles near a metallic film,” *Opt. Express*, vol. 16, no. 26, pp. 22029–22038, 2008.
- [34] J. R. Krenn, B. Lamprecht, H. Ditlbacher, G. Schider, M. Salerno, A. Leitner, and F. R. Aussenegg, “Non-diffraction-limited light transport by gold nanowires,” *Europhys. Lett.*, vol. 60, no. 5, pp. 663–669, 2002.
- [35] Y. Sun, L. Jiang, L. Zhong, Y. Jiang, and X. Chen, “Towards active plasmonic response devices,” *Nano Res.*, vol. 8, no. 2, pp. 406–417, 2015.
- [36] D. Dai and S. He, “Low-loss hybrid plasmonic waveguide with double low-index nano-slots,” *Opt. Express*, vol. 18, no. 17, pp. 17958–17966, 2010.

- [37] D. K. Gramotnev and S. I. Bozhevolnyi, “Plasmonics beyond the diffraction limit,” *Nat. Photonics*, vol. 4, no. 2, pp. 83–91, 2010.
- [38] J. Takahara, S. Yamagishi, H. Taki, A. Morimoto, and T. Kobayashi, “Guiding of a one-dimensional optical beam with nanometer diameter,” *Opt. Lett.*, vol. 22, no. 7, pp. 475–477, 1997.
- [39] M. L. Brongersma, J. W. Hartman, and H. Atwater, “Electromagnetic energy transfer and switching in nanoparticle chain arrays below the diffraction limit,” *Phys. Rev. B*, vol. 62, no. 24, pp. 356–359, 2000.
- [40] M. Quinten, A. Leitner, J. R. Krenn, and F. R. Aussenegg, “Electromagnetic energy transport via linear chains of silver nanoparticles,” *Opt. Lett.*, vol. 23, no. 17, pp. 1331–1333, 1998.
- [41] C. Girard and R. Quidant, “Near-field optical transmittance of metal particle chain waveguides,” *Opt. Express*, vol. 12, no. 25, pp. 6141–6146, 2004.
- [42] S. A. Maier, P. G. Kik, H. A. Atwater, S. Meltzer, E. Harel, B. E. Koel, and A. A. G. Requicha, “Local detection of electromagnetic energy transport below the diffraction limit in metal nanoparticle plasmon waveguides,” *Nat. Mater.*, vol. 2, no. 4, pp. 229–232, 2003.
- [43] L. De Sio, G. Klein, S. Serak, N. Tabiryan, A. Cunningham, C. M. Tone, F. Ciuchi, T. Bürgi, C. Umeton, and T. Bunning, “All-optical control of localized plasmonic resonance realized by photoalignment of liquid crystals,” *J. Mater. Chem. C*, vol. 1, no. 45, pp. 7483–7487, 2013.
- [44] S. I. Bozhevolnyi, V. S. Volkov, E. Devaux, J.-Y. Laluet, and T. W. Ebbesen, “Channel plasmon subwavelength waveguide components including interferometers and ring resonators,” *Nature*, vol. 440, pp. 508–511, 2006.
- [45] H. Ditlbacher, A. Hohenau, D. Wagner, U. Kreibig, M. Rogers, F. Hofer, F. R. Aussenegg, and J. R. Krenn, “Silver nanowires as surface plasmon resonators,” *Phys. Rev. Lett.*, vol. 95, no. 25, pp. 1–4, 2005.
- [46] Y. Fang, Z. Li, Y. Huang, S. Zhang, P. Nordlander, N. J. Halas, and H. Xu, “Branched silver nanowires as controllable plasmon routers,” *Nano Lett.*, vol. 10, no. 5, pp. 1950–

- 1954, 2010.
- [47] Y. Fang and M. Sun, “Nanoplasmonic waveguides: towards applications in integrated nanophotonic circuits,” *Light Sci. Appl.*, vol. 4, no. 6, p. e294, 2015.
- [48] V. K. S. Hsiao, Y. B. Zheng, B. K. Juluri, and T. J. Huang, “Light-driven plasmonic switches based on au nanodisk arrays and photoresponsive liquid crystals,” *Adv. Mater.*, vol. 20, no. 18, pp. 3528–3532, 2008.
- [49] D. Neuhauser and K. Lopata, “Molecular nanopolaritonics: Cross manipulation of near-field plasmons and molecules. I. Theory and application to junction control,” *J. Chem. Phys.*, vol. 127, no. 15, 2007.
- [50] K. Lopata and D. Neuhauser, “Nonlinear nanopolaritonics: Finite-difference time-domain Maxwell-Schrödinger simulation of molecule-assisted plasmon transfer,” *J. Chem. Phys.*, vol. 131, no. 1, pp. 1–6, 2009.
- [51] K. Lopata and D. Neuhauser, “Multiscale Maxwell-Schrödinger modeling: A split field finite-difference time-domain approach to molecular nanopolaritonics,” *J. Chem. Phys.*, vol. 130, no. 10, 2009.
- [52] C. Arntsen, K. Lopata, M. R. Wall, L. Bartell, and D. Neuhauser, “Modeling molecular effects on plasmon transport: Silver nanoparticles with tartrazine,” *J. Chem. Phys.*, vol. 134, no. 8, 2011.
- [53] D. Neuhauser, “Nanopolaritonics with a continuum of molecules: Simulations of molecular-induced selectivity in plasmonics transport through a continuous Y-shape,” *J. Chem. Phys.*, vol. 135, no. 20, 2011.
- [54] S. A. Maier, “Waveguiding: The best of both worlds,” *Nat. Photonics*, vol. 2, no. 8, pp. 460–461, 2008.
- [55] M. C. Gather, K. Meerholz, N. Danz, and K. Leosson, “Net optical gain in a plasmonic waveguide embedded in a fluorescent polymer,” *Nat. Photonics*, vol. 4, no. 7, pp. 457–461, 2010.
- [56] Y. Bian and Q. Gong, “Metallic-nanowire-loaded silicon-on-insulator structures: a route to low-loss plasmon waveguiding on the nanoscale,” *Nanoscale*, vol. 7, no. 10, pp. 4415–4422, 2015.



- [57] S. Kena-Cohen, P. N. Stavrinou, D. D. C. Bradley, and S. A. Maier, “Confined surface plasmon– polariton amplifiers,” vol. 13, pp. 1323–1329, 2013.
- [58] A. Yamada, D. Neuhauser, and R. Vallée, “Path-selective lasing in nanostructures based on molecular control of localized surface plasmons,” *Nanoscale*, pp. 18476–18482, 2016.

## **CHAPTER 2**

# **SYNTHESIS OF BUILDING BLOCKS FOR PLASMONIC NANODEVICES**



## 1. INTRODUCTION

Since decades, noble metal nanoparticles are commonly used as building blocks in plasmonic nanodevices due to their exceptional optical properties.

The first documented investigation of such properties dates back from 1857, when M. Faraday noticed a red color of nanometer-sized gold particles solution, unlike the yellow color of bulk gold [1]. 50 years later, G. Mie attributed the color of noble metal colloids to their unique interaction with the incident light [2].



**Figure 2.1 : The intense color of gold nanoparticles arises from surface plasmon resonance modes, resulting in photon absorption at various wavelengths.**

Under the irradiation of light, the conduction electrons in a plasmonic nanoparticle undergo a collective coherent oscillations inducing a strong light absorption, reflected in their brilliant colors [3], [4]. The nanoparticle interaction with light and thus its LSPR are determined by its size, shape and composition, as well as the surrounding environment. Through the modification of those parameters, the optical properties of the metal nanostructures can be engineered to produce powerful plasmonic tools required for different applications.

Therefore, a great scientific effort is focused on the development of synthetic methods to obtain noble metal nanoparticles with different morphologies as well as on the variety of novel techniques that provide their accurate characterization [5].

In this chapter, we will review common synthetic approaches to achieve variety of high-quality noble metal nanostructures. Particular focus will be put on the synthesis of the nanoparticles used as building blocks for our target nanodevice: gold nanorods, gold hollow triangles and gold nanotripods.

## 2. NOBLE METAL NANOPARTICLES

### 2.1. Colloidal synthesis of noble metal nanoparticles

As the size and the shape of nanostructures define and control their unique plasmonic properties, there is a rapid development of synthetic methods to produce plasmonic nanoparticles. Generally, the methods for nanostructures synthesis can be classified as “top-down” or “bottom-up”. Top-down approaches refer to etching of a bulk material to obtain nanostructures, mainly by photolithography, electron beam lithography or mechanical processes (grinding and polishing). On the other hand, the “bottom-up” synthetic methods imply the assembly of atoms (produced from reduction of ions) to form the nanostructures. Such approaches are advantageous because the produced nanostructures have more homogenous chemical composition with fewer defects, owing to the high degree of control starting from the atomic level. Moreover, these methods are less expensive since no specialized equipment is required [6], [7]. Various synthetic routes such as seed-mediated growth, template-based electrochemical synthesis or photochemical synthesis have been employed to produce high-quality noble metal nanoparticles with different morphologies (Figure 2.2) [5].

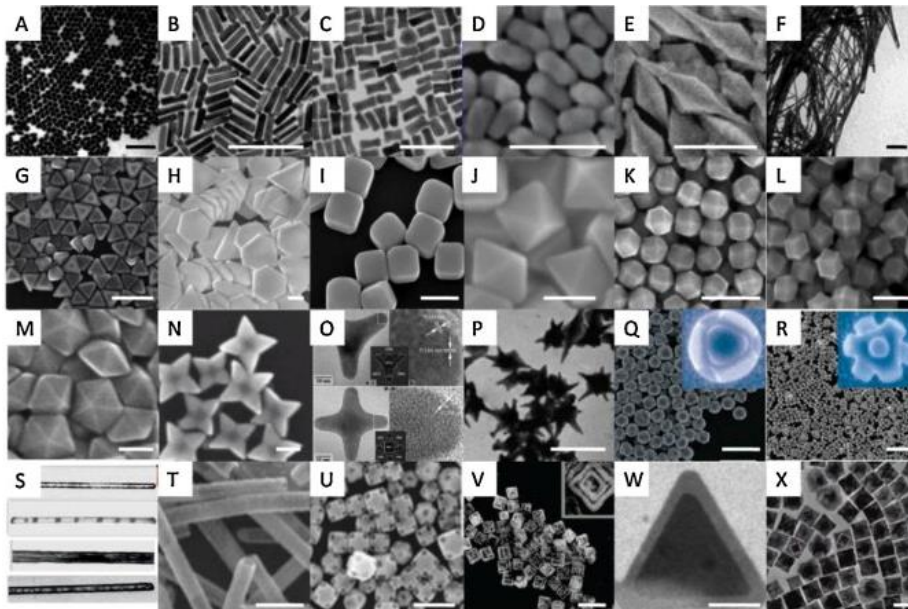


**Figure 2.2 : Noble metal NC building blocks with different geometries: (A) sphere; (B) rod; (C) dog bone; (D) peanut; (E) penta-branch; (F) wire; (G) triangular plate; (H) hexagonal plate; (I) cube; (J) octahedron; (K) cubooctahedron; (L) rhombic dodecahedron; (M) pentagonal bipyramid; (N) star-like octapod; (O) tripod (up) and**

**tetrapod (down); (P) star; (Q) edge truncated octahedron; (R) octapod; (S) core—shell wire/cylinder; (T) tube; (U) cage; (V) double-walled box; (W) core—shell triangular plate and (X) core—shell cube. Scale bars are 200 nm for A—E, G—I, K, L, P, R and T—V; 1  $\mu\text{m}$  for F and Q and 50 nm for J, M, N, W and X [8].**

The most popular “bottom-up” synthetic technique is the seed-mediated growth, which uses preformed small seeds, typically 2-5 nm in diameter, to direct the shape of the final nanostructures. This method is performed in two steps, the nucleation and the growth, which allows the high control over the morphology. This strategy is highly versatile and can be used to carefully design a variety of nanostructures through the choice of seed particles.

In this method, the metal precursor is first reduced with a suitable agent to form nuclei. When the nuclei grow to a certain size, they become seeds with a single-crystal, singly twinned, multiply twinned or plate-like structure with stacking faults. In the second step of the synthesis, the seeds are introduced in a growth solution containing metal ions and in most of the cases capping agents. Metal ions are reduced at the surface of the seeds via heterogeneous nucleation, allowing the growth of the nanoparticles. For example, the growth of a single-crystal seed can give rise to an octahedron or a cube by tuning the relative growth rates along the  $\langle 100 \rangle$  or  $\langle 111 \rangle$  directions, which is typically achieved by the introduction of a capping agent. Right bipyramids or nanobeams are formed from singly twinned seeds, while multiply twinned seeds with a decahedral shape can be grown into rods or nanowires with a pentagonal cross section. If the seeds contain a plate with stacking faults, hexagonal and triangular plates can be formed (Figure 2.3) [9].

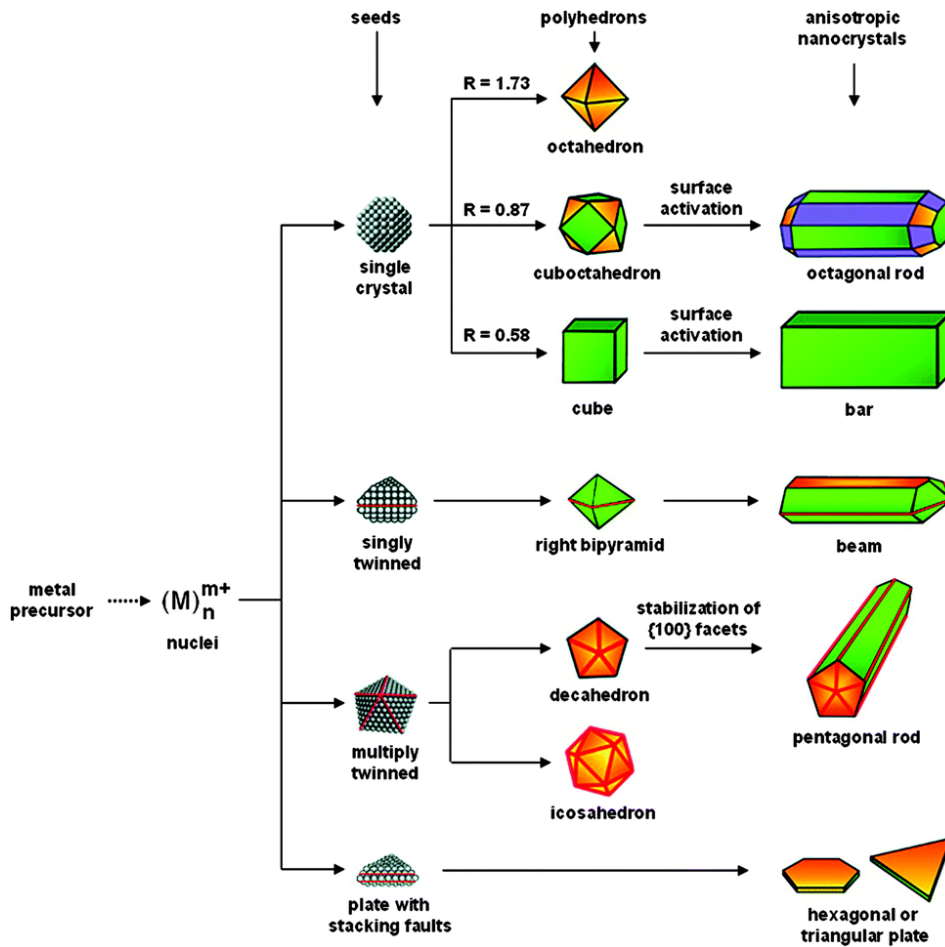


**Figure 2.3 :** The seed structure determines the final shape of the nanoparticle. Green, orange and purple colors represent the  $\{100\}$ ,  $\{111\}$ , and  $\{110\}$  facets, respectively. The parameter  $R$  is defined as the ratio between the growth rates along the  $\langle 100 \rangle$  and  $\langle 111 \rangle$  directions [9].

Apart of the shape of the initial seed, the shape anisotropy of the nanostructure is also generated by the presence of capping agents (e.g., ligands, polymers). They provide the colloidal stability, but also alter the growth rates of different crystallographic facets by their preferential adsorption onto some of them. The addition of a capping agent which has a stronger binding energy to a specific facet leads to the “facet blocking” and consequently its slower growth. For example, single crystalline Ag seeds can be used to form Ag octahedrons in the presence of citrate ions, or nanocubes/nanobars in the presence of PVP. As the citrate ions bind more strongly to Ag  $\{111\}$  than Ag  $\{100\}$  surfaces, the  $\{111\}$  facets are expected to grow more slowly than the  $\{100\}$  facets. Thus, the  $\{100\}$  facets will disappear gradually while the  $\{111\}$  facets will become dominant on the surface, leading to the formation of Ag octahedrons. If PVP is used as a capping agent, the binding is stronger at the  $\{100\}$  than

{111} facets of Ag, causing the reduced growth rate along the  $\langle 100 \rangle$  direction and the formation of nanocubes or nanobars with lateral {100} facets [7], [10].

Due to the ability to tune the seed morphology and growth rate of different crystallographic facets, the seed-mediated growth method allows a good control of the size and the shape of the synthesized nanostructures. Hence, this method will be used to obtain the nanometric building blocks used in our work, namely gold nanorods, gold hollow triangles and gold tripods.

## **2.2. Tuning the optical properties of metallic nanoparticles**

Within the wide range of existing plasmonic materials (copper, aluminium, heavily doped semiconductors and metal oxides, and graphene), nanoparticles composed of gold and silver have received the biggest interest as they can greatly enhance the absorption and scattering of light due to their unique and strong interactions with electromagnetic field, known as localized surface plasmon resonance. Due to their rich optical response, noble metal nanoparticles are used for many different applications, such as biomedicine, sensing, catalysis and computer sciences [11].

The optical properties of these nanoparticles are strongly affected by structural parameters such as size and shape, the material composition and the surrounding dielectric environment. However, not all the nanoparticle modifications are equally effective for tailoring of the optical response. For example, the enlargement of gold spheres can induce slight red-shift of the LSPR peak (Figure 2.4 a), while the elongation of the spheres along one direction to form rods produces greater changes in the plasmon peak position (Figure 2.4 c) [12]. Indeed, when a nanosphere is elongated into a rod, the free electrons oscillate along two distinctive directions parallel to the short and long axes of the rod, splitting the LSPR peak into two modes called transverse and longitudinal, respectively. This phenomenon occurs due to the change in the degree of polarizability caused by deviations from spherical geometry. Anisotropic (rod-like, triangular, branched) nanoparticles possess several crystal surfaces, different surface roughness, and many corners, steps, edges, and defects which strongly affect the modification of their chemical and physical properties compared to the spherical systems. Owing to the highly localized charge polarizations at corners and edges, anisotropic nanoparticles support multiple plasmon modes (e.g., quadrupolar modes that arise from two dipoles in opposite direction), while the symmetrical nanospheres show a single plasmon resonance due to their dipolar nature [13]. While the dependence of the transverse mode of



gold nanorods on their size is negligible, the position of the longitudinal one is very sensitive to the nanorod aspect ratio (length divided by width) (Figure 2.4 c).

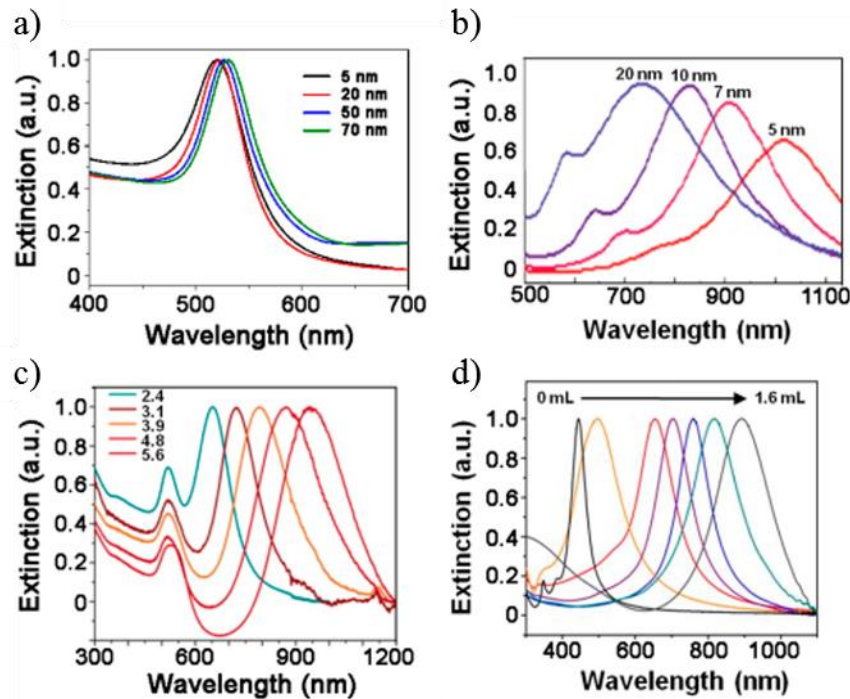


**Figure 2.4 : Modification of the optical properties of gold nanoparticles as a function of several parameters: a) nanospheres with different diameters; b) nanoshells with different shell thicknesses; c) nanorods with different aspect ratios; d) nanocages prepared by titrating silver nanocubes with different volumes of  $\text{HAuCl}_4$  solution [3].**

The formation of a core-shell or hollow structures can also cause changes in the optical properties of Au nanostructures. Halas *et al.* [14] demonstrated the tuning of the LSPR of silica-gold nanoshell system by the variations in the shell thickness. By decreasing the thickness of the gold shell deposited on the 120 nm diameter silica core, the LSPR peak was red-shifted from 700 nm to more than 1000 nm (Figure 2.4 b). The “plasmon hybridization theory” explains such sensitive structural tunability of the plasmon resonance frequency of the nanoshell as the interaction between plasmons supported by a nanosphere and the cavity. The sphere and cavity plasmons are electromagnetic excitations that induce surface charges at both inner and outer surface of the metal shell. Due to the finite thickness of the nanoshell, the two plasmons interact with each other, and the coupling strength is determined by the shell thickness [15]. Based on the concept of Au nanoshells, Xia and co-workers [16] synthesized gold nanocages from silver nanocubes via the galvanic replacement reaction. By controlling

the amount of  $\text{HAuCl}_4$  added into an aqueous suspension of nanocubes, they showed that the hollow nanostructures with controllable morphologies can be used to tailor SPR peaks within both visible and near-IR regions (Figure 2.4 d).

Owing to their broad and intense LSPR peaks in the visible and NIR regions, Ag and Au nanoparticles can be used to enhance the Raman signal. The SERS (Surface-enhanced Raman scattering) activity strongly depends on the nanoparticle shape. In anisotropic nanostructures, the local electromagnetic fields are not homogeneously distributed on the surface. They are highly concentrated just in specific regions, causing the strong SERS enhancement at these sites. For example, SERS enhancement factors on the order of  $10^4$ – $10^5$  were noticed on the surface of AuNRs, while no enhancement was observed when nanospheres of a similar size were used. Also, the tips of sharp anisotropic nanostructures were shown to exhibit great SERS enhancement, because the electromagnetic field is concentrated on the tips of such nanostructures [17].

Another important application of plasmonic nanoparticles is the photothermal treatment. Plasmonic nanostructures can absorb electromagnetic energy and convert it into heat through the photothermal effect. The induced hyperthermia can destroy tumor cells, as they are more prone to destruction due to their poor blood supply, compared to healthy cells. The interesting optical properties of gold and silver nanoparticles can also be exploited in optical imaging techniques, drug delivery and modern nanodevices [18].

### **2.3. Self-assembly of plasmonic nanoparticles**

The formation of complex hierarchical nanostructures in a controllable manner using the self-assembly of noble metal nanoparticles provides another route towards nanomaterials with new optical properties which can be exploited for uses in the field of plasmonics. It refers to the process by which the nanoparticles spontaneously organize into ordered structures by thermodynamic and other constraints [19].

Within the multi-nanoparticle systems, LSPRs of individual particles can couple, resulting in characteristic shifts of the resonance frequencies (Figure 2.5). In assemblies, the optical response can be tuned by changing the number of NPs, by varying the directionality of NP organization, by tuning the interparticle distance or by changing the geometry and composition of the individual nanoparticle forming the structure.

Since the interparticle gap size and the degree of order play a great role in these phenomena, methods for self-assembly ensuring a high level of direction and control are required. Thus,

the great efforts are made to organize the plasmonic particles into well-defined nanostructures, which is an essential step towards the control, optical routing and light switching in future plasmonics nanodevices [20].

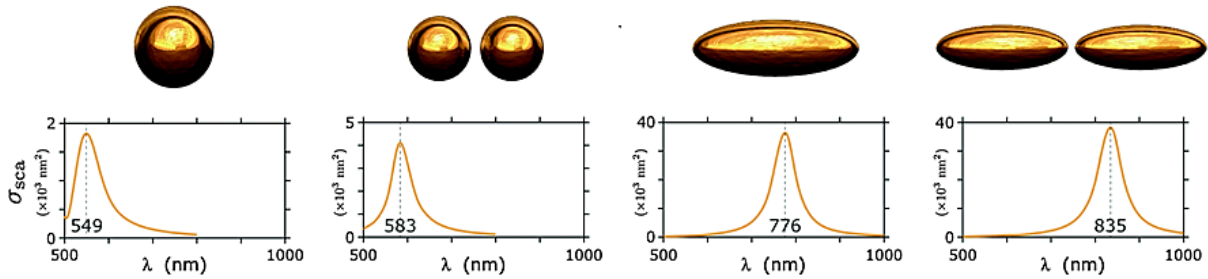


**Figure 2.5 : Modeling of the optical properties of gold nanospheres and gold nanorods through their self-assembly [21].**

Many different methods for the assembly of plasmonic nanostructures have been developed. Generally, they can be divided into two groups - direct (non-assisted) assembly in solution and assisted assembly supported by template surfaces or external fields.

Direct assembly implies the careful tuning of the interparticle forces to create ordered assemblies in solution. By suppressing their electrostatic stabilization and making attraction forces as van der Waals or solvophobic forces dominant, nanoparticles can be driven to self-assembly. On the other hand, assisted (indirect) self-assembly of plasmonic NPs takes place under the action of magnetic or electric fields or with the use of templates such as silicon wafers or DNA origami [22]. Both self-assembly methods will be described in detail in the following chapters.

### 3. GOLD NANORODS

Gold nanorods are anisotropic nanoparticles which offer a means to manipulate electromagnetic fields at the nanoscale due to their broadly tunable surface plasmon resonances, opening up numerous applications, from biosensing, imaging and drug delivery to data storage, solar energy conversion, and opto-electronics [23].

To provide high control over the size, shape, and crystallographic facets of gold nanorods with high yield, quality, monodispersity and consequential spectral tunability, great efforts

have been made to develop different synthetic routes [4], [24]. During the last 20 years, several bottom-up methods for AuNRs synthesis have been developed. The first described synthetic technique was the template method, based on the deposition of gold and silver salts in hard templates, such as single-walled carbon nanotubes [24]. Nanorods were also prepared via electrochemical oxidation/reduction within a simple two-electrode type cell, using ionic surfactants as both the supporting electrolytes and the stabilizers which lead to nanorod formation [25]. The third common technique is the seed-mediated chemical growth in aqueous medium. It was pioneered by Jana *et al.* [26] who prepared colloidal gold nanorods by the addition of citrate-capped small gold nanospheres into a  $\text{HAuCl}_2$  solution, previously obtained by the reduction of  $\text{HAuCl}_4$  with ascorbic acid in the presence of CTAB. The drawback of their method was the low yield, since many gold nanospheres were produced. The method was later improved by Nikoobakht and El-Sayed [27] who made two modifications: i) the introduction of a strong stabilizer, cetyltrimethylammonium bromide (CTAB), during the seed-formation process and ii) the use of silver ions to control the NRs aspect ratio. Due to the extremely high yield of AuNRs obtained from single-crystal seeds, the method has become the most popular synthetic route and it will be described in detail in the following section.

### 3.1. Synthesis of gold nanorods

The seed-mediated growth method includes two steps: The formation of gold seeds with diameter around 2 nm by the reduction of  $\text{HAuCl}_4$  with  $\text{NaBH}_4$  in the presence of CTAB, followed by the seed anisotropic growth in a growth solution containing additional gold salt, silver ions, CTAB and ascorbic acid as a weak reducing agent [27]. The anisotropic growth on the initial, single-crystal seeds originates from binding of the  $\text{Au}^{3+}$  and  $\text{Au}^+$  ions to the cationic micelles of the surfactant, as explained by Pérez-Juste *et al* [28]. Ascorbic acid reduces  $\text{Au}^{3+}$  ions bound to CTAB micelles to  $\text{Au}^+$  ions, which then form even stronger complexes with CTAB. The formed complexes diffuse to CTAB-capped seeds at high points of curvature by electric field interactions, breaking the symmetry of the sphere into different facets with preferential binding of CTAB molecules onto the {110} facets. Another key point for the control of the aspect ratio of AuNRs is the presence of silver ions which deposit onto the {110} side facets with a faster rate than they do onto the {100} facets of the growing particle (Figure 2.6). This results in the underpotential deposition of a thin silver layer on the sides of the growing particles and in the rod-shaped growth along the {110} direction. After a

certain amount of time, a layer of silver also covers the {100} facets of the rods, inducing the termination of the growth. The AuNRs aspect ratio can thus be tuned by adjusting the concentration of silver ions [29].

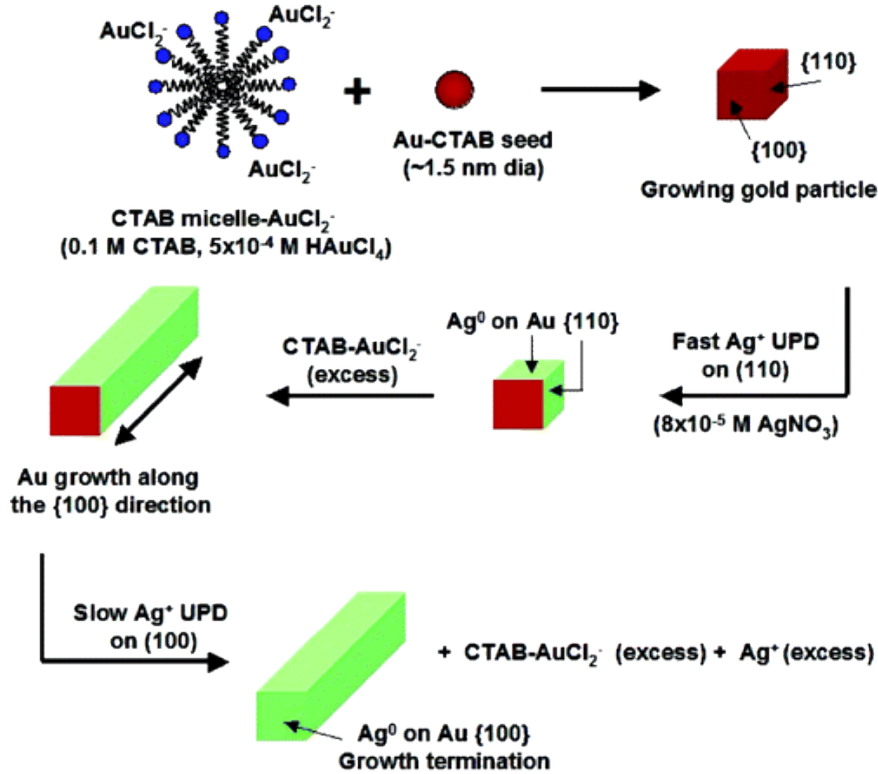


**Figure 2.6 : Mechanism of nanorod growth from CTAB-capped gold seeds in the presence of silver ions [29].**

In general, the decrease of the Ag<sup>+</sup> concentration results in a decrease in length, and consequently, short aspect ratio nanorods. However, further decrease induces incomplete deposition of silver on the sides and an increase in the width, making the synthesis of short AuNRs rather difficult [30]. To overcome such limitation of shape and size uniformity of the short nanorods, Murray and co-workers demonstrated an “improved” seed-mediated synthesis of uniform short AuNRs with negligible impurities through the addition of salicylate-based sodium salts in the growth solution. The hydrophobic benzene ring of the additive penetrates into the hydrophobic alkyl chain of the CTAB molecules meanwhile the COO<sup>-</sup> groups of salicylate anions orientate perpendicular to the surfactant and project radially from the surface of the micelles into the bulk aqueous solution (Figure 2.7). These two factors synergistically change the micellar packing, promoting the spherical to rodlike micellar transition. Due to the

electrostatic screening, modified CTAB layers have lower affinity for negatively charged Au (III) precursors, resulting in the formation of short AuNRs [31].

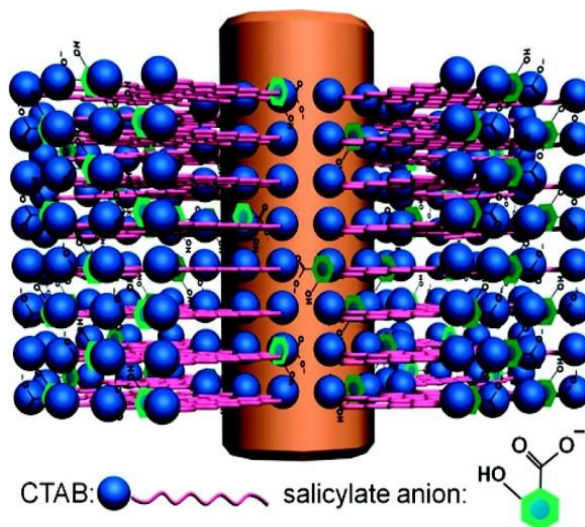


**Figure 2.7 :** A mechanism proposed to explain the role of sodium salicylate in mediating the binding between CTAB bilayers and certain facets of growing AuNRs [31].

### **Protocol: Synthesis of AuNRs with an aspect ratio equal to 2**

- **Preparation of Au@CTAB seeds**

CTAB solution (5 mL, 0.2 M) was mixed with  $\text{HAuCl}_4$  solution (5 mL, 0.5 mM). Fresh  $\text{NaBH}_4$  solution (0.6 mL, 0.01 M) was diluted with 0.4 mL of water, and injected into the reaction mixture under vigorous stirring. Color of the solution immediately changed from yellow to brown. After 2 min, the seeds solution was left at 27 °C to age for 30 min before use in order to ensure the decomposition of remaining borohydride ions.

- **Preparation of growth solution**

CTAB (9.0 g) and sodium 3-methylsalicylate (1.1 g) were dissolved in 250 mL of water pre-heated at 70 °C. When the solution cooled down to 30 °C,  $\text{AgNO}_3$  solution (6 mL, 4 mM) was added and the mixture was incubated at 30 °C during 20 min.  $\text{HAuCl}_4$  solution (250 mL, 1 mM) was then added and the mixture was stirred for 1 h. After the addition of ascorbic acid (1 mL, 0.064 M), color of the solution changed from orange to colorless. Finally, 0.8 mL of prepared seeds was injected into the growth solution which was then incubated at 30 °C for 12 h. The blue color of the solution indicated the formation of short AuNRs with aspect ratio = 2.

### 3.2. Characterization of AuNRs

AuNRs were prepared from single crystalline gold seeds of around 3.5 nm in diameter (Figure 2.8 a), following a synthetic protocol for the controlled reduction of silver ions onto AuNRs in the presence of 3-methylsalicylate, adapted from the work of Murray and co-workers [32]. The length ( $36 \pm 2$  nm) and the thickness ( $17 \pm 1$  nm) of the AuNRs were determined by analysis of TEM images (Figure 2.8 b, c). The success of the synthesis is also evidenced by Figure 2.9, where the UV-vis absorbance spectra of both the gold seeds and the obtained AuNRs are shown. One can see that the AuNRs exhibit a transverse LSPR band at 520 and a longitudinal one at 628 nm, as expected for AuNRs with an aspect ratio equal to 2.

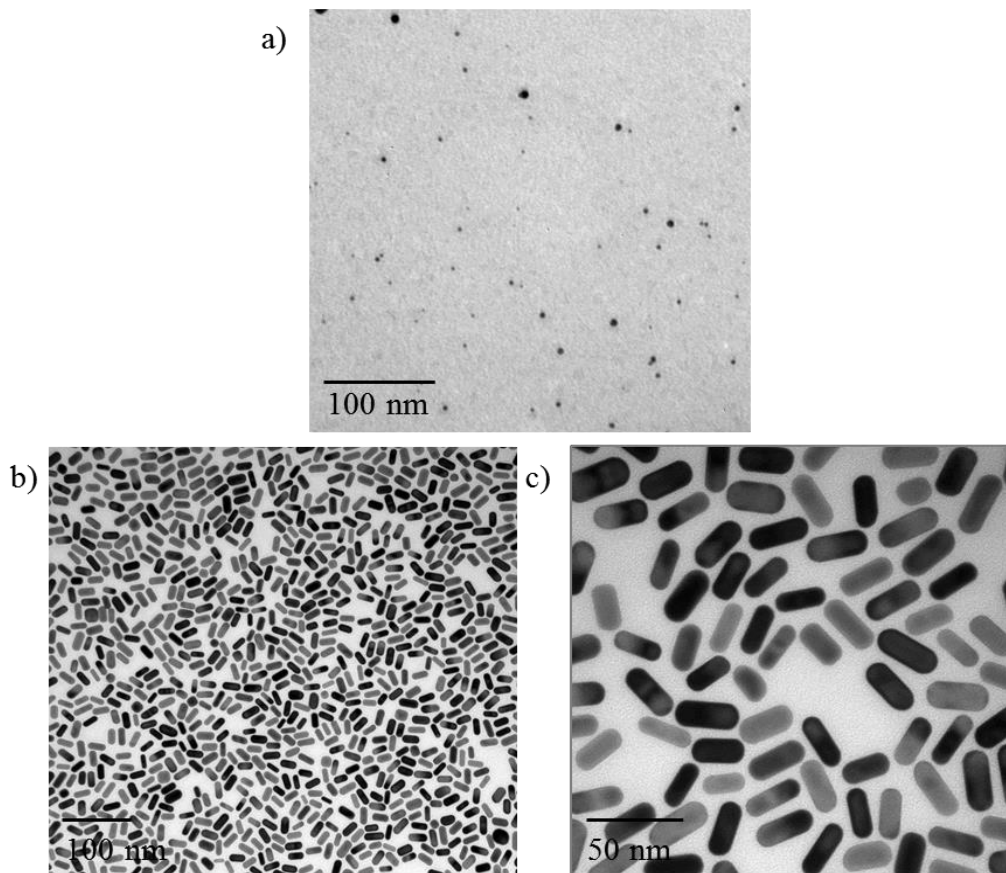


**Figure 2.8 : TEM images of the gold seeds (a) and of the AuNRs with an aspect ratio equal to 2 under low (b) and high magnification (c).**

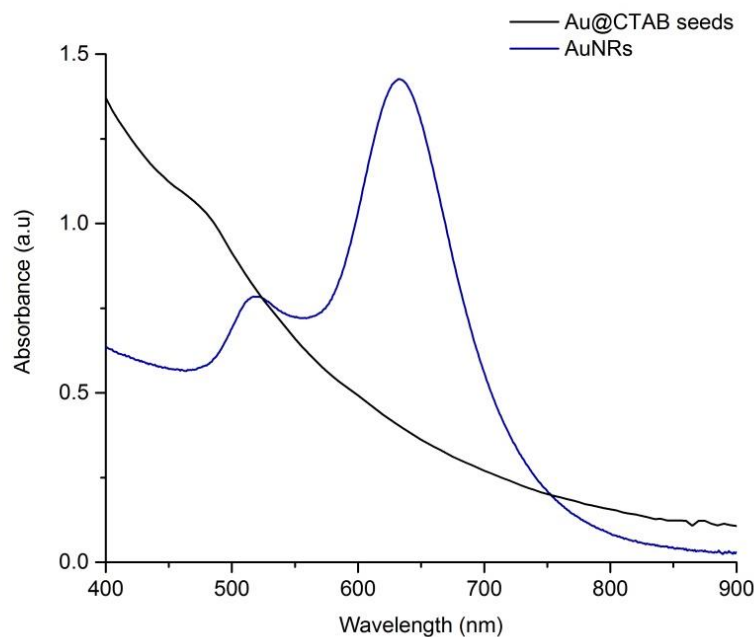


**Figure 2.9 : Absorption spectra of the Au@CTAB seeds and of the synthesized AuNRs in water.**

#### 4. GOLD HOLLOW NANOTRIANGLES

Hollow plasmonic nanostructures display unique properties such as low mass density, high porosity, fast ion and electron transfer and large surface area. These characteristics enable their great application potential in many fields such as catalysis and drug delivery [33]. Also, metal nanoframes can generate plasmonic fields with extremely high intensities, promoting their application in sensing, photoacoustic imaging, SERS and plasmonic nanodevices. Such enhanced plasmonic properties of hollow nanostructures compared to their solid counterparts originate from the plasmon hybridization mechanism. The coupling between their interior and exterior surface gives these nanoparticles additional surface fields which are expected to have greatly enhanced plasmon fields along with more homogeneous distribution [34].

Up to now, many strategies to generate different hollow nanostructures as spheres, cubes, rods and triangles have been developed. For our work, triangular nanoframes are particularly interesting due to their well-defined anisotropy, but also sharp edges and corners. The increased electromagnetic fields at the tips of the triangle together with plasmon enhancement due to plasmon hybridization mechanism make such nanostructures promising candidates for building blocks in plasmonic nanodevices.



In this section, we will describe the three-step chemical synthesis of gold hollow nanotriangles: i) the synthesis of a sacrificial template, i.e. silver nanoprisms; ii) the formation of hybrid gold-framed silver nanotriangles upon the selective deposition of gold on the silver template and iii) the chemical etching of silver to form hollow gold nanotriangles in a high yield with minimal silver impurities (Figure 2.10).

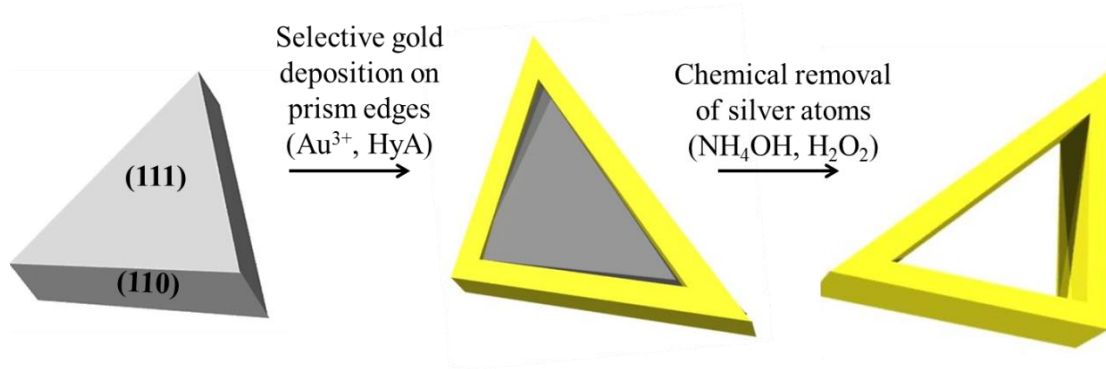


**Figure 2.10 : From silver nanoprisms to gold hollow nanotriangles: i) selective gold deposition onto the (110) facets of the nanoprisms; ii) etching of silver atoms with a H<sub>2</sub>O<sub>2</sub>/NH<sub>4</sub>OH mixture.**

#### 4.1. Synthesis of the sacrificial template - Ag nanoprisms

To synthesize the silver nanoprisms, we adopted the seed-mediated growth protocol developed by Xia and co-workers [35] and improved by Le Beulze *et al.* [36]. The method is based on the formation of crystalline silver seeds by the reduction of AgNO<sub>3</sub> with sodium borohydride in the presence of citrate, followed by the silver-seed-catalyzed reduction of AgNO<sub>3</sub> by ascorbic acid in the presence of citrate and PVP at pH = 5.6. By adjusting the experimental parameters such as the reagents/capping ligands ratio, the order of reagent addition or pH of the solution, we established the control over the size and shape uniformity and a spectral tunability of Ag nanoprisms.

##### **Protocol: Synthesis of silver nanoprisms**

- **Preparation of Ag@citrate seeds**

*In a standard experiment, ultrapure water (47.5 mL), trisodium citrate solution (0.5 mL, 30 mM) and AgNO<sub>3</sub> solution (1 mL, 5 mM) were introduced in a 100 mL two-necked round bottom flask immersed in an ice-bath. The mixture was bubbled with argon under stirring*

during 30 min to remove oxygen. The argon flow was transferred at the surface of the solution and cold, freshly prepared aqueous solution of  $\text{NaBH}_4$  (0.5 mL, 50 mM) was rapidly injected in the mixture under vigorous stirring. The reaction was allowed to proceed during 16 min during which 4 drops of the prepared  $\text{NaBH}_4$  solution were added every 2 minutes to ensure complete reduction of silver ions. Finally, a mixture of a polystyrene sulfonate solution (0.5 mL, 5 mg/mL) and the prepared  $\text{NaBH}_4$  solution (0.25 mL) was added drop-wise to the yellow reaction mixture. The solution was stirred at room temperature under argon flow during 4 h to complete decomposition of the remaining borohydride ions.

During the Ag@citrate seeds synthesis, the addition of  $\text{NaBH}_4$  caused the immediate color change of a clear solution to yellow which intensified as the seeds aged for 5h, indicating the formation of Ag particles. The seed diameter was estimated to  $3 \pm 1$  nm by the statistical analysis of TEM images (Figure 2.11). The absorbance spectra showed a band at 384 nm, consistent with the SPR of small Ag nanospheres (Figure 2.11).

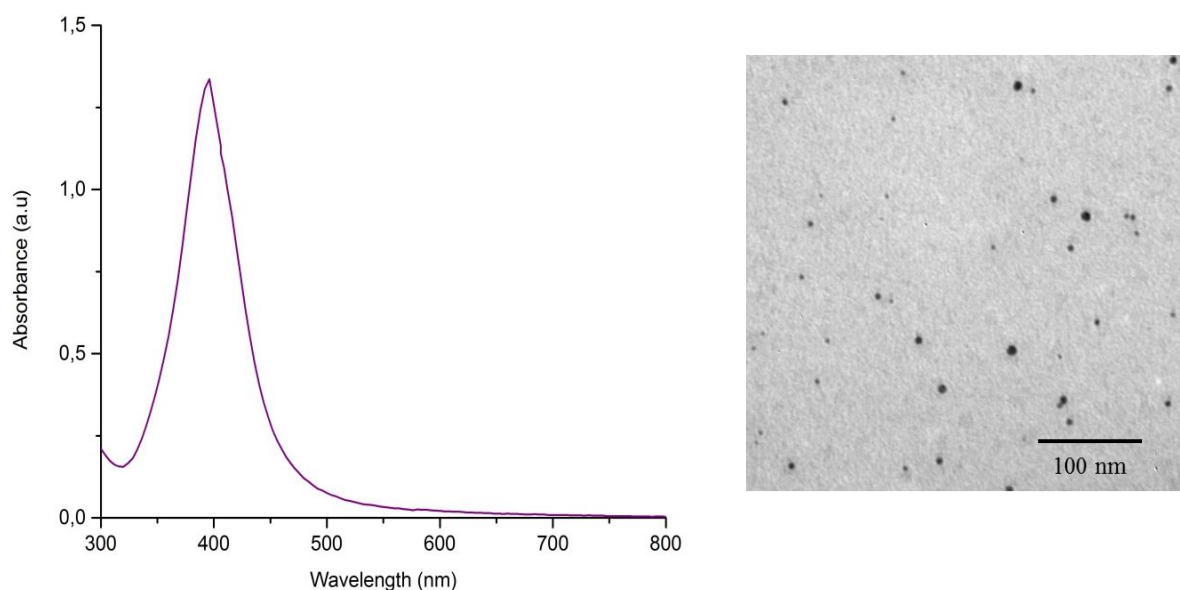


**Figure 2.11 : Absorbance spectra of the Ag@citrate seeds in water and the corresponding TEM image.**

- **Seeded growth of the nanoprisms**

Prepared silver seeds (3.5 mL) were added to the mixture of ultrapure water (100 mL), ascorbic acid solution (100 mL, 0.5 mM), trisodium citrate solution (38 mL, 30 mM), and polyvinylpyrrolidone solution ( $M_w \sim 55\,000$ , 38 mL, 0.7 mM). The  $\text{AgNO}_3$  solution (12.5 mL, 2.5 mM) was introduced in the mixture with a syringe pump. The addition rate was set to 10

*mL/h. The reaction was performed at room temperature, under vigorous stirring, protected from the light exposure. The solution progressively changed color via yellow, orange, pink, purple, and finally intense blue.*

The addition of the seeds in the growth solution containing ascorbic acid, citrate and PVP was followed by the introduction of the silver precursor. Owing to their large surface area, the seeds served as a substrate for the decomposition of ascorbic acid which was used to reduce the  $\text{Ag}^+$  ions and cause their deposition on the Ag nuclei. The seeds can grow in circular, hexagonal or triangular plates, depending on the reaction kinetics and the ratio of the growth rates of  $\{111\}$  and  $\{100\}$  faces of the seed (Figure 2.12). If the reduction rate is very fast, the number of atoms supplied from the bulk is too large for the seeds to incorporate them, resulting in the formation of spherical particles. Thus, to promote the growth of triangular nanoparticles, a moderate reduction rate is required. Citrate was shown to have a crucial role in the decrease of the reaction kinetics. As it adsorbs on the seed surface, a negatively charged monolayer is formed on the surface, delaying the penetration of the ascorbate anions and the citrate-silver complexes to the seed surface. Consequently the rate of silver reduction is slowed down, leading to the smooth nanoprism formation. Another key parameter for the nanoprism formation is the growth ratio between  $\{111\}$  and  $\{100\}$  faces of Ag seeds. Both capping agents adsorb onto the growing seed and thus alter the kinetics of the relative growth rates. The protonation state of the citrate ions can be adjusted to favor the growth rate in the  $[111]$  direction, leading to the smooth nanoprism formation [36].

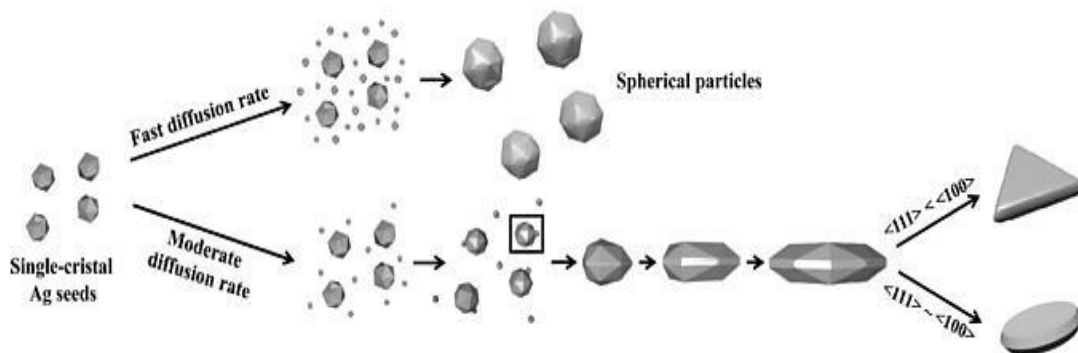


**Figure 2.12 : Mechanism of Ag nanoprism formation – Reduction of  $\text{Ag}^+$  takes places on silver seeds. Control of the reaction kinetics is required in order to promote the formation of triangular particles instead of that of spherical or disc-like ones.**

The absorption spectrum of the synthesized nanoprisms shows four characteristic surface plasmon bands (Figure 2.13), indicating the formation of thin and flat nanocrystals. The first three weak signals centered at 340 nm, 400 nm and 456 nm correspond to out-of-plane quadrupole, out-of-plane dipole and in-plane quadrupole plasmon resonances, respectively. The strong absorption peak at 616 nm is attributed to the in-plane resonance mode and it highly depends on the nanoprism length, thickness and tip truncation [37].

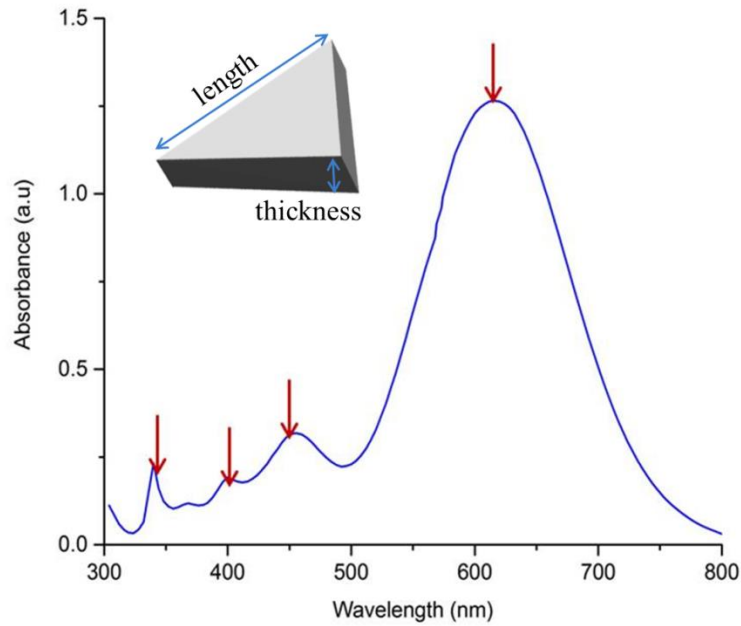


**Figure 2.13 : Absorbance spectra of the Ag nanoprisms in water.**

The obtained silver nanoparticles were characterized by TEM. Figure 2.14 shows that they mainly have the target triangular morphology, even though they coexist with some spherical nanoparticles. The average edge length and thickness of the silver nanoprisms were estimated to be  $44 \pm 5$  nm and  $6 \pm 1$ , respectively.

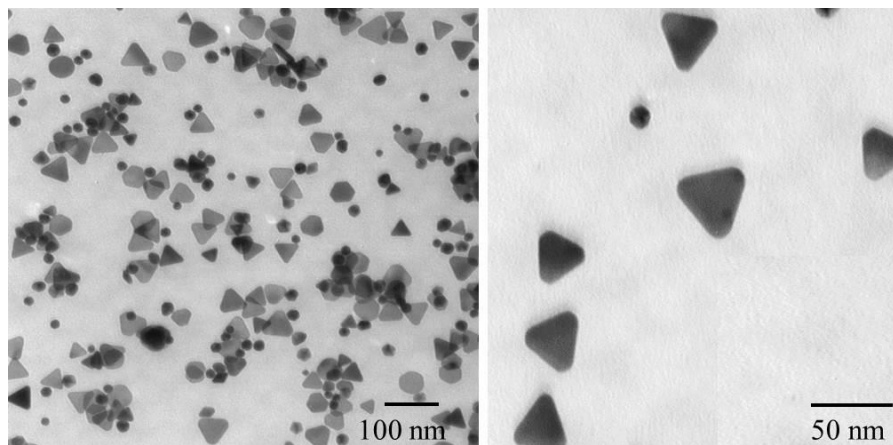
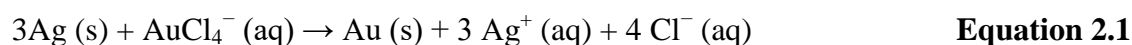


**Figure 2.14: TEM images of the Ag nanoprisms recorded under low and high magnification.**

#### 4.2. Synthesis of Au-framed Ag nanoprisms

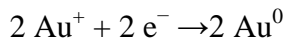
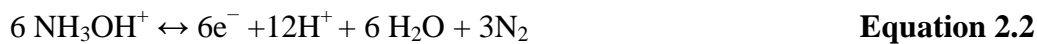
A gold layer was successfully deposited on the edges of the Ag nanoprisms following a protocol adapted from the one published by Shahjamali *et al.* [38]. Each individual Ag nanoprism contains two main (111) facets on the triangular planes and three (100) facets on the edges. Since the (100) facets have a higher surface energy than that of the (111) ones, the gold atom deposition preferentially takes place at the prism edges [39]. The epitaxial growth of gold layer is favored by the lattice mismatch between gold and silver (<0.3 %). While the Au@Ag core-shell nanostructures can be easily synthesized, the formation of the reverse structures with Ag core and Au shell is limited by the galvanic replacement process. It is an electrochemical process which involves oxidation of one metal by the ions of another more noble metal. However, such process has limited capability to achieve monometallic hollow nanostructures with precise control over morphology. As it involves simultaneous oxidative etching of the template and the atom deposition of the more noble metal onto the template, it leads to the formation of semi hollow nanostructures with many pinholes (Figure 2.15 left). Therefore, a mild reducing agent HyA was used to deposit the gold on the sides of the nanoprism [38]. However, the selective deposition is not guaranteed if the gold concentration is not carefully tuned. Any excess of gold above the critical Ag/Au ratio can lead to Ag etching by galvanic replacement, following the equation:



- **Protocol - Preparation of Au-framed Ag nanoprisms**

*In a typical experiment, the as-prepared silver nanoprism solution (20 mL) was centrifuged (10 000 rpm, 40 min) and redispersed in ultrapure water (20 mL). Hydroxylamine hydrochloride (HyA) solution (3 mM) and HAuCl<sub>4</sub> solution (0.3 mM) were then added simultaneously via two separate syringe pumps. The addition rate was set to 2 mL/h. After 5 min of addition, original HyA solution was replaced with basic HyA solution for additional 15 min of addition. Basic HyA solution was prepared by mixing original HyA solution (15 mL, 3 mM) and sodium hydroxide solution (0.30 mL, 0.5 M). The reducing power of HyA is enhanced at higher pH values, so NaOH was introduced to increase pH and boost the gold deposition rate. Ag@Au nanoprisms solution was then centrifuged (12 000 rpm, 45 min) and redispersed in an aqueous solution of trisodium citrate (15 mL, 0.3 mM).*

We performed a set of experiments to find the highest concentration of gold salt which results in the nanoprism edge coating but without pinhole formation. We observed that for the given volume of synthesized Ag nanoprisms, 0.67 mL of HAuCl<sub>4</sub> solution is the optimal amount. This concentration was shown to be too low to induce the etching but high enough to ensure the deposition of Au atoms on the (100) facets of the Ag nanoprism, as the high surface energy of these facets enables effective activation of the reaction between HyA and HAuCl<sub>4</sub>. The chemical reactions involved in the gold coating process are the following:



At this stage of the synthesis, Au-framed Ag nanoprisms were obtained, as shown in Figure 15 where one can see nanostructures with darker edges as a consequence of the higher electron density of gold by comparison with silver. The gold coating process was also monitored by UV-vis spectroscopy, revealing a red shift and a decrease of the intensity of the LSPR band with time. This spectral change is assigned to the gold deposition on the Ag prism edges, as gold has a higher refractive index than silver in the visible range.

With the increase of the volume of HAuCl<sub>4</sub> solution above 0.67 mL, the (111) facets of the silver nanoprisms start to be etched through galvanic corrosion, but the Ag nanoprism edges stay protected by the initially deposited Au layers. The oxidation of Ag nanoprisms by gold

ions occurs due to the difference in the redox potentials between  $\text{Ag}^+/\text{Ag}$  (0.8 V vs.SHE; SHE = standard hydrogen electrode) and  $\text{AuCl}_4^-/\text{Au}$  (0.99 V vs. SHE). The galvanic oxidation of the silver nanoprisms results in the formation of triangular nanostructures with many pinholes (Figure 2.15 right).

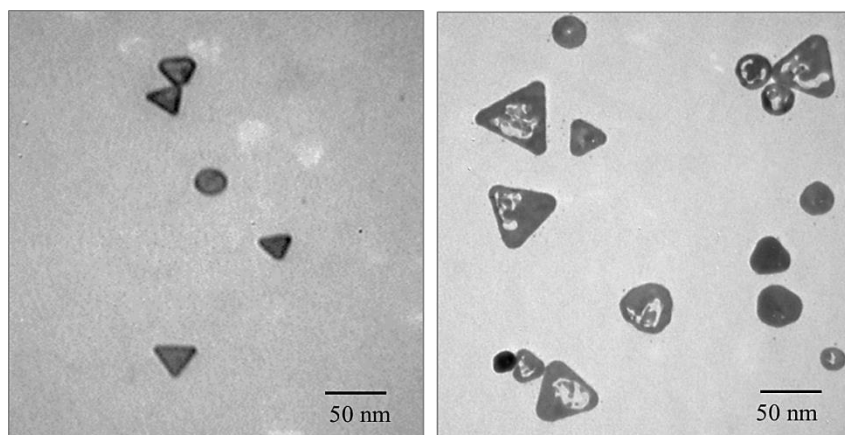


**Figure 2.15 :** TEM image of Au-framed Ag nanoprisms obtained by the addition of the optimal amount (left) and an excess of the gold salt (right).

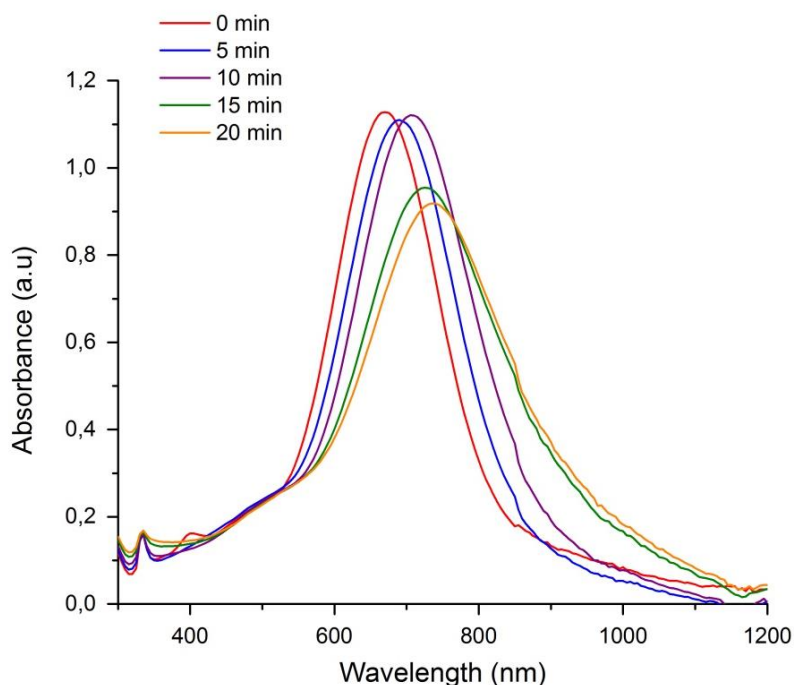


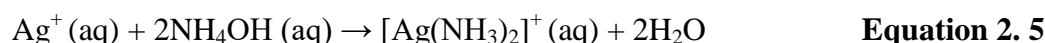
**Figure 2.16 :** Temporal evolution of the UV-Vis spectra of the silver nanoprisms during the gold deposition onto their edges.

### 4.3. Synthesis of gold hollow nanotriangles

- **Protocol - Etching of Au-framed Ag nanoprisms**

Hydrogen peroxide (50 mM) and ammonium hydroxide (50 mM) were mixed in 1:1 volume ratio and the mixture (0.8 mL) was introduced by a syringe pump (addition rate: 3 mL/h) to a freshly prepared solution of Au-framed Ag nanoprisms (4 mL). The mixture was then centrifuged (9 000 rpm, 30 min) and the gold triangular nanoframes were redispersed in an aqueous solution of trisodium citrate (4 mL, 0.3 mM).

The etching of the Ag nanoprism template was carried out through treatment with a mixture of hydrogen peroxide and ammonium hydroxide, as reported by Shahjamali *et al.* [40]. In such mixture, H<sub>2</sub>O<sub>2</sub> oxidizes Ag atoms according to reaction shown by equation 2.4, while NH<sub>4</sub>OH acts as a clean coordination agent to dissolve the oxidized silver following reaction shown by equation 2.5, and prevents the formation of AgOH or Ag<sub>2</sub>O that may precipitate onto the prisms and protect their surface against further etching reaction [40]. Such mixture behaves like a mild wet etchant as it induces the etching of Ag without contaminating the particles with ligands or ions. The slow addition of certain amount of the etchant, high control over the synthesis of monometallic nanoframes was established.



TEM image shown in Figure 2.17 revealed that upon the etching process, the silver template was removed from the Au-framed Ag nanoprisms, leading to hollow gold nanotriangles with an average size of  $52 \pm 14$  nm. The etching process was also followed by UV-vis spectroscopy. Figure 2.18 shows a red-shift and a decrease in the intensity of the characteristic LSPR band of Au-framed Ag nanoprisms, probably due to the decrease of the metal content of the nanostructures.



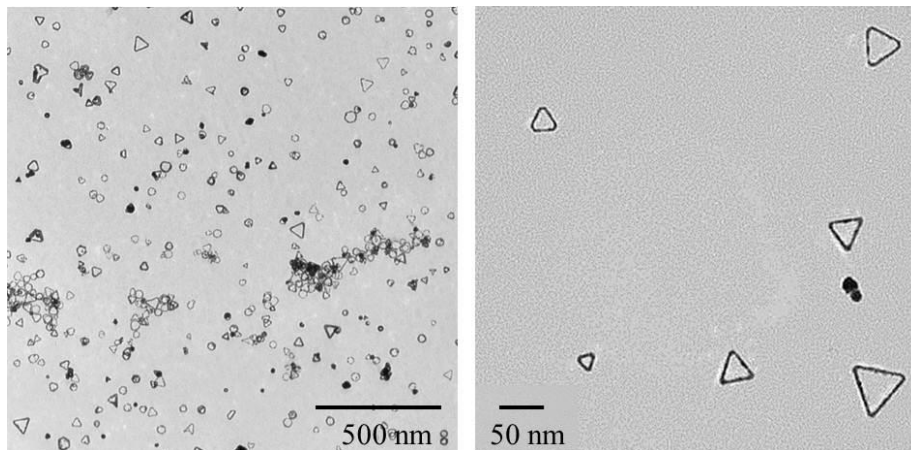


**Figure 2.17 : Low and high magnification TEM images of the gold hollow nanotriangles.**

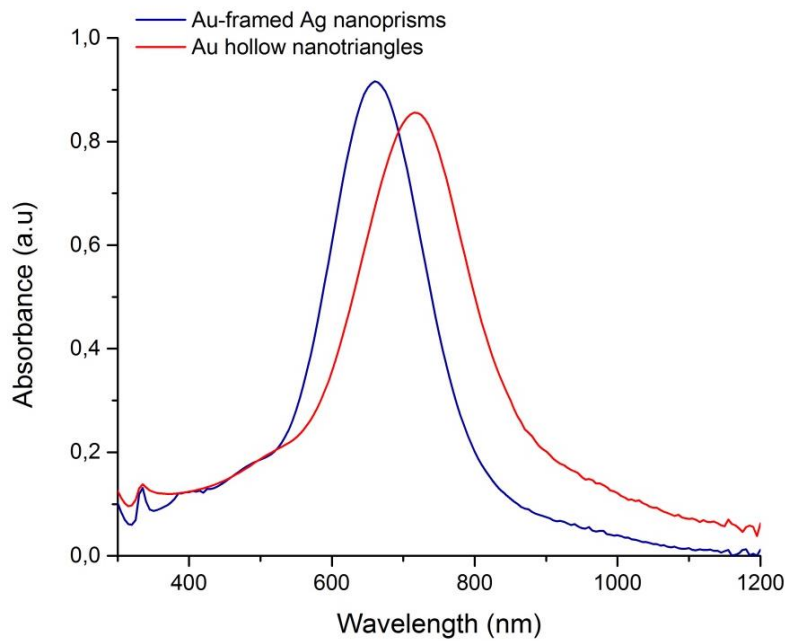


**Figure 2.18 : Absorbance spectra Au-framed Ag nanoprisms and Au hollow nanotriangles in water.**

The hollow nanotriangles were also characterized by AFM phase images (Figure 2.19) confirm the polydispersity in size of the gold nanoframes and show that their thickness is  $9 \pm 1$  nm. Height profiles along a cross-section of the nanotriangles (Figure 2.20) confirm that they are fully empty. The optical properties of the triangles were analyzed at the particle level by dark-field scattering microscopy. Figure 2.21 shows that a 42 nm nanotriangle exhibits a

LSPR band at 684 nm and an expected red shift of 18 nm is observed when the size of the nanostructure increases up to 68 nm.

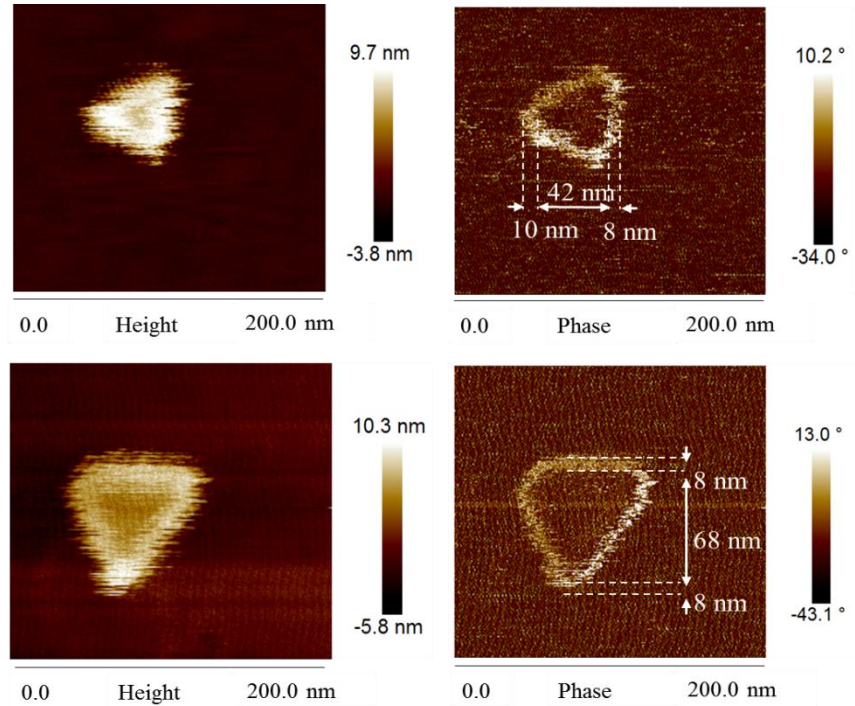


**Figure 2.19 : AFM height and phase images of two gold nanotriangles with different sizes.**

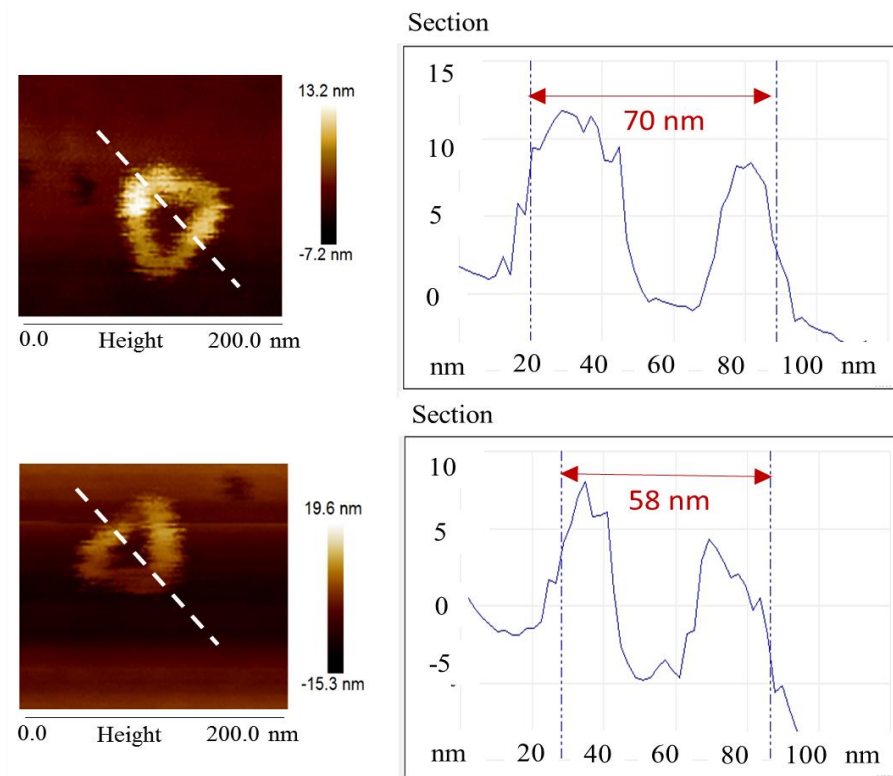


**Figure 2.20 : Height profiles along a cross-section of the gold nanotriangles.**

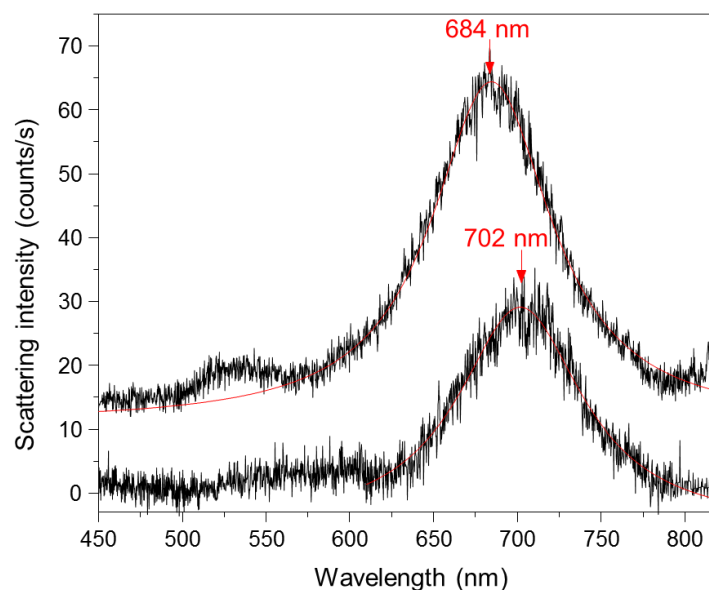


**Figure 2.21 :** Scattering spectra of a 42 nm (top) and a 68 nm (bottom) gold nanotriangles. The red curves are Lorentzian fits of the spectra.

## 5. PdCu@Au CORE-SHELL NANOTRIPODS

Recently, anisotropically branched plasmonic nanostructures have received an increasing attention owing to the enhanced properties which result from their branched architectural features. Properties such as porosity, large specific surface area, tips with small radii of curvatures and high densities of edges, corners, and stepped atoms are particularly attractive for catalytic applications. For example, Xia and co-workers described the superior catalytic activity of the PdCu bimetallic nanotripods compared with commercial Pd black catalyst. Such nanostructures were shown to enhance mass activity, specific activity and stability for the formic acid oxidation reaction [41]. In addition, Zhu *et al.* have shown that branched Au nanostructures display far better activity for catalytic reduction of 4-nitrophenol than spherical Au nanostructures [42].

Nanomultipods also have an important role in plasmonics. The branched nanostructures show well-defined optical response with two resonance modes assigned to dipolar resonances localized at the central core of the particles or at the tips, respectively. The second, more intense, plasmon band is dependent on the number, the length and the tip sharpness of the branches and can be tuned within the visible and NIR regions [43]. Furthermore, Walker and co-workers have shown that the largest field enhancements occur at the tips of the branched

structures. They evaluated the Raman enhancement factors of star-shaped Au nanostructures. Using crystal violet and 2-mercaptopyridine as probe molecules, they have shown that the star shaped gold nanoparticles produce much more enhanced Raman signals for both probe molecules, in comparison with nanospheres or nanorods of similar size [17].

A large variety of bottom-up synthetic methods have provided different types of plasmonic nanoparticles with branched morphology like monopods, bipods, tripods, tetrapods, hexapods, and multipods such as nanoflowers, nanostars, urchins and nanodendrites [44]. One of these methods is based on the in situ formation of the metal core and the subsequent branching in the presence of foreign ions and capping agents employed to break the symmetry of the face-centered cubic structure of the metal. Another synthetic strategy of branched metal nanostructures is the template-assisted growth where templates such as nanoparticle arrays or DNA–protein assemblies are used to facilitate the nucleation and branching of the nanoarchitectures. Also, different methods can be combined to achieve nanoarchitectures with complex structures [44]. For example, core–shell tripods were prepared through a two-step procedure that involved the seed-mediated synthesis of PdCu bimetallic tripods, which then were coated by a gold shell. Such nanostructures display perfect Y-shaped morphology with uniform, controllable arm lengths and well-defined absorption in visible or NIR regions, making them ideal candidates for building blocks of plasmonic nanoswitching systems.

### 5.1. Synthesis of the PdCu nanotripods

To form PdCu tripods, two requirements have to be fulfilled: formation of triangular, plate-like seeds during the nucleation step and the preferential deposition of atoms onto the three corners of the seeds during the growth step. Recently, Zhang *et al.* reported the evolution of Pd seeds to tripods by controlling the amount of CuCl<sub>2</sub> and KBr in the growth solution. They showed that Cu atoms help to reduce the energy barrier associated with the formation of plate-like seeds, while Br<sup>-</sup> ions direct the growth of Pd atoms on the three corners of the seeds to generate nanotripods [45]. We adopted their protocol to synthesize the PdCu bimetallic tripods which will serve as a template for the formation of PdCu@Au core-shell tripods.

#### Protocol: Synthesis of PdCu nanotripods

*In a typical synthesis of PdCu tripods, PVP ( $M_w \sim 55\,000$ , 116.70 mg), ascorbic acid (67.00 mg), potassium bromide (583.30 mg) and copper (II) chloride dihydrate (10.00 mg) were dissolved in 10 mL of water. 3 mL of the mixture were introduced in a 25 mL two-necked*

round bottom flask, placed in the oil bath pre-heated at 80 °C and stirred under reflux for 10 min. Sodium tetrachloropalladate (19.00 mg) was then dissolved in 1 mL of water and quickly injected in the reaction mixture. The mixture was stirred for 2 h. The flask was then transferred to ice and allowed to cool down during 15 min. The obtained black solution was transferred to a test tube and washed with water by three centrifugation cycles (12 000 rpm, 20 min). There was a clear separation of black precipitate containing mainly PdCu tripods, and grey supernatant containing the rest of the reaction mixture. The supernatant was discarded and the PdCu tripods were redispersed in 5 mL of water.

As explained by Zhang *et al.* [45], PdCu tripods can evolve only from plate-like seeds with planar defects such as stacking fault or twin planes. However, the defects are associated with relatively high energy and the formation of plate-like seeds is not favored by thermodynamics. Thus, such seeds can only be prepared using a very slow reduction process, in which CuCl<sub>2</sub> and KBr play the crucial roles. The kinetically controlled synthesis (i.e., the slow reduction rate) can be achieved by the coordination between Br<sup>-</sup> and Pd<sup>2+</sup> ions, but also by the incorporation of Cu atoms in the nanostructure through the potential deposition (UPD) process. As shown in Figure 2.22, the introduction of Cu<sup>2+</sup> promotes the formation of plate-like seeds at the early stage of the synthesis, as opposed to single-crystal Pd seeds formed in the absence of Cu<sup>2+</sup> ions. This seed structure change originates from the difference in stacking fault energies between Pd and Cu. Generally, the total free energy of a plate-like seed is much higher than a single-crystal seed due to the high lattice strain energy caused by defects. Yet, as the Cu atoms have lower stacking fault energy than Pd (41 vs 220 mJ·m<sup>-2</sup>), they can further reduce the energy barrier for the formation of plate-like seeds.

Additionally, the growth of seeds into tripods is controlled by the amount of Br<sup>-</sup> ions. For the formed hexagonal plates, the top and bottom faces are bonded by {111} planes while six side faces are covered by alternating {111} and {100} planes. The {100} facets are more active, leading to the preferential binding of Br<sup>-</sup> ions to the three {100} side faces of a triangular seed. As the amount of Br<sup>-</sup> ions increases, the side surface becomes completely blocked, allowing the deposition of Pd atoms only onto the three corners to form a tripod. Thus, the control over the amount of KBr present in the solution provides fine tuning of the length of the arms from a few to tens of nanometers.

In our work, the amount of KBr was optimized to obtain PdCu tripods with an average arm length of 30 ± 6 nm and an average thickness of 6 ± 0.5 nm. Even though the prepared PdCu

tripods were uniform in terms of size, 20 % of the nanostructures in the solution were monopods, bipods or tetrapods, as observed by TEM (Figure 2.23).

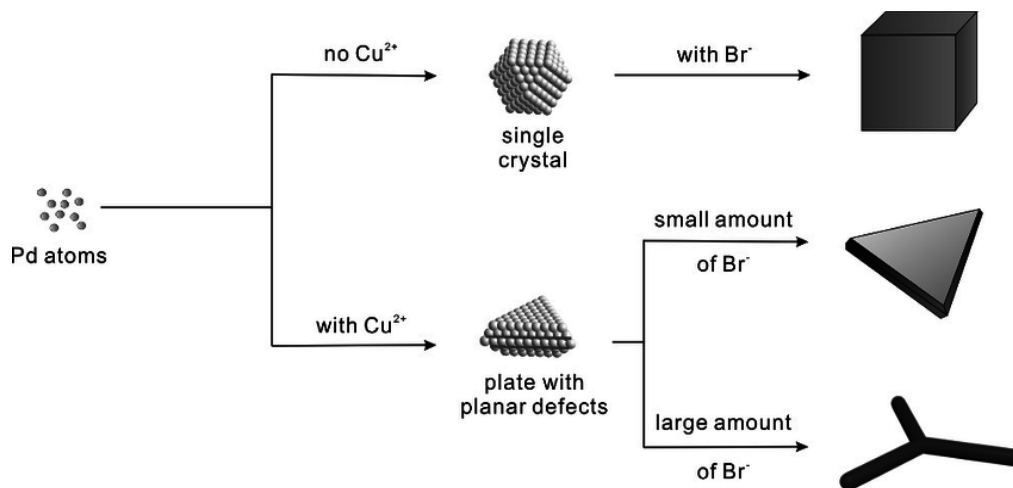


**Figure 2.22 :** Scheme of the formation of Pd or PdCu nanostructures with different morphologies, as the function of the amounts of Cu<sup>2+</sup> and Br<sup>-</sup> ions [45].



**Figure 2.23 :** TEM image of PdCu tripods.

## 5.2. Synthesis of PdCu@Au core-shell nanotripods

The gold tripods were obtained by depositing a gold shell on the surface of the PdCu tripods through the reduction of  $\text{HAuCl}_4$  with AA, in the presence of PVP as a colloidal stabilizer [46].

### Protocol: Synthesis of PdCu@Au core-shell nanotripods

*In a typical synthesis, AA (0.14 g) and PVP ( $M_w \sim 55\,000$ , 0.024 g) were dissolved in 5 mL of water and the solution was stirred slowly for 10 min. 100  $\mu\text{L}$  of the as-prepared PdCu tripod solution were then injected inside the mixture. The  $\text{HAuCl}_4$  solution (5 mL, 0.5 mM) was introduced by a syringe pump (addition rate 5 mL/h). The color of the solution changed from grey to dark purple, indicating the formation of the gold layer on the PdCu tripods.*

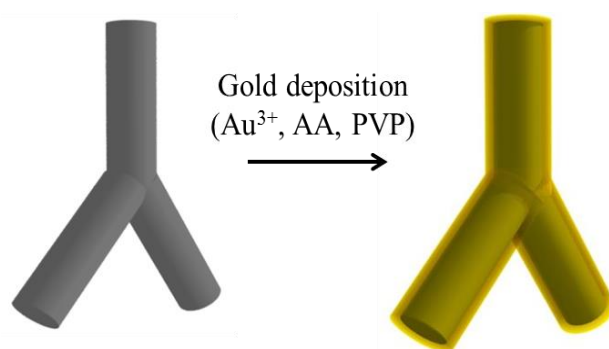


**Figure 2.24 : Synthesis of PdCu@Au nanotripods via the deposition of gold on the PdCu templates.**

The oxidation-reduction reaction between gold and PdCu tripods occurs fast, which can result in the complete dissolution of the template during the reduction of  $\text{Au}^{3+}$ . Thus, it is necessary to precisely tune the amount of gold added in the PdCu solution, but also to slow down the reduction rate of the  $\text{Au}^{3+}$ . The presence of PVP enables the control over reaction kinetics. The specific adsorption of PVP on the high energy (110) facets of PdCu tripods decreases their surface energy and consequently allows the precise formation of the gold shell (Figure 2.24). The uniform and conformational coating of the PdCu tripods with gold was confirmed by TEM, SEM and AFM characterizations (Figures 2.25 and 2.26). In addition, HRTEM was combined with EDX to observe the elemental mapping patterns. The EDX elemental mapping confirmed that the PdCu@Au tripods consisted of a core containing Cu and Pd, surrounded by a gold shell (Figures 2.27 and 2.28).

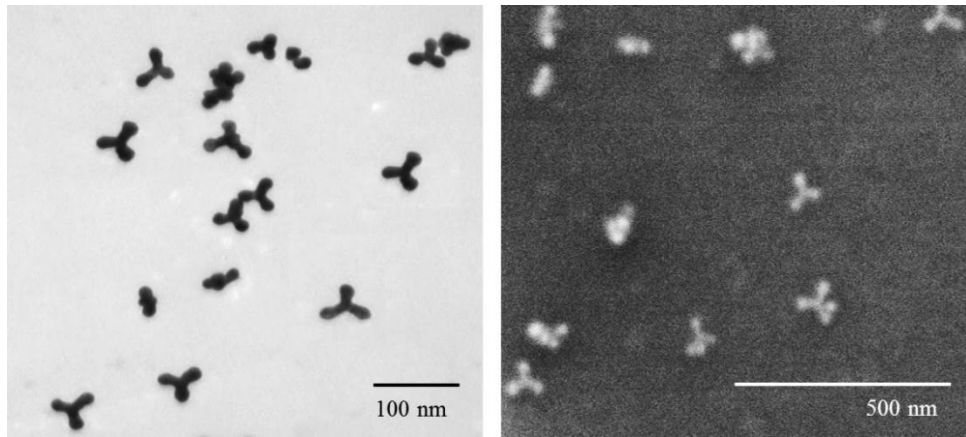


Figure 2.25 : TEM and SEM images of the PdCu@Au core-shell tripods.

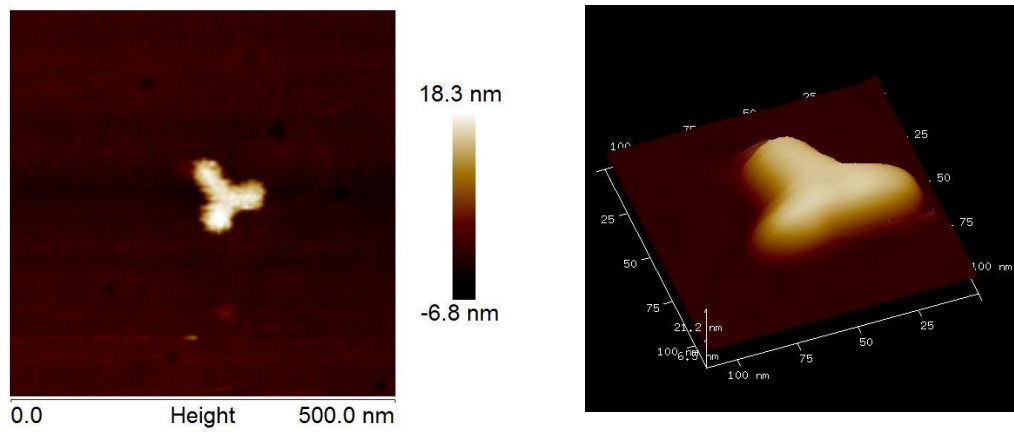
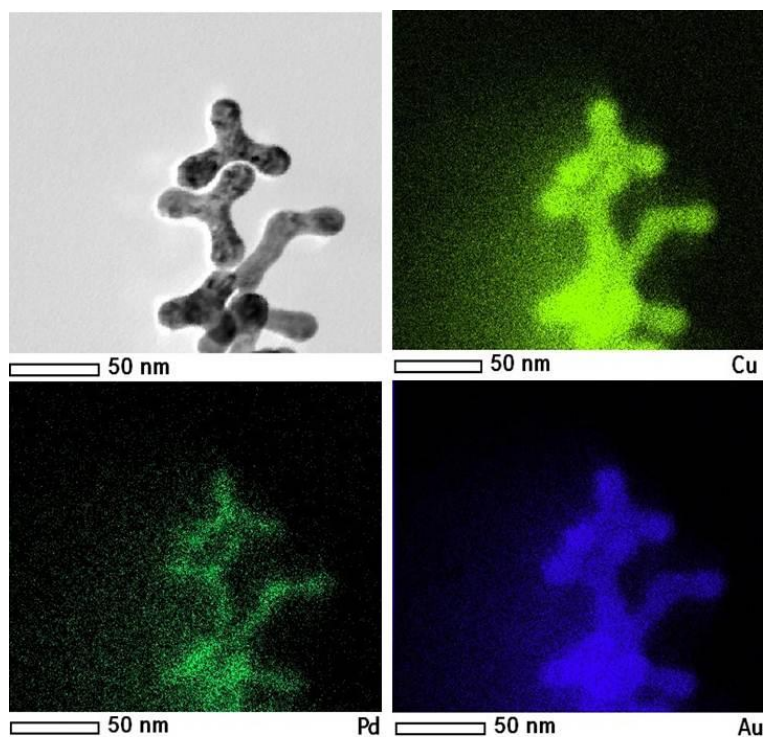
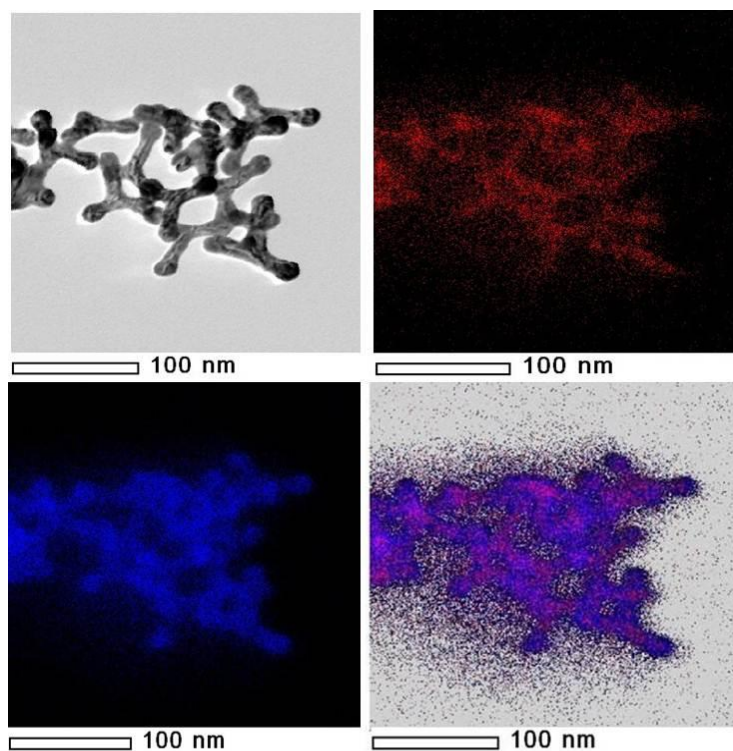


Figure 2.26 : AFM images of a PdCu@Au core-shell tripod.





**Figure 2.27 : HRTEM image of PdCu@Au tripods and EDX elemental mappings of Cu (yellow), Pd (green) and Au (blue).**



**Figure 2.28 : HRTEM image of PdCu@Au tripods and EDX elemental mappings of Pd (red), Au (blue) and both elements (red + blue).**

The TEM images of Figure 2.29 show that the thickness of the gold shell can be tuned by varying the added volume of the  $\text{HAuCl}_4$  solution. This tendency was also confirmed by UV-vis spectroscopy. Since the PdCu tripods do not exhibit any absorption band between 400 and 1200nm, the growth of the gold shell is revealed by the appearance of two SPR bands which both increase in intensity with the added volume of gold precursor (Figure 2.30). While the transverse mode remains at 520 nm when the gold shell thickness increases, the longitudinal one simultaneously blue shifts from 900 to 780 nm, as expected [46].

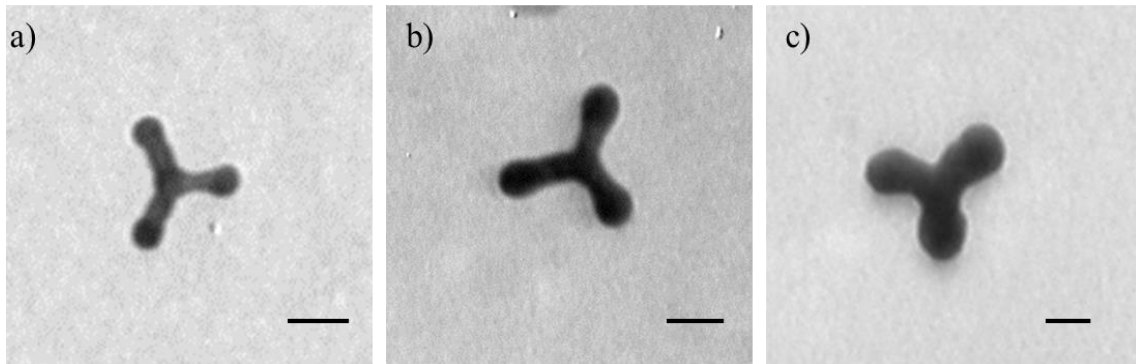


**Figure 2.29 : TEM images of PdCu@Au core-shell tripods showing the difference in arm thickness upon the addition of an increasing volume of the  $\text{HAuCl}_4$  solution: a) 2 mL; b) 4 mL; c) 6 mL. The scale bar is 20 nm.**

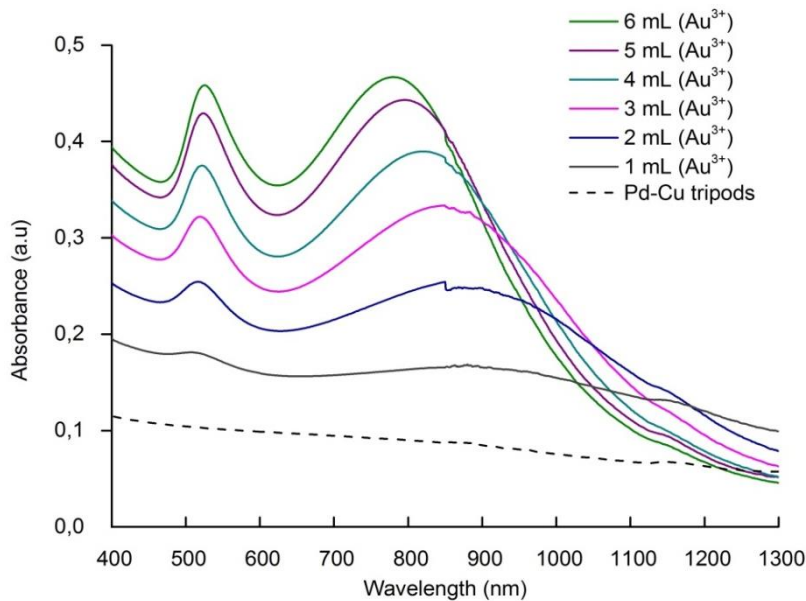


**Figure 2.30 : Absorption spectra of PdCu tripods and PdCu@Au as a function of the added volume of the  $\text{HAuCl}_4$  solution.**

The PdCu@Au tripods that were used in the experiments described in the following chapters were prepared by the introduction of 4 mL of H<sub>AuCl</sub><sub>4</sub> solution into the solution of PdCu tripods. They exhibit a longitudinal LSPR peak at 820 nm and have an average arm length of  $33 \pm 4$  nm and an average arm thickness of  $14 \pm 4$  nm. The thickness of the gold shell is estimated to be  $\sim 6$  nm.

## 6. CONCLUSION

In this chapter, we have described the synthesis and characterization of various plasmonic nanoparticles.

Short AuNRs with an aspect ratio equal to 2 were synthesized by a seed-mediated growth method. The AuNRs were uniform in shape and size and stable over a long period of time.

Gold hollow nanotriangles were synthesized by a three-step method. Firstly, a sacrificial template, *i.e.* silver nanoprisms, was synthesized through a seed-mediated growth. Subsequently, gold was selectively deposited on the edges of the silver template, resulting in the formation of gold-framed silver nanotriangles. The detail study of these hybrid nanostructures allowed us to control the thickness of the gold frame and thus tune their optical properties. Finally, the silver template was chemically etched from the hybrid structures and hollow gold nanotriangles with minimal silver impurities were produced in a high yield.

PdCu-Au core-shell nanotripods were prepared through a two-step procedure that involved the seed-mediated synthesis of PdCu bimetallic tripods, which then were coated by a gold shell. By controlling the reaction kinetics, we were able to tune the tripod morphology as well as the size and the thickness of the gold shell.

All of these nanostructures will be used as building blocks for the fabrication of the target plasmon switching nanodevice, presented in the following chapters.

## REFERENCES

- [1] M. Faraday, "The Bakerian Lecture : Experimental relations of gold (and other metals) to light," *Philos. Trans. R. Soc. London*, vol. 147, pp. 145–181, 1857.
- [2] G. Mie, "Beiträge zur Optik trüber Medien, speziell kolloidaler Metallösungen," *Ann. Phys.*, vol. 330, no. 3, pp. 377–445, 1908.
- [3] X. Yang, M. Yang, B. Pang, M. Vara, and Y. Xia, "Gold nanomaterials at work in biomedicine," *Chem. Rev.*, vol. 115, no. 19, pp. 10410–10488, 2015.
- [4] X. Huang, S. Neretina, and M. A. El-Sayed, "Gold nanorods: From synthesis and properties to biological and biomedical applications," *Adv. Mater.*, vol. 21, no. 48, pp. 4880–4910, 2009.
- [5] N. E. Motl, A. F. Smith, C. J. DeSantis, and S. E. Skrabalak, "Engineering plasmonic metal colloids through composition and structural design," *Chem. Soc. Rev.*, vol. 43, no. 11, pp. 3823–3834, 2014.
- [6] T. K. Sau and A. L. Rogach, "Nonspherical noble metal nanoparticles: Colloid-chemical synthesis and morphology control," *Adv. Mater.*, vol. 22, no. 16, pp. 1781–1804, 2010.
- [7] A. R. Tao, S. Habas, and P. Yang, "Shape control of colloidal metal nanocrystals," *Small*, vol. 4, no. 3, pp. 310–325, 2008.
- [8] J. Gong, G. Li, and Z. Tang, "Self-assembly of noble metal nanocrystals: Fabrication, optical property, and application," *Nano Today*, vol. 7, no. 6, pp. 564–585, 2012.
- [9] X. Lu, M. Rycenga, S. E. Skrabalak, B. Wiley, and Y. Xia, "Chemical synthesis of novel plasmonic nanoparticles," *Annu. Rev. Phys. Chem.*, vol. 60, no. 1, pp. 167–192, 2009.
- [10] M. Rycenga, C. M. Cobley, J. Zeng, W. Li, C. H. Moran, Q. Zhang, D. Qin, and Y. Xia, "Controlling the synthesis and assembly of silver nanostructures for plasmonic applications," *Chem. Rev.*, vol. 111, no. 6, pp. 3669–3712, 2011.
- [11] D. J. de Aberasturi, A. B. Serrano-Montes, and L. M. Liz-Marzan, "Modern applications of plasmonic nanoparticles: From energy to health," *Adv. Opt. Mater.*, vol. 3, no. 5, pp. 602–617, 2015.
- [12] P. K. Jain, X. Huang, I. H. El-Sayed, and M. A. El-Sayed, "Noble metals on the nanoscale: Optical and photothermal properties and some applications in imaging, sensing, biology, and medicine," *Acc. Chem. Res.*, vol. 41, no. 12, pp. 1578–1586,

- 2008.
- [13] S. J. Tan, M. J. Campolongo, D. Luo, and W. Cheng, "Building plasmonic nanostructures with DNA," *Nat. Nanotechnol.*, vol. 6, no. 5, pp. 268–276, 2011.
- [14] S. J. Oldenburg, R. D. Averitt, S. L. Westcott, and N. J. Halas, "Nanoengineering of optical resonances," *Chem. Phys. Lett.*, vol. 288, no. 2–4, pp. 243–247, 1998.
- [15] E. Prodan, C. Radloff, N. J. Halas, and P. Nordlander, "A hybridization model for the plasmon response of complex nanostructures," *Science*, vol. 302, no. 5644, pp. 419–422, 2003.
- [16] Y. Sun and Y. Xia, "Mechanistic study on the replacement reaction between silver nanostructures and chloroauric acid in aqueous medium," *J. Am. Chem. Soc.*, vol. 126, no. 9, pp. 3892–3901, 2004.
- [17] E. Ye, M. D. Regulacio, S.-Y. Zhang, X. J. Loh, and M.-Y. Han, "Anisotropically branched metal nanostructures," *Chem. Soc. Rev.*, vol. 44, pp. 6001–6017, 2015.
- [18] C. M. Cobley, J. Chen, E. C. Cho, L. V Wang, and Y. Xia, "Gold nanostructures: a class of multifunctional materials for biomedical applications," *Chem. Soc. Rev. Chem. Soc. Rev.*, vol. 40, no. 40, pp. 44–56, 2011.
- [19] M. Grzelczak, J. Vermant, E. M. Furst, and L. M. Liz-Marzán, "Directed self-assembly of nanoparticles," *ACS Nano*, vol. 4, no. 7, pp. 3591–3605, 2010.
- [20] M. Tebbe, M. Mayer, B. A. Glatz, C. Hanske, P. T. Probst, M. B. Mueller, M. Karg, M. Chanana, T. König, C. Kuttner, and A. Fery, "Optically anisotropic substrates via wrinkle-assisted convective assembly of gold nanorods on macroscopic areas," *Faraday Discuss.*, vol. 181, no. 0, pp. 243–260, 2014.
- [21] G. Baffou and R. Quidant, "Nanoplasmonics for chemistry," *Chem. Soc. Rev.*, vol. 43, no. 11, pp. 3898–3907, 2014.
- [22] A. Klinkova, R. M. Choueiri, and E. Kumacheva, "Self-assembled plasmonic nanostructures," *Chem. Soc. Rev.*, vol. 43, pp. 3976–3991, 2014.
- [23] K. Park, L. F. Drummy, R. C. Wadams, H. Koerner, D. Nepal, L. Fabris, and R. A. Vaia, "Growth mechanism of gold nanorods," *Chem. Mater.*, vol. 25, no. 4, pp. 555–563, 2013.
- [24] J. Pérez-Juste, I. Pastoriza-Santos, L. M. Liz-Marzán, and P. Mulvaney, "Gold nanorods: Synthesis, characterization and applications," *Coord. Chem. Rev.*, vol. 249, no. 17–18, pp. 1870–1901, 2005.
- [25] S.-S. Chang, C.-L. Lee, and C. R. C. Wang, "Gold nanorods: Electrochemical synthesis and optical properties," *J. Phys. Chem. B*, vol. 101, no. 34, pp. 6661–6664, 1997.

- [26] N. R. Jana, L. Gearheart, and C. J. Murphy, "Seed-mediated growth approach for shape-controlled synthesis of spheroidal and rod-like gold nanoparticles using a surfactant template," *Adv. Mater.*, vol. 13, no. 18, pp. 1389–1393, 2001.
- [27] B. Nikoobakht and M. El-Sayed, "Preparation and growth mechanism of gold nanorods (NRs) using seed - mediated growth method," *Chem. Mater.*, vol. 15, no. 16, pp. 1957–1962, 2003.
- [28] J. Pérez-Juste, L. M. Liz-Marzán, S. Carnie, D. Y. C. Chan, and P. Mulvaney, "Electric-field-directed growth of gold nanorods in aqueous surfactant solutions," *Adv. Funct. Mater.*, vol. 14, no. 6, pp. 571–579, 2004.
- [29] C. J. Orendorff and C. J. Murphy, "Quantitation of metal content in the silver-assisted growth of gold nanorods," *J. Phys. Chem. B*, vol. 110, no. 9, pp. 3990–3994, 2006.
- [30] S. Si, C. Leduc, M. H. Delville, and B. Lounis, "Short gold nanorod growth revisited: The critical role of the bromide counterion," *ChemPhysChem*, vol. 13, no. 1, pp. 193–202, 2012.
- [31] X. Ye, L. Jin, H. Caglayan, J. Chen, G. Xing, C. Zheng, V. Doan-Nguyen, Y. Kang, N. Engheta, C. R. Kagan, and C. B. Murray, "Improved size-tunable synthesis of monodisperse gold nanorods through the use of aromatic additives," *ACS Nano*, vol. 6, no. 3, pp. 2804–2817, 2012.
- [32] X. Ye, L. Jin, H. Caglayan, J. Chen, G. Xing, and C. Zheng, "Improved Size-Tunable Synthesis of Monodisperse Gold Nanorods through the Use of Aromatic Additives," no. 3, pp. 2804–2817, 2012.
- [33] Q. Lu and F. Gao, "Synthesis and property studies of hollow nanostructures," *CrystEngComm*, vol. 18, no. 39, pp. 7399–7409, 2016.
- [34] M. A. Mahmoud and M. A. El-Sayed, "Gold nanoframes: Very high surface plasmon fields and excellent near-infrared sensors," *J. Am. Chem. Soc.*, vol. 132, no. 36, pp. 12704–12710, 2010.
- [35] J. Zeng, X. Xia, M. Rycenga, P. Henneghan, Q. Li, and Y. Xia, "Successive deposition of silver on silver nanoplates: Lateral versus vertical growth," *Angew. Chemie - Int. Ed.*, vol. 50, no. 1, pp. 244–249, 2011.
- [36] A. Le Beulze, E. Duguet, S. Mornet, J. Majimel, M. Tréguer-Delapierre, S. Ravaine, I. Florea, and O. Ersen, "New insights into the side-face structure, growth aspects, and reactivity of Ag nanoprisms," *Langmuir*, vol. 30, no. 5, pp. 1424–1434, 2014.
- [37] R. Jin, Y. C. Cao, E. Hao, G. S. Métraux, G. C. Schatz, and C. a Mirkin, "Controlling anisotropic nanoparticle growth through plasmon excitation," *Nature*, vol. 425, no.

- 6957, pp. 487–490, 2003.
- [38] M. M. Shahjamali, M. Bosman, S. Cao, X. Huang, S. Saadat, E. Martinsson, D. Aili, Y. Y. Tay, B. Liedberg, S. C. J. Loo, H. Zhang, F. Boey, and C. Xue, “Gold coating of silver nanoprisms,” *Adv. Funct. Mater.*, vol. 22, no. 4, pp. 849–854, 2012.
- [39] M. M. Shahjamali, M. Salvador, M. Bosman, D. S. Ginger, and C. Xue, “Edge-gold-coated silver nanoprisms: Enhanced stability and applications in organic photovoltaics and chemical sensing,” *J. Phys. Chem. C*, vol. 118, no. 23, pp. 12459–12468, 2014.
- [40] M. M. Shahjamali, M. Bosman, S. Cao, X. Huang, X. Cao, H. Zhang, S. S. Pramana, and C. Xue, “Surfactant-free sub-2 nm ultrathin triangular gold nanoframes,” *Small*, vol. 9, no. 17, pp. 2880–2886, 2013.
- [41] R. Zhao, M. Gong, H. Zhu, Y. Chen, Y. Tang, and T. Lu, “Seed-assisted synthesis of Pd@Au core-shell nanotetrapods and their optical and catalytic properties,” *Nanoscale*, vol. 6, no. 15, pp. 9273–9278, 2014.
- [42] M. Zhu, B. Lei, F. Ren, P. Chen, Y. Shen, B. Guan, Y. Du, T. Li, and M. Liu, “Branched Au nanostructures enriched with a uniform facet: Facile synthesis and catalytic performances,” *Sci. Rep.*, vol. 4, p. 5259, 2014.
- [43] P. S. Kumar, I. Pastoriza-Santos, B. Rodriguez-Gonzalez, F. J. Garcia de Abajo, and L. M. Liz-Marzán, “High-yield synthesis and optical response of gold nanostars,” *Nanotechnology*, vol. 19, no. 1, p. 15606, 2008.
- [44] N. Li, P. Zhao, and D. Astruc, “Anisotropic gold nanoparticles: Synthesis, properties, applications, and toxicity,” *Angew. Chemie - Int. Ed.*, vol. 53, no. 7, pp. 1756–1789, 2014.
- [45] L. Zhang, S.-I. Choi, J. Tao, H.-C. Peng, S. Xie, Y. Zhu, Z. Xie, and Y. Xia, “Pd-Cu bimetallic tripods: A mechanistic understanding of the synthesis and their enhanced electrocatalytic activity for formic acid oxidation,” *Adv. Funct. Mater.*, vol. 24, no. 47, pp. 7520–7529, 2014.
- [46] B. Pang, Y. Zhao, H. Luehmann, X. Yang, L. Detering, M. You, C. Zhang, L. Zhang, Z.-Y. Li, Q. Ren, Y. Liu, and Y. Xia, “64 Cu-doped PdCu@Au tripods: A multifunctional nanomaterial for positron emission tomography and image-guided photothermal cancer treatment,” *ACS Nano*, vol. 10, no. 3, pp. 3121–3131, 2016.

## **CHAPTER 3**

### **DIRECTED ASSEMBLY OF GOLD NANORODS**





## 1. INTRODUCTION

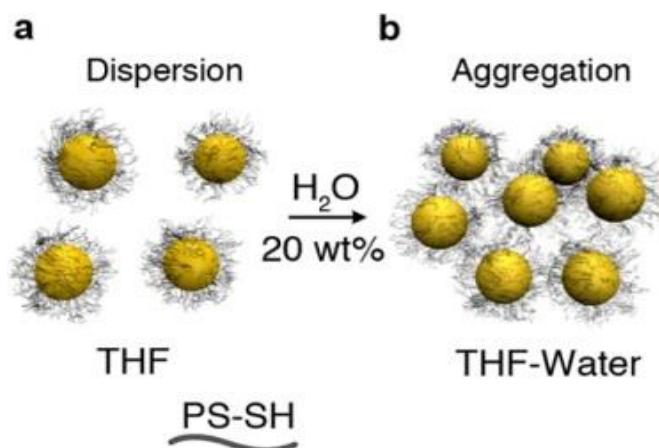
Self-assembly of plasmonic NPs implies their organization into ordered nanoarchitectures, which consequentially acquire new optical properties through the coupling of plasmons of adjacent NPs and the enhancement of the electric field in the interparticle gaps.

Variations in certain features of self-assembled structures such as number of NPs, the directionality of NP organization and the interparticle distance lead to new plasmonic systems. However, the precise tuning of those parameters is highly challenging, despite the tremendous progress in the nanostructural organization during the last decade. Thus, there is still plenty of room to investigate the new assembly techniques for precise control of nanoparticle arrangement into structures that can form the next generation of plasmonic devices [1], [2].

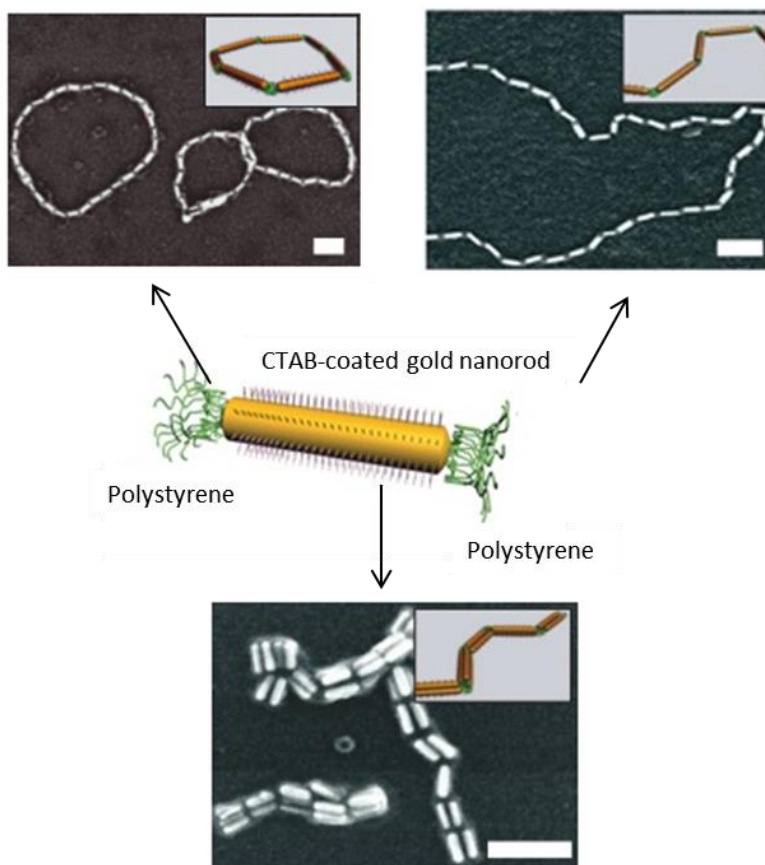
The previous studies have shown that the self-assembly of plasmonic nanoparticles can be achieved through direct interactions between NPs, or indirectly using different templates or external fields (e.g., magnetic or electric field) [3].

The directed self-assembly can be realized either by molecular cross-linking [4] or by the careful tuning of the interparticle forces. Although one major force triggers the assembly process, the formation of new nanoarchitectures originates from the interplay of several forces. The particular dominant force can cause the spatial distribution of NPs by applying different stimuli including temperature, electromagnetic radiation, polarity of the medium, redox activity or pH [5].

The hydrophobic interactions due to the rearrangement of water molecules as two hydrophobic species approach each other, have a longer range than the typical covalent bond [6]. It was shown that the quality of the solvent plays an important role in tuning the interactions between nanoparticles [7]. For instance, polystyrene-coated gold nanoparticles can undergo hydrophobic interaction in THF-water mixture. In pure THF, steric repulsions between the polymer chains of adjacent particles overcome the attractive van der Waals interactions, leading to a stable dispersion. The addition of water molecules causes the attraction between the hydrophobic polystyrene chains which compress to expel solvent molecules into the bulk and minimize the free energy of the system, resulting in the formation of aggregates (Figure 3.1) [8].



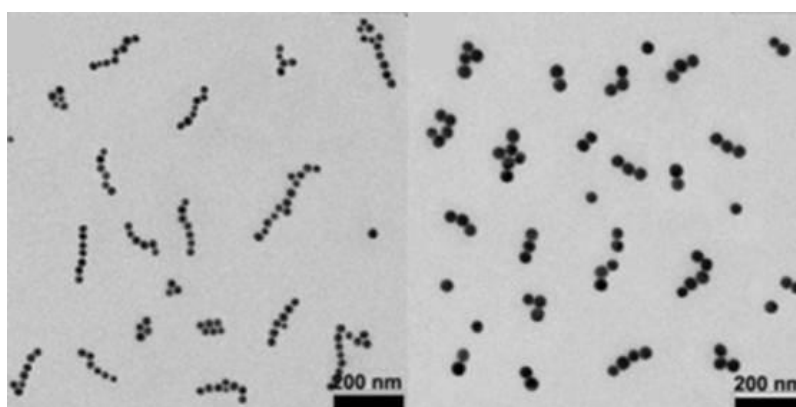
**Figure 3.1 : Scheme of assembly of AuNPs modulated by hydrophobic interactions : a) Colloidal dispersion of polystyrene-coated AuNPs in THF; b) cluster formation upon the addition of water [8].**



**Figure 3.2 : Scheme and representative TEM images of amphiphilic gold nanorods coated with a double layer of CTAB along the longitudinal side and polystyrene ligands grafted onto both tips assembled in different shapes (rings, chains and bundled chains), depending on the solvent quality [10]. Scale bar: 100 nm.**

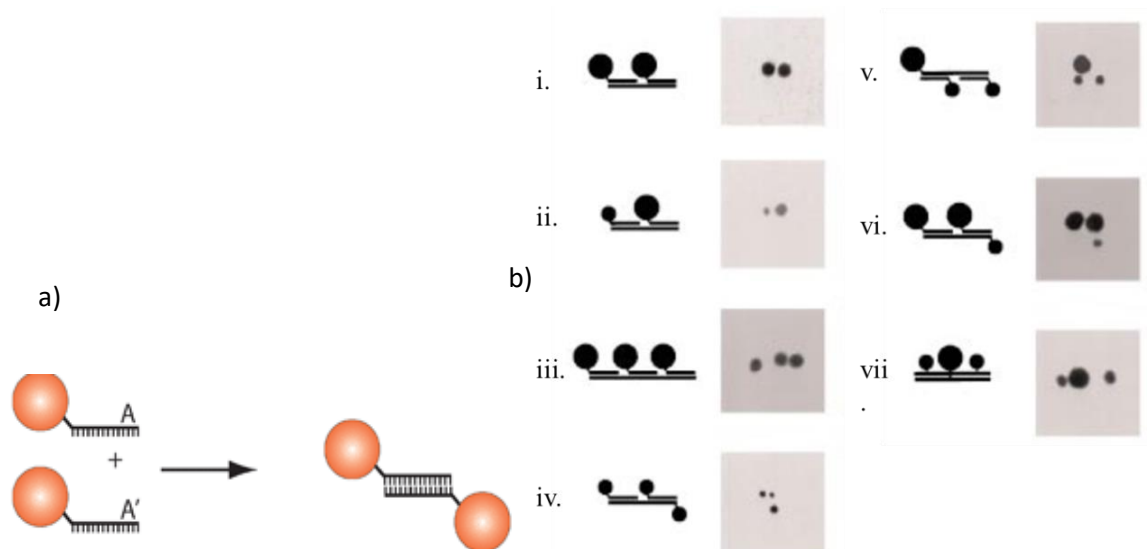
In a similar way, Kumacheva and co-workers have demonstrated the AuNR self-assembly based on solvophobic forces. In their work, AuNRs were capped with polymer and dispersed in a good solvent for such polymer ligand. Upon the addition of a non-solvent, NRs formed clusters to minimize the surface energy of the system by screening the unfavorable interactions between the polymer ligands and the solvent via NRs association. The changes in the volume ratio of good and bad solvent resulted in the formation in the various self-assembled nanorod structures such as rings, chains or bundled chains (Figure 3.2) [7], [9].

Xia *et al.* reported the self-assembly of spherical AuNPs driven mainly by the pH-dependent electrostatic repulsions between the NPs. The electrostatic stabilization of the NPs was suppressed by the tuning of the pH of the medium, leading to the self-assembly of gold nanoparticles coated with pH-responsive polymers into nanochains. Moreover, they showed that the length of the formed chains is determined by the value of the environmental pH (Figure 3.3) [11].

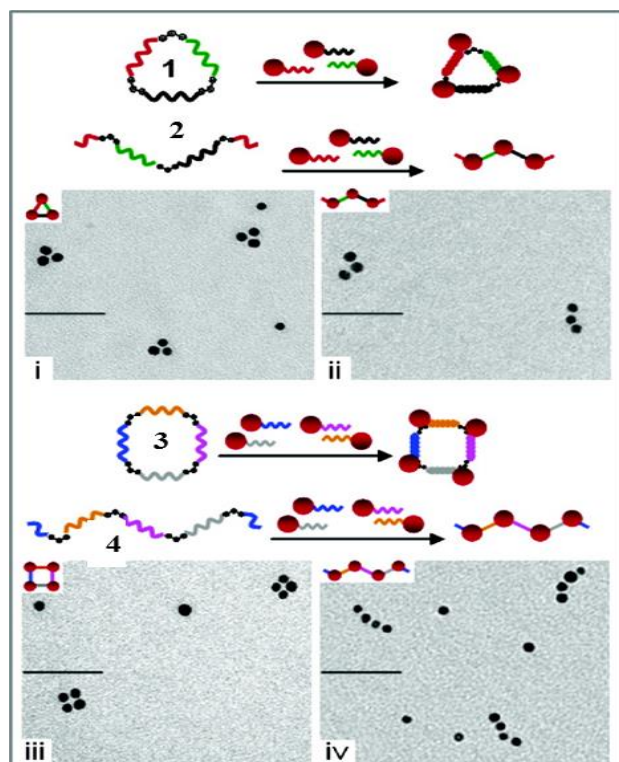


**Figure 3.3 : TEM image of gold NPs chains formed in response to the change of the environmental pH: long chains observed at pH=3 and short chains at pH=2.5 [11].**

Functionalization of NPs with biological molecules can also initiate the self-assembly process. In particular, DNA provides a pragmatic platform for assembly of NPs into ordered nanostructures due to its programmability and the selective molecular recognition ability. Schultz *et al.* showed that AuNPs modified with single strand DNA can arrange into homodimeric, heterodimeric, homotrimeric and heterotrimeric assemblies through Watson–Crick base-pairing with AuNPs modified with complementary strands (Figure 3.4) [12].



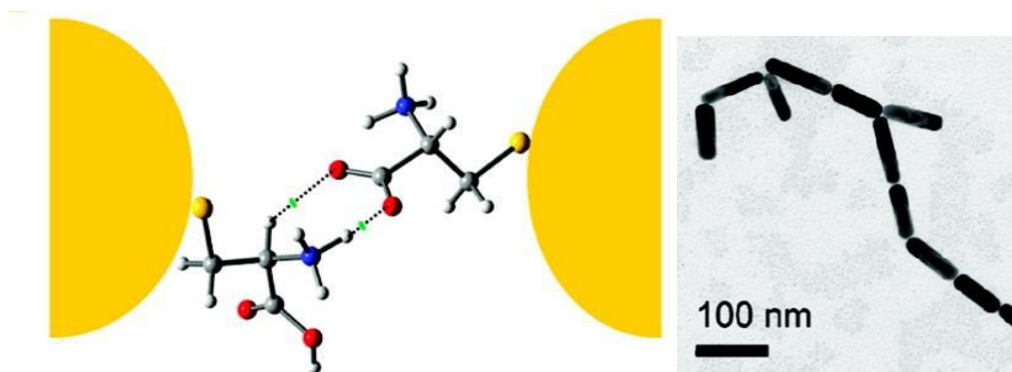
**Figure 3. 4 :** (a) Scheme of AuNPs assembly based on DNA double strand formation, (b) Illustrations of different assembly strategies and corresponding TEM images: i) 10-nm homodimer; ii) 10-/5-nm heterodimer; iii) 10-nm homotrimer; iv) 5-nm homotrimer; v) 10-/5-/5-nm heterotrimer ; vi) 5-/10-/10-nm heterotrimer; vii) 5-/10-/5-nm heterotrimer [12].



**Figure 3. 5 :** DNA cyclic oligomers 1 and 3 organize AuNPs into triangles and squares, while their linear analogues trimer 2 and tetramer 4 direct the assembly of AuNPs in chains of three and four particles. Scale bar is 50 nm [13].

Sleiman and Aldaye [13] reported a directed assembly of AuNPs by using single-stranded, cyclic DNA templates. Hybridization of cyclic templates with DNA-labeled AuNPs allowed the precise positioning of the nanostructures on the complementary arms of the templates, creating triangles and squares of AuNPs (Figure 3.5). Also, the specific streptavidin-biotin interaction is known as being an effective method to obtain nanoparticles arrays with controlled spacing [14].

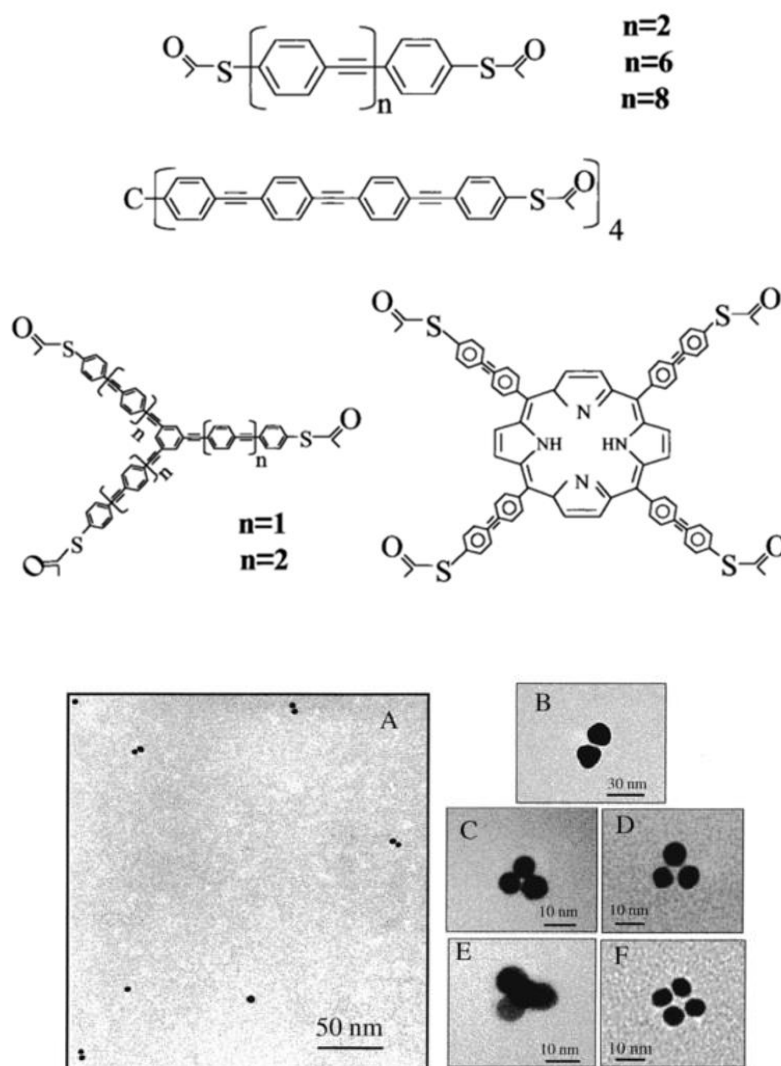
Another route to control the assembly of plasmonic NPs consists in using organic molecules as linkers. Due to the easy tuning of their size, stability and topology, organic linkers offer a unique tool to assemble NPs into spatially and symmetrically well-defined aggregates. Moreover, introduction of various functional groups into the organic molecule structure provides different types of interactions between the nanoparticles and thus induces a variety of self-assembly processes. The self-assembly of AuNRs driven by hydrogen bonding was reported by Liz-Marzán and co-workers [15]. Upon the modification of AuNRs with bifunctional molecules such as cysteine, aggregates were formed due to hydrogen bonding between carboxylate and protonated amine groups of two distinct cysteine molecules. Since the degree of hydrogen bonding strongly depends on the pH, its gradual changes were shown to lead to the tip-to-tip self-assembly of AuNRs (Figure 3.6).



**Figure 3.6 : Scheme and TEM image showing the pH-controlled assembly of AuNRs modified with cysteine [15].**

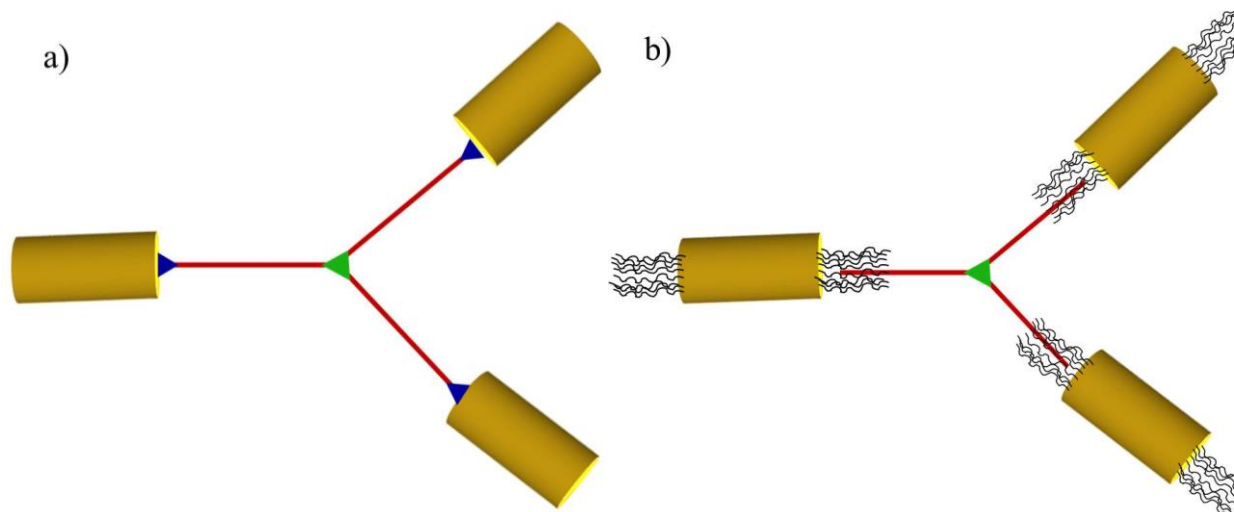
Feldheim and co-workers assembled gold nanoparticles into dimer, trimer and tetramer superstructures by rigid thiol-functionalized polyacetylene oligomers. The different geometries of the organic linkers provided variety of cluster morphologies, while their rigidity

ensured the fixed distance between the nanoparticles inside the clusters (Figure 3.7) [16], [17].



**Figure 3.7 : Phenylethynyl di-, tri- and tetra-phenylethynyl thiols used to form the gold NP dimers (A,B), trimers (C,D,E) and tetramers (F) observed by TEM [17].**

Inspired by all these works, we have designed and synthesized new organic molecules able to be used as linkers to assemble AuNRs in nanoarchitectures with well-defined geometry, namely trimers, *i.e.* three gold nanorods cross-linked by various organic molecules, which can be used as building blocks in the fabrication of the target plasmon switching nanodevice (Figure 3.8).

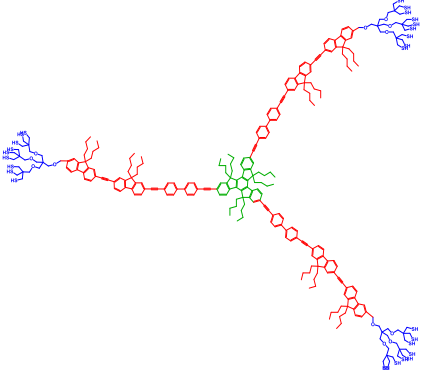
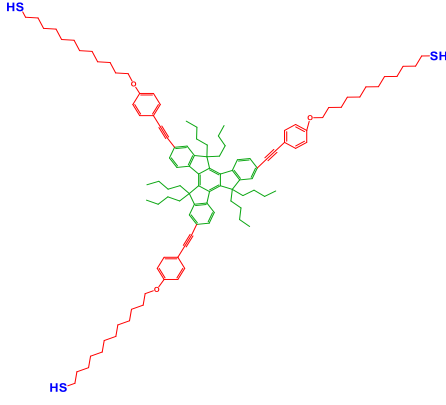
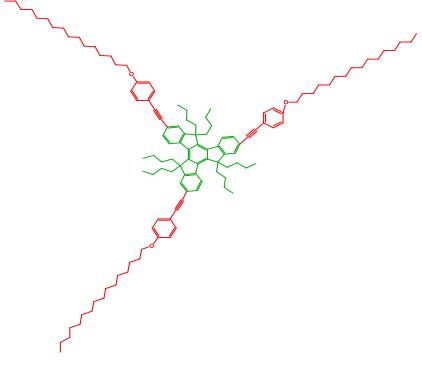
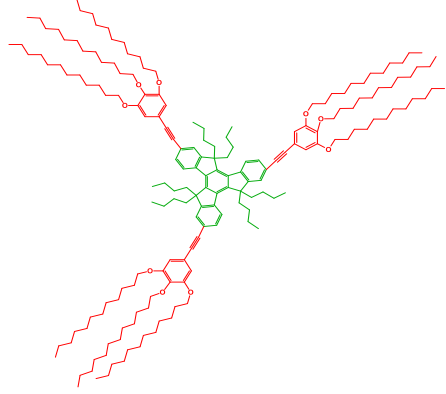


**Figure 3.8 : Scheme of a trimer (not to scale) resulting from the assembly of three AuNRs. a) AuNRs assembled through an organic linker consisting of a trigonal planar core (green), three elongated arms (red) and terminal groups able to interact with AuNRs (blue); b) AuNRs@PS assembled through an organic linker consisting of a trigonal planar core (green) and three elongated hydrophobic arms (red).**

The structure of the organic linkers was chosen in order to fulfill the requirements resulted from the FDTD simulations: i) trigonal planar molecular geometry which ensures the nanorod trimer directionality; ii) average interparticle distance close to 5 nm, iii) high rigidity to keep coupled nanorods at a fixed distance; and iv) terminal groups able to interact with the tips of the nanorods. Four different organic assemblers were targeted (Table 3.1). Two of them (assemblers I and II) bear thiol functions as terminate groups to ensure a covalent coupling with the tips of the AuNRs, while assemblers III and IV possess peripheral long alkyl chains to allow hydrophobic attractions with polymer-capped AuNRs. The multistep organic synthesis of these organic molecules is going to be described and their use to promote the assembly of AuNRs into Y-shaped nanostructures will be subsequently presented.



**Table 3.1 : Structures of the target organic assemblers I – IV**

Organic assembler	Structure	Branch length (nm) <sup>*</sup>	Interaction with AuNRs
I		5.4	Covalent bonding
II		2.7	
III		3.1	Hydrophobic interactions
IV		2.7	

<sup>\*</sup> Branch length implies the distance from the middle of the core until the end-groups of the molecule.

## 2. AuNRs COVALENTLY LINKED THROUGH A THIOL-TERMINATED ORGANIC ASSEMBLER

We first designed the organic assembler I - a molecule with a  $C_3$ -symmetry core with a diameter of 0.7 nm, extended by three 3.4 nm long, rigid arms and bearing 1.2 nm long thiol-terminated dendron-like modules (Table 3.1). In such structure, one branch of the tripodal molecule was expected to bear nine thiol groups, to prompt the effective binding with the tips of the nanorods.

### 2.1. Synthesis of the organic assembler I<sup>†</sup>

Truxene (10,15-dihydro-5H-diindeno[1,2-a;1',2'-c]fluorene) was used as a core of the tripodal assembler due to its structural features such as rigidity,  $C_3$ -symmetry, good thermal and chemical stability. This planar heptacyclic polyarene exhibits poor solubility in most of the organic solvents. However, easy functionalization at the methylene groups allows the introduction of solubilizing units, and also impedes aggregation phenomena via steric constrains, while halogenation of peripheral aromatic rings provides high reactivity in metal-catalyzed cross-coupling reactions, making truxene an ideal scaffold for wide range of applications in material science [18], [19].

Truxene (**1**) was prepared from 1-indanone in aldol cyclotrimerization using concentrated HCl in hot acetic acid. Alkylation of truxene with *n*-butyllithium was carried out in the 5-, 10- and 15- positions and finally iodination with iodic acid and iodine gave the target building block **3** in a 51% yield (Figure 3.9).

---

<sup>†</sup> All the detailed experimental protocols are given in Annex 1

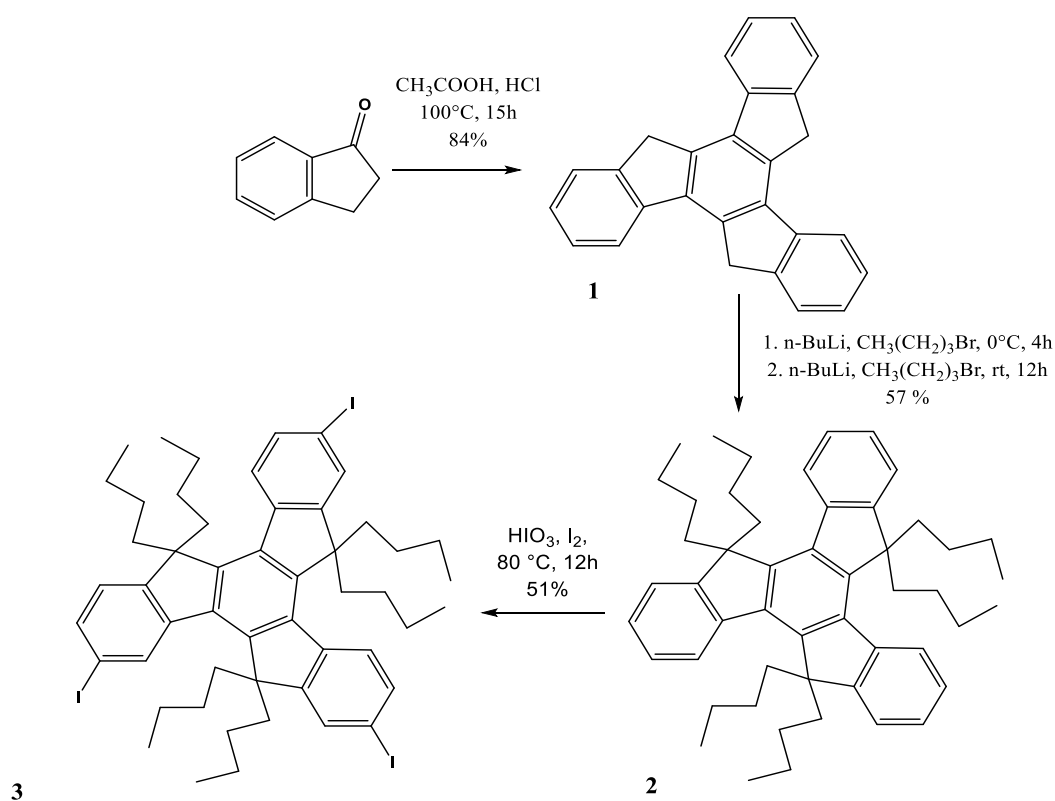


**Figure 3.9 : Synthesis of the iodinated truxene core**

The core synthesis was followed by the formation of long, rigid branches that will be coupled to iodinated truxene. The branches consisted of fluorene- and biphenyl-based units cross-linked together by ethynyl groups. Three different building blocks (**5**, **7**, **9**) were prepared in a multistep synthesis and afterwards linked in palladium-catalyzed Sonogashira cross coupling reaction to obtain new, conjugated molecular rods (**22**) with well-defined structure and size.

Firstly, building block **7** was obtained in a high yield in four-step synthesis, starting from commercially available fluorene. Iodination with periodic acid and iodine, followed by alkylation with *n*-butyl bromide gave the intermediate **5**. Lithiation of the intermediate, subsequent formylation with DMF, and finally Sonogashira cross coupling with ethynyltrimethyl silane in the presence of palladium (II) and copper (I) were performed to obtain **7** in a 70% yield (Figure 9).

Another building unit of a molecular rod is compound **9**. It was obtained in a two-step synthesis, starting from commercially available 4,4'-diiodobiphenyl. Two different protecting groups were introduced by sequential Sonogashira cross coupling with 2-methyl-3-butyn-2-ol and ethynyltrimethylsilane to give **9** in a 67% yield (Figure 3.10).

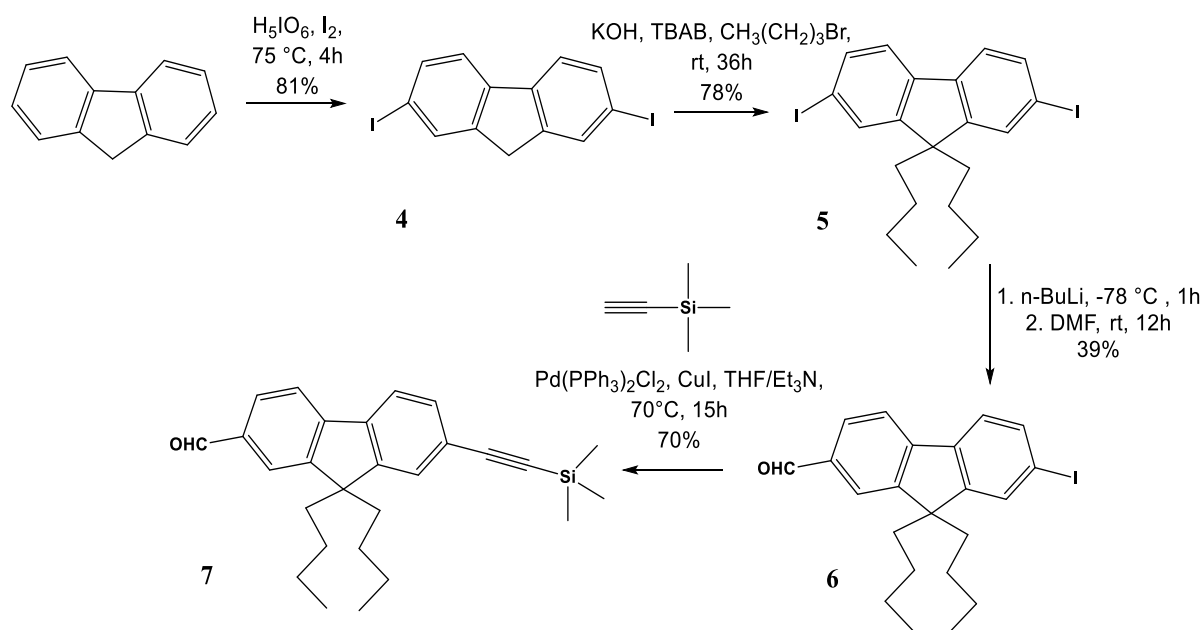


**Figure 1: Synthesis of fluorene-based building block**

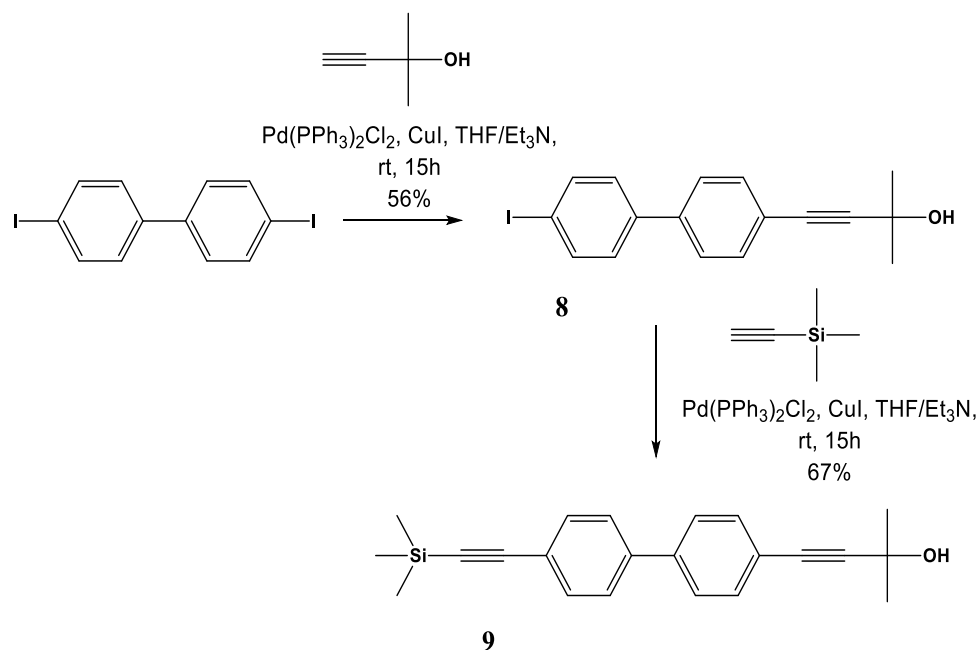


**Figure 3.10 : Synthesis of biphenyl-based building block**

The target molecular rod **22** was prepared by means of *in situ* deprotection/Sonogashira coupling of the synthesized building blocks. *In-situ* deprotection of trimethylsilyl group of biphenyl derivative **9** and Sonogashira coupling with an excess of **5** were performed to obtain intermediate **21**, which was then coupled with **7** after the second *in-situ* deprotection to obtain **22** in a 30% yield (Figure 3.11).

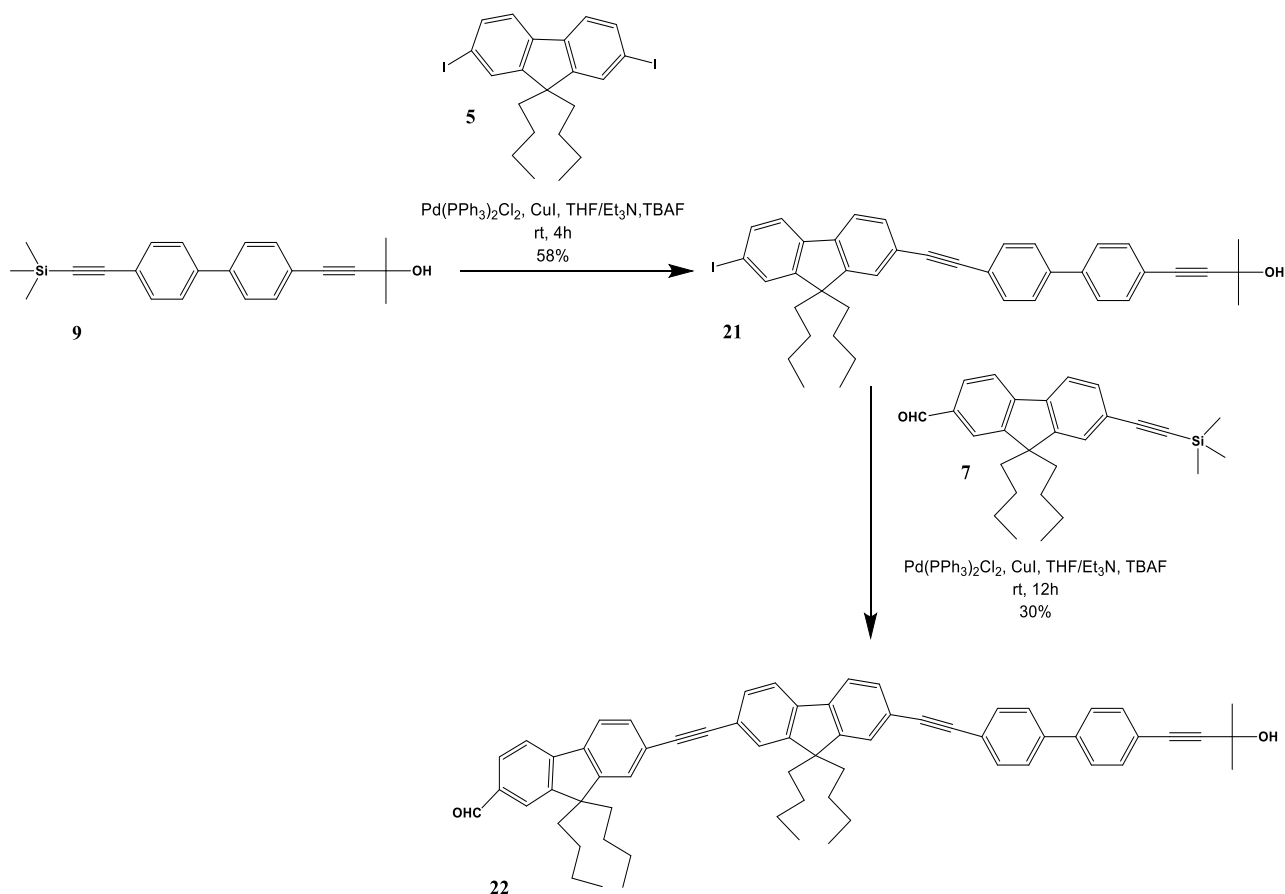


**Figure 3.11 : Synthesis of long, rigid molecular rods**

To precisely link three gold nanorods in the desired Y-shaped geometry via the organic assembler, it was necessary to introduce thiol groups in its structure, since they can be covalently grafted onto gold. Truxene core extended with three molecular rods was designed to couple a dendron bearing several peripheral thiols to ensure several gold binding sites per one nanorod.

Dendrons are branched molecules that possess three key architectural features: the core, interior branching units and defined number of functional surface groups. Thus, we designed a thiol terminated poly(ether) dendron based on branched pentaerythritol. Pentaerythritol served both as the core and the branching unit – when one of the four hydroxyl groups in the pentaerythritol moiety was protected, the remaining three could be used as divergent growth sites for the dendron formation (Figure 3.12) [20], [21]. However, the synthesis of such dendron was shown to be very challenging and time consuming. Due to the lack of time we were not able to finish it and thus the complete organic assembler I composed of the core, the molecular rods and the gold binding moieties could not be obtained. Therefore, we designed

the substitute organic assembler II, which fulfills the given size and shape requirements, but defers in the structures rigidity and in the number of terminal thiols (Table 1).

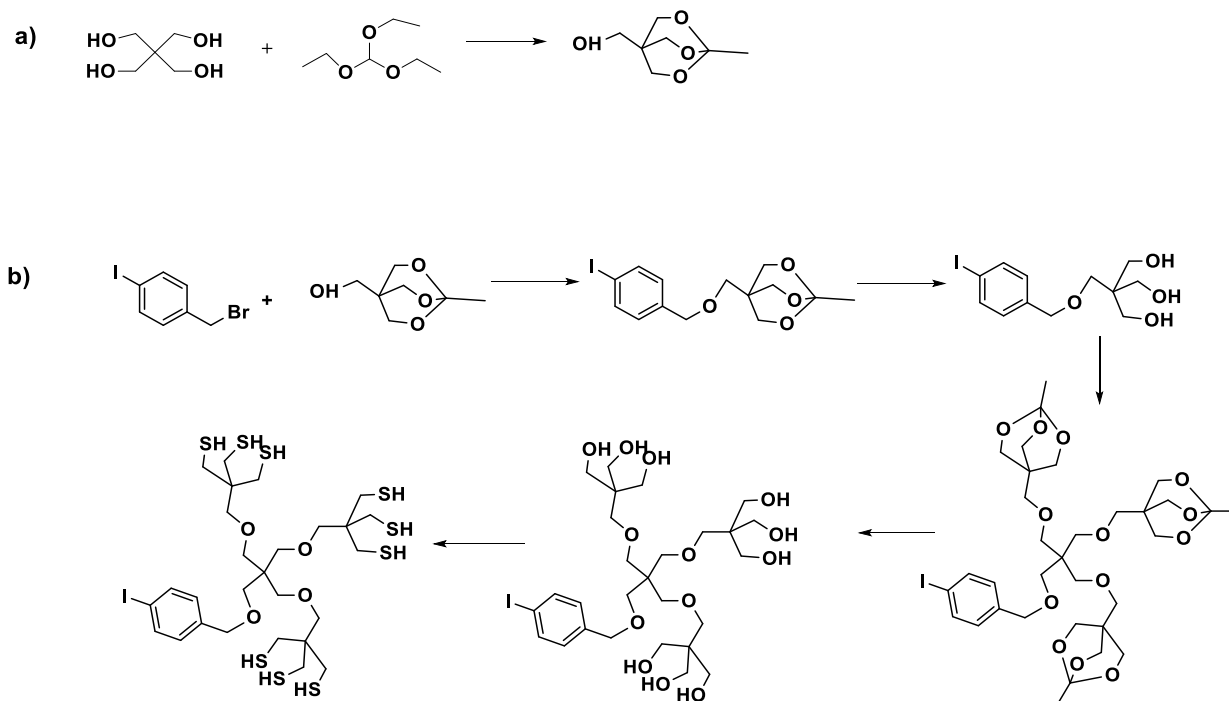


**Figure 3.12 : Synthesis of the pentaerythritol-based dendron**

## 2.2. Synthesis of the organic assembler II<sup>‡</sup>

The organic assembler II (compound **23b**) was obtained by a multistep synthesis from two main building blocks: the truxene core and thiol terminated dodecane derivatives.

Thioester **10** was obtained in 41% yield by the nucleophilic substitution of one bromine atom of 1,12 dibromododecane by a thioacetate group (Figure 3.13). It reacted with 4-iodophenol in Williamson ether synthesis, leading to intermediate **11**, which was then coupled with ethynyltrimethyl silane in Sonogashira cross coupling reaction to give trimethylsilylalkyne derivative **12**. Compound **23a** was obtained after *in-situ* deprotection and Sonogashira coupling between the entities **12** and **3** (Figure 3.14).

<sup>‡</sup> All the detailed experimental protocols are given in Annex 1

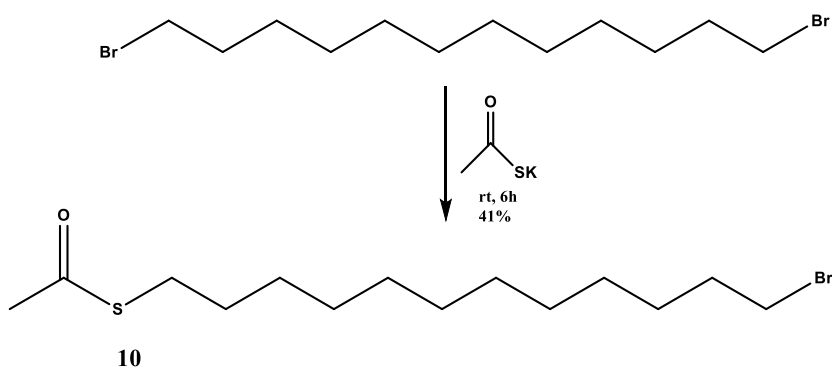


Figure 3.13 : Synthesis of the thioester building block

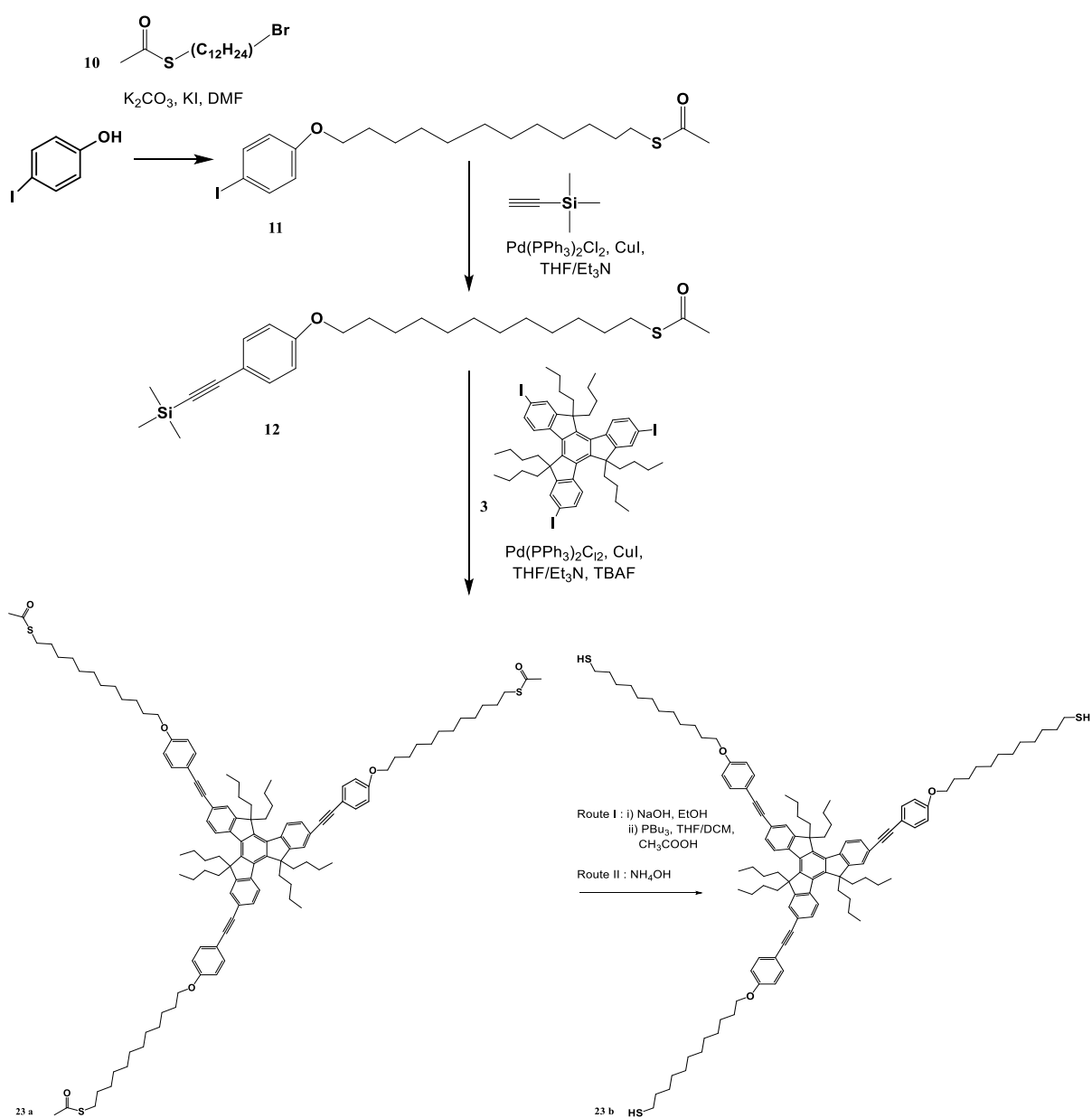


Figure 3.14 : Synthesis of the organic assembler II

Initially, deacetylation of thioacetate to thiol was done by refluxing **23a** with sodium hydroxide in ethanol. Due to the polycondensation of the thiolate moieties in basic media, an insoluble precipitate was formed (probably via disulfur bridges) which was then reduced with tributylphosphine. After reduction, the precipitate was dissolved in a mixture of THF and DCM (2:1 v/v) and a trace of acetic acid and subsequently washed with water but NMR analysis revealed the presence of remaining thioester functions, as well as residues of tributylphosphine. Despite such impurities, the obtained compound **23b** (organic assembler II) was used for AuNRs self-assembly in DCM.

In the second set of experiments, which were carried out in water, deacetylation of compound **23a** was done *in situ* by the addition of NH<sub>4</sub>OH. Two different routes of deacetylation were shown to have different impact on the AuNRs self-assembly process. This observation will be explained in detail in the following sections.

### 2.3. Phase transfer of AuNRs from water to DCM

Due to the insolubility of the deacetylated compound **23b** in water, a phase transfer of the AuNRs into DCM was necessary. To do so, polyethylene glycol chains were grafted onto the AuNRs.

#### Protocol - Phase transfer of AuNRs from water to DCM

*Prior to the phase transfer, CTAB concentration in the aqueous solution of gold nanorods (5 mL) was decreased to 1 mM by centrifugation (9 000 rpm, 20 min). The nanorod solution was then added in the solution of mPEG-thiol ( $M_n = 5000 \text{ g mol}^{-1}$ ; 0.0001 g) in DCM (5 mL) and stirred for 5 min. Upon the addition of methanol (7.50 mL), which induced the phase transfer, the two phases were clearly separated. The lower organic phase containing functionalized gold nanorods was collected using a separation funnel and then purified by centrifugation (9 000 rpm, 20 min). The supernatant was discarded and the sediment containing gold nanorods was dispersed in DCM (5 mL).*

The number of PEG-SH molecules was calculated following equation 1, where  $N_{\text{AuNR}}$  is the number of the gold nanorods in a given volume,  $S_{\text{AuNR}}$  is the total surface of one gold nanorod,  $S_{\text{mPEG-SH}}$  is the area occupied by one mPEG-SH molecule (0.35 nm<sup>2</sup> [22]) and  $N_A$  is the Avogadro's number.



$$n_{m\text{PEG-SH}} = \frac{N_{\text{AuNR}} (S_{\text{AuNR}}/S_{m\text{PEG-SH}})}{N_A} \quad \text{Equation 3.1}$$

The UV-Vis spectrum of the solution of AuNRs in DCM was recorded in order to verify the absence of aggregates. Figure 15 shows that no broadening of the LSPR band of the AuNRs is observed in comparison with the spectrum recorded in water, confirming the good dispersibility of the PEG-capped Au NRs in DCM. The small red-shift of the absorption band is due to the change of the refractive index of the solvent ( $n_{\text{water}} = 1.33$ ;  $n_{\text{DCM}} = 1.43$  at  $20^\circ\text{C}$ ). The success of the phase transfer of the AuNRs was also confirmed by TEM observation, as no aggregates can be seen in the TEM picture of Figure 3.15.

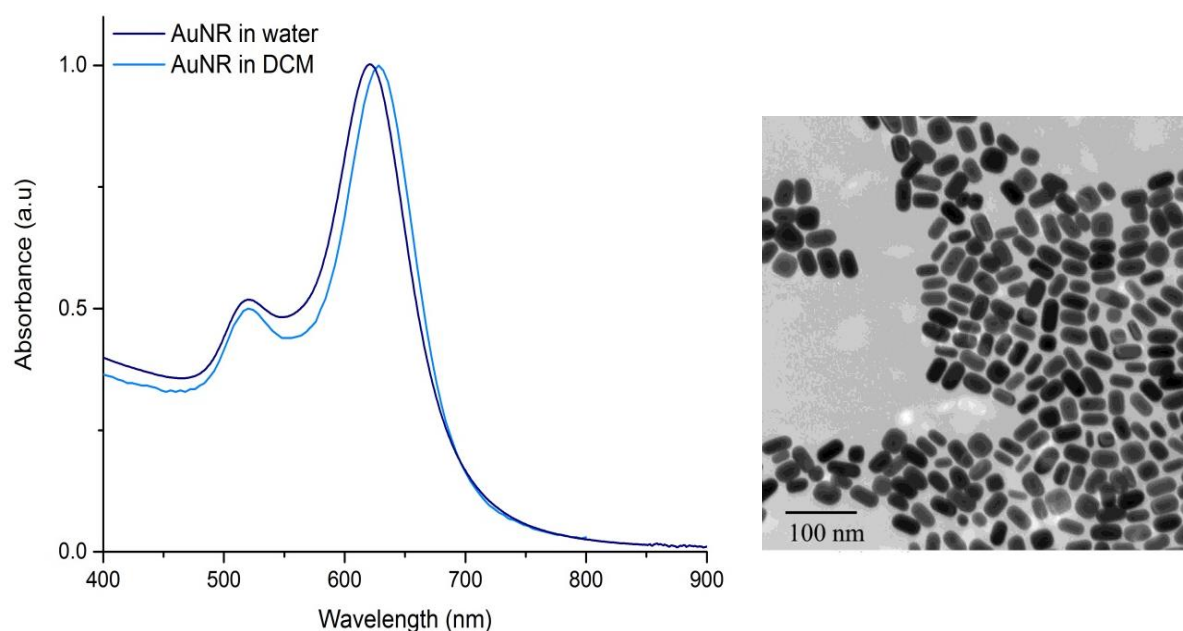


**Figure 3.15 :** Absorption spectra of AuNRs before and after the phase transfer from water to DCM and TEM image of the PEG-capped AuNRs dispersed in DCM.

#### 2.4. AuNRs self-assembly in DCM

##### Protocol – Self-assembly of AuNRs in DCM

A stock solution of compound **23b** was prepared by dissolving approximately 10 mg of compound in 20 mL of DCM.

Self-assembly of PEGylated gold nanorods dispersed in DCM (1 mL) was carried out by dropwise addition of the stock solution of compound **23b** (0-50  $\mu\text{L}$ ) followed by sonication

during 5 min. One control sample (A) and three test samples (B-D) were prepared in the same final volume, typically 3 mL, to ensure the same final AuNRs concentration (Table 2). Solutions were stirred for 20 min before the preparation of the TEM grids and the recording of the absorption spectra.

**Table 3.2 : Experimental conditions for AuNR self-assembly in DCM**

	V (AuNR in DCM)	V (DCM)	V (stock solution of assemblerII)
<b>A</b>	1 mL	2 mL	-
<b>B</b>	1 mL	1.995 mL	5 $\mu$ L
<b>C</b>	1 mL	1.990 mL	10 $\mu$ L
<b>D</b>	1 mL	1.950 mL	50 $\mu$ L

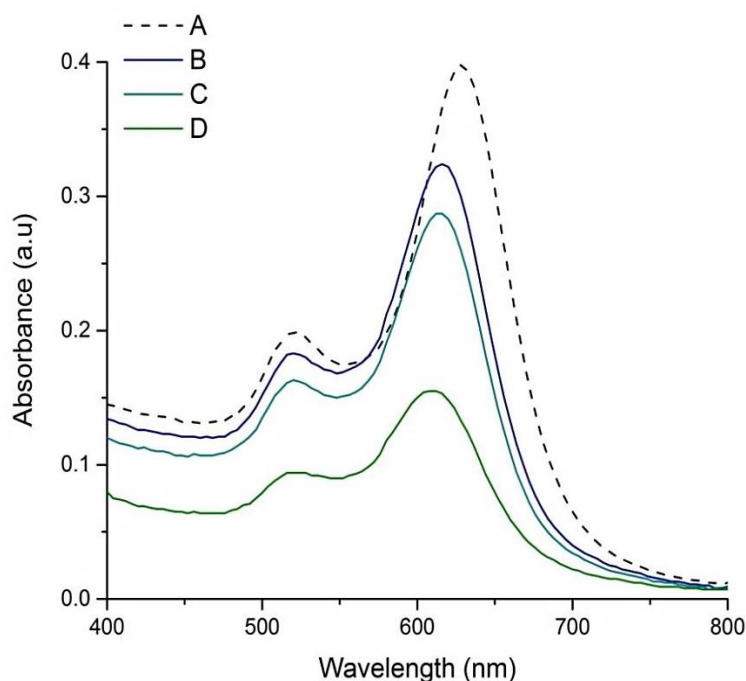


**Figure 3.16 : Absorption spectra of PEG-capped AuNRs in DCM in the presence of different volumes of organic assembler.**

After 20 min of reaction, a change of color from blue to purple was observed for test samples, while the control sample remained blue. This observation was confirmed by recording the UV-Vis spectra of the solutions. Figure 3.16 shows that as the concentration of organic assembler in the test samples increases, the longitudinal plasmon band gradually blue-shifts from 630 to 610 nm and decreases in intensity, while the transverse plasmon band decreases

in the intensity but remains at 520 nm. This result suggests a shortening of the nanorods, probably due to an etching process induced by assembler II. The etching of the nanorods was confirmed by TEM, as shown in Figure 3.17. Statistical analysis of TEM images (Figure 3.17) allowed us to determine that the average length of AuNRs decreases from 36 nm to 32 nm when the added volume of the solution of assembler II increases from 0 to 50  $\mu\text{L}$ , while their average width remains equal to 17 nm.

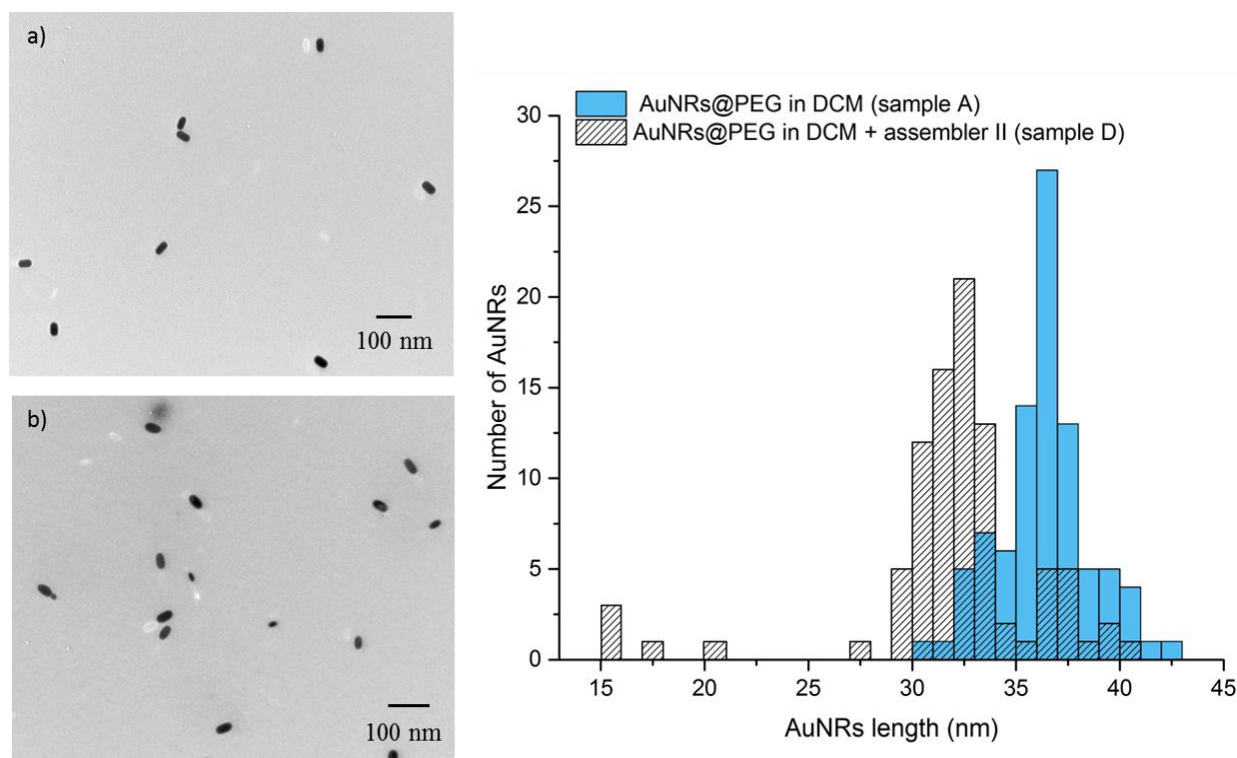


**Figure 3.17 : TEM images of AuNRs in DCM before (a) and after (b) the addition of 50  $\mu\text{L}$  of organic assembler II solution and corresponding statistical analysis of their length.**

## 2.5. AuNRs self-assembly in water

- **Preparation of citrate-stabilized AuNRs**

Citrate ions are well known to stabilize gold nanostructures during their surface functionalization. In fact, due to their moderate gold affinity, citrate molecules can be easily replaced by the other ligands. Therefore, prior to the self-assembly process, citrate-coated AuNRs were prepared by surfactant exchange from CTAB-coated AuNRs, according to the adjusted protocol published by J. G. Mehtala and co-workers [23]. Free CTAB molecules

were firstly removed by two washing cycles. Since CTAB is a cationic surfactant, the direct addition of citrate anions neutralizes the surface charge causing the irreversible AuNRs destabilization. Thus, the residual CTAB molecules were removed through the addition of PSS molecules, leading to the formation of a PSS-CTAB complex. Due to complementary electrostatic and hydrophobic interactions, the complexation of CTAB with PSS is strong and very stable. Nevertheless, the adsorption of the PSS-CTAB complex at the GNR surface is weak and it can thus be desorbed from the AuNR surface upon the addition of citrate ions (Figure 3.18) [24].

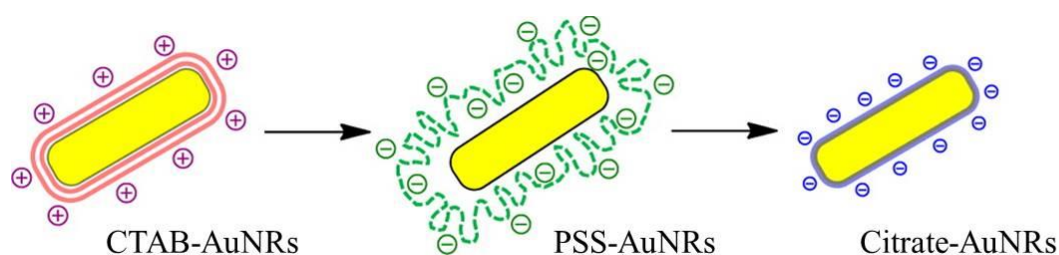


**Figure 3. 18 : The preparation of citrate-stabilized AuNRs [23].**

#### **Protocol – Preparation of citrate-stabilized AuNRs**

*Prior to the assembly, AuNRs were stabilized by citrate following a protocol reported by J.G. Mehtala et al [23]. 5 mL of CTAB-stabilized AuNRs were centrifuged (8000 rpm, 25 min) and the sediment was dispersed in 5 mL of water. After a second centrifugation cycle (8000 rpm, 25 min), the supernatant was discarded and the sediment containing the AuNRs was dispersed in 5 mL of 0.15 wt% sodium polystyrenesulfonate (Na-PSS,  $M_w = 70$  kDa). The solution was stirred for 1 h and then subjected to two centrifugation cycles, washing with 5 mL of 0.15 wt% Na-PSS. The centrifugation enabled the removal of the excess of PSS and the remaining CTAB molecules which easily adsorb on PSS. After the last centrifugation (8000 rpm, 25 min), the sediment was redispersed in 10 mL of 5 mM sodium citrate. The solution was kept under slow shaking overnight. PSS molecules were removed by three centrifugation cycles (8000 rpm, 25 min) and subsequent washing with 5 mM sodium citrate. After the last centrifugation, the sediment was redispersed in 10 mL of 5 mM sodium citrate, yielding citrate-stabilized AuNRs.*

- **AuNRs self-assembly via organic assembler II in water**

The formation of AuNR@citrate trimers was triggered by the *in-situ* deprotection of compound **23a**.

**Protocol – AuNRs self-assembly via organic assembler II in water**

Three solutions (A-C) of the organic compound **23a** at different concentrations (2 mM, 2  $\mu$ M and 2 nM) were prepared in 10 mL of a THF/EtOH mixture (3:2 v/v). 150  $\mu$ l of a solution of **23a** was mixed with 150  $\mu$ l of an aqueous solution of sodium citrate (5mM) and added drop-wise in 3 mL of the citrate-stabilized AuNR solution (0.1 nM) under vigorous stirring. Finally, 30  $\mu$ L of 30% NH<sub>4</sub>OH were added for *in-situ* deprotection of the thiol endgroups to form the assembler II (Table 3). The solutions were left to stir overnight. A control sample was also prepared in the absence of the organic linker. TEM samples were prepared by diluting 10 times the solution of AuNRs and placing a drop onto a carbon-coated Cu grid. The solvents were removed with a filter paper to prevent particle aggregation.

**Table 3.3 : Experimental conditions for in-situ deprotection of terminal thiol groups of compound 23a and the AuNRs assembly via organic assembler II.**

	V (AuNR@citrate)	V (23a)	V (citrate)	V (NH <sub>4</sub> OH)	V (total)
<b>control</b>	3 mL	150 $\mu$ L (citrate)	150 $\mu$ L	30 $\mu$ L	3.33 mL
<b>A</b>	3 mL	150 $\mu$ L (2 mM)	150 $\mu$ L	30 $\mu$ L	3.33 mL
<b>B</b>	3 mL	150 $\mu$ L (2 $\mu$ M)	150 $\mu$ L	30 $\mu$ L	3.33 mL
<b>C</b>	3 mL	150 $\mu$ L (2 nM)	150 $\mu$ L	30 $\mu$ L	3.33 mL

By comparing the TEM images of the test samples A-C with those of the blank sample, we observed that the addition of the organic assembler induces the formation of dimers, trimers and small clusters (Figure 3.19). A statistical analysis of the TEM images shows that the morphology of aggregates is dependent on the concentration of assembler (Figure 3.20).

In sample A, containing the largest amount of the organic assembler, the formation of clusters is predominant. By dividing by one thousand the concentration of the organic assembler (sample B), the formation of gold nanorod trimers was favored. No significant difference by comparison with the blank sample was observed when the concentration of the assembler was divided once more by one thousand (sample C).

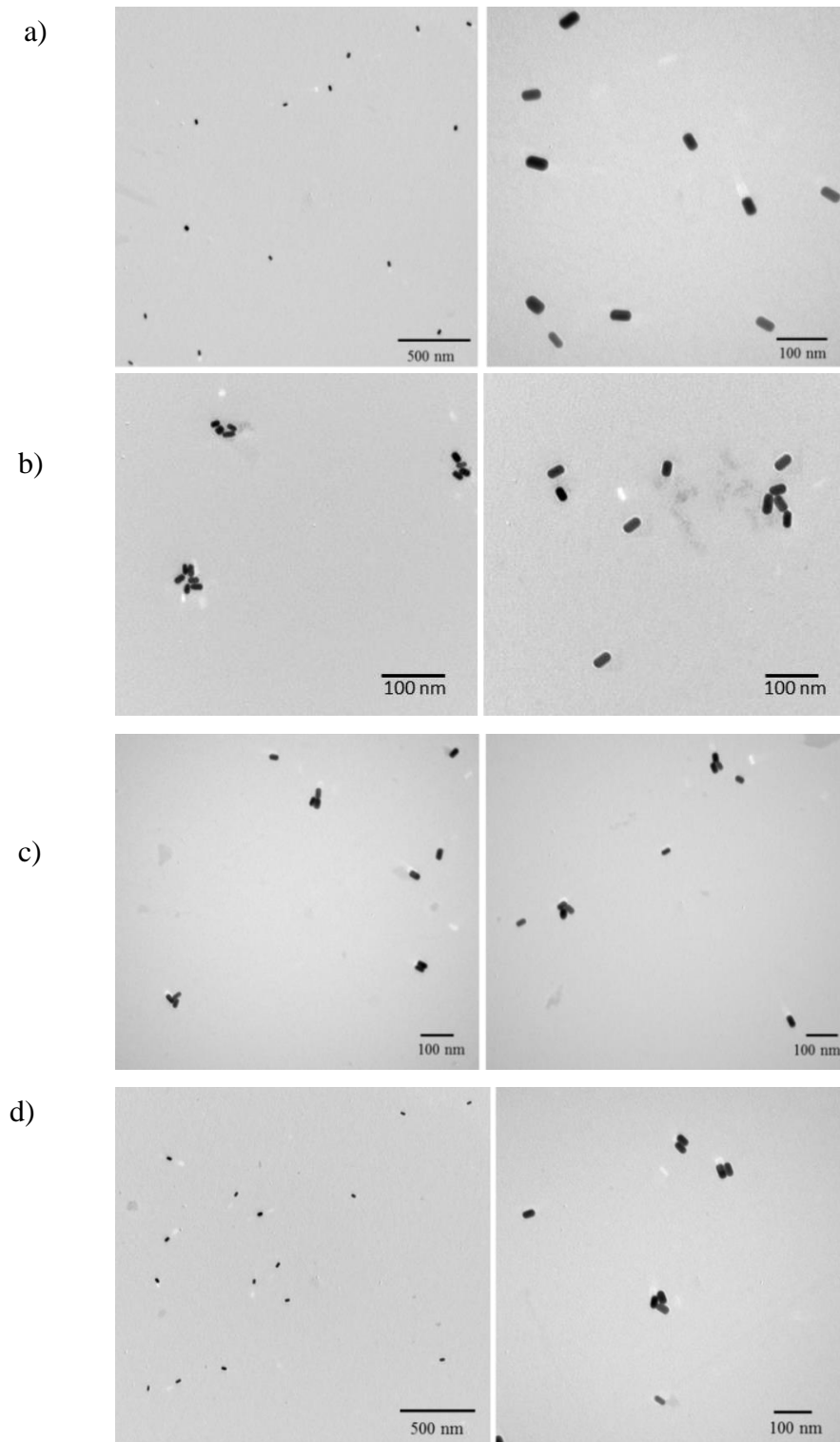


**Figure 3.19** : TEM images of control sample (a), test sample A [assembler II] = 2 mM (b), test sample B [assembler II] = 2 μM (c), test sample C [assembler II] = 2 nM (d).

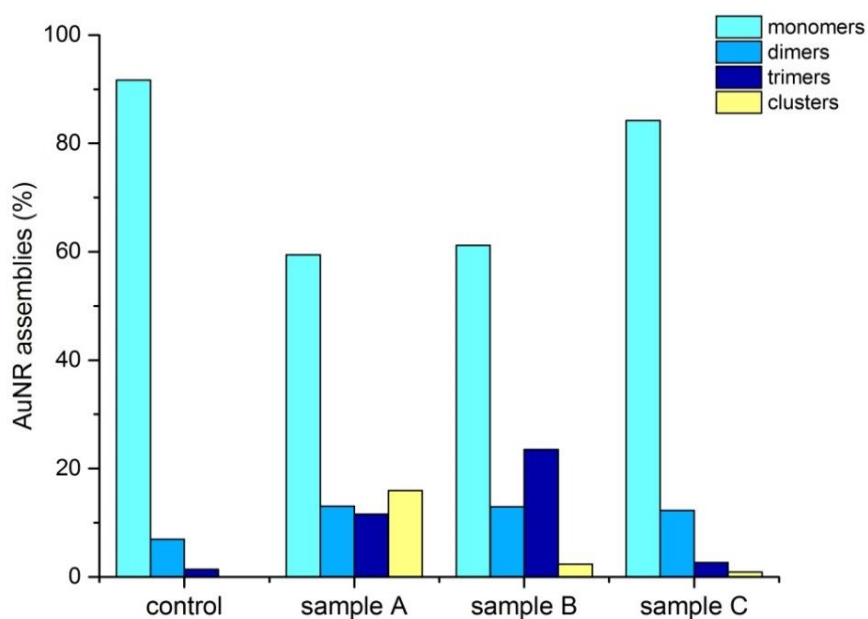


**Figure 3.20 : Dependence of the percentages of AuNR monomers, dimers, trimers and clusters on the concentration of the organic assembler II. The results were obtained by analyzing approximately 150 nanostructures for each sample.**

The addition of the organic assembler was also followed by UV-Vis spectroscopy. Figure 3.21 shows the absorption spectra of the blank sample and of the samples A-C. As the concentration of the organic assembler increases, the LSPR bands decrease in intensity and a shoulder appears at 720 nm, indicating the progressive formation of small clusters.

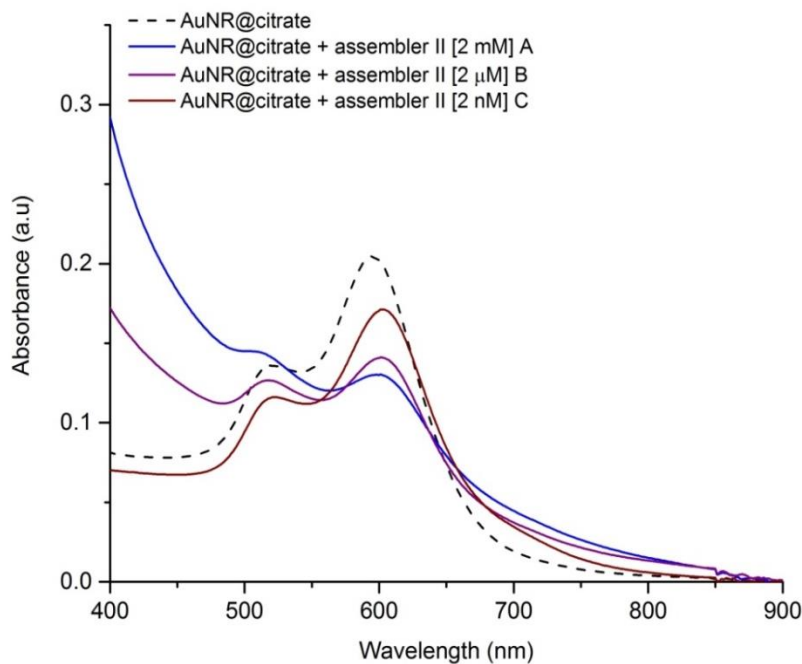


**Figure 3.21 : Absorption spectra of citrate-stabilized AuNRs (dash curve), test sample A [assembler II] = 2 mM (blue curve), test sample B [assembler II] = 2  $\mu$ M (purple curve) and test sample C [assembler II] = 2 nM (dark red curve).**

A closer observation of the gold nanorod trimers, obtained in the presence of assembler II at 2  $\mu$ M, allows one to note that they have different morphologies (Figure 3.22). Some of the trimers have the desired Y-shape structure, which corresponds to the tip-to-tip assembly with an angle close to  $120^\circ$ . Nevertheless, most of the trimers exhibit a tip-to-side assembly of nanorods. This might be due to the grafting of one arm of the organic assembler onto one lateral facet of an AuNR, as both tips and lateral facets of AuNRs are homogeneously coated by citrate ions.



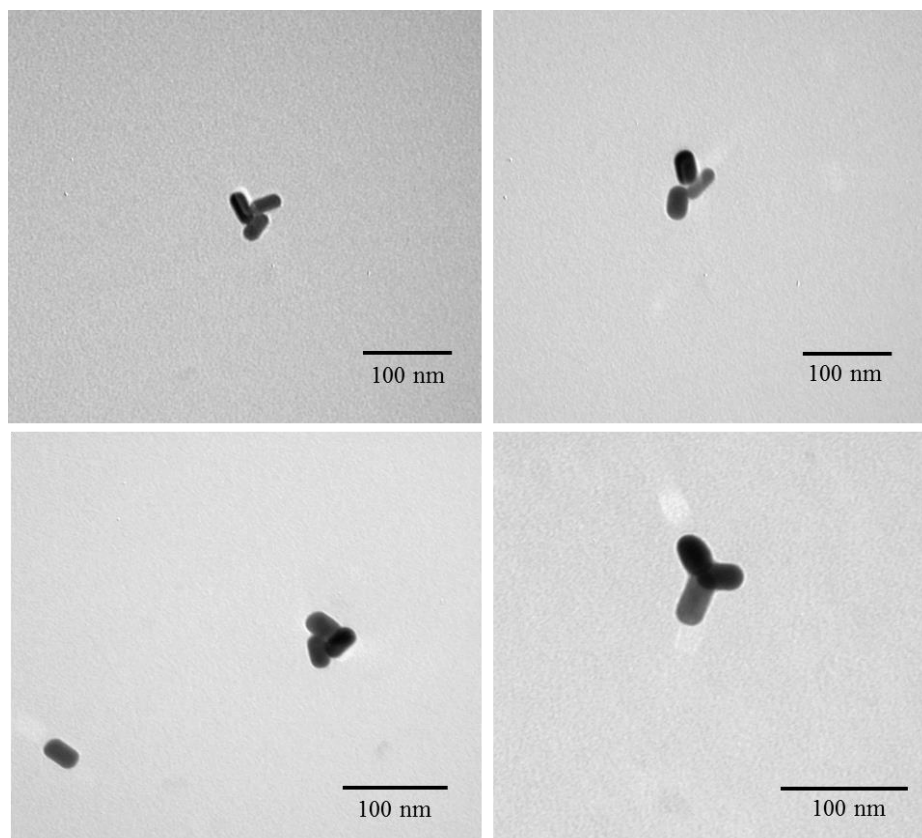
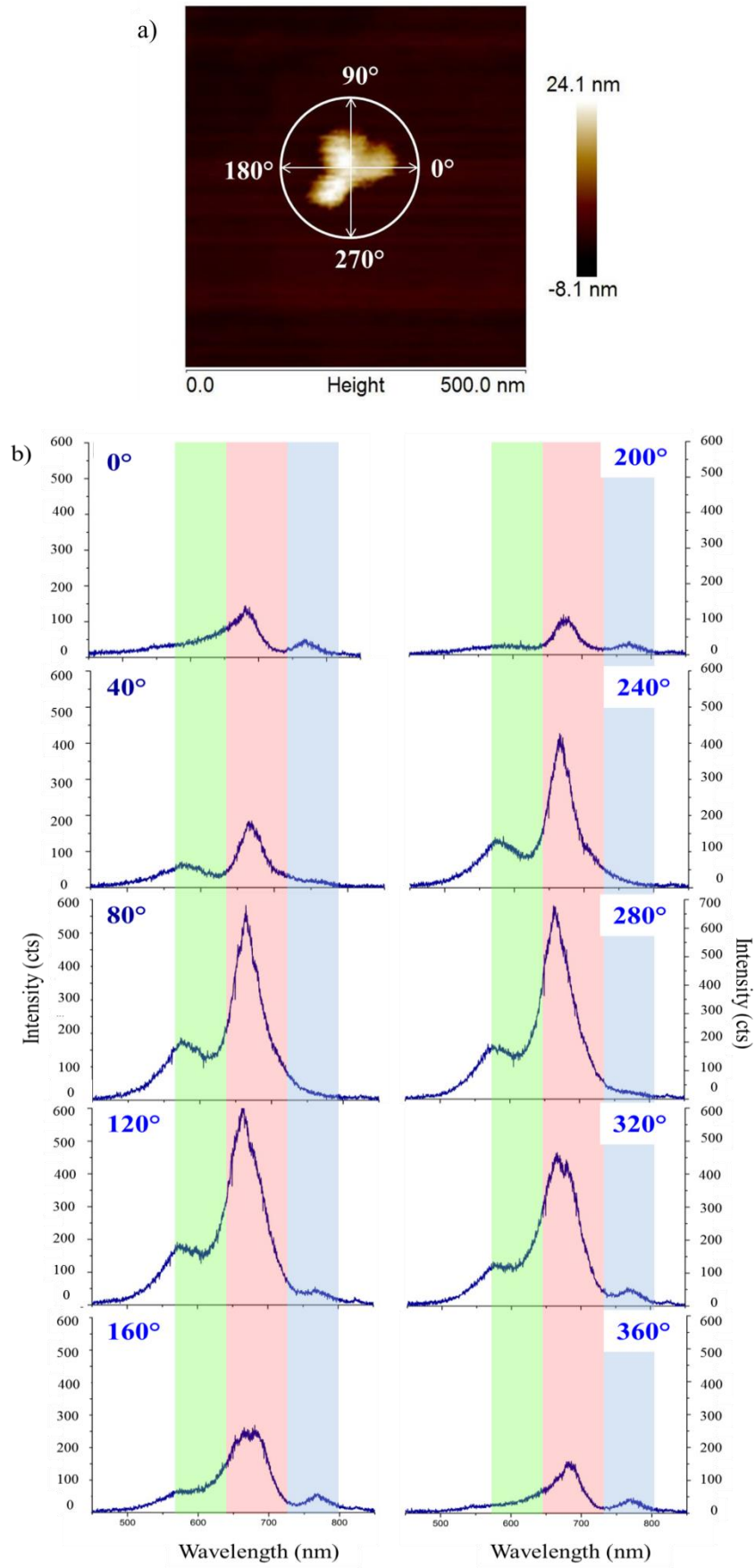


**Figure 3.22 : TEM images of AuNRs trimers with different morphologies obtained in the presence of the assembler II at 2  $\mu$ M.**

## 2.6. Optical characterization of AuNRs trimers

In order to study the optical properties of AuNRs trimers, dark-field spectra of single AuNRs trimer was measured as a function of polarization, with direction ranging from  $0^\circ$  to  $360^\circ$  by step of  $40^\circ$  in the anticlockwise manner.

The dark field spectra exhibit essentially three peaks centered at 575, 660 and 770 nm, respectively (Figure 3.23 b). In the following paragraph, we will tentatively assign these peaks to the particular resonances of our structure. To do so, we first integrated the shown shaded area around the peak maximum. We then plotted separately these integrated signals on a polar plot as a function of polarization (Figure 3.23 c).



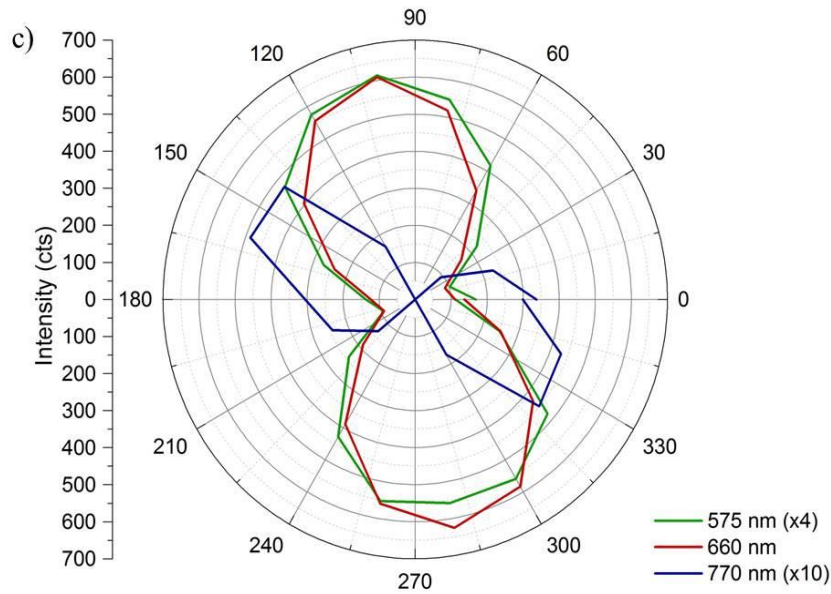


**Figure 3.23 : a) AFM image of the AuNRs trimer together with the zero of the polarization angle; b) dark-field spectra of a single gold nanorod trimer measured at different polarization angles; c) polar plot of the scattered intensities integrated in the shown shaded areas (green, red and blue for the peaks at 575 nm, 660 nm and 770 nm, respectively) as a function of polarization.**

For the peak at 660 nm (red area), we observe the strongest signal around 105° and 285° angle. We attribute this dipolar type of signal ( $\infty$ ) to the longitudinal plasmon resonance of the upper left AuNR. This resonance corresponds to the sloshing of the electrons along the long axis of the rod.

For the peak at 575 nm (green area), we observe a second strongest signal at 105° and 285° as well. We attribute this signal to the transversal plasmon resonance, which corresponds to electron oscillations along the short axes of the upper right AuNR.

Finally, the third signal was mainly detected at 150° and 330° angles. The signal is observed in the NIR region with a peak maximum at 770 nm (blue area). As a single AuNR does not exhibit such peak in solution, we attribute this signal to the coupling effect of the AuNRs assembled in a trimer, with a final dipole-like overall charge displacement.

As we expected to observe signals corresponding to the longitudinal and transverse plasmon resonances of the three AuNRs forming the trimer, the obtained results are very intriguing and require further studies to be fully explained.

### 3. SELF-ASSEMBLY OF AuNRs VIA HYDROPHOBIC INTERACTIONS

In order to get Y-shape structures with a higher yield, we have studied the assembly of AuNRs directed by hydrophobic interactions between polystyrene chains grafted on their tips and the hydrophobic arms of an organic tripodal assembler. This study was inspired by the end-to-end self-assembly of AuNRs based on solvophobic forces reported by Kumacheva and co-workers [7], [25].

We have thus synthesized two tripodal organic assemblers with three hydrophobic branches (Table 3.1). The assembler III is composed of a  $C_3$ -symmetry core and three hexadecane chains as hydrophobic arms, while the assembler IV has nine dodecane chains grafted on the tripodal core, in order to develop stronger attractions with the PS chains grafted onto the AuNR tips. In the next section the synthesis of both organic assemblers is described, and their use to assemble AuNRs will subsequently be presented.

#### 3.1. Synthesis of the organic assembler III

The organic assembler III (**24**) was obtained in a multistep synthesis from two main building blocks: the truxene core and three hexadecane chains.

The first building unit, namely compound **15**, was obtained in a high yield in a three-step synthesis. 4-iodophenol was first treated with 1-bromohexadecane in a Williamson ether synthesis under strong basic conditions, leading to compound **13**, which was then coupled to 2-methylbutyn-2-ol in the presence of palladium (II) and copper (I), affording **14** in a high yield. Finally, after the deprotection in the presence of sodium hydroxide, compound **15** was obtained.

The target C-3 symmetry assembler III bearing three long alkyl chains was synthesized by a Sonogashira cross coupling between moieties **15** and **3** in a 78 % yield (Figure 3.24).

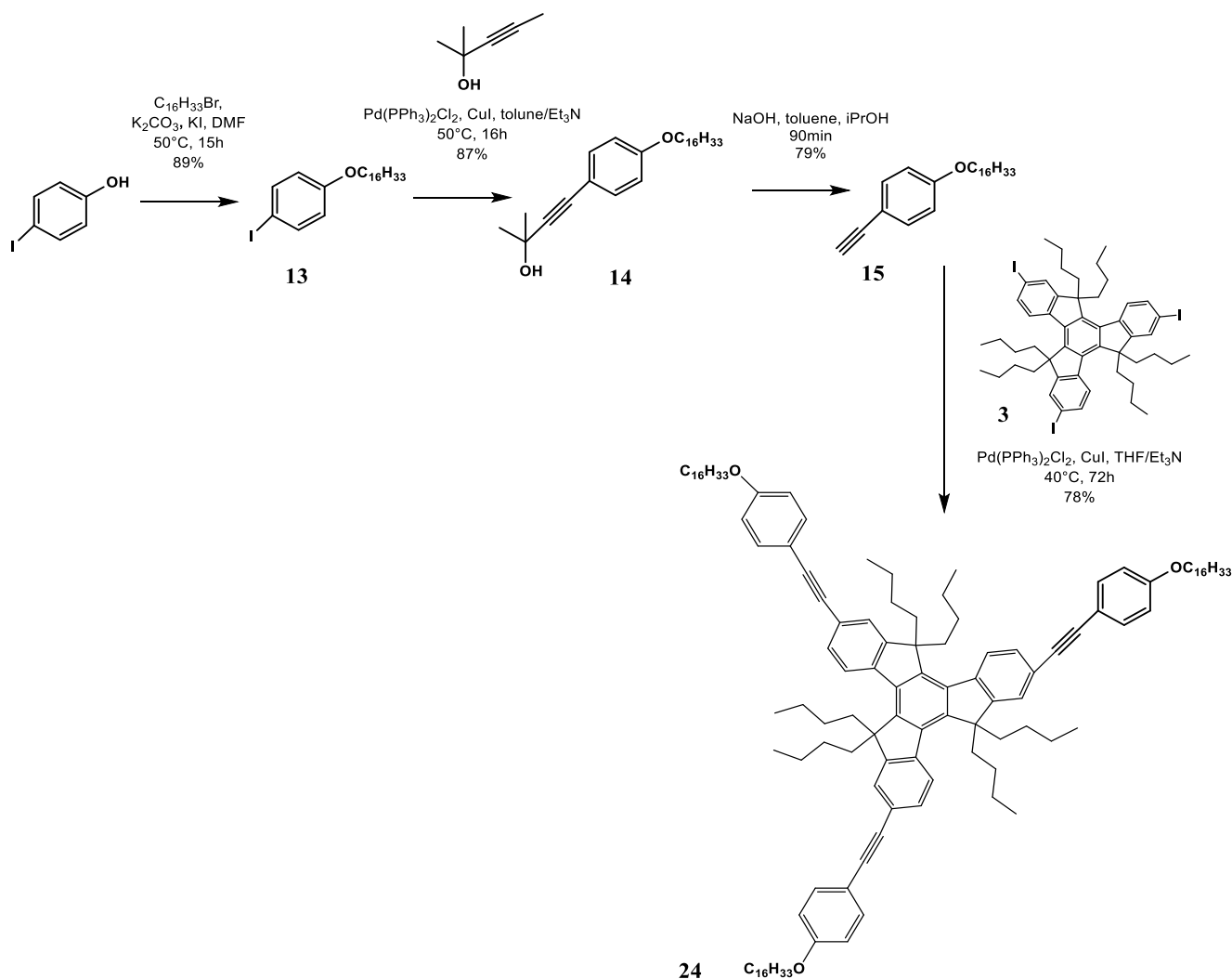


Figure 3.24 : Synthesis of the assembler III

### 3.2. Synthesis of the organic assembler IV

The organic assembler IV (**25**) was obtained in a multistep synthesis from two main building blocks: the truxene core and nine dodecane chains.

The building unit 20 was synthesized in a five-step reaction. Diazotisation in acidic conditions followed by an iodination of commercially available 3,4,5-trimethoxyaniline was performed to obtain the compound **16**. After the full demethylation of the methyl ether **16** in the presence of boron tribromide, the compound **17** was obtained. It was treated with 1-bromododecane in a Williamson ether synthesis under strong basic conditions to afford the intermediate **18** in a high yield. After the Sonogashira cross coupling of **18** with 2-methylbutyn-2-ol and the deprotection in the presence of sodium hydroxide, the alkyne derivative **20** was obtained in a

71 % yield. Finally, a Sonogashira coupling between moieties **20** and **3** gave the target C-3 symmetry molecule **25** bearing nine long alkyl chains in a 48 % yield (Figure 3.25).

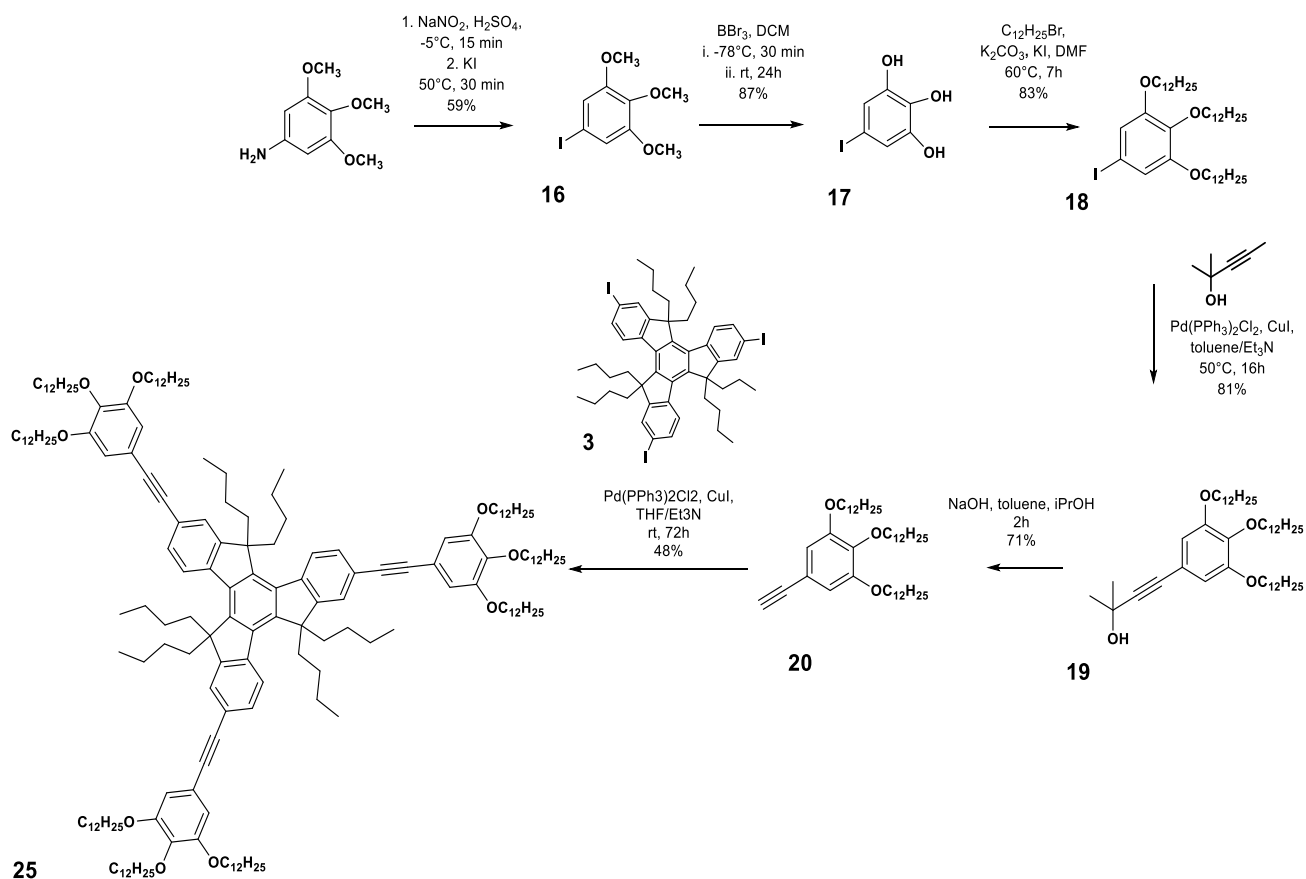


Figure 3.25 : Synthesis of the assembler IV

### 3.3. Grafting of PS chains onto the tips of the AuNRs

It has been reported that the CTAB molecules form a bilayer that preferentially binds to the  $\{100\}$  longitudinal facets of the AuNRs [26]. Therefore, the  $\{111\}$  facets located at the tips of the NRs has a higher reactivity, leading to a site-selective bonding of thiol bearing molecules [27].

The exchange of CTAB with thiol-terminated polystyrene chains at the nanorods tips was carried out at the polymer concentration of 0.2 wt%. Higher amount of PS chains led to the replacement of CTAB molecules at both the tips and the sides of the rods.

### **Protocol - Grafting of PS chains onto the tips of the AuNRs**

*The solution of gold nanorods (20 mL) was centrifuged at 9 000 rpm during 30 min and redispersed in water to obtain a gold concentration of 1 mg/mL. 0.5 mL of the AuNRs solution was rapidly injected into a 0.2 wt% thiol-terminated polystyrene chains ( $M_w=12\ 000$  g/mol, Polymer Source Inc) solution in THF (10 mL). The solution was sonicated for 30 min and incubated for 24 h. The excess of HS-PS was removed by four centrifugation cycles at 9 000 rpm during 30 min, followed by redispersions in DMF. After the last centrifugation cycle, the PS-modified AuNRs were diluted in DMF to obtain a gold concentration of 0.015 mg/mL.*

### **3.4. AuNRs self-assembly via organic assembler III**

#### **Protocol - Assembly of PS-capped AuNRs by the addition of the assembler III**

*PS-modified AuNRs dispersed in DMF (gold concentration of 0.015 mg/mL) were introduced in a solution of organic assembler III (5.00 mg, corresponding to ~33 molecules of linker per AuNR). The assembly was triggered by dropwise addition of a DMF/water mixture to the mixture of PS-modified AuNR and the organic assembler in DMF until the water volume in the final solution reached 20%. The concentration of AuNRs in the final solution was 0.0075 mg/mL.*

The TEM image of the blank sample which did not contain the organic assembler shows that the PS-modified AuNRs assembled in chains upon the addition of water, as previously reported [7] (Figure 3.26 a). In fact, DMF is a good solvent for both CTAB molecules and polystyrene chains. With the addition of water, the mixture became a poor solvent for PS chains attached to the tips, but remained a good solvent for CTAB molecules [28]. To reduce the surface energy of the system, polystyrene chains of neighbored NRs interdigitated, resulting in the formation of chains of AuNRs. Such end-to-end assembly induced the plasmon coupling along the chains and consequently a red shift of the longitudinal plasmon band, as shown in Figure 3.28 (blue curve).

The addition of the assembler III didn't induce the self-assembly of the AuNRs, as observed by TEM characterization (Figure 3.26 b). Even though several short nanochains were observed, the majority of AuNRs were isolated. Thus, the assembler IV with nine dodecane chains grafted on the tripodal core was synthesized to develop stronger attractions with the PS

chains grafted onto the AuNR tips. The solubility was improved by the addition of a small amount of toluene in the solution.

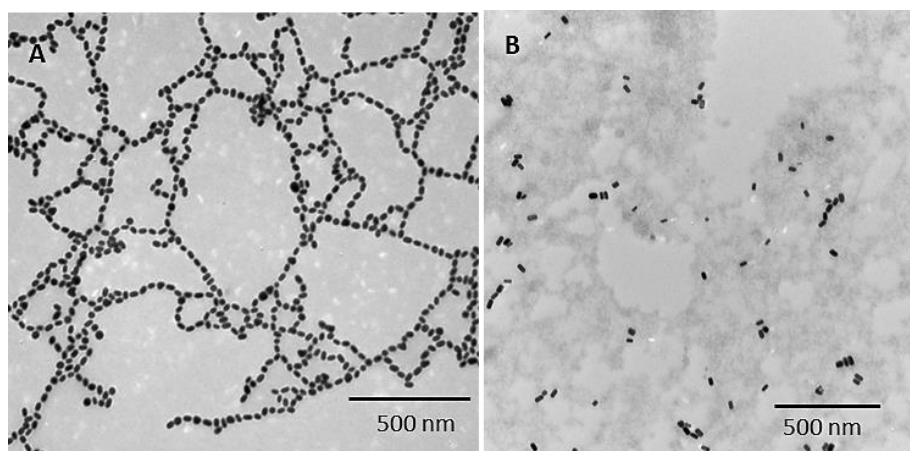


**Figure 3.26 : TEM images of the chains of AuNRs obtained in the control sample (A) and of the clusters formed upon the addition of the assembler III (B).**

### 3.5. AuNRs self-assembly via organic assembler IV

#### **Protocol - Assembly of PS-capped AuNRs by the addition of the assembler IV**

*PS-modified AuNRs dispersed in DMF (gold concentration of 0.015 mg/mL) were introduced in a solution of organic assembler IV (5.00 mg, corresponding to ~33 molecules of linker per AuNR) dissolved in 1 ml of DMF and one drop of toluene. Toluene was necessary to ensure the solubility of the linker. The assembly was triggered by dropwise addition of a DMF/water mixture to the mixture of PS-modified AuNR and the organic assembler in DMF until the water volume in the final solution reached 20%. The concentration of AuNRs in the final solution was 0.0075 mg/mL.*

The addition of the organic assembler IV in the solution induced the assembly of AuNRs in small clusters, which was evidenced by both TEM characterization (Figure 3.27 b-f) and UV-Vis spectroscopy (Figure 3.28). Indeed, the characteristic longitudinal LSPR band at 625 nm broadened and decreased in intensity.

A closer look at the clusters reveals that the clusters contain from 3 to 8 NRs and the target Y-shape structures are only rarely observed. This is probably due to the structure of the assembler IV, which is made of 3 alkyl chains of only 2.7 nm long, whereas the length of the



PS chains grafted at the nanorod tips is  $\sim 4.5$  nm when the nanorods are dispersed in 80/20 v/v DMF/water mixture [10]. Therefore, the overall size of the organic assembler is probably too small to firmly link three nanorods in a Y-shape structure.

Additional studies including the synthesis of new organic linkers with more numerous longer hydrophobic arms have to be realized to obtain a full control over size, shape and interparticle distance in Y-shape trimers.

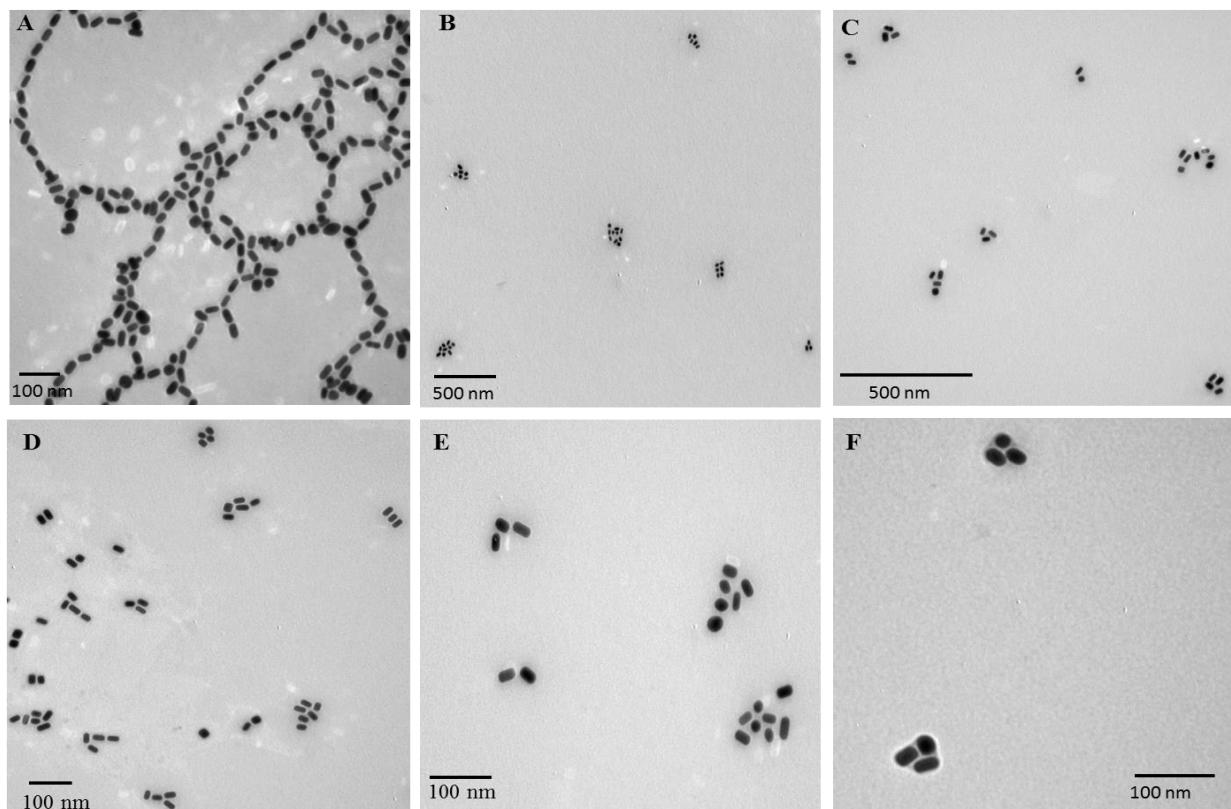


**Figure 3.27 : TEM images of the chains of AuNRs obtained in the control sample (A) and of the clusters formed upon the addition of the assembler IV (B-F).**

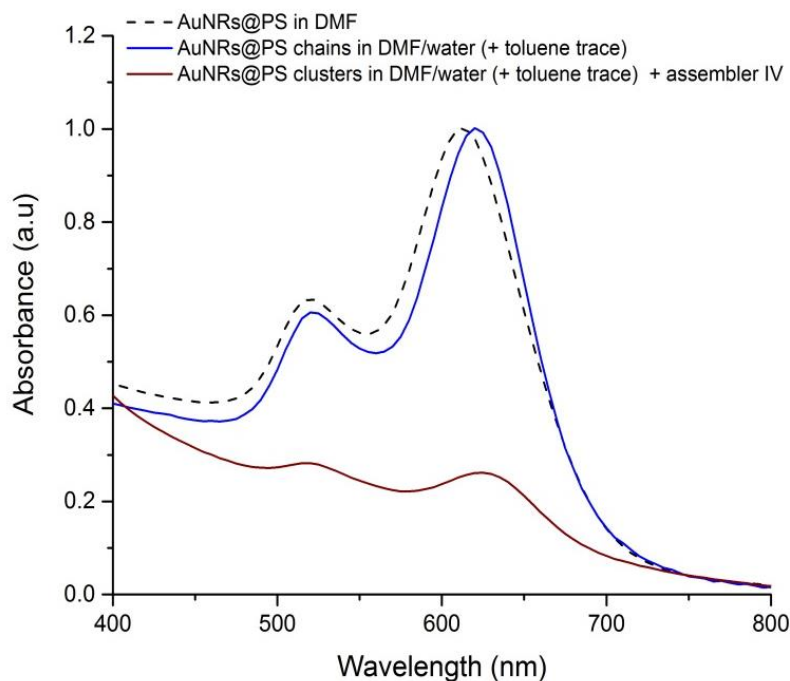


**Figure 3.28** : Normalized absorption spectra of PS-modified AuNRs in DMF (dash curve), of nanochains of AuNRs in a (80/20 v/v) DMF/water mixture (blue curve), and of nanostructures assembled by the assembler IV in a (80/20 v/v) DMF/water mixture (red curve).

#### 4. CONCLUSION

The aim of the work presented in this chapter was to investigate the assembly of short AuNRs into nanoarchitectures with well-defined Y-shaped geometry, *i.e.* NRs trimers, via organic molecules.

We have shown the design and the multistep synthesis of new organic molecules and their use in the self-assembly of AuNRs into AuNRs trimers. The structure of the synthesized organic assemblers was carefully chosen to ensure the trimer directionality while keeping the linked AuNRs at a fixed distance.

Hence, we designed molecules with trigonal planar geometry, bearing three long and rigid arms to ensure the average interparticle distance close to 5 nm, and the terminal groups able to interact with the nanorods. Three (II, III, IV) of the four (I - IV) initially designed organic assemblers were successfully synthesized and used in experiments. Initially, the assembler II was employed to covalently cross-link three AuNRs via the thiol groups at its periphery.

In such experiments, TEM characterization revealed AuNRs trimer formation, but in a relatively low yield (~30%). Moreover, trimers were not uniform in their morphology; tip-to-tip assembly with an angle close to 120°, but also tip-to-side assembly of nanorods, were observed. Even though thiol groups of the assembler have a high affinity for gold, and can easily access the surface of the AuNRs coated by citrate, grafting of thiol specifically on the tip of the AuNRs was shown to be very challenging as both tips and lateral facets of AuNRs are homogeneously coated by citrate ions. In addition, the synthesized assembler II might not be rigid enough to preserve the interparticle distance and directionality. Thus, a new assembler with more rigid arms and more numerous thiol groups at its periphery has to be synthesized to obtain AuNRs trimers with a perfect Y-shape.

To improve the yield of the AuNRs assembly and the uniformity of trimers, we developed an alternative approach where three-branched assemblers III and IV containing peripheral long alkyl chains were used to establish hydrophobic attractions with the polymer chains grafted on the AuNRs tips. However, this strategy did not give the expected result. Instead of tip-to-tip assembly of AuNRs into trimers, we observed the formation of small gold clusters composed of two to five AuNRs. This might be due to the fact that the hydrophobic arms or the assembler are not long enough to establish strong interactions with the PS chains grafted on the AuNRs tips. Thus, additional studies including the synthesis of new organic linkers with more numerous and longer hydrophobic arms have to be realized to obtain a full control over size and shape in such assemblies.

## REFERENCES

- [1] A. Klinkova, R. M. Choueiri, and E. Kumacheva, “Self-assembled plasmonic nanostructures.,” *Chem. Soc. Rev.*, vol. 43, pp. 3976–91, 2014.
- [2] J. Gong, G. Li, and Z. Tang, “Self-assembly of noble metal nanocrystals: Fabrication, optical property, and application,” *Nano Today*, vol. 7, no. 6, pp. 564–585, 2012.
- [3] F. Westerlund and T. Bjørnholm, “Directed assembly of gold nanoparticles,” *Curr. Opin. Colloid Interface Sci.*, vol. 14, no. 2, pp. 126–134, 2009.
- [4] M. Li, H. Schnablegger, and S. Mann, “Coupled synthesis and self-assembly of nanoparticles to give structures with controlled organization,” *Nature*, vol. 402, no. 6760, pp. 393–395, 1999.
- [5] M. Grzelczak, J. Vermant, E. M. Furst, and L. M. Liz-Marzán, “Directed self-assembly of nanoparticles,” *ACS Nano*, vol. 4, no. 7, pp. 3591–3605, 2010.
- [6] J. Israelachvili and R. Pashley, “The hydrophobic interaction is long range, decaying exponentially with distance,” *Nature*, vol. 300, no. 5890, pp. 341–342, 1982.
- [7] Z. Nie, D. Fava, M. Rubinstein, and E. Kumacheva, “‘Supramolecular’ assembly of gold nanorods end-terminated with polymer ‘pom-poms’: Effect of pom-pom structure on the association modes,” *J. Am. Chem. Soc.*, vol. 130, no. 11, pp. 3683–3689, 2008.
- [8] A. Sánchez-Iglesias, M. Grzelczak, T. Altantzis, B. Goris, J. Pérez-Juste, S. Bals, G. Van Tendeloo, S. H. Donaldson, B. F. Chmelka, J. N. Israelachvili, and L. M. Liz-Marzán, “Hydrophobic interactions modulate self-assembly of nanoparticles,” *ACS Nano*, vol. 6, no. 12, pp. 11059–11065, 2012.
- [9] A. Lukach, K. Liu, H. Therien-Aubin, and E. Kumacheva, “Controlling the degree of polymerization, bond lengths, and bond angles of plasmonic polymers,” *J. Am. Chem. Soc.*, vol. 134, no. 45, pp. 18853–18859, 2012.
- [10] Z. Nie, D. Fava, E. Kumacheva, S. Zou, G. C. Walker, and M. Rubinstein, “Self-assembly of metal–polymer analogues of amphiphilic triblock copolymers,” *Nat. Mater.*, vol. 6, no. 8, pp. 609–614, 2007.
- [11] H. Xia, G. Su, and D. Wang, “Size-dependent electrostatic chain growth of pH-sensitive hairy nanoparticles,” *Angew. Chemie Int. Ed.*, vol. 52, no. 13, pp. 3726–3730, 2013.
- [12] C. J. Loweth, W. B. Caldwell, X. Peng, A. P. Alivisatos, and P. G. Schultz, “DNA-based assembly of gold nanocrystals,” *Angew. Chemie Int. Ed.*, vol. 38, no. 12, pp.

- 1808–1812, 1999.
- [13] F. A. Aldaye and H. F. Sleiman, “Dynamic DNA templates for discrete gold nanoparticle assemblies: Control of geometry, modularity, write/erase and structural switching,” *J. Am. Chem. Soc.*, vol. 129, no. 14, pp. 4130–4131, 2007.
- [14] Y. Ofir, B. Samanta, and V. M. Rotello, “Polymer and biopolymer mediated self-assembly of gold nanoparticles,” *Chem. Soc. Rev.*, vol. 37, no. 9, pp. 1814–1825, 2008.
- [15] W. Ni, R. A. Mosquera, J. Pérez-Juste, and L. M. Liz-Marzán, “Evidence for hydrogen-bonding-directed assembly of gold nanorods in aqueous solution,” *J. Phys. Chem. Lett.*, vol. 1, no. 8, pp. 1181–1185, 2010.
- [16] L. C. Brousseau, J. P. Novak, S. M. Marinakos, and D. L. Feldheim, “Assembly of phenylacetylene-bridged gold nanocluster dimers and trimers,” *Adv. Mater.*, vol. 11, no. 6, pp. 447–449, 1999.
- [17] J. P. Novak, C. Nickerson, S. Franzen, and D. L. Feldheim, “Purification of molecularly bridged metal nanoparticle arrays by centrifugation and size exclusion chromatography,” *Anal. Chem.*, vol. 73, no. 23, pp. 5758–5761, 2001.
- [18] F. Goubard and F. Dumur, “Truxene: a promising scaffold for future materials,” *RSC Adv.*, vol. 5, pp. 3521–3551, 2015.
- [19] A. W. Amick and L. T. Scott, “Trisannulated benzene derivatives by acid catalyzed aldol cyclotrimerizations of cyclic ketones. Methodology development and mechanistic insight,” *J. Org. Chem.*, vol. 72, no. 9, pp. 3412–3418, 2007.
- [20] B. Huang and D. A. Tomalia, “Poly(ether) dendrons possessing phosphine focal points for stabilization and reduced quenching of luminescent quantum dots,” *Inorganica Chim. Acta*, vol. 359, no. 6, pp. 1961–1966, 2006.
- [21] B. A. Padias, D. A. Tomalia, J. R. McConnell, and H. K. Hall, “Starburst polyether dendrimers,” *J. Org. Chem.*, vol. 52, no. 24, pp. 5305–5312, 1987.
- [22] W. P. Wuelfing, S. M. Gross, D. T. Miles, and R. W. Murray, “Nanometer gold clusters protected by surface-bound monolayers of thiolated poly(ethylene glycol) polymer electrolyte,” *J. Am. Chem. Soc.*, vol. 120, no. 48, pp. 12696–12697, 1998.
- [23] J. G. Mehtala, D. Y. Zemlyanov, J. P. Max, N. Kadasala, S. Zhao, and A. Wei, “Citrate-stabilized gold nanorods,” *Langmuir*, vol. 30, no. 46, pp. 13727–13730, 2014.
- [24] A. P. Leonov, J. Zheng, J. D. Clogston, S. T. Stern, A. K. Patri, and A. Wei, “Detoxification of gold nanorods by treatment with polystyrenesulfonate,” *ACS Nano*, vol. 2, no. 12, pp. 2481–2488, 2008.
- [25] D. Fava, Z. Nie, M. A. Winnik, and E. Kumacheva, “Evolution of self-assembled

- structures of polymer-terminated gold nanorods in selective solvents,” *Adv. Mater.*, vol. 20, no. 22, pp. 4318–4322, 2008.
- [26] C. J. Orendorff and C. J. Murphy, “Quantitation of metal content in the silver-assisted growth of gold nanorods,” *J. Phys. Chem. B*, vol. 110, no. 9, pp. 3990–3994, 2006.
- [27] J.-Y. Chang, H. Wu, H. Chen, Y.-C. Ling, and W. Tan, “Oriented assembly of Au nanorods using biorecognition system,” *Chem. Commun.*, no. 8, p. 1092, 2005.
- [28] A. Petukhova, J. Greener, K. Liu, D. Nykypanchuk, R. Nicolaÿ, K. Matyjaszewski, and E. Kumacheva, “Standing arrays of gold nanorods end-tethered with polymer ligands,” *Small*, vol. 8, no. 5, pp. 731–737, 2012.



## **CHAPTER 4**

# **ASSEMBLY OF GOLD HOLLOW NANOTRIANGLES ON DNA ORIGAMI TEMPLATES**





## 1. INTRODUCTION

Plasmonic nanoparticles allow the manipulation of light, which makes them ideal building blocks for nanophotonic devices and “smart” materials. However, the precise organization of NPs into nanoarchitectures is of vital importance for their implementation in functional devices. Despite the recent advances in colloidal synthesis and self-assembly, it remains a significant challenge to assemble elementary plasmonic nanoparticles into well-defined structures owing to the difficulties in controlling nanoparticle bond interactions [1], [2].

Since 1982 when Seeman and Kallenbach [3] described the use of nucleic acid junctions for the assembly of geometrically defined nanoobjects, DNA-based templates have emerged as a powerful tool to construct complex nanoarchitectures with a high control over the placement of the building blocks.

Based on complementary Watson-Crick base pairing between oligonucleotides, many rigid DNA motifs (DNA tiles) were developed and used for further assembly into discrete finite objects. For example, Le *et al* [4] demonstrated the self-assembly of AuNPs into high density 2D arrays by a DNA scaffolding approach. They assembled 21 oligonucleotides into 4 DNA tiles, which formed a DNA scaffold. One of the tiles were extended with ssDNA to hybridize to the complementary single strand DNA (ssDNA) grafted to the NPs, establishing the control over the position of different elements in a complex nanostructure (Figure 4.1). However, the construction of such templates requires the exact stoichiometric control and the purification of the constituent oligonucleotides and tiles, resulting in experimental errors. In addition, such strategies are limited to simple geometric shapes and the repetition of basic building blocks [5].

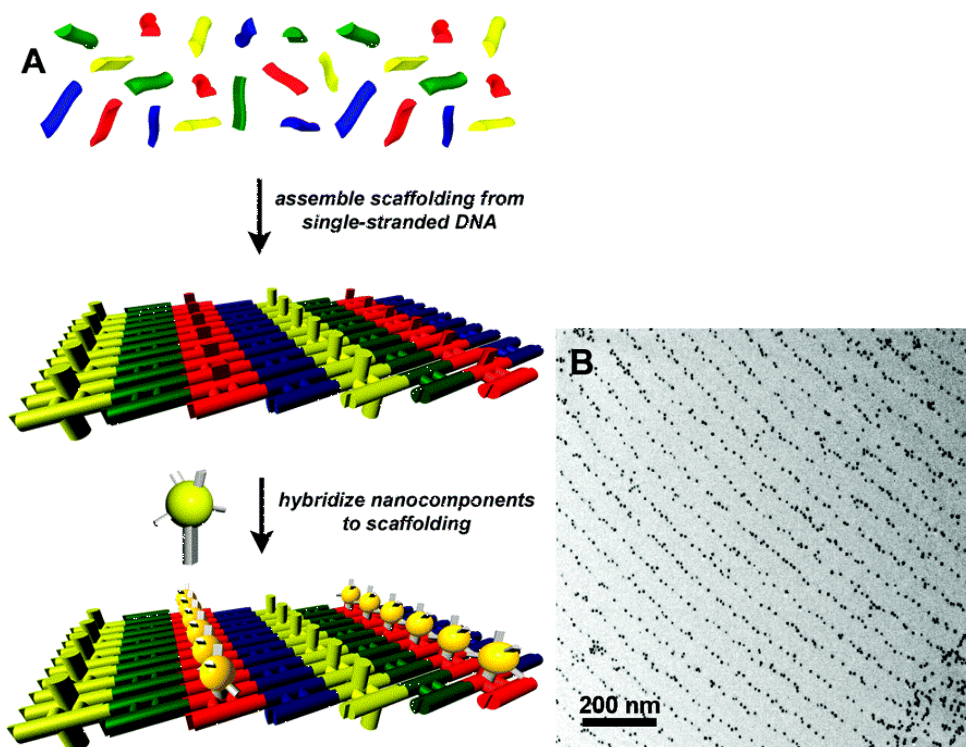


**Figure 4.1 :** a) Schematic illustration of the DNA scaffold assembly in solution from the set of 21 strands and the deposition on mica. It is composed entirely of double-stranded DNA, except for the open, single-stranded hybridization sites (red) which allow the attachment of DNA-encoded Au nanocomponents; b) TEM image of a NPs array [4].

An extraordinary breakthrough in DNA nanotechnology occurred in 2006 when Paul W.K. Rothemund [6] developed a new synthetic technique called DNA origami, which amplified the complexity and the functionality of DNA templates. Similar to the Japanese art of paper folding, the DNA-origami technique consists in programmed folding of DNA sequences into complex geometries. In this “one pot” synthesis of DNA template, rationally designed short single strands of DNA (staple strands) are used to direct the folding of a long single strand scaffold into desired shapes, following the principle of Watson-Creek base pairing (Figure 4.2). In such structures, the staple strands hybridize with the scaffold strand rather than with each other, reducing the experimental errors and synthesis time.

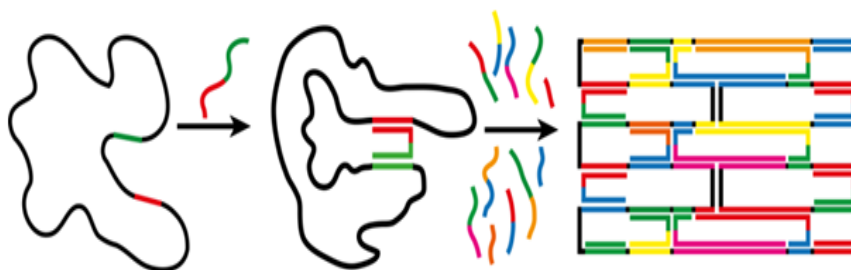


**Figure 4.2 :** Schematic illustration of the construction of DNA origami - Folding of the DNA origami structure is based on the high specificity of Watson–Crick binding interactions which allow the hybridization of ssDNA scaffold (in black) with numerous staple strands (in color).

In this original work, Rothemund designed DNA structures with different shapes, such as squares, disks and five-pointed stars with a spatial resolution of 6 nm, by raster-filling the shape with a 7-kilobase single-stranded scaffold and by employing over 200 staple strands to hold the scaffold in place. In addition, he showed that the structures could be programmed to bear complex patterns such as words and images on their surfaces, since each oligonucleotide can serve as a 6-nm pixel (Figure 4.3).

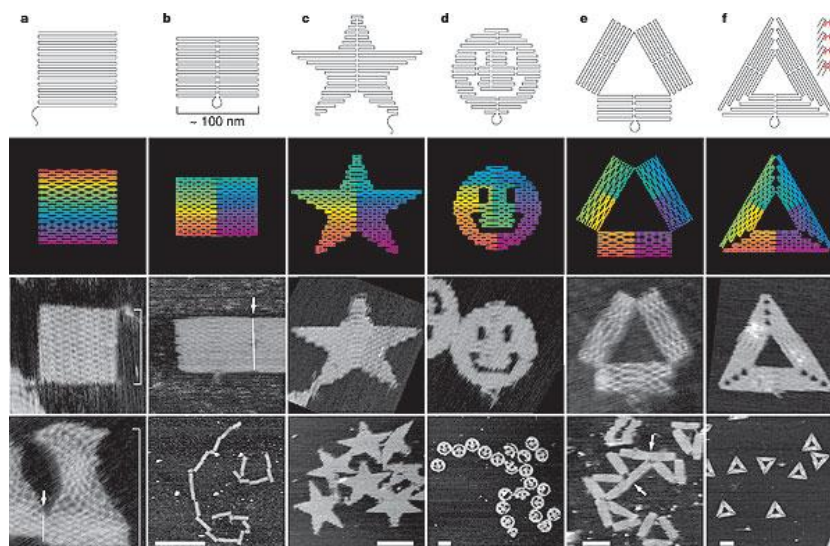


**Figure 4.3 :** DNA origami shapes: a) square; b) rectangle; c) star; d) disk with three holes; e) triangle with rectangular domains; f) sharp triangle with trapezoidal domains and bridges between them. All images without a scale bar are the same size, 165 nm x 165 nm. Scale bars for lower AFM images are 1  $\mu$ m (b) and 100 nm (c-f) [6].

Owing to its capability to form nanoobjects with complex shapes of predefined dimensions and full molecular addressability, DNA origami became a powerful tool for uses in different fields such as molecular biology and device physics. However, the chemical modification and functionalization of DNA nanostructures are often necessary due to the limited chemical, optical, and electronic functionality of DNA. The most common modification of the origami is based on the hybridization of the extended staples, which expand out of the origami plane, with complementary DNA sequences covalently attached to different nanoobjects. Another common method includes biotinylation of the staple strands. For example, Ko *et al.* used biotinylated DNA origami to assemble streptavidin-functionalized QDs [7]. In addition, the functionalization of a staple strand with thiol groups can induce AuNPs assembly via specific gold-sulfur bonding [5], [8]. Such versatile chemical modifications, together with the programmable and predictable Watson-Creek base pairing and the rigidity of the double helix, make DNA origami an ideal template for the precise assembly of NPs into programmable, spatially ordered arrays.

Several previous works have demonstrated the generation of such hybrid materials with the potential applications in nanodevices for photonics and optoelectronics. Gür *et al.* [1] generated plasmonic waveguides by hybridizing a DNA origami nanotube containing binding sites for eight complementary oligonucleotides and the oligonucleotide-functionalized AuNPs (Figure 4.4).

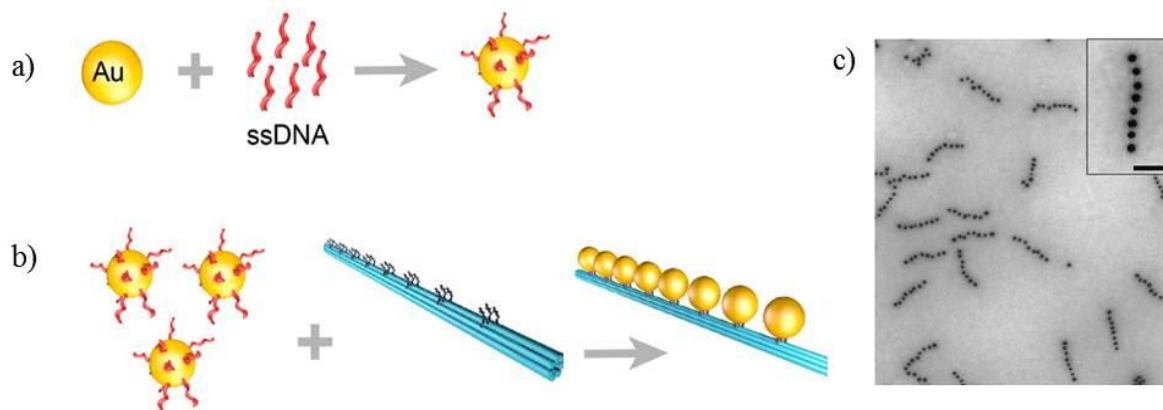


**Figure 4.4 : a,b) Scheme of the self-assembly of AuNPs on DNA origami: AuNPs functionalized with oligonucleotides (a) hybridize to complementary tethers displayed on the DNA origami structure (b); c) SEM image of AuNPs waveguides (scale bar = 500 nm, inset scale bar = 100 nm) [1].**

Another type of plasmonic waveguides was reported by Schreiber et al [9]. They designed flower-shaped DNA origami structure, with a DNA-functionalized AuNP at the center. They assembled two types of nanoflowers hybridized with complementary linking sequences (A or B type) into AuNPs chains. Following the same principle, they have also showed the assembly of AuNPs into lattices whose geometries are controlled by the relative position and the number of the linking sequences (Figure 4.5).

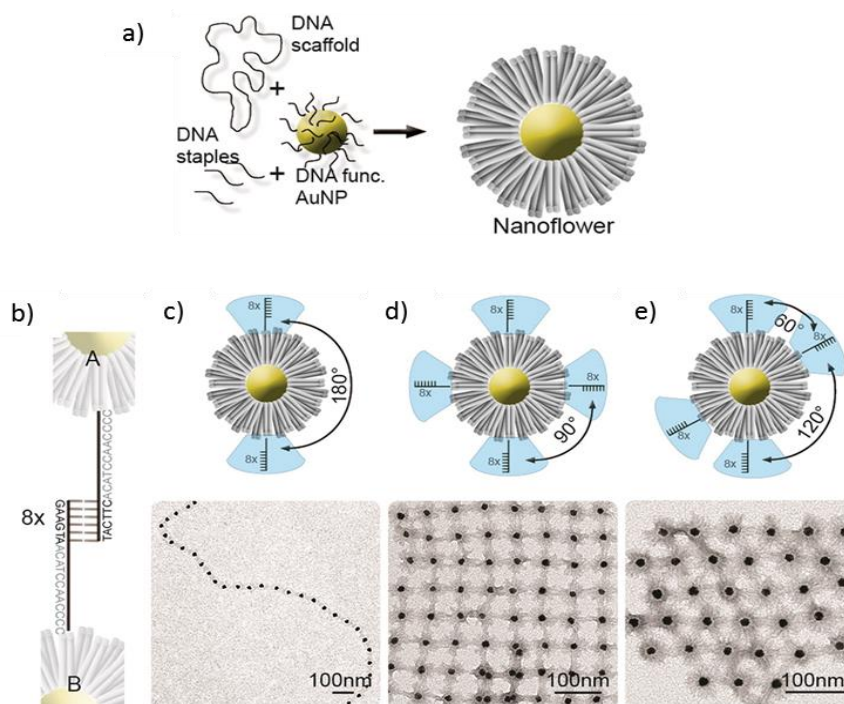


**Figure 4.5 :** a) A nanoflower formation by annealing a ssDNA scaffold with staple strands and an oligonucleotide-functionalized AuNP; b) nanoflowers functionalized with A or B type complementary oligonucleotides and subsequently hybridized; c) chains of AuNPs obtained by mixing A and B nanoflowers with two hybridization sites separated by 180°; d) square lattices obtained from nanoflowers with four hybridization sites at 90°; e) hexagonal lattices obtained from nanoflowers with four hybridization sites with approximately 60° and 120° separation [9].

To assemble sub-10-nm AuNPs over macroscopic areas, bottom-up DNA self-assembly can be combined with top-down lithography, as shown by Cha and co-workers [10]. They hybridized small poly-thymine coated AuNPs (<5 nm) with poly-thymine strands at the corners of a poly-adenine corner-modified triangular DNA origami and deposited such structures onto electron-beam patterned oxide substrates. By combining two nanofabrication

techniques, they established the control over placement and orientation of AuNPs arrays and networks, expanding the generality of DNA origami-directed self-assembly towards many types of patterns and sizes (Figure 4.6).

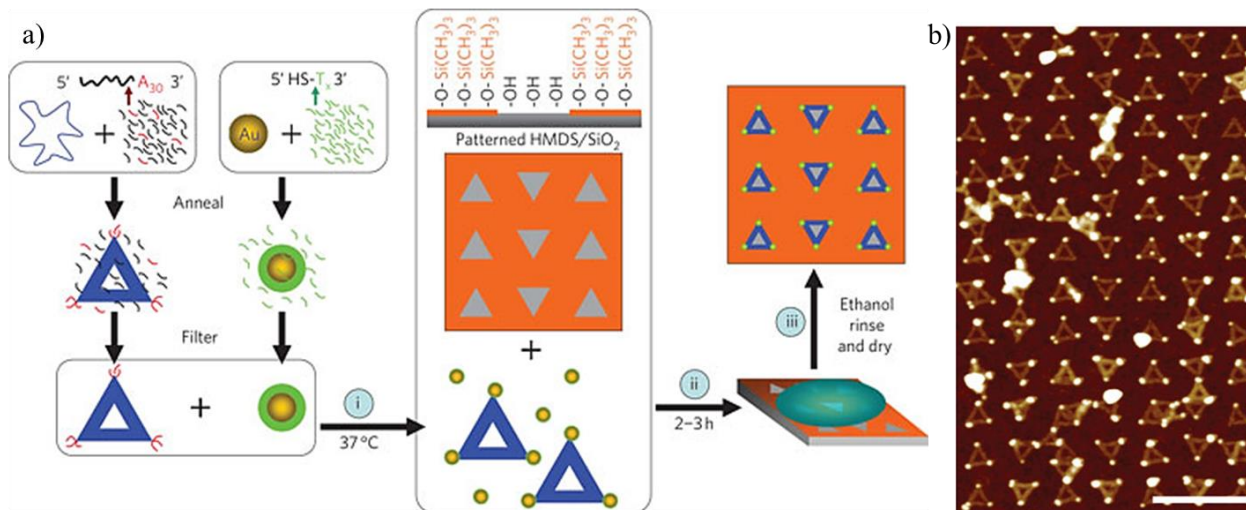


**Figure 4.6 :** a) The schematic illustration of the assembly of AuNPs into spatially ordered two-dimensional arrays : (i) DNA origami and AuNPs binding, (ii) controlled DNA origami adsorption onto patterned substrate and (iii) rinsing and drying of the sample; b) AFM image of the obtained AuNPs arrays [10].

Due to the unique sequence of each staple strand, DNA origami is a fully addressable template to spatially organize nanostructures and single molecules. Taking the advantages of such strategy, we designed a nanoarchitecture composed of gold hollow nanotriangles and fluorescent dyes assembled via rectangular DNA origami. In this chapter, we will describe the synthesis of such structure. In addition, we will study the plasmon propagation in this nanoarchitecture.

## **2. FORMATION OF A RECTANGULAR DNA ORIGAMI**

The double helical structure of DNA is constituted of two ssDNA that wind around each other. Each strand has a backbone made of alternating phosphate groups, a sugar group and one of the four bases: adenine (A), cytosine (C), guanine (G) and thymine (T). The strands are held together owing to Watson-Crick interactions where an adenine forms a hydrogen bond with a thymine and a guanine with a cytosine. When all the bases of the two strands are associated according to this pairing rule, the binding energy reaches its maximum and such strands are called complementary. Such selective and precise spatial positioning of the two strands provides the basis for the DNA origami formation.

DNA origami consists of a long, circular ssDNA scaffold, typically of a phage M13mp18 (~7000 bases), and of roughly 200 short staple ssDNA strands (20-60 bases). Based on the defined sequence of a scaffold, the chemical composition of the staples can be programmed by Watson-Crick complementarity to fold the scaffold into a parallel array of helices.

The staple strands can have subsections which bind to different positions along the viral scaffold (typically separated by Holliday junction-like crossovers in the target structure), and each subsequence can form dsDNA independently of the others.

The binding of a staple to the scaffold is hindered by an entropic penalty. The entropy is reduced as the circular viral scaffold folds due to the binding of an individual staple. As each staple binds at a certain temperature (melting temperature), the binding of a staple depends on the state of the previously bound staples, leading to a field of interacting loops of various sizes [11].

Once the 200 staples with the corresponding sequences are synthesized, they are mixed with the scaffold (at nM range) in a buffer rich with magnesium ions. Magnesium ions are necessary as they screen the intra-helical electrostatic repulsion and stabilize formed dsDNA. DNA origami is formed in the annealing process – the mixture is heated to 90 °C and then allowed to slowly cool down to room temperature.



### 3. MODIFIED DNA ORIGAMI FOR THE ASSEMBLY OF AuHTs AND FLUORESCENT DYES

Our target plasmonic nanodevice was composed of a gold hollow nanotriangle and fluorescent dyes placed in the close proximity of each tip of the triangle.

To control the plasmon propagation along a hollow nanotriangle, three different fluorescent dyes were employed: a trigger, which shows strong absorption near the excitation wavelength, and the two probes with a strong absorption and good fluorescence in the near-infrared spectral region. The list of the used dyes is shown in Table 4.1.

In such system, the local excitation of the plasmon trigger results in the excitation of a gold structure and the propagation of EM energy along the two branches of a hollow nanotriangle, enhancing the EM field around the triangle. The particularly strong EM field enhancement at the tips of a triangle leads to the excitation of the two probes, which respond by emitting the fluorescent signals.

**Table 4.1 : A list of commercially available fluorescent DNA labels used to trigger or to detect plasmon propagation in the target nanodevice.**

	Fluorescent dye	$\lambda_{\max}$ absorption (in EtOH)	$\lambda_{\max}$ emission (in EtOH)
<b>Trigger</b>	DY-681	691 nm	708 nm
<b>Probe 1</b>	DY-781	783 nm	800 nm
<b>Probe 2</b>	ATTO 740	740 nm	764 nm

To precisely position each dye near one tip of a hollow triangle, and to ensure 2.5 nm distance between them, we used a modified DNA origami as a template. The scheme of such nanoarchitecture is shown in Figure 4.7.

In order to attach the AuHTs onto the DNA origami template, staples at the defined positions were elongated with a short, thiol-terminated poly-T sequence extending from the origami surface. The positions of the thiol-modified sequences were programmed to form a shape of a triangle with the size of 40 nm, which corresponds to the average size of the synthesized gold hollow nanotriangles. Since thiol groups bind to gold surfaces with high affinity, we hope that the gold hollow triangles could be precisely localized onto the DNA origami. The scheme of

the DNA origami is shown in figure X. The yellow dots show the position of the thiol-modified DNA staples.

In addition, staple strands positioned 2.5 nm away from the corners of the triangle-shaped thiol path were modified with the chosen fluorescent dyes (Table 4.1). The obtained DNA origami structure exhibit strong affinity for the gold hollow nanotriangles and enable the accurate positioning of the fluorophores.

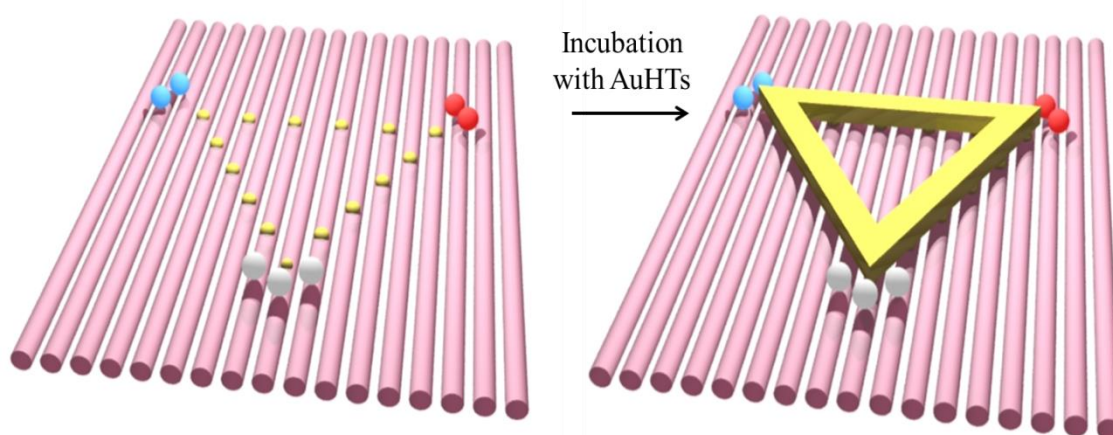


**Figure 4.7 : Deposition of gold hollow triangles onto modified DNA origami template. Staples elongated with a thiol-terminated sequence are illustrated as yellow spheres, while staples modified with DY-681, DY-781 and ATTO 740 are shown in white, blue and red, respectively.**

### 3.1. Synthesis of a nanostructure

#### **Protocol – Synthesis of rectangular DNA origami modified with thiols and fluorescent dyes**

*The precise position and sequence of staple strands used to assemble the rectangular DNA origami structure from the viral scaffold (ssDNA isolated from bacteriophage M13mp18), together with the list of thiol-modified and fluorophore-labeled oligonucleotides, are given in Annex 2. All ssDNA staples were purchased from Eurogentec and kept as 100  $\mu$ M aqueous stock solutions. The same protocol was used to assemble DNA origami containing just thiol-modified staples and DNA origami containing both thiol-modified and fluorophore-modified staples.*

*DNA origami assembly was done by mixing scaffold and staples to a final concentration of 10 nM and 50 nM, respectively, in a TAE buffer that contained 40 mM Tris, 20 mM acetic acid, 1*

*mM EDTA and 10 mM magnesium acetate. The mixture was then subjected to thermal annealing. The temperature was first raised to 90 °C, then decreased to 60 °C during 1 h, and finally decreased to 20 °C during 2 h. The assembled origami structures were purified from the excess staple strands by centrifugation with 100 kDa MWCO filters and collected at the end of the second cycle of centrifugation.*

The AFM image of synthesized rectangular DNA origami structures before the incubation with AuHTs is shown in Figure 4.8.

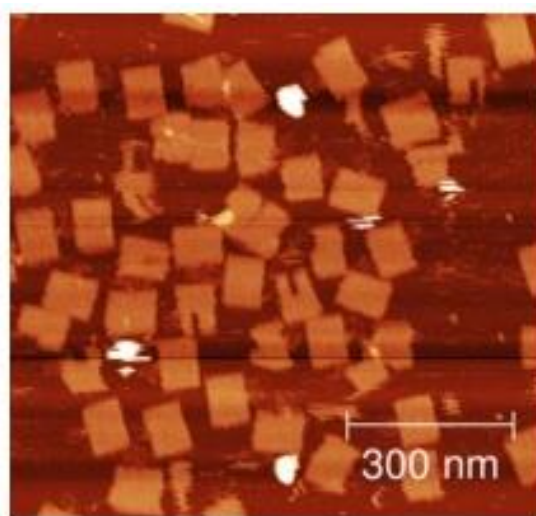


**Figure 4.8 : AFM image of rectangular DNA origami.**

#### **Protocol - Stabilization of gold hollow nanotriangles in TAE buffer**

*10  $\mu$ L of an aqueous stock solution of mPEG-thiol ( $M_n = 5000 \text{ g mol}^{-1}$ ; 6.5 mg/mL) were added to a solution of the freshly prepared gold hollow nanotriangle solution (4 mL). The number of particles was estimated to be  $6.5 \times 10^{11}$  and the number of mPEG-SH molecules needed for the stabilization of nanotriangles in a buffer was calculated by the equation described in section 3.2. The mixture was stirred for 2h and then washed with water by two centrifugation cycles (7 500 rpm, 20 min), to remove free mPEG-SH. After the second centrifugation, the supernatant was discarded and PEG-coated hollow nanotriangles were redispersed in a Tris base, acetic acid and EDTA (TAE) buffer which contained magnesium ( $[\text{Mg}^{2+}] = 10 \text{ mM}$ ).*

Despite the high degree of stability in bulk solution, Au@citrate nanotriangles were immediately aggregated in the buffer solution (Figure 4.9 a) probably due to the neutralization

of citrate anions caused by the high concentration of  $Mg^{2+}$  ions. Therefore, the electrostatically attached citrate molecules have been replaced by more stable PEG-thiol molecules, which covalently bound to the surface of gold hollow triangles. The PEG-coated hollow nanotriangles were stable in TAE buffer during at least few weeks (Figure 4.9 b).

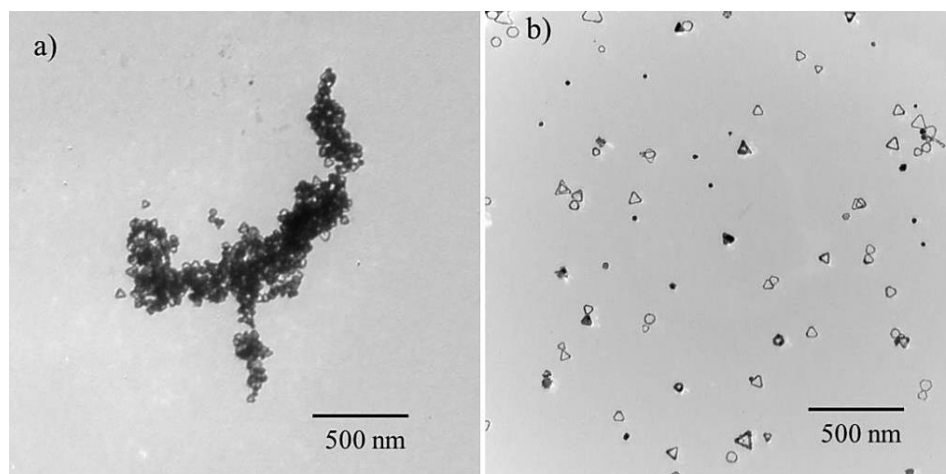


**Figure 4.9 : TEM image of AuHTs aggregates (a) and of PEG-capped AuHTs (b) in TAE buffer.**

#### **Protocol – Deposition of gold hollow triangles onto the DNA origami template**

*The assembled and purified thiol-modified DNA origami (5  $\mu$ L) was mixed with freshly prepared PEG-capped gold hollow nanotriangles (100  $\mu$ L) in TAE buffer. The mixture was incubated overnight at 4 °C. For the imaging and the optical characterization, 10-fold dilution of the mixture was prepared.*

AFM confirmed that the rectangular DNA origami structures displayed the AuHTs at the positions prescribed by the design shown in Annex 2 (Figure 4.10). The height of the attached nanostructures was  $\sim 8$  nm, corresponding to the sum of the height of AuHTs ( $\sim 6$  nm) and DNA origami ( $\sim 2$  nm). However, not all of the nanotriangles were precisely positioned onto the DNA origami templates.

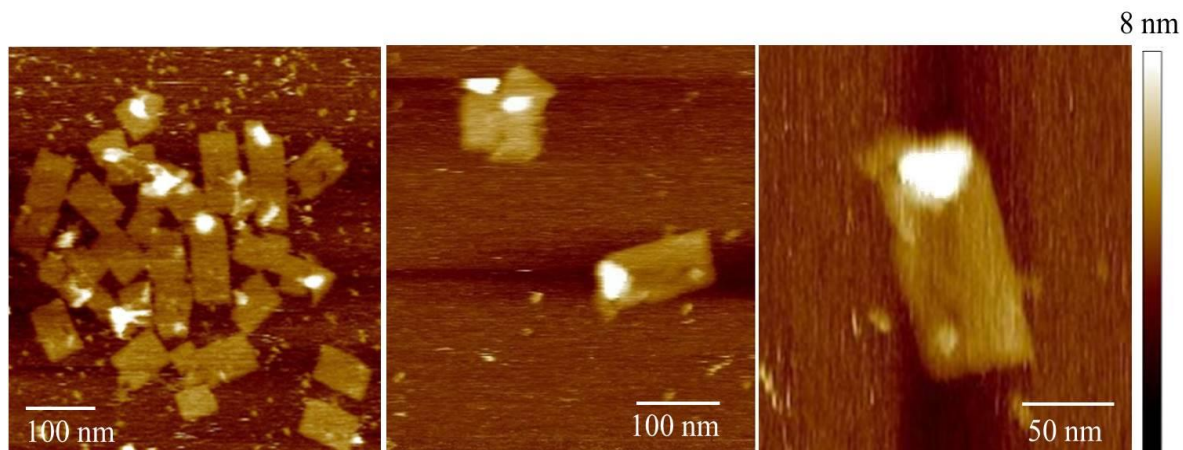


**Figure 4.10 : AFM images of gold hollow nanotriangles organized by rectangular DNA origami.**

### 3.2. Optical characterization of a nanostructure

Colocalized dark-field scattering and AFM were performed on the complex nanostructures containing AuHTs and fluorescent dyes, in order to characterize their optical properties on single objects. Each nanostructure was irradiated by a He-Ne laser, operating in continuous mode at a wavelength of 633 nm, focused through a high NA objective.

In the original frame of the project, the idea was to selectively excite the trigger molecules situated near the one corner of the AuHT. The excitation wavelength is chosen to be at 633 nm to satisfy this purpose, as this wavelength nicely excite the trigger molecules (DY-681), while it barely excites the two probe molecules (ATTO 740 and DY-781) situated near the two arms of the AuHT (Figure 4.11).

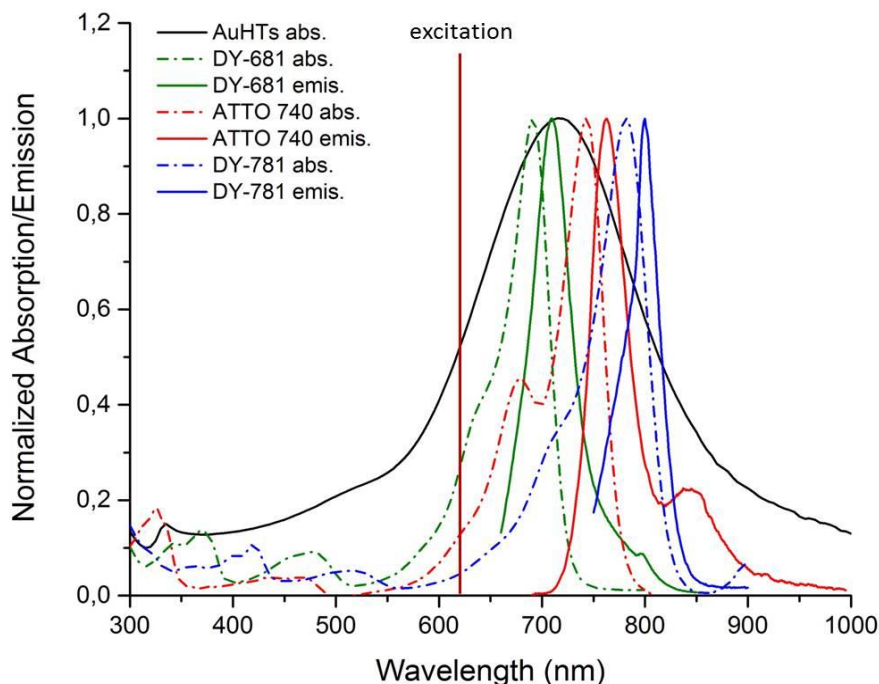


**Figure 4.11 : Absorption spectrum of AuHTs (black curve) and absorption and emission spectra of fluorescent dyes used to trigger (DY-681, green) or to detect (ATTO 740 (red) and DY-781 (blue)) the plasmon propagation in AuHTs.**

In an ideal experiment, such a spatially and spectrally selective excitation of the trigger molecule, owing to a near-field tip located in its proximity, would promote the molecule in the excited state, from which it would relax by emitting a photon triggering the plasmon resonance of the AuHT structure. Figure 12 shows indeed a nice overlap between the emission of the trigger molecules (green) and the plasmon resonance (black). Once the plasmon resonance is excited, the signal can propagate in the two arms of the AuHT and reach the probe molecules, which, in turn, get excited owing to the good spectral overlap of the plasmon resonance and the absorption spectra of these two molecules. These probe molecules can then also emit, indicating a good propagation of the signals in the structure.

This ideal experiment requires a very challenging near field technique. For a first test of a working principle, we preferred to choose an excitation beam large enough to illuminate the whole structure. By exciting at 633 nm, we can excite efficiently the trigger molecules and the plasmon resonance. As the UV-visible spectrum nicely overlaps the absorption spectra of the various emitters, these molecules all emit simultaneously, as shown in Figure 4.12 a. In this figure, we can recognize three peaks centered at 705 nm, 760 nm and 815 nm. The strongest

scattering, with the maximum at 705 nm is attributed to the signal released by the trigger, DY-681, while the 2 peaks at 760 nm and 815 nm correspond to the fluorescent signal emitted by the two receiver molecules, ATTO 740 and DY-781, respectively.

The intensity of the relative peaks is regulated by the spectral overlap of the absorption and emission spectra of the fluorophores with the plasmon resonance. Obviously, the trigger molecule is the one profiting the most of the increased local field induced by the plasmon resonance as its absorption and emission maxima nicely match the maximum of the plasmon resonance.

This test experiment thus clearly shows the expected trends and demonstrates the correct synthesis of the whole nanoarchitecture. The plasmon resonance of the structure can mediate the enhanced emission of the molecules. Among these, the probe molecules are clearly distinguishable owing to their characteristic maxima, indicating an enhanced signal measured in one of the two arms of the AuHT.

In order to clearly identify the role of the plasmon resonance in the measured signal, we performed a second measurement where we studied the DNA origami containing only the three fluorophores. Figure 4.12 b shows the observed dark field spectra of the DNA origami. In the absence of the AuHT, only one peak centered at 705 nm is observed. The peaks centered at 760 nm and 815 nm in the Figure 4.12 a were thus clearly due to the plasmon enhanced energy transfer, further demonstrating the energy transfer in the branched nanoarchitectures.

As shown in Figure 4.11, a Förster energy transfer could occur directly between the dye molecules, owing to a consequent spectral overlap between the emission spectrum of the trigger molecule and the absorption spectra of the probe molecules. However, these molecules are spatially too far apart from each other for this to occur: energy transfer between donor and acceptor molecules can occur only efficiently within a Förster radius (5-6 nm), which is far from the current situation.

The immediate decrease of the emission intensity of the fluorophores upon illumination occurs due to the irreversible photobleaching of the DY-681 (Figure 4.12 b). As this dye would serve as a trigger for the energy transfer in the ideal experiment, it will be very challenging to visualize the plasmon propagation through the assembled nanostructures. Thus, in the next step of the nanodevice fabrication, we will replace to fluorescent dyes with the quantum dots, which are less sensitive to the photobleaching process.

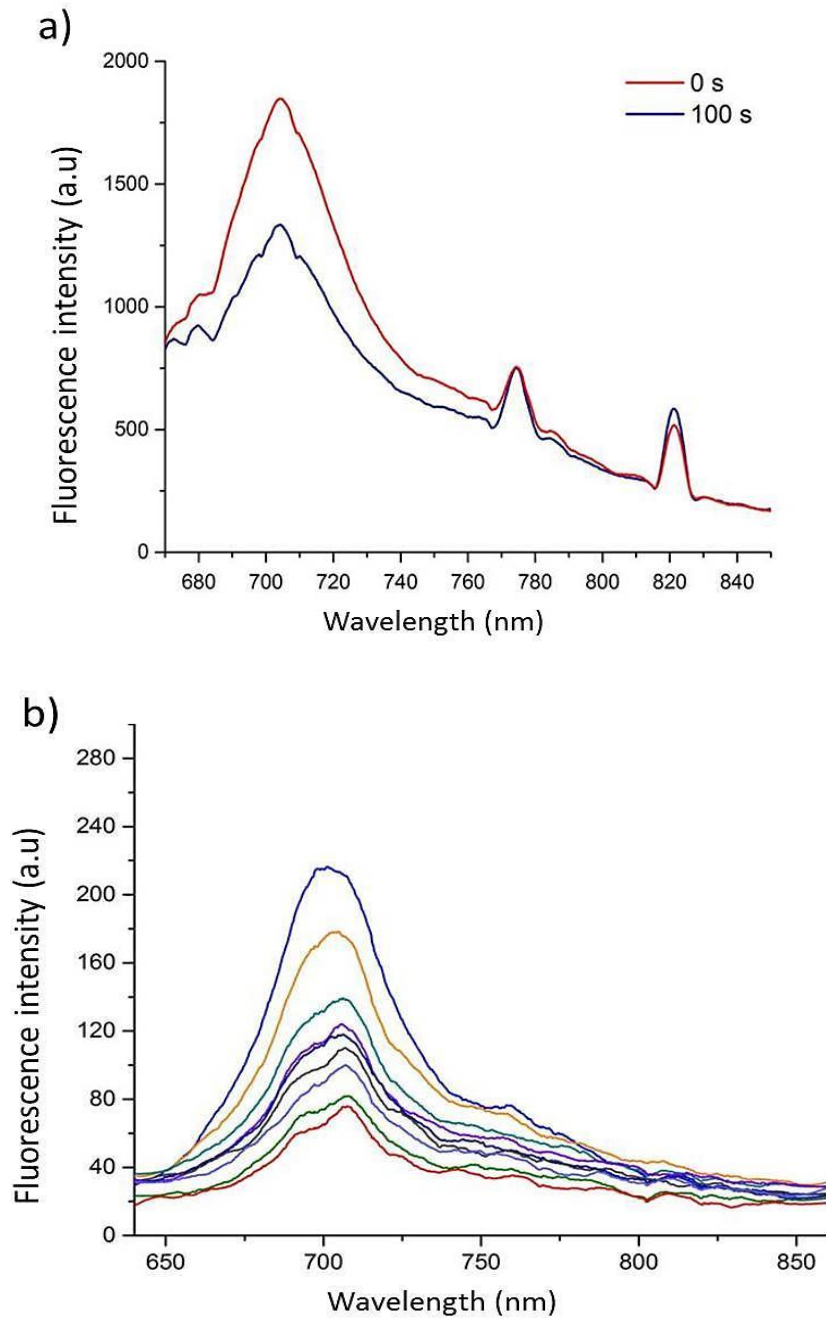


**Figure 4.12 : a) Fluorescence spectra of a nanostructure comprising AuHT and three fluorescent dyes recorded upon the illumination with a laser at 633 nm. They show the scattering intensity of fluorescent dyes at the different laser exposure times. b) Fluorescence spectra of DNA origami containing only the three fluorescent dyes. The spectra of a single DNA origami structure were recorded repeatedly within 3 min.**



## **4. CONCLUSION**

In this chapter, we have presented the assembly of hollow gold nanotriangles and three different fluorescent dyes directed by DNA origami. By modifying the DNA origami with thiol groups, we precisely localized AuHTs onto the origami scaffold, showing the controlled arrangement of gold nanoparticles into a functional nanodevice.

We also studied the optical properties of the fabricated complex nanoarchitecture. By selectively exciting one fluorophore located near one tip of the branched gold nanostructure, we induced the plasmon enhanced energy transfer towards the two branches, which led to the enhanced emission of the two different probes located near the tips of the each branch, demonstrating the energy transfer in the branched nanoarchitectures.

## REFERENCES

- [1] F. N. Gür, F. W. Schwarz, J. Ye, S. Diez, and T. L. Schmidt, "Toward self-assembled plasmonic devices: High-yield arrangement of gold nanoparticles on DNA origami templates," *ACS Nano*, vol. 10, p. 5374–5382, 2016.
- [2] S. J. Tan, M. J. Campolongo, D. Luo, and W. Cheng, "Building plasmonic nanostructures with DNA," *Nat. Nanotechnol.*, vol. 6, no. 5, pp. 268–276, 2011.
- [3] N. C. Seeman and N. R. Kallenbach, "Design of immobile nucleic acid junctions," *Biophys. J.*, vol. 44, no. 2, pp. 201–209, 1983.
- [4] J. D. Le, Y. Pinto, N. C. Seeman, K. Musier-Forsyth, T. A. Taton, and R. A. Kiehl, "DNA-templated self-assembly of metallic nanocomponent arrays on a surface," *Nano Lett.*, vol. 4, no. 12, pp. 2343–2347, 2004.
- [5] B. Saccà and C. M. Niemeyer, "DNA origami: The art of folding DNA," *Angew. Chemie Int. Ed.*, vol. 51, no. 1, pp. 58–66, 2012.
- [6] P. W. K. Rothemund, "Folding DNA to create nanoscale shapes and patterns," *Nature*, vol. 440, no. 7082, pp. 297–302, 2006.
- [7] S. H. Ko, G. M. Gallatin, and J. A. Liddle, "Nanomanufacturing with DNA origami: Factors affecting the kinetics and yield of quantum dot binding," *Adv. Funct. Mater.*, vol. 22, no. 5, pp. 1015–1023, 2012.
- [8] M. R. Jones, K. D. Osberg, R. J. MacFarlane, M. R. Langille, and C. A. Mirkin, "Templated techniques for the synthesis and assembly of plasmonic nanostructures," *Chem. Rev.*, vol. 111, no. 6, pp. 3736–3827, 2011.
- [9] R. Schreiber, I. Santiago, A. Ardavan, and A. J. Turberfield, "Ordering gold nanoparticles with DNA origami nanoflowers," *ACS Nano*, vol. 10, no. 8, pp. 7303–7306, 2016.
- [10] A. M. Hung, C. M. Micheel, L. D. Bozano, L. W. Osterbur, G. M. Wallraff, and J. N. Cha, "Large-area spatially ordered arrays of gold nanoparticles directed by lithographically confined DNA origami," *Nat. Nanotechnol.*, vol. 5, no. 2, pp. 121–126, 2010.

- [11] J. M. Majikes, J. A. Nash, and T. H. LaBean, “Competitive annealing of multiple DNA origami: Formation of chimeric origami,” *New J. Phys.*, vol. 18, no. 11, 2016.

## **CONCLUSIONS AND PERSPECTIVES**



## **1. CONCLUSIONS**

In this thesis, we have attempted to design and fabricate plasmonic nanodevices via bottom-up self-assembly of various branched gold nanostructures and investigate their ability to guide the light at the nanoscale.

In Chapter 1, we reviewed the plasmonic concepts relevant for this work, as well as the recent developments in light guiding and optical addressing via metallic nanostructures. We have performed FDTD simulations to investigate the selective routing of electromagnetic pulse through a branched gold nanostructure. We showed that the active control over the plasmonic response could be achieved through the use of Y-shape gold nanostructure overfilled with anisotropic material.

In Chapter 2, we have described common bottom-up techniques to synthesize several types of plasmonic nanoparticles used as building blocks for the plasmonic nanodevice fabrication. In particular, gold nanorods, silver nanoprisms, gold hollow triangles, and PdCu@Au core-shell tripods were synthesized in a high yield, quality, monodispersity and consequential spectral tunability of their optical properties.

In Chapter 3, we have successfully demonstrated the multistep synthesis of new organic molecules with trigonal planar molecular geometry, high rigidity and terminal groups able to interact with the metallic NPs. We used them as linkers to assemble gold nanorods into nanoarchitectures with well-defined Y-shaped geometry, namely NRs trimers. First developed strategy was based on covalent cross-linking of the three AuNRs via the thiol groups at the periphery of the linker molecule. Assembled AuNRs trimers were characterized by TEM. In addition, the optical properties of the fabricated trimers were studied, showing a near-field coupling effect between the linked nanorods. However, the trimers were fabricated in a relatively low yield and were not uniform in their morphology. Thus, we developed an alternative approach where three-branched assemblers containing peripheral long alkyl chains were used to establish hydrophobic attractions with the polymer chains grafted on the AuNRs tips. However, this strategy did not give the expected result, as we observed the formation of AuNRs clusters contacting several AuNRs. The next step of this work is to improve the low yield of trimer formation by synthesizing organic linkers with more numerous and longer

branches, in order to incorporate those assemblies into devices that can take benefit of their optical properties.

In Chapter 4, we showed that DNA origami can be used as a fully addressable template to spatially organize gold hollow nanotriangles and fluorescent molecules into a functional nanodevice. This approach was developed as an alternative approach for the nanodevice fabrication where the main plasmonic building block, well-defined Y-shaped geometry nanoarchitecture (AuNRs trimer), was replaced by gold hollow triangles deposited on the DNA origami template containing fluorescent dyes. Fluorescent dyes were placed in the close proximity of each tip of the hollow triangles, and the fabricated nanostructures were used to study the propagation of EM energy along their different branches. We succeeded in selectively exciting fluorescent dye located near one tip of the gold triangles, which consequently excited the gold nanostructure and caused the EM energy propagation along it. By studying the fluorescent signals emitted by the dyes located near the two other tips of the hollow triangles, we demonstrated the plasmon enhanced energy transfer in the nanodevice. However, the photobleaching of the dyes is the most challenging hurdle that has to be overcome in order to fully exploit the optical properties of such nanostructure for applications in nanophotonic integrated circuits.

Compared to the nanodevice that uses AuNRs trimers as main branched building blocks, the approach based on DNA origami has several advantages. First, gold hollow nanotriangles are easier to synthesize, compared to the organic rigid, branched assemblers with complex structures. Second, the programmed synthesis and modification of DNA origami provides the accurate positioning of gold structures and fluorophores with the precision of a nanometer. Thus, future work will be focused on the use of modified DNA origami to assemble different branched plasmonic nanoarchitectures and fluorophores into functional nanodevices able to direct and route the light at the nanoscale.

## **2. PERSPECTIVES**

### **2.1. Fabrication of a plasmonic switching device based on a DNA origami template**

As we synthesized nanoarchitectures composed of gold hollow nanotriangles and fluorescent dyes assembled via rectangular DNA origami and confirmed the plasmon enhanced energy

transfer in them, we aim to further improve this work by studying the selective routing of light in such nanostructure. More work must be performed by inducing perturbations in the electromagnetic field around one branch of a nanotriangle, which could favor the selective EM energy propagation towards another branch and consequently enhance the light emission of the emitter located close to the tip of another branch. The perturbations can be caused by one gold nanoparticle located near one of the branches of the gold hollow triangle. For that purpose, we aim to introduce two small gold nanoparticles in the fabricated passive plasmonic nanodevice, turning it into an active switching device. The scheme of such device is shown in Figure 1. Two gold NPs are coated by dsDNA and attached to the DNA origami such as one NP is close to one branch of the nanotriangle (the so-called OFF position) and the other one is far from another branch of the nanotriangle (the so-called ON position). The track between ON and OFF positions is specifically designed to ensure the directional displacement of the NPs between them (see colored lines in Figure 1). Through the sequential addition of blocking and removal strands in the appropriate order, one can promote the displacement of one gold NP from the ON position to the OFF position, while the other gold NP moves from OFF to ON locations [1]. Such process is reversible and thus offers a way to switch the plasmonic signal between the two possible pathways in the branched nanostructure.



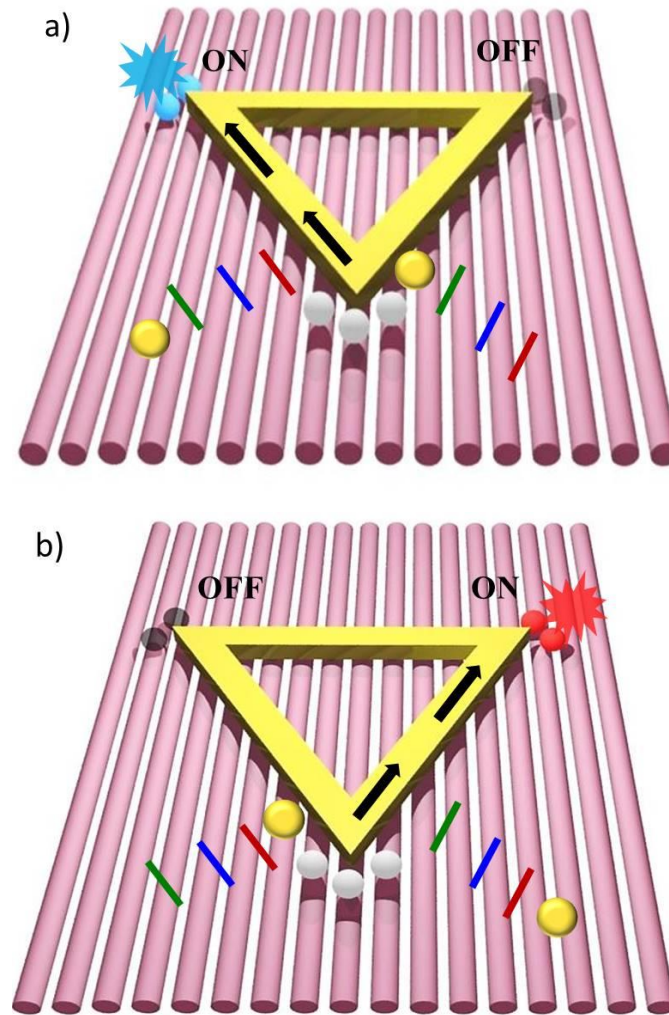


**Figure 1 : Schematic illustration of a plasmonic switching device: spherical AuNPs can be reversibly localized from OFF to ON positions through the addition of complementary ssDNA, favoring the selective light propagation by near-field coupling. a) NP near the left branch is in ON position, while the NP near the right branch is in OFF position, favoring the selective light propagation and the consequential excitation of the dye located near the tip of the left branch of a hollow triangle. b) NP near the left branch is in OFF position, while the NP near the right branch is in ON position, favoring the selective light propagation and the consequential excitation of the dye located near the tip of the right branch of a hollow triangle.**

## **2.2. Fabrication of a plasmonic switching device by surface plasmon-triggered two-photon polymerization**

Another approach to fabricate the target plasmonic switching nanodevice was initiated in collaboration with Professor R. Bachelot from the University of Technology of Troyes.

In their previous work, Bachelot and co-workers [2] fabricated multicolor nanoemitters and selected the dominant emission wavelength by varying the polarization of the incident light. The scheme of a nanoemitter is shown in Figure 2 a. Nanoemitters were fabricated via surface plasmon-triggered two-photon polymerization (TPP). In such process, laser pulses initiate two-photon absorption and subsequent polymerization in an extremely localized focal volume. Typically, the polymerization is induced when the exposure energy dose exceeds a given threshold ( $D_{th}$ ). In the case of plasmonic near-field TPP, the electromagnetic field enhanced by surface plasmons is used to induce the polymerization reaction. In that case, an exposure dose below the  $D_{th}$  is used to guarantee the selective polymerization in the close vicinity of the nanostructures via surface plasmons, which enhance the dose of the electromagnetic field that locally exceeds the polymerization threshold.

In their experiment, Bachelot and co-workers used gold nanodisks with highly symmetric geometry in the XY plane and polymerizable solutions that contained two different types of QDs, ones that emit in the green and the others emitting in the red. Firstly, they performed a polymerization along the X axis to position green QDs in the X direction. Figure 2 b shows the polymer along the X axis in the vicinity of the nanodisk, as a replica of the dipolar near-field intensity. Then, they exposed the same structure to a light with an incident polarization oriented along the Y axis, resulting in the selective polymerization of the red QD-grafted solution, as shown in Figure 2 c.

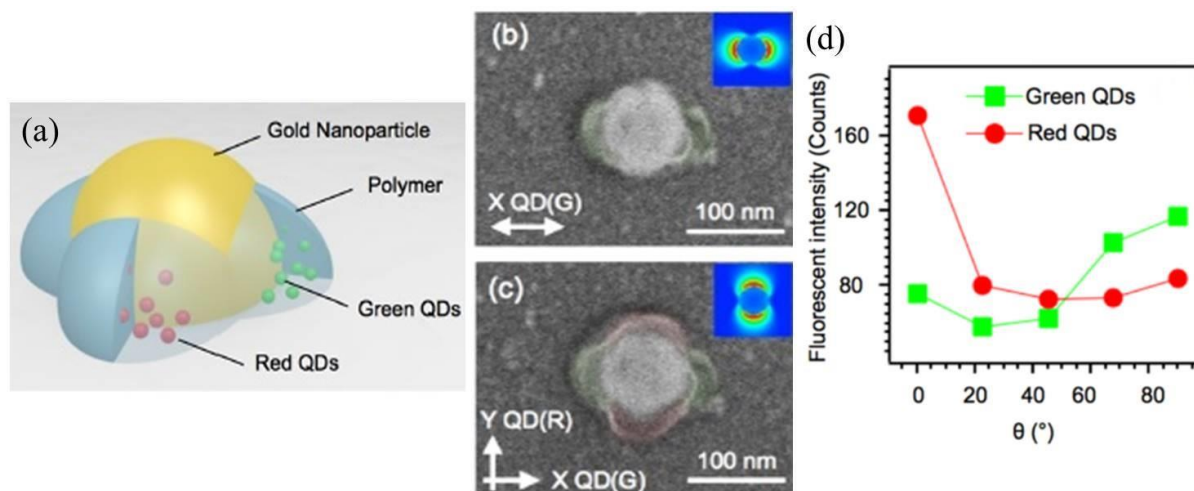


**Figure 2 :** a) Schematic illustration of a hybrid two-color nanoemitter; b,c) SEM images of an Au nanodisk after the first exposure that positions green QDs along the X axis and the second exposure that trapped red QDs along the Y axis. Insets show the plasmonic near- field intensity of dipole emission; d) Intensities of emission peaks of the green and red QDs as a function of the polarization angle [2].

Following the same principle, we aim to fabricate nanoemitters composed of branched gold building blocks (i.e. gold tripods or gold hollow triangles) and fluorescent dyes trapped in the photopolymer. In such architectures, the photopolymerization is triggered by the electromagnetic field concentrated near the nanostructures tips. To experimentally confirm the design of the hybrid nanoemitter, we started the fabrication of a nanoarchitecture composed of a gold tripod and a fluorescent dye (Rhodamine 6G) trapped in polymer that is precisely positioned on the tips of the tripod. The scheme of the structure is shown in Figure 3.

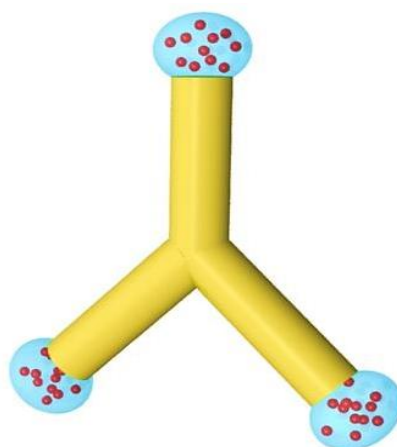


**Figure 3 :** A schematic illustration of a hybrid single-color nanoemitter.

The polymerizable solution was made of titanocene (1%) and Rhodamine 6G dissolved in pentaerythritol triacrylate (PETIA, 99%). Titanocene, which was used as photoinitiator, was excited by a laser operating at  $\lambda = 532$  nm. The wavelength was selected in order to match the absorption of the initiator, which is typically up to 560 nm [3]. Upon the photopolymerization, the Rhodamine is trapped inside the acrylic polymer.

In order to achieve the selective polymerization at the tips of the nanostructure, triggered by the plasmon-enhanced field, the energy threshold had to be determined. It represents the lowest energy that allows the photopolymerization of the monomer on a glass substrate without the presence of metal nanoparticles. Thus, a set of experiments was performed in the absence of any metallic nanostructure to obtain the ideal condition for the photopolymerization process.

The laser power was increased while the exposure time was kept constant at 1 s, resulting in an increase of the polymer spot diameter (Figure 4). Thus, the obtained results have narrowed down the threshold range to  $246.02 \text{ mJ/cm}^2 - 276.67 \text{ mJ/cm}^2$ . However, to obtain the exact energy threshold, more experiments have to be performed before starting the fabrication of a gold tripod nanoemitter based on near-field polymerization triggered by field enhancement.

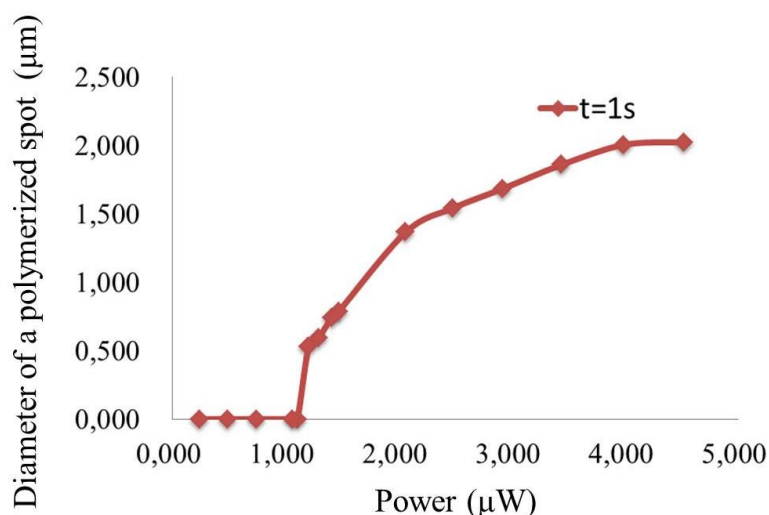


**Figure 4 : Threshold determination by increasing the laser power, while the exposure time is kept constant at 1 seconde.**

Moreover, the experiments performed on the polymerizable solution containing titanocene/Rhodamine/PETIA showed that there is a significant photobleaching of

Rhodamine, which loses its fluorescence after 3 seconds of light exposure. Thus, this problem has to be overcome, possibly by replacing the dye with quantum dots.

Further studies to determine the energy threshold and to overcome the photobleaching are thus necessary to establish the control over the plasmonic near-field TPP.

Once all the parameters will be optimized, we hope to apply this knowledge to the fabrication of a hybrid two-color nanoemitter, shown in Figure 5. By changing the incident polarization, we aim to accurately polymerize the two solutions containing dyes or QDs that emit two different colors, at the different tips of a branched nanostructure. However, the most challenging hurdle is to promote the path selectivity of light by using such nanoarchitectures. In the future work, we will immerse the fabricated nanodevice into an anisotropic molecular medium with molecular polarization direction oriented toward one branch. Upon the local excitation of one tip of the structure, the selective light propagation through the branch oriented parallel to the molecular dipoles could enhance the light emission of the emitters localized near to its tip, potentially producing a switchable plasmonic nanoemitter with extensive applications in nanophotonics.

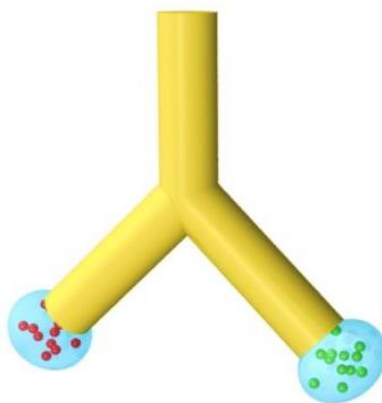


**Figure 5 : A schematic illustration of a hybrid multi-color nanoemitter.**

**REFERENCES**

- [1] C. Zhou, X. Duan, and N. Liu, “A plasmonic nanorod that walks on DNA origami,” *Nat. Commun.*, vol. 6, p. 8102, 2015.
- [2] X. Zhou, J. Wenger, F. N. Viscomi, L. Le Cunff, J. Béal, S. Kochtcheev, X. Yang, G. P. Wiederrecht, G. Colas Des Francs, A. S. Bisht, S. Jradi, R. Caputo, H. V. Demir, R. D. Schaller, J. Plain, A. Vial, X. W. Sun, and R. Bachelot, “Two-Color Single Hybrid Plasmonic Nanoemitters with Real Time Switchable Dominant Emission Wavelength,” *Nano Lett.*, vol. 15, no. 11, pp. 7458–7466, 2015.
- [3] N. Davidenko, O. Garcia, and R. Sastre, “The efficiency of titanocene as photoinitiator in the polymerization of dental formulations,” *J. Biomater. Sci. Ed.*, vol. 14, no. 7, pp. 733–746, 2003.



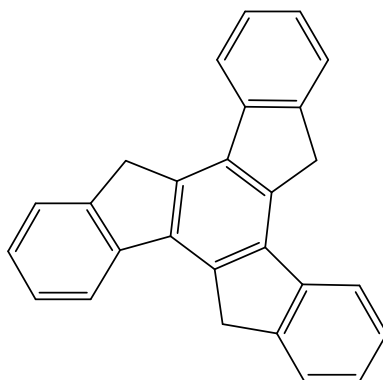
## **ANNEXES**





## ANNEX 1: SYNTHESIS OF THE ORGANIC ASSEMBLERS I-IV

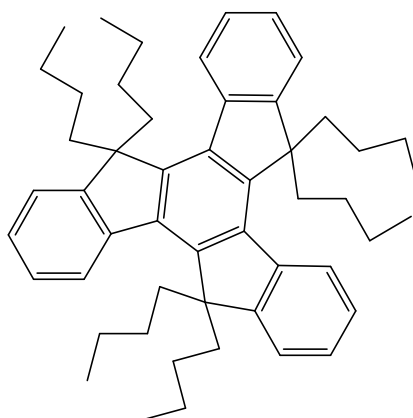
- Synthesis of synthons



**5H-Tribenzo[*a,f,k*] trindene, 10,15-dihydro- (1).** 1-indanone (5.00 g, 37.83 mmol) was dissolved in a mixture of acetic acid (22 mL) and hydrochloric acid (11 mL)[1]. The mixture was kept under stirring for 15 h at 100 °C, then cooled to room temperature and poured onto ice, filtered under suction and washed with water and acetone. Finally, the product was recrystallized in toluene, affording **1** as a light brown solid (10.80 g).

**Yield:** 84 %

**<sup>1</sup>H NMR (300 MHz, CDCl<sub>3</sub>):** δ 7.94 (d, 3H), 7.69 (d, 3H), 7.50 (t, 3H), 7.40 (t, 3H) 4.24 (s, 6H).

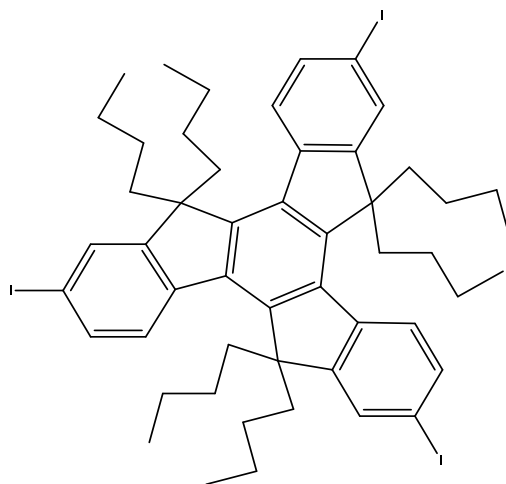


**5,5,10,10,15,15-hexabutyltruxene (2).** To a solution of **1** (1.00 g, 2.92 mmol) in THF (5mL), n-butyllithium (0.65 g, 10.22 mmol) was added at 0 °C. The low temperature was maintained

for 30 min. 1-bromobutane (2.00 g, 14.60 mmol) was then added and the mixture was stirred at the room temperature during 4h. The reaction mixture was cooled down to 0°C, then second portions of the same quantities of n-butyllithium and 1-bromobutane were added and the stirring was continued for 12 h[2]. The solvent was then evaporated and the oily crude residue was extracted with DCM. The organic extracts were collected, dried over Na<sub>2</sub>SO<sub>4</sub> and concentrated under vacuum. The crude solid was purified by flash chromatography (SiO<sub>2</sub>, petroleum ether) to afford **2** as a yellow solid (1.13 g).

**Yield:** 57 %

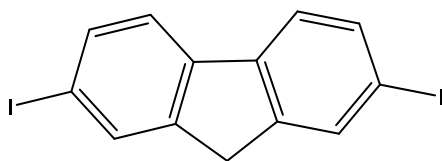
**<sup>1</sup>H NMR (300 MHz, CDCl<sub>3</sub>):** δ 8.37 (d, 3H), 7.47 - 7.44 (m, 3H), 7.42 – 7.33 (m, 6H), 3.02 – 2.93 (m, 6H), 2.14- 2.05 (m, 6H), 0.96 – 0.78 (m, 12H), 0.58 – 0.37 (m, 30H).



**2,7,12-triiodo-5,5,10,10,15,15-hexabutyltruxene (3).** Compound **2** (0.20 g, 0.29 mmol) was dissolved in a mixture of acetic acid (10 mL), sulfuric acid (0.5 mL), water (2 mL) and carbon tetrachloride (0.8 mL) and the mixture was heated to 40°C. When iodic acid (0.05 g, 0.32 mmol) and I<sub>2</sub> (0.11 g, 0.44 mmol) were added to the mixture, the temperature was increased to 80 °C and the mixture was stirred for 12 h[2]. The mixture was then allowed to cool down to room temperature and filtered under suction. The residue was refluxed in methanol for 2 h, cooled down to room temperature and filtered under suction. Finally, the crude residue was purified by flash chromatography (SiO<sub>2</sub>, 5% DCM in petroleum ether) to obtain **3** as a white solid (0.16 g).

**Yield:** 51 %

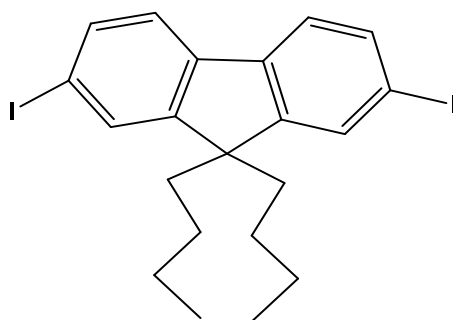
**<sup>1</sup>H NMR (300 MHz, CDCl<sub>3</sub>):** δ 8.13 – 7.33 (m, 9H), 3.02 – 2.93 (m, 6H), 2.14- 2.05 (m, 6H), 0.96 – 0.78 (m, 12H), 0.58 – 0.37 (m, 30H).



**2,7-diiodo-9H-fluorene (4).** A solution of fluorene (10.00 g, 60.20 mmol) in acetic acid (100 ml), sulfuric acid (1.4 ml) and water (4 ml) was heated to 75 °C. I<sub>2</sub> (10.54 g, 41.50 mmol) and periodic acid (6.50 g, 28.50 mmol) were then added and the resulting dark purple solution was kept under stirring during 4 h at 75 °C[3]. The reaction mixture was cooled down to room temperature, filtered under suction and washed with aqueous solution of KOH, water, saturated aqueous solution of Na<sub>2</sub>S<sub>2</sub>O<sub>3</sub> and petroleum ether. The brown powder was recrystallized in cyclohexane (100 mL), filtered under suction and washed with pentane to afford **4** as a brown solid (20.38 g).

**Yield:** 81 %

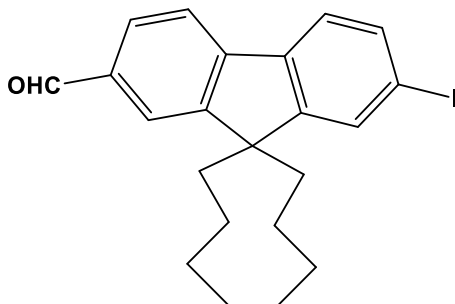
**<sup>1</sup>H NMR (300 MHz, CDCl<sub>3</sub>):** δ 7.88 (s, 2H), 7.70 (d, 2H), 7.50 (d, 2H), 3.84 (s, 2H).



**9,9-dibutyl-2,7-diiodo-9H-fluorene (5).** Tetra-*n*-butylammonium bromide (0.77 g, 2.39 mmol) was added to the solution of potassium hydroxide (6.71 g, 119.60 mmol) in water (10 mL) and the mixture was stirred for 15 min. Fluorene derivative **4** (5.00 g, 11.96 mmol) and dry toluene (16 mL) were then added and the mixture was stirred for 2 min. Finally *n*-butyl bromide (9.83 g, 71.76 mmol) was added dropwise and the reaction mixture was stirred for 36 h[3]. After extraction with DCM and washing with water and saturated sodium chloride brine, the solution was evaporated to dryness. Dark crude was further purified by flash chromatography (SiO<sub>2</sub>, 5% DCM in petroleum ether) to obtain **5** as a pale yellow solid (5.00 g).

**Yield:** 78 %

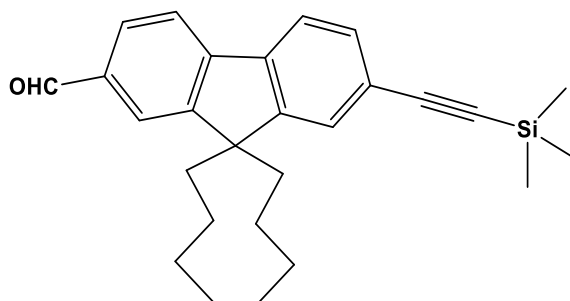
$^1\text{H NMR}$  (300 MHz,  $\text{CDCl}_3$ ):  $\delta$  7.66 (d, 4H), 7.41 (d, 2H), 1.93-1.87 (m, 4H), 1.13-1.03 (m, 4H), 0.69 (t, 6H), 0.61-0.51 (m, 4H).



**9,9-dibutyl-7-iodo-9H-fluorene-2-carbaldehyde (6).** A 1.6 M solution of n-butyl lithium in hexane (0.26 g, 4.15 mmol) was added dropwise to a stirred solution of fluorene derivative **5** (2.00 g, 3.77 mmol) in dry THF (25 ml) at  $-78^\circ\text{C}$  under argon. The mixture was stirred during 1 h before dry DMF (0.41 g, 5.66 mmol) was added dropwise. The mixture was then allowed to warm up to room temperature and stirred for 12 h[4]. The reaction was quenched with 5% HCl and the solution was extracted with diethyl ether. The organic liquid was washed with water and brine, dried over  $\text{Na}_2\text{SO}_4$  and concentrated under vacuum. The crude product was purified by flash chromatography ( $\text{SiO}_2$ , 50 % DCM and 50 % petroleum ether) to afford **6** as a white solid (0.34 g).

**Yield:** 39 %

$^1\text{H NMR}$  (300 MHz,  $\text{CDCl}_3$ ):  $\delta$  10.05 (s, 1H), 7.87-7.79 (m, 3H), 7.72 (d, 2H), 7.51 (d, 1H), 2.08-1.90 (m, 4H), 1.13-1.03 (m, 4H), 0.67 (t, 6H), 0.61-0.47 (m, 4H).

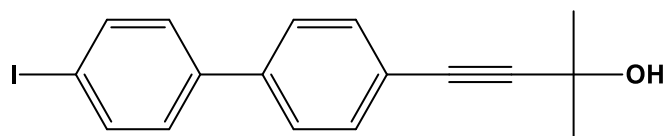


**9,9-dibutyl-7-((trimethylsilyl)ethynyl)-9H-fluorene-2-carbaldehyde (7).** Air was removed from the solution of **6** (0.40 g, 0.93 mmol) and triethylamine (2 mL) in dry THF (8 ml) by argon bubbling for 15 min. Then  $\text{Pd}(\text{PPh}_3)_2\text{Cl}_2$  (0.03 g, 0.04 mmol) and CuI (0.008 g, 0.04 mmol) were added, and argon bubbling was continued for 5 min before ethynyltrimethylsilane

(0.40 g, 4.16 mmol) was added dropwise in the solution. When the addition was complete, the reaction mixture was heated up to 70 °C and kept under stirring for 15 h[5]. The mixture was then poured onto ice/water mixture, extracted with ethyl acetate, dried over Na<sub>2</sub>SO<sub>4</sub> and concentrated under vacuum. The crude product was dissolved in a mixture of petroleum ether and ethyl acetate (3:2 v/v) and filtered through short silica gel plug affording **7** (0.26 g) as a brown solid.

**Yield:** 70 %

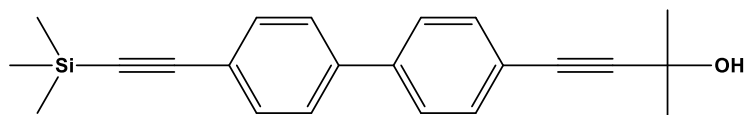
**<sup>1</sup>H NMR (300 MHz, CDCl<sub>3</sub>):** δ 10.06 (s, 1H), 7.87-7.79 (m, 3H), 7.70 (d, 1H), 7.51 -7.46 (m, 2H), 1.29-1.22 (m, 4H), 0.89-0.82 (m, 5H), 0.65 (t, 6H), 0.55-0.50 (m, 3H), 0.29 (s, 9H).



**4-(4'-iodo-[1,1'-biphenyl]-4-yl)-2-methylbut-3-yn-2-ol (8).** Air was removed from a solution of 4,4'-diiodobiphenyl (2.00 g, 4.93 mmol), 2-methyl-3-butyn-2-ol (0.41 g, 4.93 mmol) and triethylamine (2 mL) in dry THF (8 ml) by argon bubbling for 20 min. Pd(PPh<sub>3</sub>)<sub>2</sub>Cl<sub>2</sub> (0.069 g, 0.098 mmol) and CuI (0.018 g, 0.098 mmol) were then added and the solution was kept under stirring for 15 h. The reaction was quenched with NH<sub>4</sub>Cl and the solution was extracted with diethyl ether. The organic liquid was dried over anhydrous Na<sub>2</sub>SO<sub>4</sub> and concentrated under vacuum. The crude product was purified by flash chromatography (SiO<sub>2</sub>, DCM in a gradient 30-50% in petroleum ether) to afford **8** as a light brown solid (0.99 g).

**Yield:** 56 %

**<sup>1</sup>H NMR (300 MHz, CDCl<sub>3</sub>):** δ 7.76 (d, 2H), 7.49 (s, 4H), 7.32 (d, 2H), 2.02 (s, 1H), 1.64 (s, 6H).

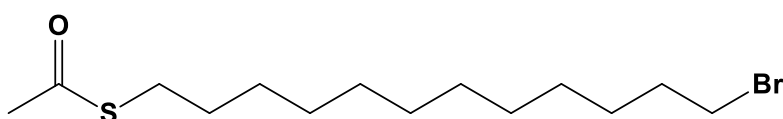


**2-methyl-4-(4'-((trimethylsilyl)ethynyl)-[1,1'-biphenyl]-4-yl)but-3-yn-2-ol (9).** Air was removed from a solution of **8** (0.48 g, 1.33 mmol) and ethynyltrimethylsilane (0.19 g, 1.99 mmol) in dry THF (8 ml) and trimethylamine (2 mL) by argon bubbling for 20 min.

$\text{Pd}(\text{PPh}_3)_2\text{Cl}_2$  (0.023 g, 0.033 mmol) and  $\text{CuI}$  (0.009 g, 0.046 mmol) were added and the reaction mixture was kept under stirring for 15 h. The suspension was then evaporated to dryness and the residue was diluted with diethyl ether and filtered over celite<sup>®</sup>. The obtained product was further purified by flash chromatography ( $\text{SiO}_2$ , 5% diethyl ether in DCM) affording **9** as a white solid (0.29 g).

**Yield:** 67 %

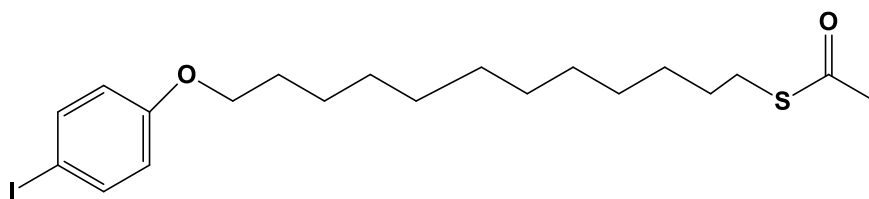
**$^1\text{H}$  NMR (300 MHz,  $\text{CDCl}_3$ ):**  $\delta$  7.53-7.46 (m, 8H), 2.03 (s, 1H), 1.64 (s, 6H), 0.26 (s, 9H).



**S-(12-bromododecyl) ethanethioate (10).** A mixture of 1,12-dibromododecane (5.00 g, 15.24 mmol) and potassium thioacetate (1.74 g, 15.24 mmol) in dry THF (100 mL) was stirred 6 h at room temperature[6]. After extraction with diethyl ether and washing with water and brine, the product was purified by flash chromatography ( $\text{SiO}_2$ , petroleum ether/ethyl acetate mixture from 30/1 to 10/1 ratio) to afford **10** as a white solid (2.04 g).

**Yield:** 41 %

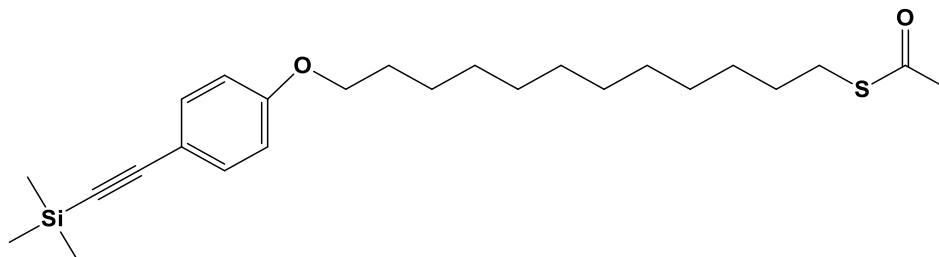
**$^1\text{H}$  NMR (300 MHz,  $\text{CDCl}_3$ ):**  $\delta$  3.44 (t,  $J=6.9\text{Hz}$ , 2H), 2.89 (t,  $J=7.3\text{Hz}$ , 2H), 2.35 (s, 3H), 1.88 (m, 2H), 1.59 (m, 2H), 1.30(m, 16H).



**S-(12-(4-iodophenoxy)dodecyl) ethanethioate (11).** Bromothioester **10** (2.13 g, 6.6 mmol), 4-iodophenol (1.45 g, 6.6 mmol) and potassium carbonate (2.00 g, 14.5 mmol) were dissolved in DMF (10 mL) and the mixture was stirred at room temperature for 16 h. The suspension was extracted with DCM and washed several times with water. After evaporation of the solvent, the residue was purified by flash chromatography ( $\text{SiO}_2$ , 2 % ethyl acetate in petroleum ether). Finally, the product was recrystallized in heptane affording **11** as a white solid (1.70 g).

**Yield:** 56 %

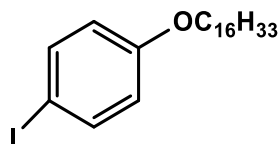
**<sup>1</sup>H NMR (300 MHz, CDCl<sub>3</sub>):** δ 7.58 (d, J=8.8Hz, 2H), 6.71 (d, J=8.8Hz, 2H), 3.94 (t, J=6.5Hz, 2H), 2.90 (t, J=7.3Hz, 2H), 2.36 (s, 3H), 1.80 (m, 2H), 1.60 (m, 2H), 1.30(m, 16H).



**S-(12-(4-((trimethylsilyl)ethynyl)phenoxy)dodecyl) ethanethioate (12).** Air was removed from a solution of 4-iododerivative **11** (1.50 g, 3.24 mmol), ethynyltrimethylsilane (0.40 g, 4.07 mmol) and trimethylamine (2 mL) in dry THF (10 ml) by argon bubbling for 20 min. Pd(PPh<sub>3</sub>)<sub>2</sub>Cl<sub>2</sub> (0.04 g, 0.057 mmol) and CuI (0.012 g, 0.063 mmol) were added and the reaction mixture was stirred for 16 h. The solvents were then evaporated and the residue was purified by flash chromatography (SiO<sub>2</sub>, 2 % ethyl acetate in petroleum ether) to afford **12** as a pale yellow solid (1.22 g).

**Yield:** 87 %

**<sup>1</sup>H NMR (300 MHz, CDCl<sub>3</sub>):** δ 7.42 (d, J=8.7Hz, 2H), 6.84 (d, J=8.7Hz, 2H), 3.98 (t, J=6.5Hz, 2H), 2.90 (t, J=7.3Hz, 2H), 2.36 (s, 3H), 1.80 (m, 2H), 1.59 (m, 2H), 1.30(m, 16H), 0,27 (s, 9H).

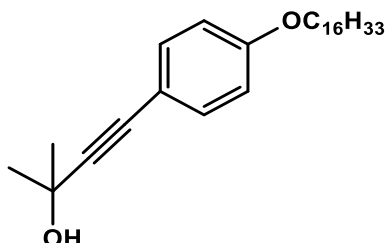


**1-(hexadecyloxy)-4-iodobenzene (13).** A mixture of 4-iodophenol (2.20 g, 10.00 mmol), 1-bromohexadecane (2.90 g, 9.50 mmol), sodium iodide (0.15 g, 1.00 mmol) and potassium carbonate (2.50 g, 18.00 mmol) in dry DMF (20mL) was heated at 50°C and kept under stirring for 15 h. The solution was extracted with diethyl ether and washed several times with water. After evaporation of solvents, the residue was purified by flash chromatography (SiO<sub>2</sub>, petroleum ether) to obtain **13** as a white solid (3.55 g).



**Yield:** 89 %

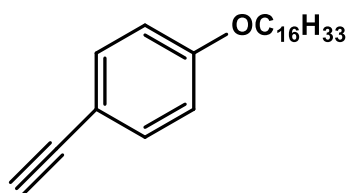
**<sup>1</sup>H NMR (300 MHz, CDCl<sub>3</sub>):** δ 7.58 (d, J=8.9Hz, 2H), 6.71 (d, J=8.9Hz, 2H), 3.95 (t, J=6.6Hz, 2H), 1.80 (m, 2H), 1.47 (m, 2H), 1.30 (m, 26H), 0.92 (t, J=6.7Hz, 6H).



**4-(4-(hexadecyloxy)phenyl)-2-methylbut-3-yn-2-ol (14).** A mixture of 4-iododerivative **13** (2.1 g, 5.0 mmol), 2-methylbutyn-2-ol (0.63 g, 7.48 mmol) and trimethylamine (3 mL) in dry toluene (15 mL) was degassed by argon bubbling for 20 min. CuI (0.018 g, 0.094 mmol) and Pd(PPh<sub>3</sub>)<sub>2</sub>Cl<sub>2</sub> (0.080 g, 0.11 mmol) were then added and the reaction mixture was stirred at 50°C for 16 h. The suspension was then evaporated to dryness and the residue was purified by flash chromatography (SiO<sub>2</sub>, 50 % DCM and 50 % petroleum ether) to obtain **14** as a white solid (1.74 g).

**Yield:** 87 %

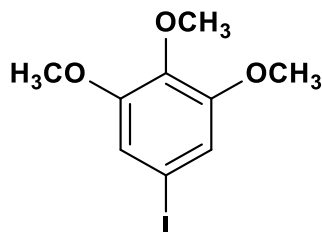
**<sup>1</sup>H NMR (300 MHz, CDCl<sub>3</sub>):** δ 7.37 (d, J=8.6Hz, 2H), 6.85 (d, J=8.6Hz, 2H), 3.98 (t, J=6.5Hz, 2H), 1.80 (m, 2H), 1.65 (s, 6H), 1.47 (m, 2H), 1.30 (m, 26H), 0.92 (t, J=6.7Hz, 6H).



**1-ethynyl-4-(hexadecyloxy)benzene (15).** Sodium hydroxide (0.17 g, 4.25 mmol) and **14** (1.60 g, 4.00 mmol) were dissolved in toluene (24 mL) and isopropyl alcohol (8 mL) and the mixture was refluxed for 90 min. The solution was then evaporated to dryness, extracted with DCM and filtered through a short silica gel plug. The residue was further purified by flash chromatography (SiO<sub>2</sub>, 5% DCM in petroleum ether), affording **15** as a white solid (1.16 g).

**Yield:** 79 %

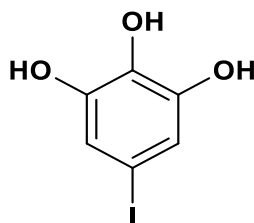
$^1\text{H NMR}$  (300 MHz,  $\text{CDCl}_3$ ):  $\delta$  7.45 (d,  $J=8.8\text{Hz}$ , 2H), 6.87 (d,  $J=8.8\text{Hz}$ , 2H), 3.99 (t,  $J=6.6\text{Hz}$ , 2H), 3.03 (s, 1H), 1.81 (m, 2H), 1.49 (m, 2H), 1.30 (m, 26H), 0.92 (t,  $J=6.7\text{Hz}$ , 6H).



**5-iodo-1,2,3-trimethoxybenzene (16).** A solution of sodium nitrite (28.50 g, 0.41 mol) in water (45 mL) was slowly added to a suspension of 3,4,5-trimethoxyaniline (7.50 g, 41.00 mmol) in water (90 mL) and sulfuric acid (6 mL) placed in an ice bath. Temperature was maintained between  $-5^\circ\text{C}$  and  $0^\circ\text{C}$ . The obtained diazonium salt was then added to a solution of potassium iodide (10.5 g, 36.25 mmol) in water (23 mL) under vigorous stirring at  $50^\circ\text{C}$ [7]. When the addition was complete, the mixture was stirred for 30 min more before cooling down to room temperature. An aqueous solution of sodium sulfite was added to neutralize the excess of iodine until no further color change was observed. The mixture was extracted with diethyl ether, washed with brine, dried over  $\text{Na}_2\text{SO}_4$  and concentrated under vacuum. The crude was filtered through a short silica gel plug eluting with a mixture of DCM (50%) and petroleum ether (50%) to obtain pale yellow crystals (7.07 g).

**Yield:** 59 %

$^1\text{H NMR}$  (300 MHz,  $\text{CDCl}_3$ ): 6.93 (s, 2H), 3.88 (s, 6H), 3.86 (s, 3H).

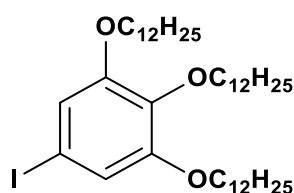


**5-iodobenzene-1,2,3-triol (17).** Solution of **16** (6.00 g, 20.4 mmol) in dry DCM (100 mL) was cooled down to  $-78^\circ\text{C}$ . Boron tribromide (5.80 mL, 61.00 mmol) was then added slowly in the solution under argon. The mixture was allowed to warm up to the room temperature and stirred for 24 h. Then, the reaction mixture was poured onto ice-water (100 mL) and stirred

for 30 min. After the extraction with ethyl acetate (3 x 100 mL), the organic liquid was washed with aqueous  $\text{Na}_2\text{SO}_3$ , dried over  $\text{Na}_2\text{SO}_4$  and concentrated under vacuum to give a brown oil that crystallizes with addition of hexane. The product **17** was obtained as a pale cream solid (4.47 g).

**Yield:** 87 %

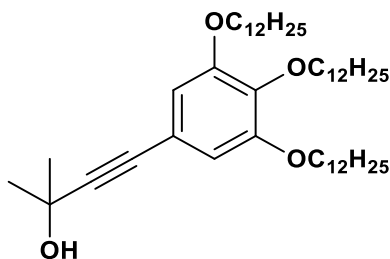
**$^1\text{H}$  NMR (300 MHz, DMSO- $d_6$ ):**  $\delta$  9.03 (s, 3H), 6.54 (s, 2H).



**1,2,3-tris(dodecyloxy)-5-iodobenzene (18).** 5-Iodo-1,2,3-trihydroxybenzene (2.52 g, 10.00 mmol) was dissolved in DMF (30 mL) and the solution was degassed by argon bubbling for 20 min. Potassium carbonate (11.00 g, 80.00 mmol), 1-bromododecane (11.20 g, 45.00 mmol) and potassium iodide (0.166 g, 1.00 mmol) were then added and the mixture was stirred at  $60^\circ\text{C}$  for 7 h. After cooling down, the brown crude solid was filtered and washed with ice-cold water. The residue was purified by flash chromatography ( $\text{SiO}_2$ , 25% DCM in petroleum ether) to obtain **18** as a white solid (6.25 g).

**Yield:** 83 %

**$^1\text{H}$  NMR (300 MHz,  $\text{CDCl}_3$ ):**  $\delta$  6.88 (s, 2H), 3.95 (m, 6H), 1.79(m, 6H), 1.49 (m, 6H), 1.30 (m, 48H), 0.92 (t,  $J=6.7\text{Hz}$ , 9H).

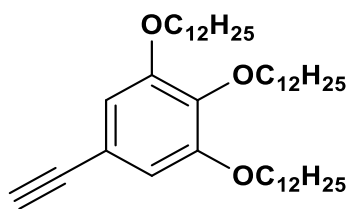


**2-methyl-4-(3,4,5-tris(dodecyloxy)phenyl)but-3-yn-2-ol (19).** A mixture of **18** (3.78 g, 5.00 mmol), 2-methylbutyn-2-ol (0.63 g, 7.48 mmol) and trimethylamine (3 mL) in dry toluene (15 mL) was degassed by argon bubbling for 20 min.  $\text{CuI}$  (0.018 g, 0.094 mmol) and  $\text{PdCl}_2(\text{PPh}_3)_2$  (0.060 g, 0.085 mmol) were then added and the reaction mixture was kept under

stirring at 50°C for 16 h. Solvents were evaporated and the residue was filtered through a short silica gel plug eluting with DCM. The product was further purified by flash chromatography on silica using a mixture of DCM in petroleum ether (increasing DCM from 5 to 50 % v/v), affording **19** as a white solid (2.88 g).

**Yield:** 81 %

**<sup>1</sup>H NMR (300 MHz, CDCl<sub>3</sub>):** δ 6.65 (s, 2H), 3.98 (t, J=6.6Hz, 6H), 2.04(s, 1H), 1.83 (m, 6H), 1.65 (s, 6H), 1.49 (m, 6H), 1.30 (m, 48H), 0.92 (t, J=6.7Hz, 9H).

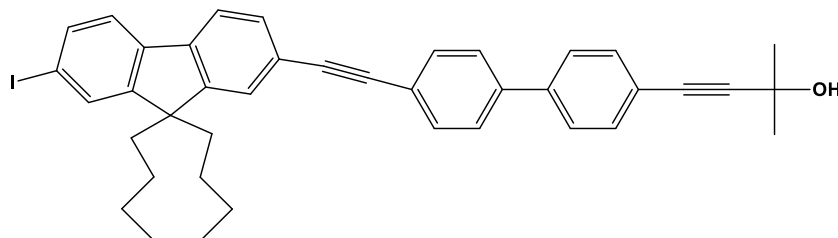


**1,2,3-tris(dodecyloxy)-5-ethynylbenzene (20).** Sodium hydroxide (0.13 g, 3.25 mmol) and **19** (2.14 g, 3.00 mmol) were dissolved in toluene (18 mL) and isopropyl alcohol (6 mL) and the mixture was refluxed for 2 h. The solution was then evaporated to dryness, extracted with DCM and filtered through a short silica gel plug. The residue was further purified by flash chromatography (SiO<sub>2</sub>, 20% DCM in petroleum ether), affording **20** as a white solid (1.37 g).

**Yield:** 71 %

**<sup>1</sup>H NMR (300 MHz, CDCl<sub>3</sub>):** δ 6.73 (s, 2H), 3.99 (m, 6H), 3.03(s, 1H), 1.82 (m, 6H), 1.49 (m, 6H), 1.30 (m, 48H), 0.92 (t, J=6.7Hz, 9H).

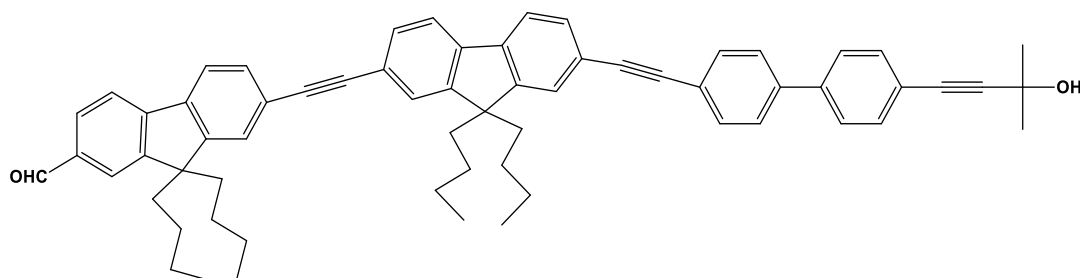
- **Assembly of the different moieties**



**4-(4'-((9,9-dibutyl-7-iodo-9H-fluoren-2-yl)ethynyl)-[1,1'-biphenyl]-4-yl)-2-methylbut-3-yn-2-ol (21).** Air was removed from a solution of **9** (0.12 g, 0.36 mmol) and **5** (0.57 g, 1.08 mmol) in THF 6 mL) and Et<sub>3</sub>N (0.5 mL) by argon bubbling for 20 min. Then [Pd(PPh<sub>3</sub>)<sub>2</sub>Cl<sub>2</sub>] (7.50 mg, 0.01 mmol) and CuI (2.06 mg, 0.01 mmol) were added and argon bubbling was continued for 5 min. *Tetra-*n*-butylammonium* fluoride (TBAF) (0.39 mL, 1.0 M in THF) was then added dropwise and the reaction mixture was stirred at room temperature for 4 h. Solution was then filtered over Celite<sup>®</sup> and concentrated under vacuum. The oily residue was purified by flash chromatography (SiO<sub>2</sub>, first petroleum ether, then a mixture DCM/petroleum ether (4:1v/v) and **21** was isolated as a pale orange solid (0.13 g).

**Yield:** 58 %

**<sup>1</sup>H NMR (300 MHz, CDCl<sub>3</sub>):** δ 7.89-7.49 (m, 14 H), 2.50 (s, 1H), 2.10-1.98 (m, 4H), 1.65 (s, 6H), 1.17-1.07 (m, 4H), 0.71-0.49 (m, 10 H).

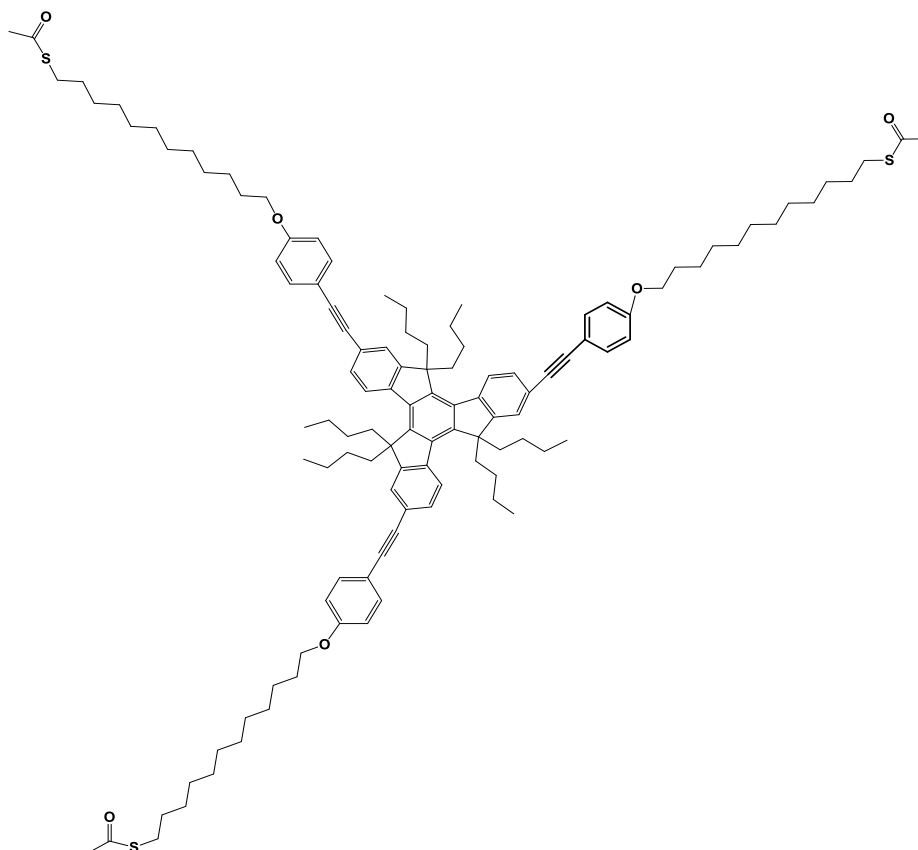


**9,9-dibutyl-7-((9,9-dibutyl-7-((4'-(3-hydroxy-3-methylbut-1-yn-1-yl)-[1,1'-biphenyl]-4-yl)ethynyl)-9H-fluoren-2-yl)ethynyl)-9H-fluorene-2-carbaldehyde (22).** Air was removed from a solution of **7** (0.05 g, 0.12 mmol) and **21** (0.1 g, 0.15 mmol) in THF (3 mL) and Et<sub>3</sub>N (0.5 mL) by argon bubbling for 20 min. Then [Pd(PPh<sub>3</sub>)<sub>2</sub>Cl<sub>2</sub>] (2.0 mg, 0.003 mmol) and CuI (1.0 mg, 0.004 mmol) were added and argon bubbling was continued for 5 min. *Tetra-*n*-*

butylammonium fluoride (TBAF) (0.13 mL, 1.0 M in THF) was then added dropwise and the reaction mixture was stirred at room temperature for 12 h. Solution was then washed with water, extracted with DCM, dried over Na<sub>2</sub>SO<sub>4</sub> and concentrated under vacuum. The oily residue was purified by flash chromatography on silica using a mixture of DCM in petroleum ether (increasing DCM from 5 to 50 % v/v) and compound **22** was isolated as a yellow solid (0.032 g).

**Yield:** 30 %

**<sup>1</sup>H NMR (300 MHz, CDCl<sub>3</sub>):** δ 10.07 (s, 1H), 7.89-7.49 (m, 20 H), 2.50 (s, 1H), 2.10-1.98 (m, 8H), 1.65 (s, 6H), 1.17-1.07 (m, 8H), 0.71-0.49 (m, 20 H).

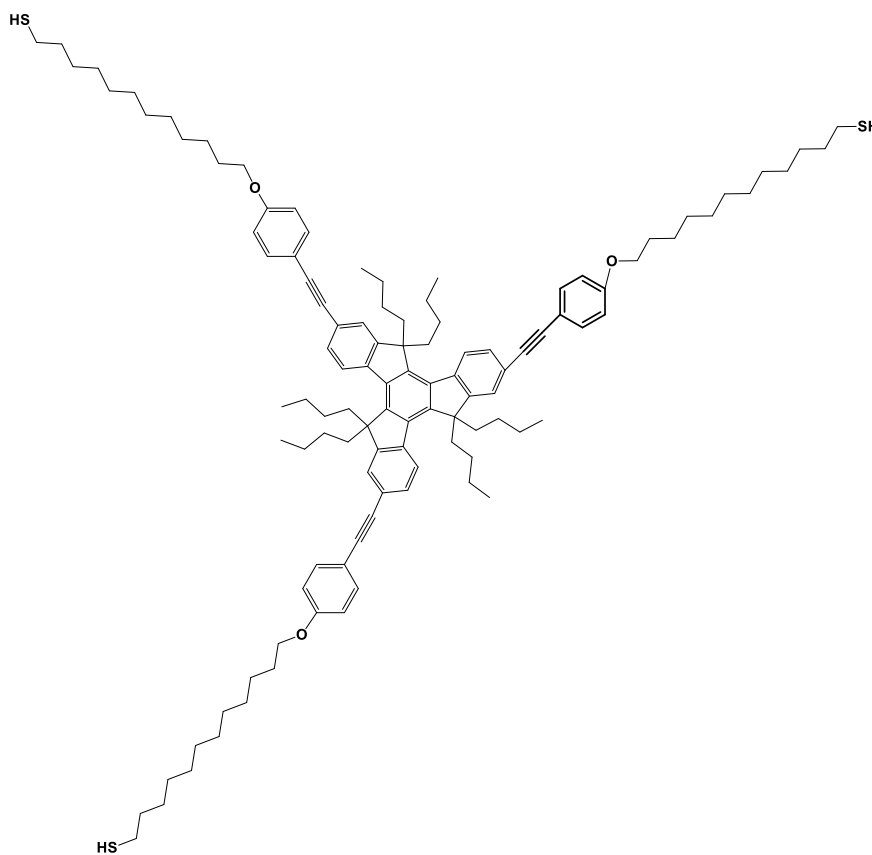


**Substituted hexabutyl truxene (23a).** A solution of triiodohexabutyltruxene **3** (0.211 g, 0.20 mmol), trimethylsilylalkyne derivative **12** (0.35 g, 0.80 mmol), CuI (0.009 g, 0.047 mmol), Pd(PPh<sub>3</sub>)<sub>2</sub>Cl<sub>2</sub> (0.015 g, 0.021 mmol), trimethylamine (0.5 mL) and tetra-*n*-butylammonium fluoride (0.8 mL, 1.0 M in THF) in THF (3 mL) was stirred under argon at 40 °C for 72 h. The mixture was evaporated to dryness and filtered on silica pad, eluting with DCM. The

residue was purified by flash chromatography on silica using a mixture of DCM in petroleum ether (gradient 40% to 60%). The product was collected as a pale yellow viscous oil (0.12 g).

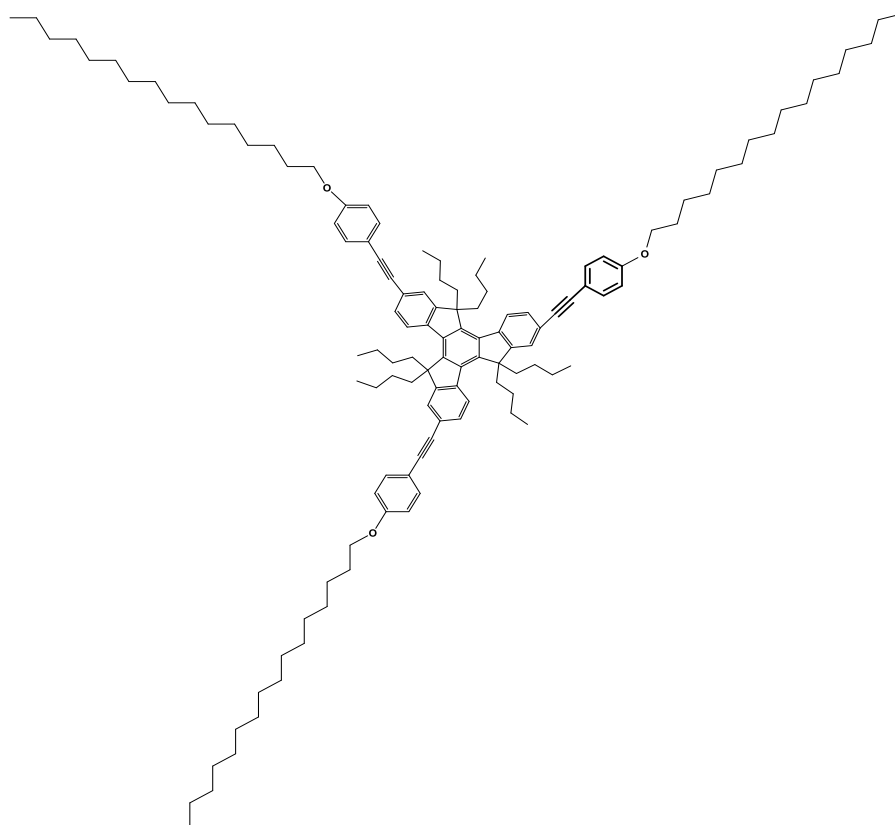
**Yield:** 34 %

**$^1\text{H}$  NMR (300 MHz,  $\text{CDCl}_3$ ):**  $\delta$  8.38 (d,  $J=8.2\text{Hz}$ , 3H), 7.65 (s, 3H), 7.60 (d,  $J=8.2\text{Hz}$ , 3H), 7.57 (d,  $J=8.8\text{Hz}$ , 6H), 7.94 (d,  $J=8.8\text{Hz}$ , 6H), 4.03 (t,  $J=6.6\text{Hz}$ , 6H), 2.99 (m, 6H), 2.91 (t,  $J=7.2\text{Hz}$ , 6H), 2.37 (s, 9H), 2.15(m, 6H), 1.85(m, 6H), 1.60 (m, 6H) 1.54 (m, 18H), 1.32 (m, 48H), 0.92 (m, 12H), 0.61(m,12H), 0.49 (t,  $J=7.2\text{Hz}$ , 18H).



**Organic assembler II: substituted hexabutyl truxene (23b).** The intermediate thioester **23a** was dissolved in ethanol (4 mL) and a solution of sodium hydroxide (0.02 g, 0.5 mmol) in water (0.2 mL). The solution was heated under argon for 24 h but an insoluble precipitate appeared due to polycondensation of the thiolate moieties in basic media. The reaction mixture was neutralized with 1 M hydrochloric acid and the precipitate was washed successively with sodium bicarbonate solution, water and methanol. It is insoluble in most organic solvents, thus it was subsequently reduced by  $\text{PBu}_3$  (0.1 mL) in a mixture of THF (6mL) and DCM (3mL) with a trace of acetic acid. The precipitate was dissolved after 6 h of

stirring at room temperature. After 3 days at room temperature, the solution was evaporated and extracted by DCM, washed with water, dried over  $\text{Na}_2\text{SO}_4$  and concentrated under vacuum, affording the product **23b** (0.182 g). However, NMR analysis revealed the presence of tributylphosphine and also remaining thioester functions.

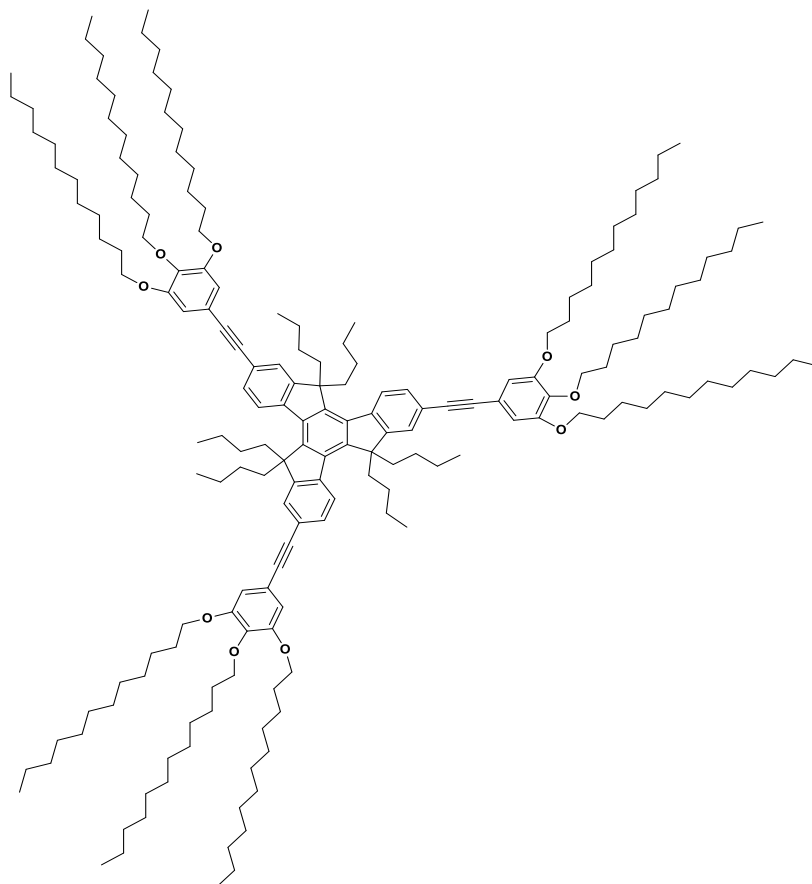


**Organic assembler III: substituted hexabutyl truxene (24).** A solution of triiodohexabutyltruxene **3** (0.264 g, 0.25 mmol), alkyne derivative **14** (0.366 g, 1.00 mmol),  $\text{CuI}$  (0.009 g, 0.047 mmol),  $\text{Pd}(\text{PPh}_3)_2\text{Cl}_2$  (0.015 g, 0.021 mmol) and trimethylamine (0.5 mL) in THF (3 mL) was kept under stirring at  $40^\circ\text{C}$  under an inert atmosphere for 72 h. After evaporation to dryness and filtration on silica pad (30% DCM in petroleum ether) the residue was purified by flash chromatography ( $\text{SiO}_2$ , 10% DCM in petroleum ether). The product was collected as a pale yellow viscous oil (0.332 g).

**Yield:** 78 %

**$^1\text{H}$  NMR (300 MHz,  $\text{CDCl}_3$ ):**  $\delta$  8.38 (d,  $J=8.2\text{Hz}$ , 3H), 7.65 (s, 3H), 7.60 (d,  $J=8.2\text{Hz}$ , 3H), 7.57 (d,  $J=8.8\text{Hz}$ , 6H), 7.94 (d,  $J=8.8\text{Hz}$ , 6H), 4.03 (t,  $J=6.6\text{Hz}$ , 6H), 2.99 (m, 6H), 2.16 (m, 6H), 1.85 (m, 6H), 1.51 (m, 6H), 1.31 (m, 72H), 0.91 (m, 21H), 0.61 (m, 12H), 0.49 (t,  $J=7.3\text{Hz}$ , 18H)





**Organic assembler IV: substituted hexabutyl truxene (25).** A solution of triiodohexabutyltruxene **3** (0.264 g, 0.25 mmol), alkyne derivative **20** (0.654 g, 1.00 mmol), CuI (0.009 g, 0.047 mmol), Pd(PPh<sub>3</sub>)<sub>2</sub>Cl<sub>2</sub> (0.015 g, 0.021 mmol) and trimethylamine (0.5 mL) in THF (3 mL) was stirred at room temperature under an inert atmosphere for 72 h. After evaporation to dryness and filtration on silica pad using a 50 % mixture of DCM in petroleum ether) the residue was purified by flash chromatography (SiO<sub>2</sub>, 20% DCM in petroleum ether). The product was collected as a pale yellow viscous oil (0.320 g).

**Yield:** 48 %

**<sup>1</sup>H NMR (300 MHz, CDCl<sub>3</sub>):** δ 8.38 (d, J=8.3Hz, 3H), 7.65 (s, 3H), 7.60 (d, J=8.3Hz, 3H), 6.85 (s, 6H), 4.04 (m, 18H), 2.99 (m, 6H), 2.15 (m, 6H), 1.85(m, 18H), 1.51 (m, 18H), 1.31 (m, 144H), 0.91 (m, 39H), 0.60(m, 12H), 0.49 (t, J=7.3Hz, 18H)

## ANNEX 2: DNA STRANDS USED FOR THE ASSEMBLY OF DNA ORIGAMI

- **A list of sequences with a thiol C6 in 5' terminus of the oligonucleotide (scale: 40 nM, purification: cartridge):**

SWTh-204: ACGTTAGTAAATGAAT TTTCTGTAAGCGGAGT

SWTh-202: TTAAAGGCCGAAAGGAAC AACTAAAGCTTTCCAG

SWTh-200: GCTCCATGAGAGGCTT TGAGGACTAGGGAGTT

SWTh-198: TTCGATTTTAGAGGACAG ATGAACGGCGCGACCT

SWTh-196: ACTGGATAACGGAACA ACATTATTACCTTATG

SWTh-194: TTTTTTTGCGCAGAAAAC GAGAATGAATGTTTAG

SWTh-192: CAAAATTAAAGTACGG TGTCTGGAAGAGGTCA

SWTh-190: TTCAGGTCACTTTTGCG GGAGAAGCAGAATTAG

SWTh-188: ACCCGTCGTCATATGT ACCCCGGTAAAGGCTA

SWTh-186: TTATTAAGTTCGCATCGT AACCGTGCGAGTAACA

SWTh-184: GCCAGCTGCCTGCAGG TCGACTCTGCAAGGCG

SWTh-182: TTTGGACTCCCTTTTCAC CAGTGAGACCTGTCGT

SWTh-179: AATAATAAGGTCGCTG AGGCTTGCAAAGACTT

SWTh-177: TTTTTCATGAAAATTGTG TCGAAATCTGTACAGA

SWTh-178: ATATATTCTTTTTTCA CGTTGAAAATAGTTAG

SWTh-176: TTCGCCTGATGGAAGTTT CCATTAAACATAACCG

SWTh-153: ATACGTAAAAGTACAA CGGAGATTTTCATCAAG

SWTh-152: TTGCGAAACATGCCACTA CGAAGGCATGCGCCGA

SWTh-151: AGTAATCTTAAATTGG GCTTGAGAGAATACCA

SWTh-150: TTACGAGTAGTGACAAGA ACCGGATATACCAAGC

SWTh-127: CCAAATCACTTGCCCT GACGAGAACGCCAAAA

SWTh-125: TTGGAATTACTCGTTTAC CAGACGACAAAAGATT

SWTh-126: GAATAAGGACGTAACA AAGCTGCTCTAAAACA

SWTh-7: TTCATAACCCGAGGCATA GTAAGAGC TTTTAAAG

SWTh-9: AAAAGTAATATCTTAC CGAAGCCCTTCCAGAG

SWTh-11: TTCCTAATTTACGCTAAC GAGCGTCTAATCAATA

SWTh-10: GCAATAGCGCAGATAG CCGAACAATTCAACCG

SWTh-12: TTTCTTACCAGCCAGTTA CAAAATAAATGAAATA  
SWTh-14: CTAATTTATCTTTTCT TATCATTCATCCTGAA  
SWTh-17: TTAATTACTACAAATTCT TACCAGTAATCCCATC  
SWTh-159: AGCTGATTACAAGAGT CCACTATTGAGGTGCC  
SWTh-160: TTAAGTGGCCGAGCTC GAATTCGTTATTACGC  
SWTh-161: CCCGGGTACTTTCCAG TCGGGAAACGGGCAAC  
SWTh-162: TTCAGCTGGCGGACGACG ACAGTATCGTAGCCAG  
SWTh-137: TCATAGCTACTCACAT TAATTGCGCCCTGAGA  
SWTh-138: TTGGCGATCGCACTCCAG CCAGCTTTGCCATCAA  
SWTh-139: GAAGATCGGTGCGGGC CTCTTCGCAATCATGG  
SWTh-140: TTAAATAATTTTAAATTG TAAACGTTGATATTCA  
SWTh-117: GCTTCTGGTCAGGCTG CGCAACTGTGTTATCC  
SWTh-118: TTGTTAAAATTTTAACCA ATAGGAACCCGGCACC  
SWTh-119: AGACAGTCATTCAAAA GGGTGAGAAGCTATAT  
SWTh-16: GCTCATTTTCGCATTA AATTTTTG AGCTTAGA  
SWTh-18: TTAAGACGTTGAAAAC ATAGCGATAACAGTAC  
SWTh-15: GCGTTATAGAAAAAGC CTGTTTAG AAGGCCGG  
SWTh-4: TTACGCTCAAATAAGAA TAAACACCGTGAATTT  
SWTh-39: GGTATTAAGAACAAGA AAAATAATTAAGCCA  
SWTh-37: TTATTATTTAACCCAGCT ACAATTTTCAAGAACG  
SWTh-40: TAAGTCCTACCAAGTA CCGCACTCTTAGTTGC  
SWTh-128: TTCTCATCTTGAGGCAAA AGAATACAGTGAATTT  
SWTh-129: TT AAACGAAATGACCCCC AGCGATTATTCATTAC

- **A list of sequences with Dy-681 (trigger) in 5' terminus of the oligonucleotide (scale: 40 nM, purification: HPLC):**

SWtrigger-38: TTTATTTTGCTCCCAATC CAAATAAGTGAGTTAA  
SWtrigger-63: TTCAAGCAAGACGCGCCT GTTTATCAAGAATCGC  
SWtrigger-42: TTAGGCGTTACAGTAGGG CTTAATTGACAATAGA

- **A list of sequences with Dy-781 (receptor 1 in the lower corner) in 5' terminus of the oligonucleotide (scale: 40 nM, purification: HPLC):**

SWRec-183: TGGTTTTTAACGTCAA AGGGCGAAGAACCATC

SWRec-185: CTTGCATGCATTAATG AATCGGCCCGCCAGGG

- **A list of sequences with ATTO 740 (receptor 2 in the upper corner) in 5' terminus of the oligonucleotide (scale: 40 nM, purification: HPLC):**

SWRec-201: ACGGCTACTTACTTAG CCGGAACGCTGACCAA

SWRec-203: GAGAATAGCTTTTGCG GGATCGTCGGGTAGCA

- **A list of sequences used to assemble QDs (trigger) into DNA origami structure:**

SWtrigger-38: TACAAACAACAAACA TTTATTTTGCTCCCAATC  
CAAATAAGTGAGTTAA

SWtrigger-63: TACAAACAACAAACA TTCAAGCAAGACGCGCCT  
GTTTATCAAGAATCGC

SWtrigger-42: TACAAACAACAAACA TTAGGCGTTACAGTAGGG  
CTTAATTGACAATAGA

The oligonucleotide TGTTTGTTGTTTGTA-NH<sub>3</sub> was then hybridized with the staples elongated with TACAAACAACAAACA sequences.

- **Expected configuration of DNA origami**

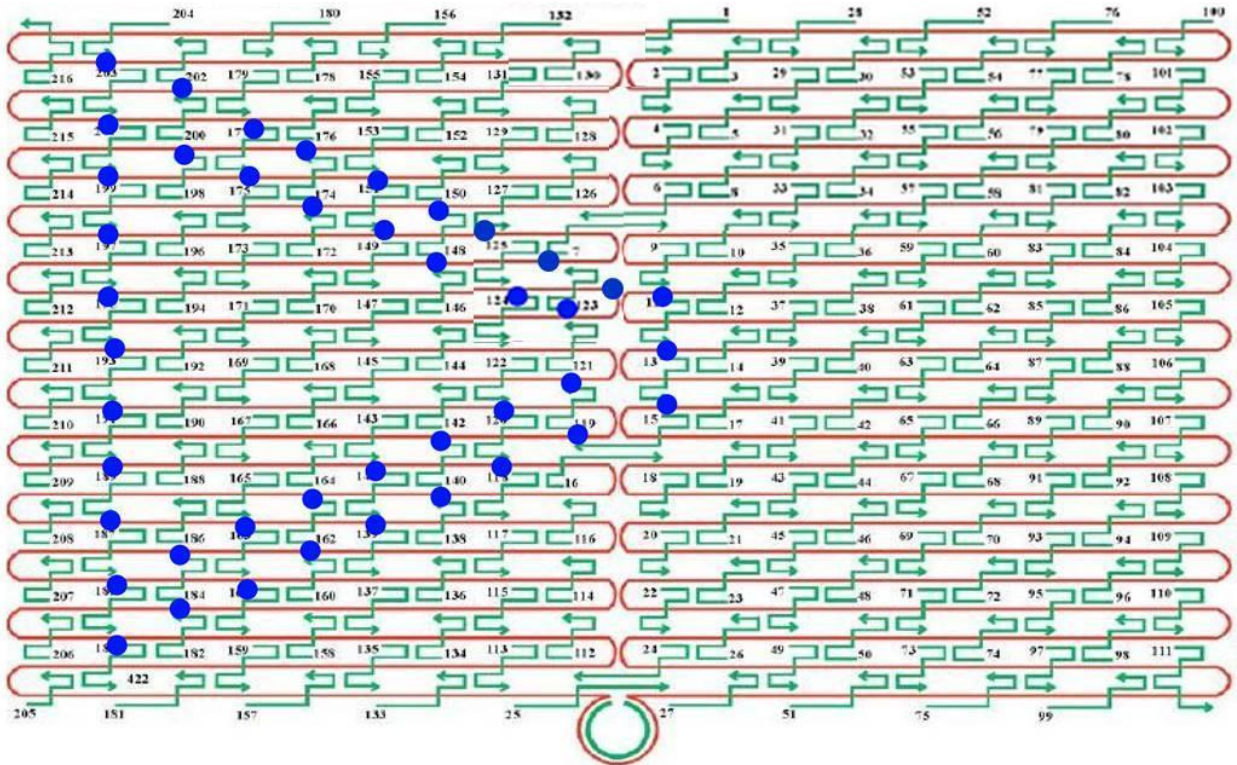


**Figure A.1 : Configuration of a rectangular DNA origami. A long viral single strand (red) is folded by short staple strands (green). Blue points denote positions where staples are elongated with short, thiol-terminated poly-T sequences.**

## ANNEX 3: CHARACTERIZATION TECHNIQUES

- **Colocalized AFM and dark-field scattering microscopy (DFSMS)**

Colocalized dark-field scattering and atomic force microscopies allow determination of the morphology, orientation, anisotropy and the electromagnetic enhancement efficiency of single gold nanoobjects as small as 35 nm. The DFSM/AFM setup developed by D. Talaga *et al.* [8], [9] is shown in the Figure 2. AFM phase images were realized in soft tapping mode by means of commercially available silicon cantilevers (Nanosensors, PPP-NCST, nominal resonance frequency 160 kHz, nominal force constant 7.4 N/m).

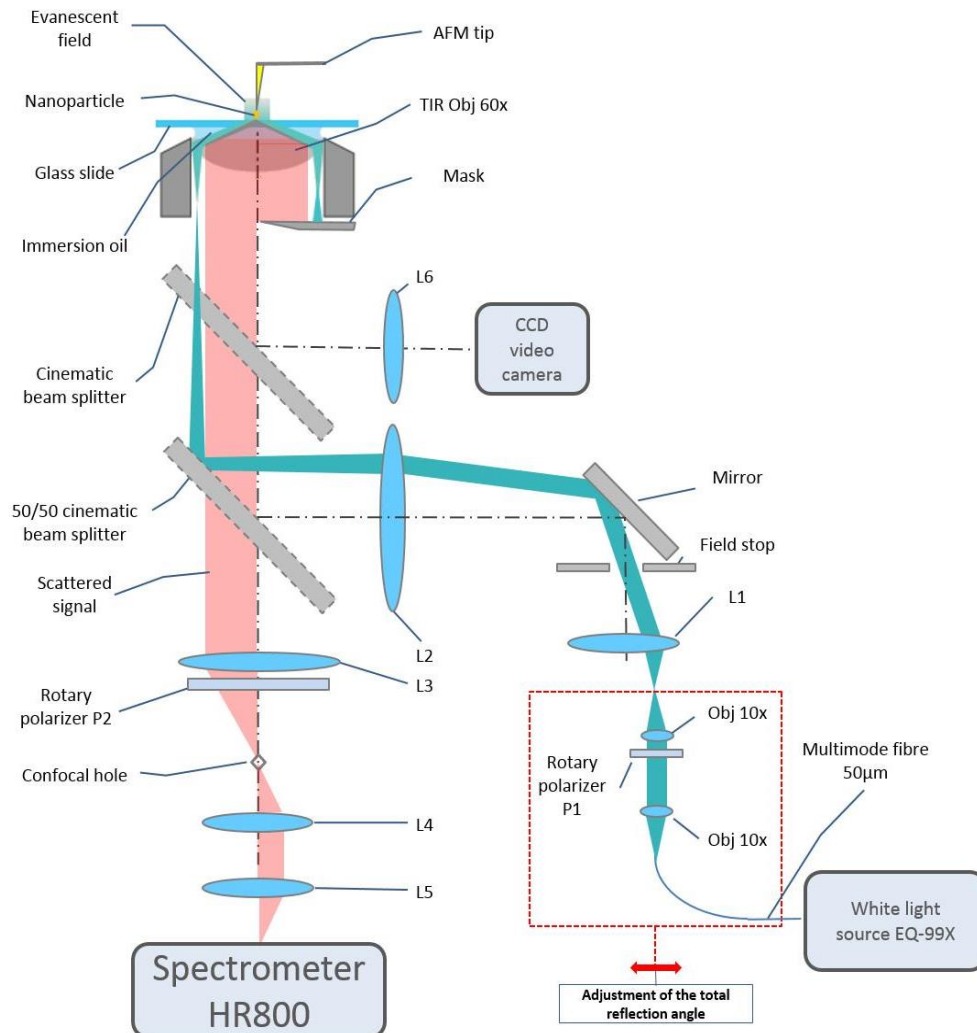


**Figure A.2 : Schematic illustration of an instrument combining AFM and DFSM.**

- **UV-Visible spectroscopy**

Optical characterization of the nanoparticles in solution was carried out by UV-Vis spectroscopy with a Lambda 950 PerkinElmer spectrophotometer. The absorption spectra were recorded in the range from 400 to 1200 nm.

- **Transmission electron microscopy (TEM)**

The electron microscopy was used to determine the morphology, the structure and the composition of the synthesized nanostructures. The images were obtained with a Hitachi H-600 microscope operating at 75 kV. The additional studies of the chemical composition of the nanostructures were performed by High Resolution TEM (HRTEM) coupled with Energy Dispersive X-ray Spectroscopy (EDX). The images were obtained with a JEOL 2200 FS microscope operating at 200kV.

A drop of the solution containing nanostructures was deposited onto a copper grid coated with carbon membrane and the excess of solution was removed by a filter paper. In the case of AuNRs trimers, the highly diluted solutions were prepared (50-fold) to avoid any unwanted aggregation of AuNRs due to drying effect.

- **An optical setup for the two-photon polymerization**

The photopolymerization process was performed with a femtosecond laser at  $\lambda = 532$  nm, focused by a 100 x /1.3NA water immersion objective. The fluorescence spectra and images were collected with a spectrometer that was coupled to an inverted microscope.

An optical setup for the photopolymerization process is shown in the Figure 3. The pinhole is placed in the focal position of Len1. The laser beam passes through the pinhole and is filtered by it. Then, Len2 with a longer focus length expands the beam, leading to high-quality light spot with homogeneous light intensity distribution. The two Irises with adjustable apertures are used to ensure the straight propagation of light. A collimated beam is then reflected by a mirror and vertically passes into the microscope. By adjusting the objective lens, a focused spot can be achieved on the substrate. Additionally, by changing the size of aperture of Iris-2, the size of focused spot can be controlled.

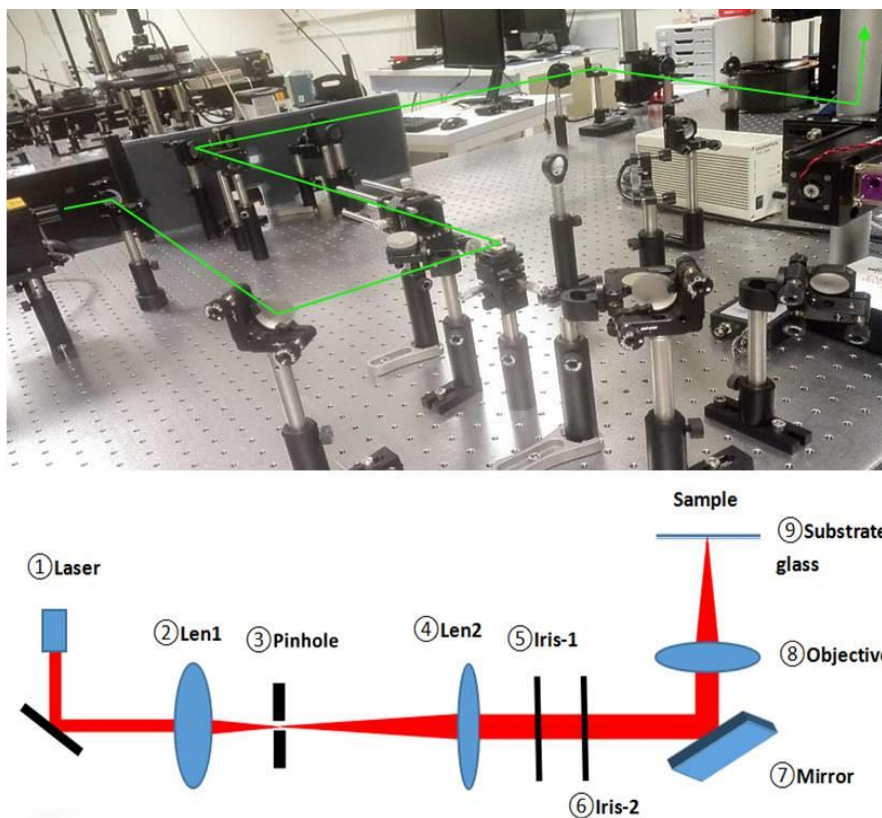


**Figure A.3 : The image and the schematic illustration of the optical setup used for the two-photon polymerization.**

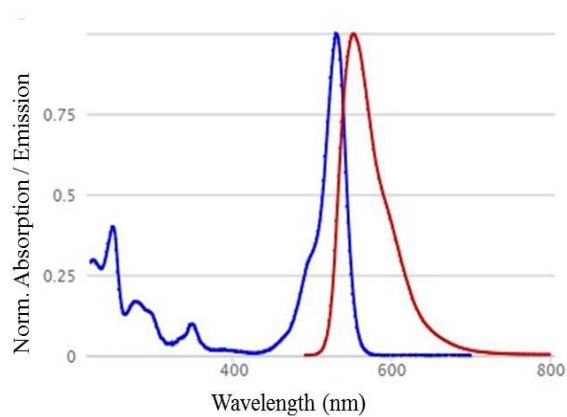


**Figure A.4 : Normalized absorption and emission spectra of Rhodamine 6G in ethanol.**



## REFERENCES

- [1] E. Dehmlow and T. Kelle, "Synthesis of new truxene derivatives: Possible precursors of fullerene partial structures?," *Synth. Commun.*, vol. 27, no. 11, pp. 2021–2031, 1997.
- [2] M. Yuan, Z. Liu, J. Guo, H. Chen, W. Yu, G. Xue, and D.-S. Liu, "Acceptor or donor (Diaryl B or N) substituted octupolar truxene : Synthesis, structure and charge-transfer enhanced fluorescence," *J. Org. Chem.*, vol. 71, no. 20, pp. 7858–7861, 2006.
- [3] O. Mongin, M. Sankar, M. Charlot, Y. Mir, and M. Blanchard-Desce, "Strong enhancement of two-photon absorption properties in synergic 'semi-disconnected' multiporphyrin assemblies designed for combined imaging and photodynamic therapy," *Tetrahedron Lett.*, vol. 54, no. 48, pp. 6474–6478, 2013.
- [4] G. Marzari, J. Durantini, D. Minudri, M. Gervaldo, L. Otero, F. Fungo, G. Pozzi, M. Cavazzini, S. Orlandi, and S. Quici, "Fluorous molecules for dye-sensitized solar cells: Synthesis and characterization of fluorene-bridged donor/acceptor dyes with bulky perfluoroalkoxy substituents," *J. Phys. Chem. C*, vol. 116, no. 40, pp. 21190–21200, 2012.
- [5] Y. Tian, W.-C. Wu, C.-Y. Chen, T. Strovas, Y. Li, Y. Jin, F. Su, D. R. Meldrum, and A. K.-Y. Jen, "2,1,3-Benzothiadiazole (BTD)-moiety-containing red emitter conjugated amphiphilic poly(ethylene glycol)-block-poly( $\epsilon$ -caprolactone) copolymers for bioimaging," *J. Mater. Chem.*, vol. 20, no. 9, pp. 1728–1736, 2010.
- [6] T. A. Gschneidner and K. Moth-Poulsen, "A photolabile protection strategy for terminal alkynes," *Tetrahedron Lett.*, vol. 54, no. 40, pp. 5426–5429, 2013.
- [7] T. Cardolaccia, Y. Li, and K. S. Schanze, "Phosphorescent platinum acetylide organogelators," *J. Am. Chem. Soc.*, vol. 130, no. 8, pp. 2535–2545, 2008.
- [8] D. Talaga, M. Comesaña-Hermo, S. Ravaine, R. A. L. Vallée, and S. Bonhommeau, "Colocalized dark-field scattering, atomic force and surface-enhanced Raman scattering microscopic imaging of single gold nanoparticles," *J. Opt.*, vol. 17, no. 11, p. 114006, 2015.
- [9] N. Vilar-Vidal, S. Bonhommeau, D. Talaga, and S. Ravaine, "One-pot synthesis of gold nanodimers and their use as surface-enhanced Raman scattering tags," *New J. Chem.*, vol. 40, no. 9, pp. 7299–7302, 2016.







# **Titre : Fabrication par voie ascendante d'un nano-dispositif plasmonique pour le guidage de la lumière**

## **Résumé :**

Le développement des nouvelles technologies de l'information et de la communication nécessite la miniaturisation et l'intégration des dispositifs optiques. La plasmonique, qui utilise des nanostructures métalliques pour manipuler la lumière à l'échelle nanométrique, permet la réalisation de dispositifs optiques jusqu'à des limites ultimes. Le but de la présente étude est de concevoir et de fabriquer des nanoarchitectures complexes qui peuvent être incorporées dans différents dispositifs plasmoniques capables de guider la lumière de manière active. Diverses nanostructures d'or, telles que des nanotriangles d'or creux ou des nanotripodes enrobés d'or, ont été synthétisés et assemblés en utilisant des liens moléculaires ou un origami d'ADN. Les propriétés optiques des nanodispositifs fabriqués ont été étudiées afin de démontrer leur capacité à guider la lumière.

**Mots clés :** plasmonique, guidage de la lumière, nanostructures d'or multi-branchées, auto-assemblage.

---

# **Title : Bottom-up fabrication of a plasmonic nanodevice for guiding light**

## **Abstract :**

The development of new information and communication technologies requires the miniaturization and integration of optical devices. Plasmonics, a field of optics that utilizes metallic nanostructures to manipulate light at the nanoscale, enables the scaling of optical devices down to ultimate limits. The purpose of the present study is to design and fabricate complex nanoarchitectures that can be incorporated into different plasmonic devices able to guide light in an active way. Various gold nanostructures, such as hollow gold nanotriangles or gold coated nanotripods, were synthesized and assembled using molecular linkers or a DNA origami template. The optical properties of the fabricated nanodevices were investigated in order to evidence their ability to guide light.

**Keywords :** plasmonics, light routing, multi-branched gold nanostructures, self-assembly.